



Corrosion Susceptibility of Multi Principal Element Alloys in Aqueous Environments

(Korrosionsanfälligkeit von Multihauptelementlegierungen in
wässrigen Medien)

Von der Fakultät für Mathematik und Naturwissenschaften
der Carl von Ossietzky Universität Oldenburg
zur Erlangung des Grades und Titels

Doktor der Naturwissenschaften (Dr. rer. nat.)
angenommene Dissertation

von Frau **Annica Wetzel**, MSc.
geboren am 04.08.1993 in Berlin

Berlin, April 2024

Die experimentelle Arbeit dieser Dissertation erfolgte im Zeitraum von Januar 2020 bis Juli 2023 im Fachbereich 6.2 für Grenzflächenprozesse und Korrosion von Dr. Özlem Özcan unter Anleitung von Dr. Julia Witt an der Bundesanstalt für Materialforschung und -prüfung (BAM), Berlin. Die finale Dissertationszusammenfassung und -vollendung wurde von Prof. Dr. Gunther Wittstock, Institut für Chemie, Fakultät für Mathematik und Naturwissenschaften der Universität Oldenburg betreut. Die BAM-interne Kooperation mit Herrn Dr. Jörg Radnik aus der Abteilung 6.1 und die Kooperation mit Herrn Dr. Paul Dietrich von der SPECS Surface Nano Analysis GmbH, Berlin erlaubten die Aufnahme von XPS-Spektren. Die respektiven XPS-Spektren finden sich in Kapitel 7.1 und 7.2 wieder. Eine zusätzliche Kooperation mit Herrn Dr. Marcus von der Au aus der Abteilung 1.4 (BAM) ermöglichte quantitative ICP-MS Analysen. Die Resultate wurden anschließend publiziert. Weitere ICP-MS Messungen, die in der Arbeit präsentiert werden, wurden von Herrn Dr. Marcus von der Au durchgeführt. Die externe Kooperation mit Herrn Jakub Czerski der AGH Technisch-Wissenschaftlichen Universität, Krakau führte zu einer weiteren Publikation zu der ich die Charakterisierung der Korrosionsprozesse mittels in-situ AFM meinerseits beitrug. Langzeitexperimente in Kooperation mit Frau Dr. Izabella Brand, Universität Oldenburg wurden meinerseits mit elektrochemischen Untersuchungen unterstützt. Die respektiven XPS-Spektren in Kapitel 7.3 wurden von Frau Dr. Brand aufgenommen. Während der Großteil der SEM-Analysen meinerseits durchgeführt wurden, wurden die SEM-Aufnahmen der Langzeituntersuchungen in Kapitel 7.3 von Frau Michaela Buchheim aus der Abteilung 5.1 (BAM) durchgeführt. Durch die Betreuung des Masterstudenten Daniel Morell wurden einige Messungen für die Aufklärung des transpassiven Bereiches unter meiner Anleitung durchgeführt. Die Resultate dienten als Grundlage für eine Publikation. Zusätzlich arbeitete ich mit Yasemin Yesilcicek aus der Arbeitsgruppe Özcan zusammen. Während des Promotionsstudiums leitete ich auszubildende Chemielaboranten und die MSc.-Abschlussarbeit von Daniel Morell an. Die im Rahmen dieser Arbeit getesteten Konzepte zur Untersuchung des Korrosionsverhaltens von Multihauptelementlegierungen wurden bei der weiteren Konzeption der eigenen Arbeiten berücksichtigt.

Gutachter: Prof. Dr. Gunther Wittstock
Zweitgutachter: Prof. Dr. Heinz Sturm
Tag der Disputation: 28.06.2024

Abstract

This thesis investigates the corrosion properties and behavior of the two Multi Principal Element Alloys (MPEAs) CrMnFeCoNi and CrCoNi in different aqueous environments. Research in MPEAs sparked in the early 2000s, with CrMnFeCoNi representing one of the initial MPEA systems that revealed solid state solutions with a single phase and desirable mechanical properties such as high strength. In the following years, MPEAs received significant attention in the material and electrocatalysis science communities due to their remarkable properties including thermal stability and hardness as well as corrosion and wear resistance. Moreover, their electrochemical stability within a wide pH range and the freedom in chemical design gained MPEAs a rising interest in corrosion and electrocatalysis research. While in the literature a substantial body of research is dedicated to the investigation of corrosion characteristics of MPEAs with 5 or more component elements (CrMnFeCoNi), MPEAs with 4 or 3 elements (CrCoNi) are underrepresented.

The focus of this work lies on the general corrosion analysis of the two MPEAs in aqueous NaCl and H₂SO₄ containing media through potentiodynamic polarization techniques in combination with the analysis of the protective passive film through electrochemical impedance spectroscopy and X-ray photoelectron spectroscopy. The respective results are further supported by the quantitative analysis of dissolved metals in the corrosion electrolytes through inductively coupled mass spectrometry. Local corrosion processes due to alloy surface imperfections (inclusions, possible defects at grain boundaries, etc.) in the microstructure of the base materials or processing related changes in the surface microstructure are investigated by ex- and in-situ methods including scanning electron microscopy and atomic force microscopy. To evaluate the alloys' corrosion characteristics when exposed to corrosive media over longer periods of time, long-term immersion tests are presented and discussed. Finally, the promising electrochemical properties of some MPEAs hold the potential for the application in electrochemical catalysis. Using scanning electrochemical microscopy with tip substrate voltammetry, the onset of the oxygen evolution reaction on CrMnFeCoNi and CrCoNi is examined in NaCl at three different pH levels. Coupling these electrochemical measurements with the quantitative analysis of corrosion electrolytes through ICP-MS and UV Vis spectroscopy, the corrosion characteristics of the transpassive region are determined.

Zusammenfassung

In dieser Arbeit werden die Korrosionseigenschaften und das Korrosionsverhalten der beiden Multihauptelementlegierungen (MPEAs) CrMnFeCoNi und CrCoNi in unterschiedlichen wässrigen Umgebungen untersucht. Die Forschung auf dem Gebiet der MPEAs begann in den frühen 2000er Jahren, wobei CrMnFeCoNi eines der ersten MPEA-Systeme war, das einphasige Mischkristalle mit wünschenswerten mechanischen Eigenschaften wie hoher Festigkeit bildete. In den folgenden Jahren erhielten MPEAs aufgrund ihrer bemerkenswerten Eigenschaften wie thermische Stabilität und Härte sowie Korrosions- und Verschleißbeständigkeit große Aufmerksamkeit in der Material- und Elektrokatalysforschung. Auch ihre elektrochemische Stabilität innerhalb eines breiten pH-Bereichs und die Freiheit bei der chemischen Zusammensetzung verschafften den MPEAs ein wachsendes Interesse in der Korrosions- und Elektrokatalysforschung. Während in der Literatur ein beträchtlicher Teil der Forschung der Untersuchung der Korrosionseigenschaften von MPEAs mit 5 oder mehr Bestandteilen (CrMnFeCoNi) gewidmet ist, sind MPEAs mit 4 oder 3 Elementen (CrCoNi) unterrepräsentiert.

Der Schwerpunkt dieser Arbeit liegt auf der allgemeinen Korrosionsanalyse der beiden MPEAs in wässrigen NaCl- und H₂SO₄-haltigen Medien mit Hilfe potentiodynamischer Polarisierungstechniken in Kombination mit der Analyse der schützenden Passivschicht durch elektrochemische Impedanzspektroskopie und Röntgen-Photoelektronen-Spektroskopie (XPS). Die entsprechenden Ergebnisse werden durch die quantitative Analyse der gelösten Metalle in den Korrosionselektrolyten mittels induktiv gekoppelter Massenspektrometrie (ICP-MS) unterstützt. Lokale Korrosionsprozesse, die auf Unvollkommenheiten der Legierungsoberfläche (z.B. Einschlüsse, mögliche Defekte an Korngrenzen usw.) im Gefüge der Grundwerkstoffe oder auf verarbeitungsbedingte Veränderungen des Oberflächengefüges zurückzuführen sind, werden mit Ex-situ- und In-situ-Methoden einschließlich Rasterelektronenmikroskopie und Atomkraftmikroskopie untersucht. Um die Korrosionseigenschaften der Legierungen zu bewerten, wenn sie über längere Zeiträume korrosiven Medien ausgesetzt sind, werden Langzeittauchversuche vorgestellt und diskutiert. Schließlich bieten die vielversprechenden elektrochemischen Eigenschaften einiger MPEAs das Potenzial für die Anwendung in der Elektrokatalyse. Mit Hilfe der elektrochemischen Rasterelektronenmikroskopie mit Tip-Substrat-Voltammetrie wird der Beginn der Sauerstoffentwicklungsreaktion auf CrMnFeCoNi und CrCoNi in NaCl bei drei verschiedenen pH-Werten untersucht. Durch Kopplung dieser elektrochemischen Messungen mit der quantitativen Analyse der Korrosionselektrolyte mittels ICP-MS und UV-Vis-Spektroskopie werden die Korrosionseigenschaften des transpassiven Bereichs der beiden MPEAs bestimmt.

Danksagung

Mein besonderer Dank gilt Frau Dr. Özlem Özcan und Frau Dr. Julia Witt für die interessante Themenstellung und Anleitung bei der Durchführung, die kontinuierliche Unterstützung durch Ratschläge und Anmerkungen sowie ihre Bereitschaft, Resultate kritisch und ausführlich zu diskutieren, haben mich stets motiviert und mir zum erfolgreichen Ausführen meiner Arbeit verholfen.

Darüber hinaus gilt mein besonderer Dank Herrn Prof. Dr. Gunther Wittstock für seine uneingeschränkte Bereitschaft meine Arbeit im finalen Stadium zu betreuen und das Erstgutachten zu übernehmen.

Des Weiteren danke ich Herrn Prof. Dr. Heinz Sturm für die freundliche Übernahme des Zweitgutachtens.

Für die finanzielle Unterstützung dieser Arbeit möchte ich mich bei der Bundesanstalt für Materialforschung und -prüfung bedanken.

Bei Herrn Matthias Dimper möchte ich mich für die fortwährende Unterstützung bei allen möglichen Labor- und technischen Angelegenheiten sowie der Einarbeitung am AFM bedanken. Es gab nichts, was Herr Dimper nicht hätte bauen oder herstellen können, sei es eine spezielle elektrochemische Zelle für das SECM oder das Herstellen von Legierungen am Lichtbogenofen.

Meinen tiefen Dank für das freundschaftliche Arbeitsklima und die vielseitigen Hilfestellungen möchte ich allen ehemaligen und aktuellen Mitarbeitern des Arbeitskreises Özcan aussprechen. Frau Yasemin Yesilcicek danke ich besonders für die Unterstützung und wunderbaren Erfahrungen bei wissenschaftlichen Tagungen. Für den Einsatz und das Interesse an meiner Arbeit möchte ich mich bei meinem ehemaligen Auszubildenden Frau Xenia Körner, Antonia Frenz und Amina Pahl und meinem ehemaligen Masterstudenten Herrn Daniel Morell bedanken.

Des Weiteren gilt mein Dank Frau Marina Staudt, an die ich mich immer bei administrativen Fragestellungen wenden konnte.

Herrn Dr. Marcus von der Au danke ich vielmals für die stete Bereitschaft meine Korrosionslösungen quantitativ mit dem ICP-MS zu messen.

Herrn Jakub Czerski danke ich für die hervorragende Zusammenarbeit, die er damals durch die Kontaktaufnahme nach einer Konferenz in die Wege geleitet hatte. Sein Durchhaltevermögen beim Publizieren unserer Ergebnisse führten trotz etlicher Hürden zum Erfolg.

Frau Dr. habil. Izabella Brand danke ich für die Unterstützung bei den Durchführungen der XPS-Messungen der Langzeituntersuchungen.

Meinen Eltern Micha und Gabriele danke ich für das Ermöglichen meiner umfangreichen Ausbildung und ihre uneingeschränkte Unterstützung. Vor allem danke ich Sol für seine uneingeschränkte und liebevolle Unterstützung während des Promotionsstudiums und des Schreibens meiner Doktorarbeit. An dieser Stelle danke ich auch meiner Schwiegerfamilie sowie der entfernten Schwiegerfamilie in Korea für ihre Überzeugung in meinen Fähigkeiten und stetige Motivation.

Abschließend möchte ich mich bei meinen Freunden und Trainern bedanken, die mich in den richtigen Momenten aufbauten und für die erforderliche Abwechslung sorgten.

Contents

1	Introduction	1
2	Materials Science of Metals	4
2.1	Metal Structures and Defects	4
2.2	Mechanical Properties of Metals.....	6
2.3	Defects and Strengthening in Metals.....	7
3	Multi Principal Elements Alloys	9
3.1	Multi Principal Element Alloys and Manufacturing Processes.....	9
3.2	Key Properties of Multi Principal Element Alloys	11
3.2.1	High Entropy Effect	11
3.2.2	Sluggish Diffusion	12
3.2.3	Lattice Distortion	13
3.2.4	Cocktail Effect	13
4	Corrosion	14
4.1	Redox Reactions and Corrosion.....	14
4.2	Effects of Metal Structures on Corrosion	15
4.3	Basics of Electrochemical Corrosion	16
4.3.1	Definitions	16
4.3.2	Thermodynamic Considerations of Electrochemical Reactions	18
4.3.3	Kinetic Considerations of Electrochemical Reactions	21
4.4	Passivity and Modes of Corrosion	24
4.5	Corrosion of MPEAs.....	30
5	Applied Characterization Methods.....	34
5.1	Electrochemical Characterization of the Corrosion Behavior	34
5.1.1	Polarization Measurements	34
5.1.2	Electrochemical Impedance Spectroscopy	37
5.2	Surface Characterization by Scanning Probe Microscopy	39
5.2.1	Atomic Force Microscopy	39
5.2.2	Scanning Electrochemical Microscopy	43

5.2.3	Scanning Electron Microscopy	45
5.3	Quantitative Surface and Electrolyte Characterization	47
5.3.1	X-Ray Photoelectron Spectroscopy	47
5.3.2	Inductively Coupled Plasma Mass Spectrometry	50
6	Experimental.....	52
6.1	Chemicals	52
6.2	Materials	53
6.3	Preparation of Metal Interface	54
6.4	Instrumentation for General Electrochemical Investigations	55
6.5	Instrumentation Used for Alloy Surface Characterization.....	58
7	Corrosion of MPEAs CrMnFeCoNi and CrCoNi in Aqueous Solutions.....	63
7.1	Behavior in NaCl Solution.....	63
7.1.1	General Electrochemical Behavior	64
7.1.2	Passive Film Characteristics	68
7.1.3	Corrosion Mechanism in Chloride-Containing Electrolyte	76
7.2	Behavior in H ₂ SO ₄ Solution	83
7.2.1	General Electrochemical Behavior	83
7.2.2	Passive Film Characteristics	86
7.2.3	Corrosion mechanism	91
7.3	Long-term Corrosion in 1 M H ₂ SO ₄	96
7.4	Conclusion	105
8	Electrochemical Behavior at High Anodic Potentials in Chloride-Containing Aqueous Media.....	107
8.1	Transpassivity and Oxygen Evolution Reaction.....	107
8.2	Transpassive Behavior of CrMnFeCoNi	109
8.2.1	Electrochemical Characteristics at pH 2	109
8.2.2	Influence of pH.....	110
8.2.3	Local Dissolution Behavior	113
8.3	Transpassive Behavior of CrCoNi	120
8.3.1	Electrochemical Characteristics at pH 2	120

8.3.2	Oxygen Evolution Reaction at High Anodic Potentials.....	121
8.3.3	Influence of pH.....	130
8.3.4	Local Dissolution Behavior.....	134
8.4	The Influence of High Anodic Potentials on CrCoNi compared to CrFeNi in simulated seawater.....	140
8.5	Conclusion.....	145
9	Summary and Outlook.....	147
10	Appendix.....	149
11	List of Abbreviations.....	160
11.1	Physical Quantities.....	160
11.2	General Abbreviation.....	162
12	References.....	164
13	Own Publications and Conference Contributions.....	175
13.1	Publications.....	175
13.2	Conference Contributions.....	175
14	Curriculum Vitae.....	177

1 Introduction

Conventional alloys such as ferrous, nickel, aluminum or copper alloys are produced based on one principal constituent to which secondary elements are added to alter the properties of the material in a desired way. For example, to be used as a durable tool or weapon, copper was alloyed with tin to overcome the inherent softness of copper. The resulting alloy, bronze, is stronger and harder than pure copper.^[1-2] As this propelled civilization from the stone age to the bronze age, so did other alloys with specific functional properties lead to application breakthroughs in our modern society. Some examples include superalloys, gum metals and stainless steels. Superalloys are classified into three subgroups, Ni, Co, and Ni-Fe based.^[3] They present outstanding heat-resistant properties and are widely used as aerospace structural materials.^[4] Gum metals are Ti-based quaternary Ti-Nb-Ta-Zr alloys with high elasticity and formability that due to their distinguished biocompatibility find applicability in medicine.^[5] While widely known, stainless steels offer a vast field of application from small surgical instruments to large structural elements because of their good corrosion resistance and mechanical strength.^[6-7]

With ongoing technological advances and demands, the search for new materials with improved functional properties does not cease. Alloys based on one principal element are limited in their total number of possible element combinations. In fact, this limitation can be observed in phase diagrams which represent stable homogeneous portions of a system with uniform chemical and physical characteristics (phases) with respect to temperature and composition for alloys.^[8] Typically, conventional alloys accumulate close to the edges and corners, leaving the numerous combinations at the phase diagram's center inevitably unexplored.^[9-10] For carbon steels, the Fe-Fe₃C phase diagram only shows the compositions of C of up to 6.7wt% C, after which Fe₃C (cementite) predominantly forms, and consequentially the 6.7wt% C are considered 100% Fe₃C (see Figure 1.1a).^[8] Moving away from one base element to which others are marginally alloyed to employing multiple main constituents yields phase diagrams that increase in dimensional space and with that generates more possible alloy combinations. To visualize the increasing complexity with the number of alloy components, Figure 1.1b shows a simulated ternary phase diagram for CrCoNi, and Figure 1.1c schematically illustrates how a quaternary phase diagram could be constructed. The complexity is underlined by the fact that binary phase diagrams allow to determine the phases formed with changing temperature and composition. Upon mixing three components, phase diagrams must be constructed at a certain temperature or composition as shown in Figure 1.1b and c which represent the phases with change in composition at a constant temperature.

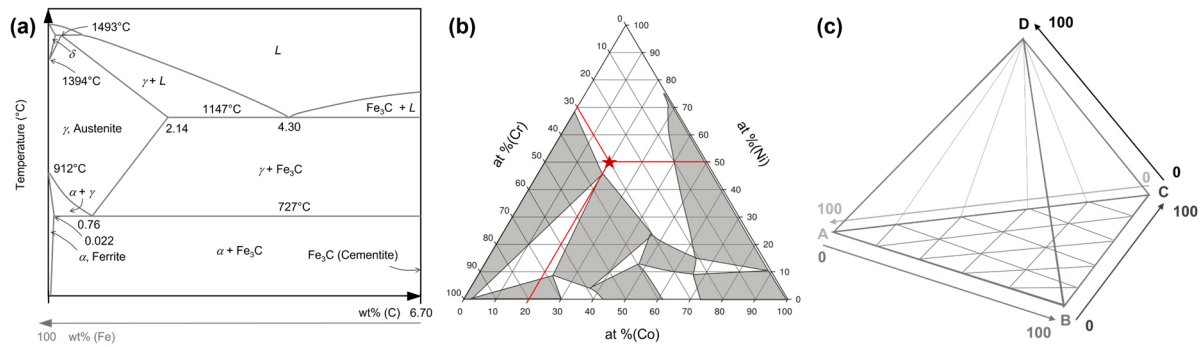


Figure 1.1. Exemplary phase diagrams of (a) binary conventional carbon steel, (b) ternary CrCoNi alloy and (c) a generic quaternary alloy. (a) The Fe-Fe₃C phase diagram where the maximum composition of C is 6.7 wt% shows the phases formed in relation to temperature and composition. (b) The CrCoNi phase diagram shows the different phases depending on composition at 600°C, simulated with Thermo-Calc. (c) The generic phase diagram represents the compositional space of formed phases of a quaternary alloy ABCD at a set temperature.

In their initial publication on equiatomic multicomponent alloys, Cantor et al.^[11] described their investigation of the central region of the phase diagram for different multicomponent transition metal alloys. Independently, Yeh et al.^[12] also reported an alloy design approach that employs multiple principal elements in equimolar and near-equimolar ratios. They introduced the non-conventional hypothesis that, due to their large configurational entropy of mixing ΔS_{conf} , the resulting solid solutions of multiple components will be more stable than alloys with less elements. More specifically, the increased configurational entropy of mixing is assumed to be large enough to overcome the formation enthalpies $\Delta_f H$ of intermetallic compounds. Due to this hypothesis, the authors coined the term “high entropy alloys”. Detailed definitions on metallurgical terms are discussed in Chapter 2.

The mere number of possible multiple element alloy combinations exceeds 5 million for 5-component equimolar alloys considering 60 elements of the periodic table as usable.^[13] Thus, many studies have focused on producing new alloys by combining multiple principal elements. The resulting alloys are consequentially termed multi principal element alloys (MPEAs). These initial studies focused on investigating the alloys’ mechanical and microstructural properties.^[14-17] To explore applications for these alloys, this thesis focuses on the two model MPEAs CrMnFeCoNi and CrCoNi, and their corrosion behavior in aqueous media. The two alloys are comparable in their random texture and grain sizes.^[18] Mechanically, they exhibit high yield strength, tensile strength, and ductility which increase with decreasing temperature.^[19-21] In their study, Laplanche et al.^[18] describe the mechanical superiority of CrCoNi over CrMnFeCoNi and report an earlier onset of twinning stresses. Deformation by twinning may increase ductility and it contributes to the observed higher yield strength and work hardening rate.^[18, 22] For exploring new fields of application, resistance to corrosive deterioration is imperative for safe and economically feasible operation of these materials aside from their promising mechanical properties. Previous corrosion studies of CrMnFeCoNi and CrCoNi demonstrated that the two systems behave dissimilarly in different aqueous environments.^[23-25]

Specifically, this thesis seeks to examine the corrosion characteristics and interfacial reactions in aqueous media of two model MPEAs (equimolar CrCoNi and CrMnFeCoNi). Accordingly, Chapter 2 briefly outlines the materials science of metals and alloy systems to then discuss the concept of MPEAs in Chapter 3. Chapter 4 discusses relevant corrosion electrochemistry including an overview on published corrosion studies of CrCoNi and CrMnFeCoNi. Chapters 5 and 6 describe the surface specific characterization methods employed within this work and the corresponding experimental details. The results are then presented in Chapters 7 and 8. While Chapter 7 focusses on the general corrosion and oxide film properties in NaCl- and H₂SO₄-based electrolytes, the dissolution and water splitting behavior at high anodic potential is elucidated in Chapter 8. Lastly, Chapter 9 summarizes the findings presented in this work and discloses an outlook for future research.

2 Materials Science of Metals

For metals and alloys the onset and progression of aqueous corrosion is largely influenced by the complexity of their surface microstructure and composition. Metal corrosion in general is a redox process, in which anodic and cathodic partial reactions proceed simultaneously at the same metal part. The structure of metallic specimens determines whether the oxidation and reduction sites are localized or fluctuate, resulting in local corrosion phenomena such as pitting or general corrosion (Chapter 4.4), respectively. This chapter will give an overview on metallic microstructures, structural heterogeneities and defects which can influence the corrosion behavior of metals and alloys.

2.1 Metal Structures and Defects

Metals and alloys, which are metallic substances made up of two or more elements, are polycrystalline solids.^[26] The individual crystals in a single-phase metallic specimen are termed grains which have the same structure and composition but are oriented differently. The boundary between grains of different orientation is referred to as grain boundary (Figure 2.1). Microstructural differentiations can be made based on the misorientation between adjoining grains, where a misorientation of more than 15 degrees is considered a high-angle grain boundary otherwise it is a low-angle grain boundary (Figure 2.1).^[27]

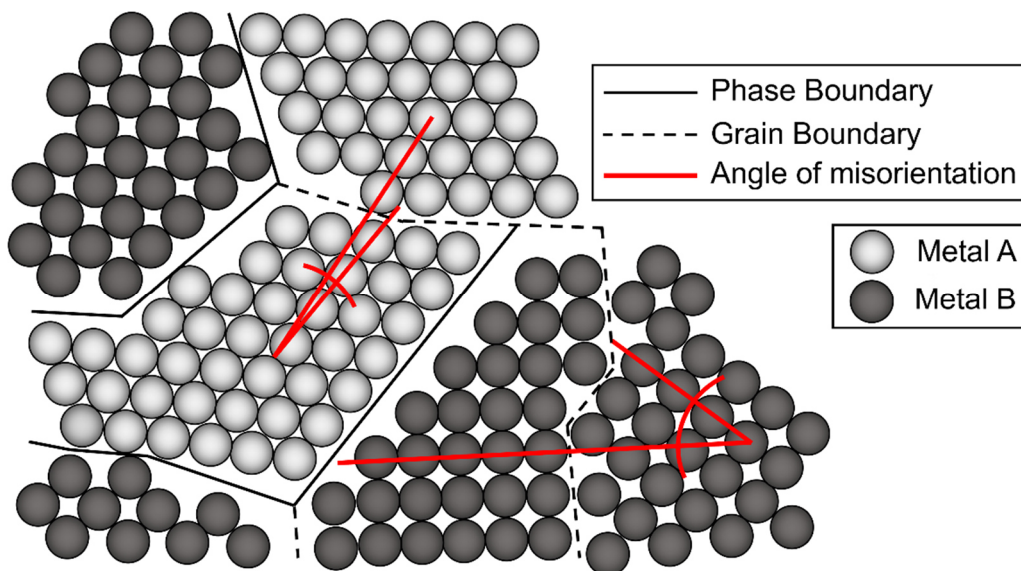


Figure 2.1. Grain and phase boundaries within a generic polycrystalline alloy.

The general structure of metal and alloy crystals encompasses 3 closed packed structures: body-centered-cubic (bcc), face-centered-cubic (fcc) and hexagonal-close-packed (hcp) (Figure 2.2a-c). Within these structures, the metal atoms are assumed to be hard spheres with a well-defined diameter that are arranged periodically in arrays (lattices) with long-range

order.^[26] The smallest structural unit is the unit cell, and its repetition gives the full 3D structure. Depending on environmental factors such as temperature and pressure certain metallic elements exhibit more than one crystal structure (polymorphism).

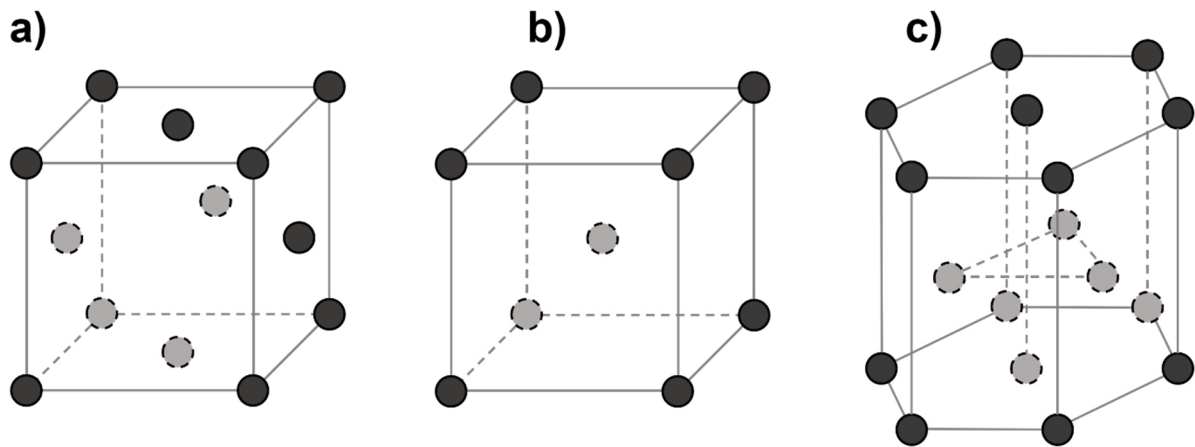


Figure 2.2. Unit cell of (a) face-centered cubic, (b) body-centered cubic and (c) hexagonal close packed structures.

In conventional alloys the host metal or solvent metal determines the crystal structure. For steels, e.g., this would be Fe. The additional elements to the solvent metal are called solutes. The resulting crystals with mixed composition are referred to as solid solutions in which the solutes are uniformly and randomly dispersed.^[28] Further distinctions can be made for conventional alloys between interstitial and substitutional solid solutions (Figure 2.3). For interstitial solid solutions smaller elements than the solvent may occupy interstitial sites and vacancies (Figure 2.3c). For MPEAs, substitutional solid solutions are applicable where solute atoms replace host atoms (Figure 2.3b). While the literature is clear on deeming MPEAs as solid solutions,^[13] the chemical complexity of MPEAs does not allow for a clear distinction between solvent and solute atoms. For appreciable solubility of solutes in the solvent metal, certain values regarding electronegativity, atomic sizes, crystal structure and valences (summarized under the semi-empirical Hume-Rothery rules)^[28] need to be met. If these rules are not met, diffusion of the alloying elements may lead to phase formation. More recent research shows that the rules do not universally apply to MPEAs,^[29] and that the complexity of the free energy landscape needs to be considered when discussing solid solution formation in MPEAs.^[30]

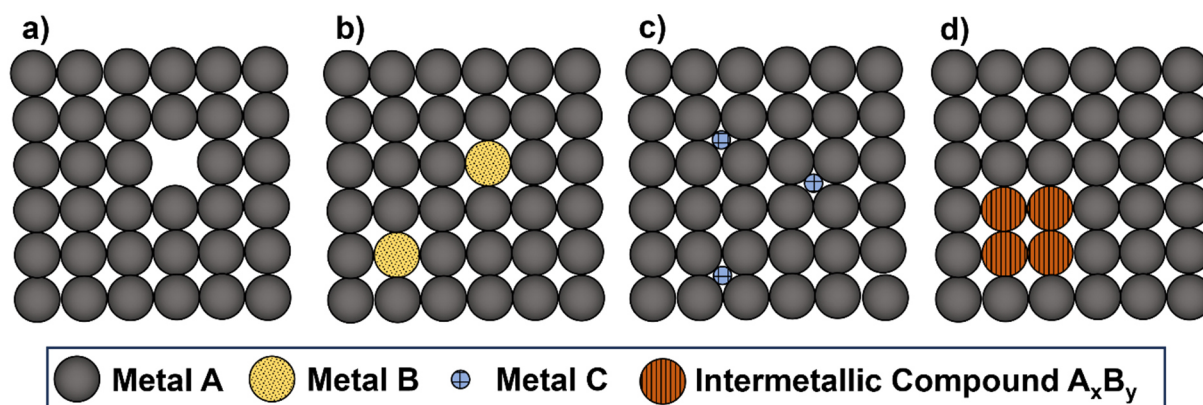


Figure 2.3. Crystal defects within a metal where a) shows a void, b) a substitutional solid solution, c) an interstitial solid solution and d) an intermetallic compound.

Phase transformations in alloys are achieved by the diffusion of atoms that can then partition into phases of different compositions.^[31] Generally, diffusion comprises the stepwise migration of atoms due to atomic motions via empty adjacent sites (vacancies or interstitials). This is an activated process because the bond energy to neighboring atoms in the metal lattice must be overcome.^[32] Diffusion in the bulk metal may occur as interdiffusion or self-diffusion. While self-diffusion (or tracer diffusion), entails the atomic movements in the absence of a concentration gradient, interdiffusion describes atoms of one metal diffusing into another. The resulting phases define homogeneous portions within the metallic system that differ in their chemical and physical characteristics (Figure 2.1). Phases may also exist in pure metals due to polymorphism but are especially relevant in alloys where deviations from the Hume-Rothery rule may lead to phase formation. While the initial research highlighted the single-phase nature of MPEAs, Raabe et al.^[13] noted that most studied MPEAs are heterogeneous systems (two or more phases present).

Furthermore, with more than one metal present in the alloy, intermetallics may form. Intermetallics are compounds of a distinct chemical formula that are typically undesirable within alloys as they reduce mechanical strength due to their brittle nature.^[13] The formation of solid solutions and intermetallics depends on the relative free energies of mixing and formation. Typically, when intermetallic compound formation is favored, they precipitate within the solid solution matrix of the respective alloy (Figure 2.3d). Generally, the possibility of intermetallic compound formation increases with the number of mixed elements which is the source of the traditional metallurgist's reluctance toward concentrated, multi-element alloys.^[13]

2.2 Mechanical Properties of Metals

In the material science context, the mechanical behavior of an alloy reflects its response towards the application of a load which leads to deformation. The load can be compressive, tensile, or sheared; it may be applied constantly or it may fluctuate over time.^[19] Typically, to determine mechanical properties such as strength, hardness, ductility and toughness, the

stress-strain behavior is investigated. In engineering, stress σ refers to the applied load divided by the original cross-section of the specimen and strain ε is the change in length divided by the original length. Figure 2.4 represents a typical stress-strain curve and characteristics that can be drawn from it.

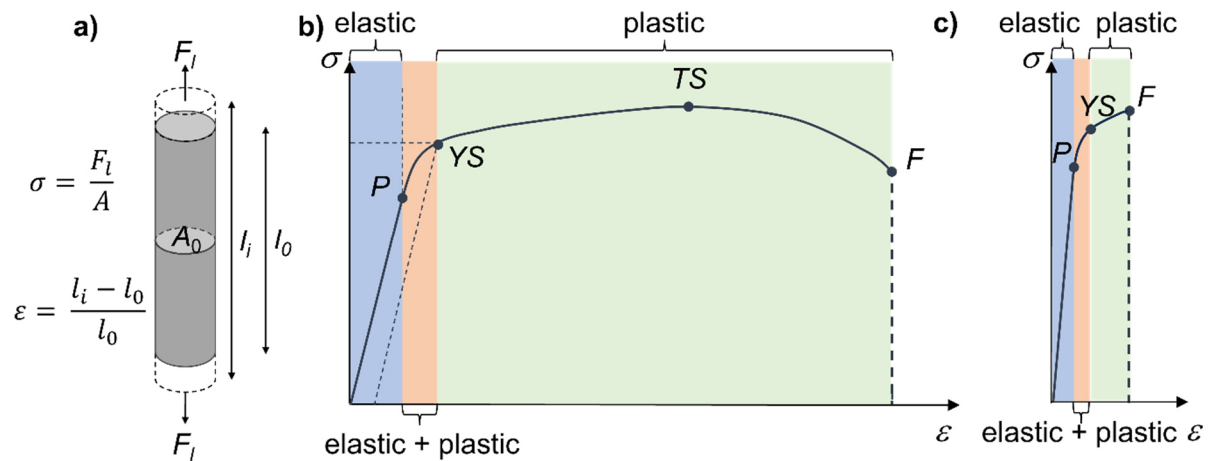


Figure 2.4. Generic stress-strain curve for (b) a ductile and (c) a brittle metallic specimen (a) with A_0 to which a load F_1 is applied. In both (b) and (c) the regions are highlighted for elastic, elastic + plastic, and plastic deformation. Points P , YS , TS and F represent the proportional limit, yield strength, tensile strength and fracture, respectively.

Elasticity is an indicator of stiffness and elastic deformation occurs when stress and strain are proportional, the quotient giving the elastic modulus (the elastic regions are indicated in Figure 2.4b and c). On the stress-strain curve, the point where plastic deformation begins represents the material's yield strength (YS) which is typically determined at a specified strain offset (indicated by a parallel dashed line in Figure 2.4b).^[19] The region following yield strength displays the degree of plastic deformation termed ductility. Towards higher strain, this region ends with the fracture (F) of the specimen. Figure 2.4c displays the opposite case of a stress-strain curve for a brittle metal where fracture occurs shortly after YS . Hardness refers to the susceptibility to plastic deformation and is typically tested by indentation. Often other properties such as tensile strength (TS) which reflects the maximum point on the stress-strain curve can be obtained from hardness measurements.^[19] Toughness as a mechanical property is used in many contexts, most importantly as fracture toughness, i.e., the ability of a metal to absorb energy before fracture. If a metal exhibits both high strength and ductility it is considered tough.^[19] Prior deformations and defects influence yield and tensile strength as well as ductility. Targeted deformation processes (e.g., rolling or bending) termed strain- or work-hardening are employed to strengthen ductile metallic materials.^[19]

2.3 Defects and Strengthening in Metals

Within the lattices of metals or alloys, defects may disrupt the 3D structure. The defects can be classified as point defects (0D), line defects (1D), interface defects (2D) and volume defects

(3D).^[13] Point defects comprise vacancies, interstitials and substitutionals (Figure 2.3). Vacancies enable diffusion, interstitials occupy interstitial sites in the crystal lattice and substitutionals substitute host atoms which, however, are difficult to differentiate in MPEA solid solutions. The main carriers of plastic deformations are line defects which can be dislocations of edge-, screw-, or mixed-type. An edge dislocation line describes an extra half-plane of atoms and a screw dislocation line results from shear distortion and runs through the center of a spiral (Figure 2.5a and b).^[33] Apart from grain and phase boundaries, interface defects include twin boundaries, stacking faults and the exposed surface to the environment.^[13] Twin boundaries are a type of grain boundary where atoms on one side of the boundary are positioned as the mirror-image to the atoms on the opposite side (Figure 2.5c). Twins result from plastic deformation either through mechanical shear forces (mechanical twins, observed for bcc and hcp phases) or through deformation after heat treatments termed annealing (annealing twins, observed for fcc phases) which are carried out to relieve stress and increase certain mechanical properties (e.g., ductility).^[3, 28] Stacking faults result from disruptions in the normal stacking sequence and the exposed surface may inhabit steps and kinks.^[33] Intermetallics, inclusions and voids constitute volume defects.^[13]

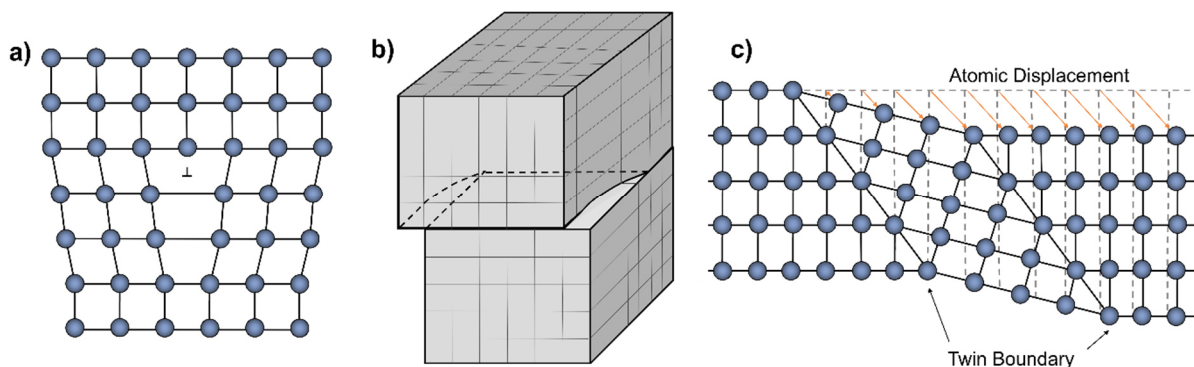


Figure 2.5. (a) Schematic of an edge dislocation indicated within the lattice by \perp . (b) Screw dislocation within a generic crystal. (c) Twin formation as a result of deformation.

The outlined defects may influence the plasticity of an alloy. Plasticity results from deformation and anything that hinders the motion of atoms during deformation makes a metal/alloy stronger.^[33] In MPEAs it has been observed that especially twin boundaries allow partial dislocations to glide along the interface defect.^[33] This in turn releases stress and enhances ductility. Unlike conventional alloys where strengthening is invariably accompanied by loss in ductility and toughness (strength-ductility trade-off), in some MPEAs such as CrCoNi and CrMnFeCoNi this trade-off is avoided and renders materials with desirable mechanical properties.^[18] In contrast to pure metals where 0D to 2D defects only disrupt the local structure, in MPEAs such defects also disrupt the local chemistry which sets them further apart from conventional alloys.^[13]

3 Multi Principal Elements Alloys

3.1 Multi Principal Element Alloys and Manufacturing Processes

Interestingly and despite the contemporary high interest in research on multi principal element alloys, the concept of combining a higher number of alloying materials in similar ratios is not a recent discovery.^[34] In fact, German metallurgist Franz Karl Achard studied alloys with five to seven elements in equimolar ratios in the late eighteenth century, culminating in his report “Recherches sur le Propriétés des Alliages Métallique”.^[35] His results comprised over 900 as-cast alloy compositions in as many possible combinations of up to seven components from a pool of 11 metals. Nearly two centuries later, Smith^[36] re-introduced Achard’s work, bestowing the modern research on MPEAs a broader historical perspective. Nevertheless, it is the two works published independently in 2004 by Cantor et al.^[11] and Yeh et al.^[12] that paved the way for the surge in research interest in MPEAs. The two publications introduced two definitions for these alloy systems, which are based on the initial motivation of rendering stable alloy systems by a high configurational entropy ΔS_{conf} , in order to overcome intermetallic compound formation and yield single-phase solid solutions. This motivation has sparked the term “high entropy alloy”.^[12, 37] ΔS_{conf} is calculated based on the Boltzmann equation which describes the relationship between the complexity and the entropy of a system.^[38] Considering the configurational entropy in the liquid state, ΔS_{conf} for any ideal alloy mixture can be given by:

$$\Delta S_{\text{conf}} = -R \sum_n x_i \ln(x_i) \quad 3.1$$

where n is the number of components, R is the gas constant and x_i the fraction of component i .^[39]

Alloys with $\Delta S_{\text{conf}} \geq 1.5 R$ are considered high entropy alloys. Accordingly, medium entropy alloys possess ΔS_{conf} values between $1.0 R$ and $1.5 R$, whereas anything below $1.0 R$ is considered a low entropy alloy.^[40] Caution should be exercised with this definition as it primarily supports the high-entropy concept and assumes that there is only one single value for ΔS_{conf} , neglecting the effects of formation enthalpies $\Delta_f H$ and other entropic contributions (e.g., vibrations, magnetic and electronic effects).^[34] To overcome this problem, the alloy is assumed to acquire a high-temperature random solid solution.^[31] However, ΔS_{conf} may change with temperature and for the determination of ΔS_{conf} , the atoms must randomly occupy the lattice positions which seldom is the case in metallic solutions.^[34] Finally, the indicated values only hold true when dealing with close-to equimolar alloy systems (see example calculations in Appendix 1) and overlooks previous findings that metallic solutions are typically not ideal.^[39]

A high entropy alloy encompasses 5 or more principal elements in equimolar ratios.^[12] However, this restriction is mitigated in the same publication to allow for compositions of 5 - 35 at. % of major elements, whereas minor elements may be present in atomic percentages below

5 at. %.^[12] This broadens the possible combinations of multi principal element alloys and avoids the confusion that comes with the conceptual challenges of the ΔS_{conf} definition. Consequentially, it also permits more complex systems with different phase formations and intermetallic compounds. This work will use the term multi principal element alloys (MPEAs).

To date MPEAs have been fabricated via three main methods, melting and casting, mechanical alloying of powders and deposition techniques. Originally, Yeh et al.^[12] obtained their MPEA specimens through arc melting. Indeed, most MPEAs studied are manufactured by vacuum arc melting as the arc may reach temperatures of up to 3000°C and may be controlled by regulating the electrical power.^[41-42] Here, the pure metals are melted and mixed in the liquid state and solidified in a cooled copper crucible repeatedly to ensure homogenization.^[43] The seminal work by Cantor et al.^[11] first used vacuum induction melting for which the pure metals are melted and mixed through eddy (“whirlpool”, i.e., swirling) currents that are induced and supplied by an electromagnetic field.^[44-45] Both arc and induction melting may experience metal loss by evaporation of metals with lower melting points than that of other alloying constituents. Alloying in the solid state by powder metallurgical methods is predominantly accomplished through spark plasma sintering (SPS) and avoids deterioration by evaporation loss. During SPS the mixed MPEA metal powders are simultaneously subjected to pressure and an electric field that results from passing a current through the sample leading to improved powder densification.^[44] Deposition techniques are mainly used either to retrieve alloy coatings of MPEAs deposited on a carrier material such as steel,^[46-47] or to produce bulk MPEA specimen by depositing the alloy matrix layer-on-layer in an additive fashion.^[48] Figure 3.1 compiles the methods outlined above with respective examples of the most common procedures. The interested reader is directed to other sources for further manufacturing procedures.^[41, 43-44, 49]

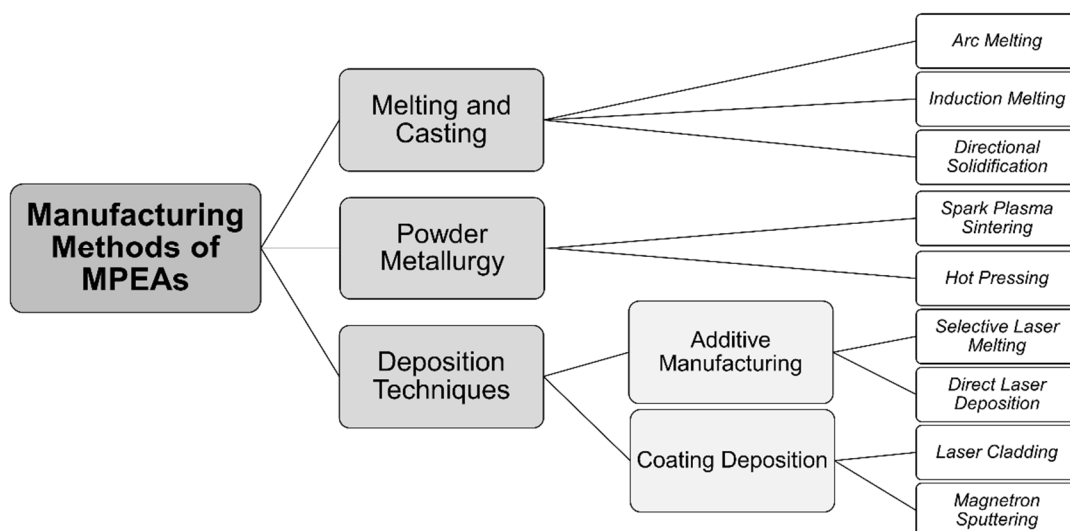


Figure 3.1. Graphic compilation of most frequently used MPEA manufacturing processes with respective examples.

The two model systems studied within this work are single-phase fcc solid solutions with equimolar concentrations of their component elements whereas one MPEA comprises five (CrMnFeCoNi) and the other three elements (CrCoNi). The main motivation behind studying MPEAs seems to be the exploration and expansion of the compositional space of alloy design offered by the interior region of MPEA phase diagrams and to investigate the resulting properties.^[10-12] These properties are governed by four core effects that define this group of alloys.^[31]

3.2 Key Properties of Multi Principal Element Alloys

Based on the research available in early publications,^[10, 50-53] Yeh^[31] proposed four core effects that determine the key properties of high entropy alloys. These effects are summarized in Figure 3.2 and arise from the material's thermodynamics, kinetics, structure, and synergistic properties.

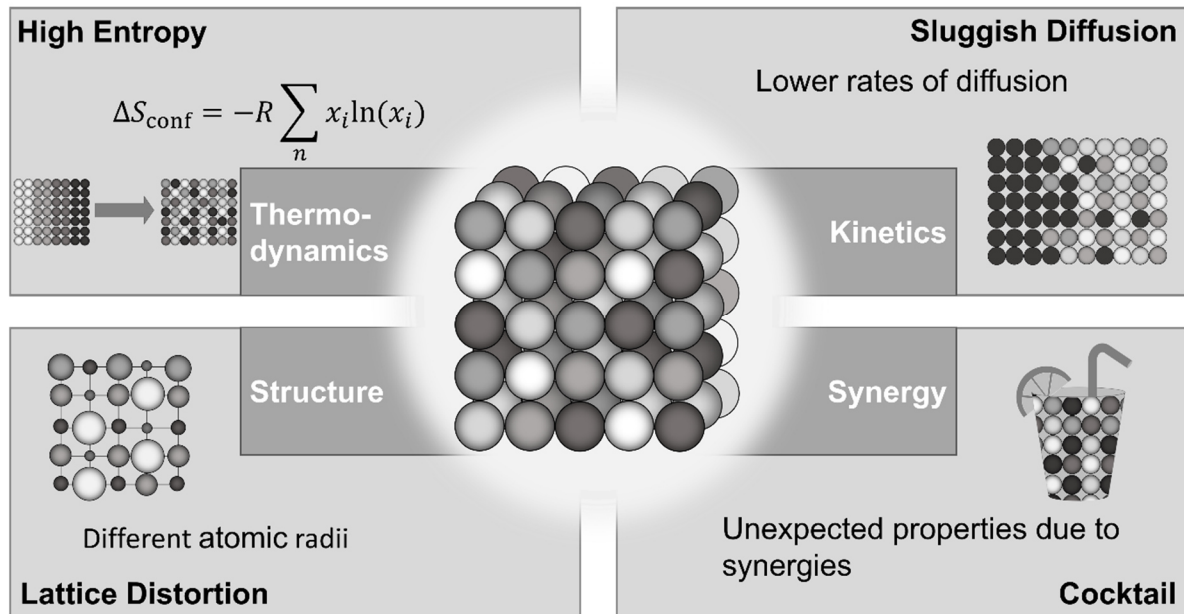


Figure 3.2. Four core effects that determine the properties of MPEAs. Adapted with permission from ^[54]. Copyright 2020, American Chemical Society.

3.2.1 High Entropy Effect

Counterintuitively, Yeh et al.^[12] reasoned that high entropic phases such as solid solution phases are stabilized through the high contribution of configurational entropy to the total free energy of mixing, ΔG_{mix} , which is given by the Gibbs-Helmholtz equation:

$$\Delta G_{\text{mix}} = \Delta H_{\text{mix}} + T\Delta S_{\text{mix}} \quad 3.2.$$

In fact, it was expected that intermetallic compound phases would favorably form with an increasing number of components. The Gibbs phase rule predicts the number of phases, P , that may form under isobaric equilibrium conditions:

$$P = C + 1 - F \quad 3.3,$$

where C is the number of alloying elements and F represents the degrees of freedom.^[42] With that, a 5-component system may assume a maximum of 6 equilibrium phases if $F = 0$.^[55] Surprisingly, early fabrication of MPEAs yielded solid solutions without intermetallic compounds and much simpler microstructures, mainly single-phase fcc, or bcc.^[11, 31, 37, 55-57] Yeh et al.^[12] argued that if the strain energy does not contribute toward the mixing enthalpy, the difference between intermetallic compounds and solid solutions caused by large negative ΔH_{mix} but small ΔS_{mix} versus medium negative ΔH_{mix} but large ΔS_{mix} for solid solutions.^[58] For that reason, the two phases compete, promoting the formation of solid solutions with increasing number of components and temperature. Equation (3.1) shows how ΔS_{conf} increases with the number of components, whereas ΔS_{conf} is assumed to be the main contributor to ΔS_{mix} ,^[59] and Equation (3.2) demonstrates how ΔG_{mix} increases with temperature.

Contrarily, further research has brought forward MPEAs that do not form single-phase solid solutions but materials that do show fcc and bcc faces or succumb to spinodal decomposition, a spontaneous phase separation due thermodynamically instable solid solutions.^[50, 60-65] Primarily, the high entropy effect was introduced to describe the formation and stabilization of solid solutions as the signature concept in high entropy alloys. It should be noted, however, that the high entropy rational disregards contributions from electronic, magnetic, and vibrational entropies toward ΔS_{mix} , and that the competition between intermetallic compound and solid solution phase formation is more complicated.^[34]

3.2.2 Sluggish Diffusion

Compared to alloys with lower configurational entropies, diffusion of single elements in MPEAs with potentially higher configurational entropies, is assumed to be sluggish.^[66] A distinction needs be made when considering the diffusion paths. While most publications on diffusion in MPEAs consider bulk diffusion and discuss the effect on mechanical properties,^[67] faster diffusion paths such as the migration of atoms along surfaces and defects (e.g., grain boundary diffusion) are typically simulated for high temperature corrosion,^[68] but are of equal importance when considering aqueous corrosion processes. However, specific investigations on the effect of such faster diffusion paths on aqueous corrosion behavior are cumbersome and remain scarce. Nevertheless, the effects are evident when analyzing the layered structure of passive films and the modified metal layers underneath.^[69]

In equimolar MPEA CrMnFeCoNi, Tsai et al.^[70] showed that the diffusion coefficients were the smallest in the fcc MPEA matrices compared to the pure metals and that the degree of sluggish diffusion increases with the number of components. However, other publications on tracer and interdiffusion in MPEAs contradict the concept of slow diffusion.^[71-75]

3.2.3 Lattice Distortion

The lattice distortion effect considers lattice displacements that arise at the atomic level of the alloy crystal structure. Since all elements in MPEAs are solute atoms and differ in their atomic sizes, the lattices of these materials may experience severe strain and stress as a result of lattice site displacement.^[76] Furthermore, because of the multi-element-solute matrix, each atom may be exposed to different chemical environments (e.g., bonding energies) due to varying non-symmetrical neighboring elements.^[58] The displacement of single atoms within the MPEA lattice implies uncertainty in their position which is suggested to increase configurational entropy and allegedly leads to increased hardness, reduced electrical and thermal conductivity and decreased thermal dependence of these properties.^[31, 34, 59] As noted by Owen and Jones,^[77] the maximum tolerable difference in atomic radii in binary solid solution alloys is 15%. Systems with lattice strains due to larger atomic radii differences are likely to decompose into multiple phases.^[77]

3.2.4 Cocktail Effect

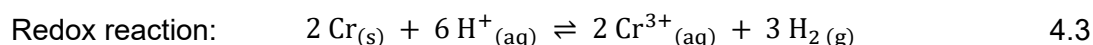
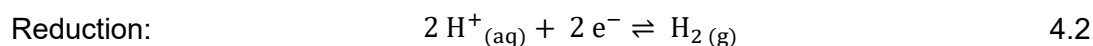
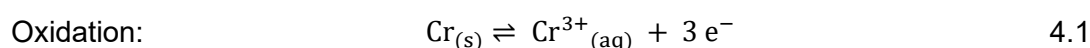
Due to alloying various constituent components, MPEAs present unique, unpredictable, and synergistic properties, which are summarized by the umbrella term of the cocktail effect.^[78] First employed by Rangathan^[10] to emphasize the pleasures in alloy design and development, the author addresses the outstanding properties of gum metals and bulk metallic glasses (amorphous alloys with unique properties) with the multi-metallic cocktail effect term. Within the concept of MPEAs, this effect summarizes all the properties that arise from the atomic (interactions among elements, diffusion, phase formation) and micro-scale (grain morphology, grain size, grain and phase boundaries) multi principal element composition.^[58] Liu et al.^[78] compiled three properties of MPEAs that can be attributed to the cocktail effect. Firstly, the multi-metallic alloying may lead to the embedding of metastable crystalline structures. These structures allow for athermal transformation processes caused by mechanical stimuli (e.g., deformation)^[79-80] that generate mechanical twinning, duplex microstructures and martensitic transformations, all of which are associated with enhanced work-hardening capacities.^[78] The second property resulting from multi-metallic alloying, entails thermodynamic transformations that drive the formation of multicomponent intermetallics.^[81-83] The final property arises from alloying interstitial elements to the metallic cocktail, which may enhance lattice distortion and give rise to short-range ordering, both of which influence the dislocation behavior and with that, again, mechanical properties.^[84-85]

4 Corrosion

4.1 Redox Reactions and Corrosion

There exist various definitions of corrosion with slight differences between them. According to the International Union of Pure and Applied Chemistry (IUPAC), corrosion generally comprises the “irreversible interfacial reaction of a material (metal, ceramic, polymer) with its environment which results in consumption of the material or in dissolution into the material of a component of the environment”.^[86] This definition is most applicable to electrochemical corrosion as an interfacial process. The IUPAC definition further specifies that other degradation processes of a mechanical (fracture or abrasion) or physical (melting or evaporation) nature are not considered under the term corrosion. However, such degradation processes may intensify corrosive deterioration and its effects will be described briefly in Chapter 4.4. Other corrosion definitions are directed to volume-related metal-physical processes like hydrogen embrittlement which are not subject of this thesis.^[87]

The corrosion of metals is an interfacial electrochemical process which involves chemical reactions that are accompanied by a flow of electrons. An electrochemical reaction can be divided into two half-cell reactions, the reduction, and the oxidation reaction; the sum of which is termed a redox reaction. Herein, the reacting species undergo a change in their oxidation state, due to donating (oxidation) or accepting electrons (reduction). Equations (4.1) to (4.3) show the reactions for the dissolution of chromium in an acidic solution.



It can be seen from the two half-cell reactions that corrosion entails the transfer of charge and mass at the metal/solution interface.^[88] In Equation (4.1), metallic Cr goes into solution incurring a loss of mass of the metallic phase and leaving behind electrons, i.e., charge, at the metallic interface (electrode). Electrochemically this is called the anodic reaction. The counter reaction to ensure the flow of charge is the cathodic reaction (Equation (4.2)), in which dissolved protons take up the electrons to produce hydrogen (hydrogen evolution reaction, HER). The reaction in Equation (4.2) is the prevalent cathodic reaction in acidic solutions. In neutral or basic media, the predominant cathodic reaction comprises the reduction of dissolved O₂ (ORR, Equation (4.4)).



Compared to bimolecular redox reactions in solution such as the redox titration of Fe^{2+} with KMnO_4 (Equation (4.5)), where the reducing (Fe^{2+}) and oxidizing reagent (KMnO_4) must meet each other in solution, electrochemical reactions are spatially separated.^[88]

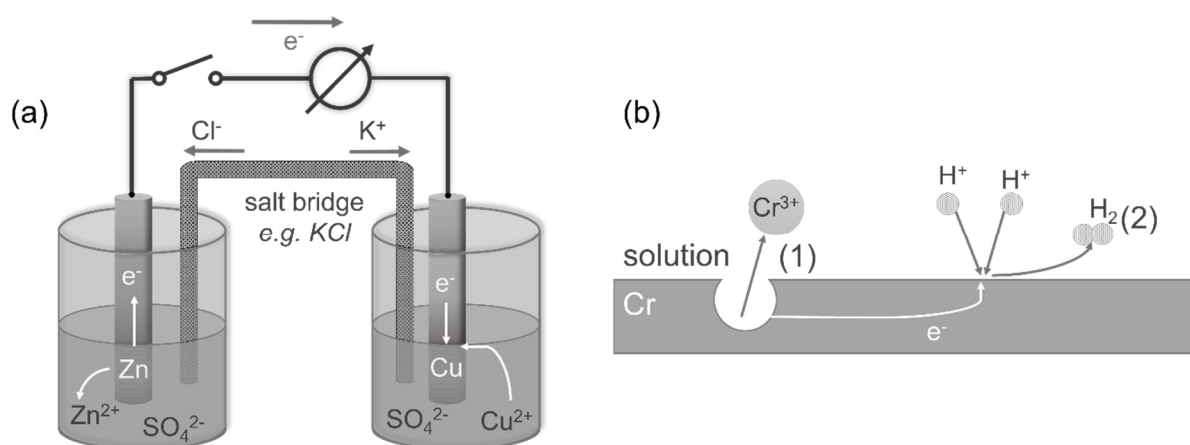
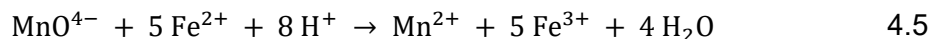


Figure 4.1. Depiction of two galvanic cell set ups. (a) Daniell cell where the Zn electrode dissolves in the anodic half-cell and dissolved Cu^{2+} deposits on the Cu electrode in the cathodic half-cell. Electron and ion flow are ensured by wire connections between the electrodes and a salt bridge between the electrolytes, respectively. (b) Galvanic cell in a corrosion system, where the Cr electrode serves both as the anode (1) and cathode (2). Here, electron and ion flow occur within the electrode material and within the electrolyte, respectively.

Figure 4.1 shows two electrochemical cells. Figure 4.1a depicts a typical laboratory set up of a Daniell cell where the anodic (Zn) and cathodic (Cu) half-cells are in separate half-cells that are connected by a salt bridge to enable ionic conduction. The anode is metallic Zn immersed in its own sulfate solution and the cathode is metallic copper immersed in its sulfate solution. Connecting the two metal rods with a wire allows electron transport: Zn spontaneously dissolves, while Cu deposits at the Cu rod. Further thermodynamic considerations that describe this so-called galvanic cell can be found in Chapter 4.3.2. Figure 4.1b on the other hand shows how anodic and cathodic sites have formed on a single metallic chromium surface that faces a single acidic electrolyte. The flow of electrons (i.e., the current) to the cathodic site (Figure 4.1b, (2)) occurs within the electrode body itself due to its metallic nature. The aqueous solution provides ionic conductivity. The ion-conductive solution is generally termed the electrolyte. Electrochemical half-cells as depicted in Figure 4.1b may arise on a metal surface due to the heterogeneity of the metal surface or due to concentration gradients in the electrolyte.^[88]

4.2 Effects of Metal Structures on Corrosion

The polycrystalline nature of metals leads to an array of different surface site morphologies and energies. The metal surfaces expose their grains, grain boundaries, and other structural

defects to the electrolyte.^[88-89] Furthermore, contaminants in the form of enclosed impurities in the crystal lattice and adsorbates such as ions from the solution also change the surface energy. MPEAs may exhibit different local chemical compositions especially when different phases are present. For the AlCoCrFeNi_{2.1} MPEA, e.g., an L₁₂ (“Legierungen” in German, alloy compound of Cu₃Au lattice structure) and a B2 (compound made up of two elements, with CsCl lattice structure)^[90] phase form, whereas the former is enriched in Cr, Co and Fe, and the latter is mainly composed of Al and Ni.^[91] This introduces potential sites for galvanic corrosion. Figure 4.2 summarizes the different variants of heterogeneities that may be present at the metal surface.

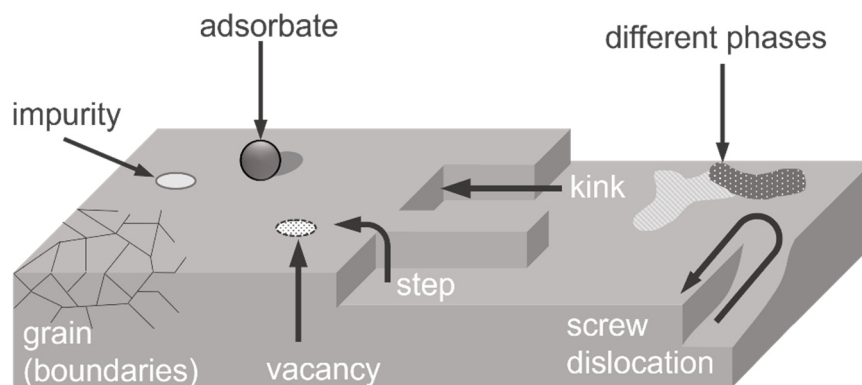


Figure 4.2. Schematic representation of possible heterogeneous site on a metallic surface.

4.3 Basics of Electrochemical Corrosion

4.3.1 Definitions

The key reactions in electrochemical corrosion are interfacial processes, where the solid (s) metal surface in contact with the liquid (l) solution forms a metal/solution interface (s/l). As stated above the solution phase (electrolyte) contains dissolved ions that enable the conduction of current. Apart from controlled laboratory settings, such electrolytes may contain a multitude of ions (e.g., Na⁺, Cl⁻) and neutral molecules such as water and organic molecules. The electrolyte must at some point meet the physical boundary of its vessel and, in the case of corrosion systems, an immersed metallic specimen (electrode). The immersed metal or alloy as an electronic conductor may be connected to an external power source like a potentiostat with which electrons may be supplied or extracted from the metal. This charging leads to the controlled formation of a particular state of the electrical double layer (EDL) at the metal/solution interface.^[92] Due to their dipole character, water molecules are attracted by the charged electrode and will orient correspondingly. Dissolved ions of opposite charge to the metal surface will also be attracted to the interface. An array of adsorbed species accumulates at the interface forming the EDL that balances the charge applied to the electrode. Closest to the electrode surface is the inner Helmholtz layer (IHL) of directly adsorbed ions and water at

the metal surface. This layer is followed by the outer Helmholtz layer (OHL) of hydrated counter-ions and then a diffuse layer (DL) with a certain concentration gradient that depends on the charge applied to the metal.^[93]

As shown schematically in Figure 4.3, there is a difference in electrostatic potential φ between the metal electrode and the electrolyte. The symbol φ is employed to clearly distinguish between the potentials of single phases (e.g., electrode, or electrolyte) and the cell potential U . The electrostatic potential difference is the work required to move a small unit charge between different phases, e.g., from solution to metal. However, this potential difference between metal and solution, or, i.e., the Galvani potential difference $\Delta\varphi_{(Me/sol)}$ cannot be measured directly. For this reason the potential of an electrode E is measured against the potential of a thermodynamically well-defined reference electrode.^[94] The electrode potential E is shifted by an unknown but constant value against $\Delta\varphi_{(Me/sol)}$.

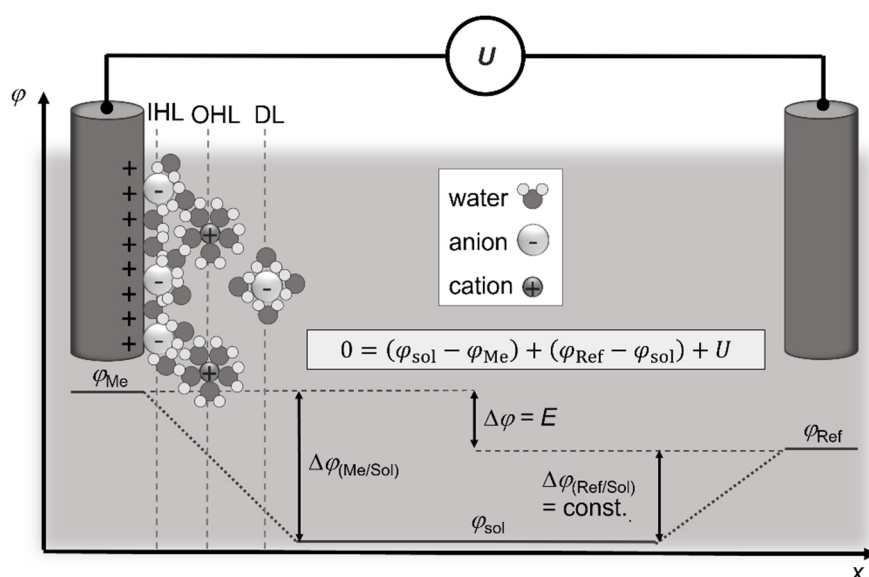


Figure 4.3. The electrostatic potentials of different phases as a function of distance x , from the metal electrode. Herein, φ_{Me} refers to the electrostatic potential of a metal electrode, φ_{sol} to the electrolyte and φ_{Ref} to a reference electrode. IHL – inner Helmholtz layer through nuclei of specifically adsorbed ions, OHL – outer Helmholtz layer through nuclei of non-specifically adsorbed ions, DL – layer indicating the extent of the double layer. For clarity only excess charges are indicated.

All standard electrode potentials E° are given versus the standard hydrogen electrode (SHE) which is set to be $E^\circ = 0.0$ V at $p = 100000$ Pa and $pH = 0$ at all temperatures.^[95] The standard electrode potentials apply to the pure metals immersed in an aqueous solution of their own cations, where the concentration activity of the cation is 1 mol L^{-1} (unit activity, $a^\circ = 1$).^[92] The order within the electrochemical series provides an overview on the nobility, i.e., the chemical stability of the electrode. The most positive standard electrode potentials belong to the noble metals, e.g., gold, and nobility decreases with decreasing standard electrode potential. The Nernst equation (Equation (4.9)) can be used to calculate electrode potentials for concentration activities deviating from a° and pH values other than zero. Since the SHE is

a rather impractical electrode, reference electrodes such as the Ag/AgCl/3M NaCl (0.204 V vs. SHE)^[95] and the saturated calomel electrode (SCE; 0.241 V vs. SHE)^[95] find regular use in corrosion studies.

4.3.2 Thermodynamic Considerations of Electrochemical Reactions

The standard electrode potentials are generally employed to determine whether a reaction proceeds spontaneously, non-spontaneously or is at equilibrium. A reaction is spontaneous when the change in Gibbs free energy $\Delta G < 0$, non-spontaneous when $\Delta G > 0$, and at equilibrium when $\Delta G = 0$. Generally, the ΔG may be presented by

$$\Delta G = \Delta H - T\Delta S \quad 4.6$$

where ΔH is the change in enthalpy, T is the temperature and ΔS is the change in entropy.^[96]

The Gibbs free reaction energy $\Delta_r G$ of an electrochemical reaction can be expressed by

$$\Delta_r G = -nUF \quad 4.7$$

where $\Delta_r G$ is a molar quantity, U is the cell potential, n is the number of exchanged electrons, F is the Faraday constant and the minus sign results from conventions.^[96-97] To obtain $\Delta_r G$ and the respective cell potential U from the standard $\Delta_r G^\circ$ or U° , $\Delta_r G$ must first be described by using the standard terms

$$\Delta_r G = \Delta_r G^\circ + RT \ln \prod_i \left(\frac{a_i}{a^\circ} \right)^{v_i}, \quad 4.8$$

where v_i is the signed stoichiometric number which depends on the direction of the reaction. Dividing by $-nF$ and applying the decadic logarithm gives the Nernst equation from which the cell potential U may be retrieved by

$$U = U^\circ - 2.303 \frac{RT}{nF} \log \prod_i \left(\frac{a_i}{a^\circ} \right)^{v_i}. \quad 4.9$$

When the reaction takes place at room temperature ($T = 298$ K) and bearing in mind that $R = 8.314$ As V K⁻¹ mol⁻¹ and $F = 96845$ As mol⁻¹, Equation (4.9) further simplifies to

$$U = U^\circ - \frac{0.059V}{n} \log \prod_i \left(\frac{a_i}{a^\circ} \right)^{v_i}. \quad 4.10$$

Since the activities are given by the concentrations for dilute solutions, the logarithmic term of activities can be substituted by the equilibrium constant K , considering the generic reaction



where the equilibrium constant can be obtained via

$$K = \frac{c_C^c c_D^d}{c_A^a c_B^b} \quad 4.12$$

K can then be employed in the general equation

$$\Delta G = \Delta G^{\circ} + RT \ln \left(\frac{c_C^c c_D^d}{c_A^a c_B^b} \right) = -nFU^{\circ} + RT \ln K \quad 4.13$$

and provides a link between the standard Gibbs free energy, the equilibrium constant and standard electrode potential. Figure 4.4 visualizes this relationship.^[96]

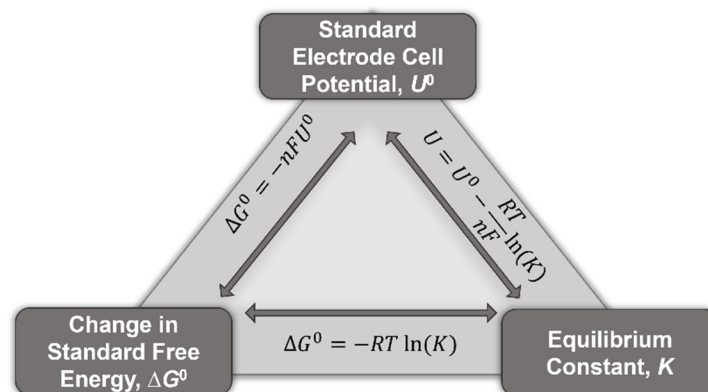
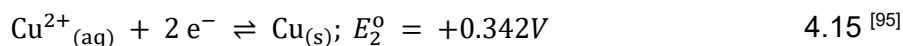
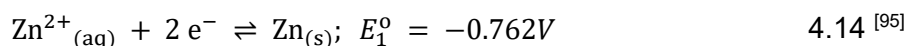


Figure 4.4. Relation between Gibbs free energy, the standard electrode potential and respective equilibrium constant.

The Daniell cell mentioned above (see Figure 4.1) is a prime example of a galvanic cell. Considering the half-cell reactions and the respective standard electrode potentials E°



the standard cell potential is the difference of the standard electrode potentials

$$U^{\circ} = E_2^{\circ} - E_1^{\circ} = +0.342 \text{V} - (-0.762 \text{V}) = +1.104 \text{V}. \quad 4.16 \text{ [98]}$$

When coupling half-cells, the metal with the lower E° (Zn) dissolves while ions are deposited on the electrode with the higher E° (Cu).^[98] Similarly to the classical Daniell cell, galvanic couplings can take place on an alloy metal surface. The most obvious coupling takes place, when the alloy composition entails phase formation of different chemical compositions. For example, in the MPEA AlCoCrFeNi_{2.1} where two phases are present, one rich in Al ($E^{\circ} = -1.676$ V) one rich in Ni ($E^{\circ} = -0.257$ V), the dissolution of Al is observed.^[91] However, the formation of solid solutions as in CrMnFeCoNi and CrCoNi renders MPEAs with homogenous surfaces where no different phases, i.e., potential sites for galvanic corrosion are present. Generally, the application of the MPEA needs to be considered. The approach to add aluminum to an MPEA composition reduces the weight of the material.^[99] Furthermore, aluminum alloys are able to form dense oxide layers that may protect well against corrosion.^[100]

Other cathodic reactions may take place on other MPEAs with simpler structures and no phase segregation. Many MPEAs contain chromium and research has shown that it is one

of the metals dissolving during corrosion.^[101-102] In acidic solution, a possible cathodic reaction of a Cr-containing MPEA may be the evolution of hydrogen as in Equation (4.2). In neutral or alkaline solutions, the cathodic reaction may be the reduction of dissolved O₂, shown in Equation (4.4). Galvanic cells may also emerge when the same metal surface is exposed to differing concentrations, generally termed differential concentration cells. Considering two Cr half-cells (set up as in Figure 4.1), one with a metal concentration of $c_{\text{Cr}^{3+}} = 0.5 \text{ mol L}^{-1}$ and one with $c_{\text{Cr}^{3+}} = 0.001 \text{ mol L}^{-1}$ at 298 K and otherwise identical conditions, the Nernst equation allows to calculate the respective electrode potentials.^[98]

$$E = E^0 - \frac{0.059 \text{ V}}{n} \log_{10} \frac{[c^0]}{[\text{Cr}^{3+}]}; \quad 4.17$$

$$E_{\text{Cr},0.5\text{M}} = -0.750 \text{ V}; E_{\text{Cr},0.01\text{M}} = -0.803 \text{ V}$$

The cell potential of this Cr concentration cell is 0.053 V and Cr will dissolve in the lower concentrated half-cell until equilibrium is reached.

Another form of concentration cell is the O₂ concentration cell. Evans was the first to demonstrate the effect of different O₂ concentrations and showed that surfaces that experience electrolytes low in O₂ will be anodic in relation to areas of the same surface that are exposed to the same electrolyte with higher O₂ concentration.^[103] This is typically the case when the electrolyte is exposed to the atmosphere and O₂ can diffuse freely at the electrolyte/atmosphere (liquid/gas) interface and O₂ concentration gradients develop within the electrolyte. Geometrically occluded sites hinder diffusion, resulting in crevice corrosion (Figure 4.8) and propagation of pitting corrosion (Figure 4.9). As with the metal concentration cell, the Nernst equation allows to determine the potential differences that arise from different O₂ concentrations.

Based on the Nernst equation (Equation (4.9)), Pourbaix or equilibrium diagrams show the chemical stability of a metal and its respective species as function of the applied potential at different pH levels.^[104] Figure 4.5 shows a simplified version of the Pourbaix diagram of chromium at $T = 25^\circ\text{C}$ and allows the reader to discern areas of metal corrosion, passivity, and immunity. The dotted lines indicate the stability of water or, i.e., at which pH and potential, H₂ (HER) or O₂ evolution (OER) are favored.^[105]

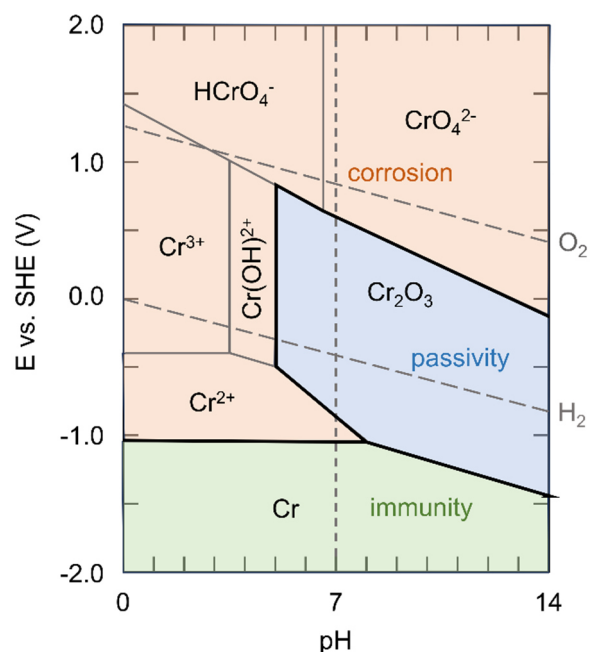


Figure 4.5. Pourbaix diagram of Cr at $T = 25^{\circ}\text{C}$ showing the thermodynamically most stable oxidation state with respect to electrolyte pH and applied electrode potential. The areas of immunity (green), passivity (blue) and corrosion (red) are indicated.

Despite their usefulness, the standard potentials, derived potentials, and pH-potential diagrams should generally be treated as guidelines for determining a metal's electrochemical stability. Corrosion studies generally investigate solutions with high contents of different dissolved ionic species (e.g., NaCl) than the respective metal salt. With that, shifts from the standard potentials arise for which the Nernst equation could be employed to determine the deviating potential. However, the thermodynamics of corroding systems are difficult to treat due to their non-equilibrium nature. Further complexity arises from the non-ideality and deviating surface composition. These problems are augmented by the strong dependence on electrode kinetics.^[104]

4.3.3 Kinetic Considerations of Electrochemical Reactions

Corrosion is a kinetically controlled process, in which the rate of the electrocatalytic reactions (HER and ORR) are very important. These rates differ largely between different metallic materials and thus require further consideration for predicting corrosion reactions. The thermodynamic treatment offers information on whether an electrochemical reaction is energetically feasible. However, no information can be drawn on how fast these reactions occur which is of the utmost importance for corrosion.

Generally, electrochemical reactions are multi-step processes, where charge transfer processes only take place at the electrode/electrolyte-interface and are coupled to mass transfer processes which may be caused by diffusion, convection, or migration.^[106] This may limit the reaction rate either through slow electrode reactions (activation polarization),

concentration changes in reacting species near the electrode (concentration polarization), or the IR drop across surface films or in solution (ohmic polarization).^[107] While a certain energy barrier E_A as determined by thermodynamics, must be overcome for the reaction to proceed,^[108] the overall reaction rate generally depends on the slowest step, i.e., the rate determining step (RDS).

Electrochemical polarization describes the deviation of the electrode potential from its equilibrium value E_{eq} to a potential where either the anodic or cathodic reaction predominates. The degree of polarization is defined as the overpotential η given by the difference of the applied potential E and the equilibrium potential E_{eq} of a specific reaction.

$$\eta = E - E_{eq}. \quad 4.18$$

Regarding corrosion processes, this deviation from E_{eq} is inherently complicated to determine since at least two redox couples react simultaneously at one electrode (Equations (4.1) and (4.2)). In this context, E_{corr} is the potential at which the currents of all four potential reactions balance each other to an external zero current. Due to the external zero current, E_{corr} is also referred to as open circuit potential E_{OCP} .

While E_{corr} is used instead of E_{eq} for a corroding system, it distinctly differs from the equilibrium potentials of the separate metal and hydrogen electrodes. For corrosion, the main anodic process would be metal dissolution (e.g., Cr dissolution) and the dominating cathodic process would be HER or ORR. This situation is typically visualized through Evans diagrams and Figure 4.6 depicts the exemplary redox couple of metal dissolution and HER (as in Equations (4.1) and (4.2)) occurring on a generic metal electrode. The potential (E_{corr}) where the metal dissolution and HER curves cross is a mixed potential and is situated between the $E^\circ(\text{Me}/\text{Me}^+)$ and $E^\circ(\text{H}/\text{H}^+)$.^[87]

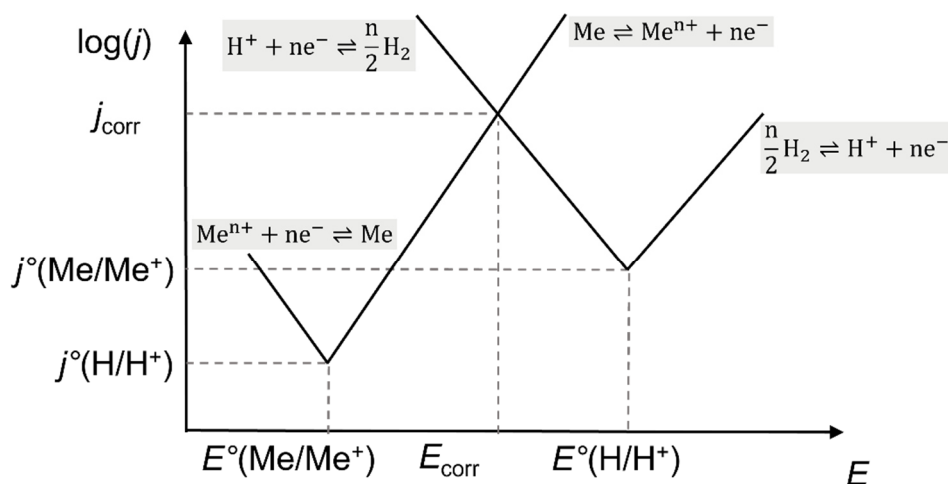


Figure 4.6. Evans diagram of a generic metal electrode corroding in an aqueous electrolyte showing the application of mixed potential theory.

For one redox process, e.g., either Equation (4.1) or (4.2), the relation between the reaction rate constant (i.e., current density) and the overpotential can be expressed by the Butler-Volmer equation (Equation (4.19)).^[87]

$$j = nFk^0(T) \left[c_R(x=0, t) \exp\left(\frac{(1-\alpha)nF\eta}{RT}\right) - c_O(x=0, t) \exp\left(\frac{-\alpha nF\eta}{RT}\right) \right] \quad 4.19$$

When the electrode is at equilibrium (E_{eq}), there is no net current density, and the corresponding current density is called the exchange current density, j_o , which may be expressed as

$$j_o = j_{an} - |j_{cat}| = 0. \quad 4.20$$

Due to the electrochemical equilibrium, the concentration of reductant R and oxidant O at the electrode surface ($x = 0$) is equal to the bulk concentrations which results in a simplified form of the Butler-Volmer equation

$$j = j_o \left(\exp\left[\frac{(1-\alpha)nF}{RT}\eta\right] - \exp\left[\frac{-\alpha nF}{RT}\eta\right] \right). \quad 4.21$$

For a typical corrosion system, two Butler-Volmer equations must be considered, one for the metal electrode and one for the hydrogen electrode (assuming that for the corroding system only these two redox couples exist). Although there is a complementarity between the anodic and cathodic process as in electrochemical equilibria, there is a very strong difference to an equilibrium, because the dominating anodic and cathodic processes involve *different* redox couples in corrosion reactions. Therefore, the dominating anodic and cathodic reactions must be treated with their own specific parameters. At sufficiently high overpotentials ($\eta > |\pm 50 \text{ to } 70 \text{ mV}|$),^[109] either the cathodic or anodic reaction predominates and the counter exponential term may be neglected.

$$\log j = \log |j_o| \left[\frac{-\alpha nF}{2.303RT} \eta \right] \quad 4.22$$

In the notation of the Tafel equation this yields

$$\eta_{cat} = -\frac{2.303RT}{\alpha_{cat}n_{cat}F} \log_{10} \left(\frac{j}{j_{o,cat}} \right) = \beta_{cat} \log_{10} \left(\frac{j}{j_{o,cat}} \right) \quad 4.23$$

$$\eta_{an} = \frac{2.303RT}{(1-\alpha_{an})n_{an}F} \log_{10} \left(\frac{j}{j_{o,an}} \right) = \beta_{an} \log_{10} \left(\frac{j}{j_{o,an}} \right) \quad 4.24$$

where β is the respective Tafel slope.

When contemplating corrosion reactions, a mix of different anodic (dissolution of different metals from an alloy electrode) and cathodic reactions (HER or ORR) may contribute towards the observed currents. The current densities of either the cathodic or anodic reactions at E_{corr} are called corrosion current density j_{corr} . It usually strongly deviates from j_o of the partial reactions.

$$\begin{aligned}
 j_{\text{corr}} &= \log_{10} |j_{\text{o,an}}| \left[\frac{\alpha_{\text{an}} n_{\text{an}} F (E_{\text{corr}} - E_{\text{eq,an}})}{RT} \right] \\
 &= \log_{10} |j_{\text{o,cat}}| \left[\frac{\alpha_{\text{cat}} n_{\text{cat}} F (E_{\text{corr}} - E_{\text{eq,cat}})}{RT} \right].
 \end{aligned}
 \tag{4.25}$$

Corrosion current densities are important parameters that are determined in polarization experiments. Since corrosion processes entail the simultaneous transfer of mass and charge across the interface between metal and solution, corrosion rates can be determined. The relationship between the transferred charge and the corresponding mass is given by Faraday's law^[110]

$$m = \frac{Q_{\text{corr}} M}{nF} = \frac{j_{\text{corr}} A t M}{nF}
 \tag{4.26}$$

where n is number of exchanged electrons for the reaction, Q is the charge, given by the product of current density j , electrode area A , time t ($Q = jAt$), and F is the Faraday constant. Equation (4.26) allows to calculate the mass lost during corrosion. Generally, the corrosion rate is given as a change in thickness over time. Considering that the mass may be expressed as the volume times density of the material and rearranging Equation (4.26) (where $x = V/A$, thickness of dissolved metal surface) gives

$$r_{\text{corr}} = \frac{dx}{dt} = \frac{j_{\text{corr}} M}{nF\rho}
 \tag{4.27}$$

where dx/dt is the corrosion rate expressed in thickness loss per unit time. Due to small numerical values, the thickness loss [cm s^{-1}] is commonly expressed per year, e.g., mm/year or $\mu\text{m}/\text{year}$. American corrosion rates are often expressed in mpy (milli-inch/year).

4.4 Passivity and Modes of Corrosion

Corrosion is sometimes referred to as reversed metallurgy because metals return to their naturally occurring and thermodynamically more stable ore (metal oxides, sulfides, silicates), whereas metallurgy expends high energy to turn metal ores into their elemental states.^[111] When these metals in their elemental or alloyed state encounter different environments such as air or aqueous solutions, they react, e.g., with O_2 and water to form passive oxide/hydroxide films that protect the metallic specimen from further corrosion.^[112-113] Passivity can be defined as the inactivity of a metal to undergo further chemical or electrochemical reactions with its environment although such features would be thermodynamically favorable. This feature enables the broad use of metallic materials. Most corrosion studies therefore dedicate their research to the physical and chemical properties of the protective passive film of metals or alloys. In anodic polarizations curves (see Chapter 5.1.1), passivity can generally be observed over potential ranges where the current density seems to remain constant.

There exist three general models on the formation of passive films. Based on Evans,^[114] the oxide film model assumes a three-dimensional thin film of oxides which separates the metal surface from the electrolyte and acts as a barrier. The film introduces two new interfaces, the metal/oxide film and oxide film/electrolyte interface. Contrarily, multiple studies indicate that the charge required to achieve initial passivation corresponds to the chemisorption of a monolayer of O₂.^[115-117] Correspondingly, in the adsorption model,^[118] the chemisorbed monolayer represents the primary cause of the reduction in metal surface reactivity. Considering that the passive film forms in a sequence of steps, Hackerman^[119] combined both models within the film sequence model. Here, passivation is initiated by the adsorption of molecular O₂ which propagates by splitting and charging to adsorbed O_{ads}⁻ species. The intrusion of by cations from the metal lattice results in the growth of the passive layer.

Depending on the metal or alloy in question these oxide films have thicknesses ranging from a few nanometers (e.g., transition metals)^[120-121] to hundreds of nanometers (e.g., non-transition metals).^[122] Generally, the films formed on transition metals tend to be thin (below 10 nm) and electronically conductive.^[123] Films on aluminum on the other hand are much thicker and less electronically conductive. While electronic conductivity may be desired especially in catalytic applications, ionic conductivity is undesirable as it may enhance attack by aggressive ions such as halides (e.g., Cl⁻).^[124] For good surface protection, the oxide layer must be chemically stable, i.e., have low solubility in the immersed medium and withstand a broad range of potentials. Chemical stability may be estimated from Pourbaix diagrams for the respective metal or alloy. Depending on the field of application, mechanical stability against abrasion, deformation or intrusion of aggressive ions is given by passive films with good adhesion and high compressive strength.^[123] The structure of the passive film, which may be amorphous or crystalline, strongly affects the properties outlined above.^[125-127] Generally, it is believed that amorphous morphologies resist corrosive attack more effectively due to the absence of grain boundaries and fewer defects. Different models on the structure of passive films have been proposed. Iron possesses one of the largest repertoires of proposed models, e.g., the bilayer model and bipolar-fixed charge model.^[128-130] Most recently, Marcus et al.^[131] proposed a duplex layer structure for the passive film formed on the CrMnFeCoNi MPEA where the inner layer is enriched in Mn oxide and the outer layer is preferentially occupied by Co and Fe oxides. Both layers contain Cr oxide whereas metallic Ni was mainly found in a modified metallic layer beneath the oxide film. Unfortunately, passive films inherently contain defects, microstructural weak points, or are exposed to aggressive media and succumb to corrosive deterioration at some point. Figure 4.7 summarizes typical forms of corrosive attack, i.e., passivity breakdown and each type will be described briefly below.^[88]

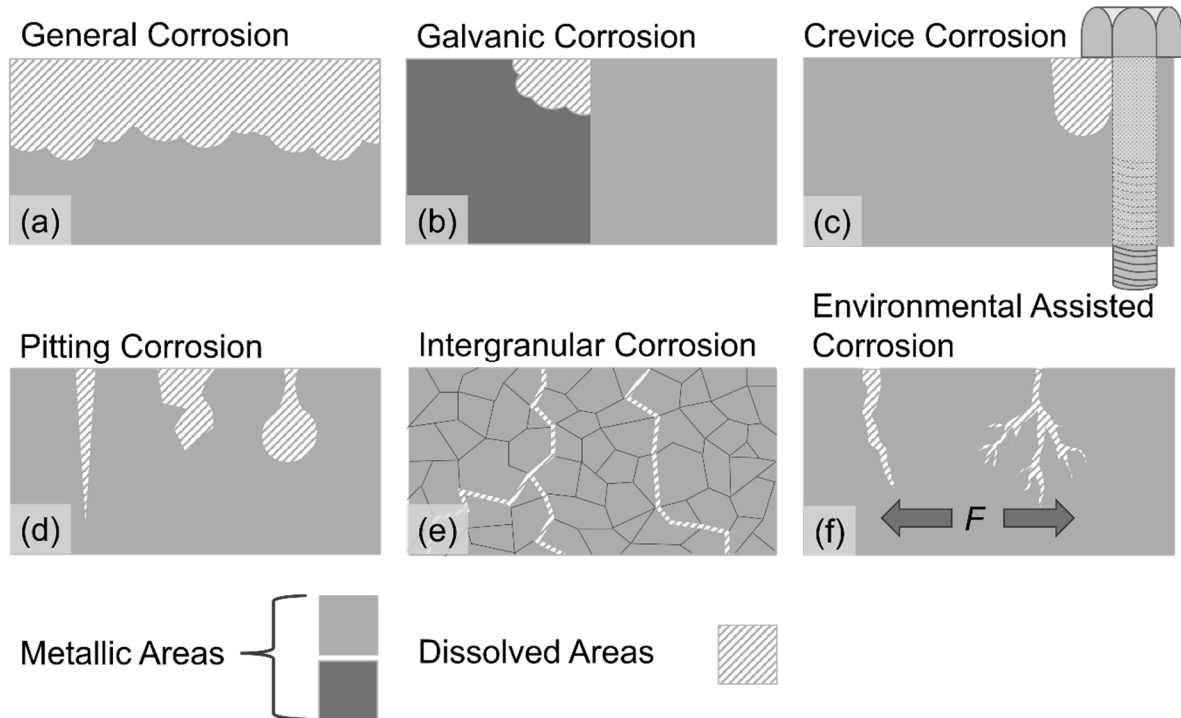


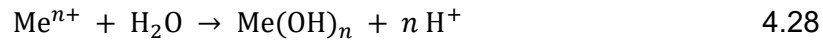
Figure 4.7. Summary of different modes of corrosion.^[88]

General corrosion (or uniform corrosion) is observed when the entire exposed metallic surface deteriorates evenly and the depth of metal loss on different areas is essentially the same.^[111] In contrast to localized corrosion (see below), no preferential attack occurs, and the metal specimen is uniformly thinned away. Even though localized anodic and cathodic sites exist on the surface, they distribute and change over time, leading to the overall general metal dissolution.^[88] This form of corrosive deterioration usually entails the greatest metal loss. Nevertheless, it is deemed the least troublesome, as its consequences are typically apparent and predictable.^[132]

Galvanic corrosion arises wherever two dissimilar metals or alloys are in contact. In contrast to the Daniell cell (see Figure 4.1), corrosion cells usually develop where two different metals or alloys are immersed in the same electrolyte or the same metal or alloy surface is immersed in a single electrolyte. As demonstrated in Chapter 4.3.2, the tendency of one metal to dissolve over another is related to its standard potential. Galvanic corrosion in alloys usually occurs due to compositional heterogeneities on the surface. For the MPEA $\text{AlCoCrFeNi}_{2.1}$ where two phases are present, one rich in Al and Ni (B2 phase), the other enriched in Cr, Co and Fe (L_{12} phase), the dissolution of the B2 phase is observed.^[91]

Crevice corrosion may occur in geometrically constricted cavities such as between overlapping metal sheets or under seals, gaskets, bolt heads and deposits (e.g., corrosion products) as illustrated in Figure 4.8. After its initiation, this form of localized corrosion can evoke severe deterioration of the crevice upon its propagation.^[133] Crevice corrosion initiation arises due to the development of differential O_2 cells. Upon immersion in an electrolyte, the metal surface exposed to the bulk electrolyte (external) and part of the metal surface within the

crevice (internal) face the same O_2 concentration. As general corrosion proceeds, the respective cathodic reaction (Equation (4.4)) consumes O_2 near the distinguished metal surfaces. The O_2 concentration is readily replenished at the external metal surface, but diffusion of O_2 into the crevice is restricted by the narrow diffusion path, causing the depletion of O_2 within the crevice. As a result, the diffusion limited current density $j_{l,crevice}$ for O_2 reduction is considerably reduced within the crevice compared to the bulk diffusion limited current, $j_{l,bulk}$, and the corrosion potential consequentially decreases. If the potential difference between the internal and external metal surface is large enough a differential O_2 cell develops, and metal dissolution occurs within the crevice. Propagation then takes place due to the concentration changes within the crevice electrolyte which become substantial because of the restricted diffusion. Thus, metal cations accumulate within the crevice and hydrolyze as seen in Equation (4.28) for a generic metal species Me.



Subsequently, the pH decreases within the crevice electrolyte. In electrolytes containing halides such as Cl^- , the accumulation of H^+ and metal cations leads to the migration of Cl^- into the crevice to sustain charge neutrality. While the initiation stage may be slow, the propagation stage is accelerated because of the highly corrosive environment that develops.^[133]

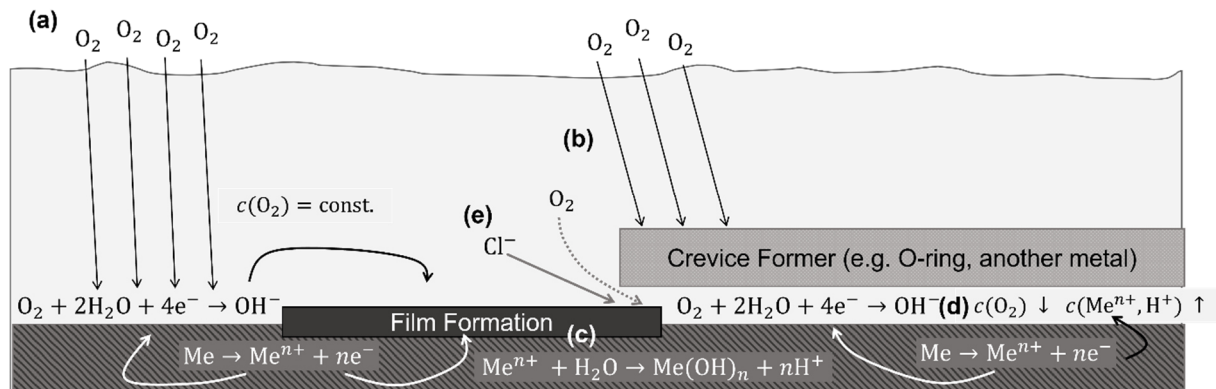


Figure 4.8. Schematic of crevice corrosion. (a) The constant diffusion of atmospheric O_2 into the electrolyte replenishes the O_2 concentration to the external metal surface. (b) O_2 diffusion is hindered by the crevice former. (c) Anodic metal dissolution and cathodic O_2 reduction contribute toward the passive film formation. (d) O_2 reduction and metal dissolution lead to O_2 depletion and dissolved cation accumulation in the crevice. Metal cations reacting with water lead to a decrease in pH. (e) Accumulation of positive species within the crevice attracts anions such as Cl^- .

Pitting corrosion is, in contrast to crevice corrosion, a stochastic event occurring at points where the passive film is locally weaker or flawed or faces a more aggressive environment. Inclusions, impurities, and surface finishing (the rougher the surface the more prone to pitting) may render locally weaker passive films.^[133] As with crevice corrosion, the pitting process can be divided into two stages: pit initiation and pit propagation. Crucial for pit propagation is the formation of a stable pit (as shown in Figure 4.9) during initiation which apart from local weak points also depends on exposure time, stagnant or moving electrolytes, surface positioning (horizontal or vertical) and the presence of aggressive ions (e.g., Cl^- , SO_4^{2-} ,

Br^- or NO_3^-)^[134] and their concentration. Due to its ubiquity reaching from the human body to sea water, Cl^- is the most extensively studied aggressive ion in pitting and crevice corrosion. Chemically, Cl^- ions are strong Lewis bases and readily interact with Lewis acids such as metal cations or protons. Compared to other anions such as SO_4^{2-} ($D = 1.065 \cdot 10^{-5} \text{ cm}^2 \text{ s}^{-1}$, where D is the diffusion coefficient), Cl^- ions are not as bulky and inhabit higher diffusivity, $D = 2.032 \cdot 10^{-5} \text{ cm}^2 \text{ s}^{-1}$.^[95] Other factors that may initiate pitting are active bacteria such as sulfur-reducing or iron-oxidizing bacteria which possess their own dedicated field of research termed microbial corrosion (MIC).^[135-136] In polarization diagrams the critical pitting potential E_{pit} marks the point where pit initiation results in stable pits, which propagate upon potential increase. Normally, pit propagation proceeds via an anodic site that resides within the pit and a cathodic site outside the pit, analogous to internal and external sites in crevice corrosion. As with crevice corrosion, the continuous metal dissolution within the pit leads to acidification inside the cavity which renders the process autocatalytic.^[137] The exact mechanisms of pit initiation are unknown and remain subject to on-going research, including computational methods.^[138] However, three main mechanisms which are the penetration, film thinning by adsorption, and film breaking mechanism are widely accepted as initiation steps.^[139-140] The first mechanism assumes that aggressive ions (e.g., Cl^-) penetrate through the passive film to the metal/oxide interface, assisting dissolution. Multiple models have been proposed to confirm this mechanism. Most notably may be the point defect model (PDM) by Macdonald et al.^[141] which postulates the migration of cations outward to the oxide/electrolyte interface and cation vacancies inward to the metal/oxide interface. The condensation of cation vacancies gives rise to voids at the metal/oxide interface and induces pit initiation due to increased stresses on the passive film. In accordance with the PDM, Cl^- ions are transported across the oxide layer via oxygen vacancies, as they are slightly larger than oxide ions with ionic radii of $r_{\text{Cl}^-} = 1.81 \text{ \AA}$ and $r_{\text{O}^{2-}} = 1.40 \text{ \AA}$.^[95, 142] The film thinning mechanism accounts for the attack of considerably larger aggressive ions that are thought to attack the oxide film by initial adsorption, subsequent clustering followed by the formation of surface complexes which then dissolve prompting local thinning. This approach has been supported by XPS analyses of passive films on iron and aluminum.^[143-144] For the film breaking mechanism, the oxide layer is assumed to have defects through which aggressive ions may intrude. Such defects may also be due to impurities, inclusions, or grain boundaries.^[123, 140]

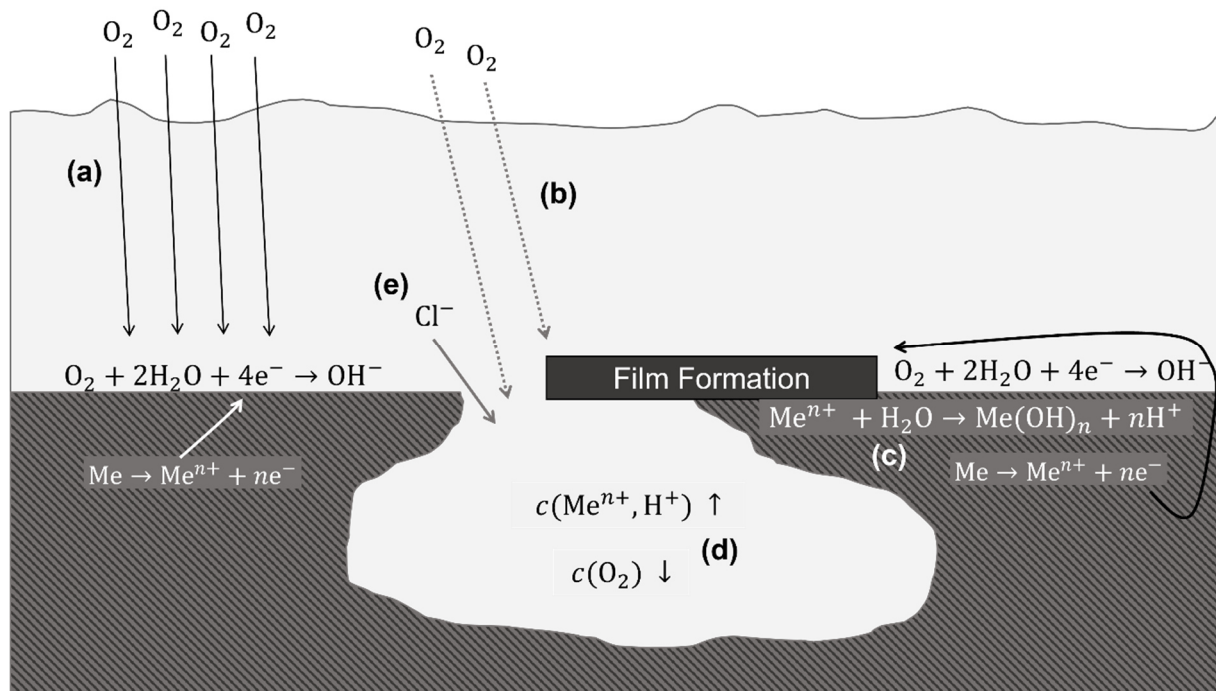


Figure 4.9. Schematic of pitting corrosion. (a) The constant diffusion of atmospheric O_2 into the electrolyte replenishes the O_2 concentration to the external metal surface. (b) O_2 diffusion is hindered geometrically by the small size of the pit, which may reduce further due to film formation. (c) Anodic metal dissolution and cathodic O_2 reduction contribute toward passive film formation. (d) O_2 reduction and metal dissolution lead to O_2 depletion and dissolved cation accumulation within the pit. Metal cations reacting with water lead to a decrease in pH. (e) Accumulation of positive species within the pit attracts anions such as Cl^- .

Intergranular corrosion describes the selective deterioration of the grain boundary (GB) network of the metal surface exposed to the electrolyte.^[145] Similar to pitting and crevice corrosion, intergranular corrosion is a local corrosion phenomenon that may penetrate deep into the material. Typically, this form of corrosion is dependent on the presence of impurities, intermetallic compounds, specific elemental accumulations, the atomic structure, and crystallographic nature of the grain boundary. Apart from intergranular corrosion due to chemical heterogeneities, data has shown that alloys are more susceptible to intergranular corrosion for high angle grain boundaries than for low angle grain boundaries (Figure 2.1).^[145] In correlation to the surface energy, which arises because surface atoms cannot bind to the optimum number of neighboring atoms compared to bulk atoms, interfacial grain boundary atoms also bind less regularly.^[89] With increasing misorientation, the grain boundary energy increases, rendering them ideal sites for corrosive attack.

Environmentally assisted corrosion generally comprises forms of corrosion under the influence of an additional mechanical load and shall only be mentioned for completion. Stress-corrosion cracking (SCC) as an interdisciplinary phenomenon combines electrochemistry, mechanics, and materials science.^[146] It typically occurs in alloys with good general corrosion resistance under tensile load in the presence of corrosive species such Cl^- . Another form of corrosion under mechanical load is corrosion fatigue which occurs because of cyclic load repetition in corrosive media.^[146] In erosion corrosion the metallic specimen is

exposed to moving liquids whereas the velocity of the flow, depending on whether it is laminar or turbulent, influences the severity of corrosion. With higher velocities and turbulent flows increasing the deterioration by corrosion. More generally, tribocorrosion has been established as a field of research and studies the combined effects of corrosion and tribology which encompasses the investigation of wear, lubrication, and friction.^[147]

4.5 Corrosion of MPEAs

Since the beginning of increased research interest in MPEAs in the early 2000s, studies have initially focused on the ductility and strength trade-off of MPEAs.^[79, 148-150] The focus then shifted to other physical and microstructural properties under specific conditions, such as cryogenic exposure and irradiation at high temperatures.^[21, 151] Finally, an increasing number of studies on MPEAs included corrosive behavior investigations.^[101, 152-153] Nevertheless, shortly after introducing the concept of MPEAs, Yeh et al.^[154] first presented results that indicated better resistance to uniform corrosion of the as-cast $\text{Cu}_{0.5}\text{NiAlCoCrFeSi}$ MPEA over 304 stainless steel (SS) in 0.5 M H_2SO_4 and 1 M NaCl. In Cl^- containing electrolytes, the MPEA experienced more severe pitting corrosion than 304 SS, but in Cl^- free solutions the MPEA exhibited resistance to pitting corrosion. However, the polarization experiments clearly display an overall better performance of 304 SS in terms of lower current densities at high anodic potentials and during re-passivation, indicating superior passivation. It should be noted that this initial and many following investigations of the corrosion behavior of MPEAs employed as-cast specimens which can differ severely in their corrosion resistance from mechanically and/or heat-treated alloys. With conventional alloys this is generally not an issue, as a vast number of engineering alloys (e.g., some aluminium alloys) are used in their as-cast state.^[155-156] However, this presents a critical lack in understanding the vast compositional space of MPEAs for which phase diagrams are widely unknown and difficult to calculate. Computational efforts are undertaken to conceive the multidimensional phase diagrams to find and investigate temperatures where phase changes occur.^[157] In turn, few corrosion studies of MPEAs investigate the influence of the microstructure on corrosion resistance which is a crucial parameter.^[158-159] Since 2015, corrosion investigations of MPEAs surged and lead to the general observation that this class of alloys exhibits inherent corrosion resistance despite microstructural heterogeneities.^[156] Qui et al.^[160] compiled a galvanic series on the basis of measured E_{corr} and E_{pit} data of a multitude of multiphase MPEAs which exhibited nobler potentials than aluminum alloys and carbon steel. Some even compared favorably to austenitic and ferritic steels which are usually more resistant to corrosion.^[3]

The corrosion characteristics of MPEAs have been investigated in a small selection of typical electrolytes including H_2SO_4 , NaCl, HCl and NaOH.^[161-165] Only a few studies

investigated the electrochemical responses of MPEAs in more specialized electrolytes such as simulated sea water, simulated body fluid (SBF), artificial saliva (AS) and microbial electrolytes.^[166-172] Studies in simulated sea water may test for the applicability in marine environments and may additionally test the resistance toward tribocorrosion due to the continuous movement of oceans or seas. The MPEAs CrCoNi and FeCrNiCoM (where M = Al or Mo) have shown that an increase in Cr-content in the former improves its resistance towards tribocorrosion whereas the FeCrNiCoMo specimen outperformed 304 SS, exhibiting the smallest wear rate.^[166-167] For medical implants, alloys need to withstand corrosion in biologically relevant media, i.e., solutions that resemble ionic concentrations in, e.g., blood plasma (SBF) and other equivalent bodily fluids. Considering that Ti inhabits excellent biocompatibility due to its high corrosion resistance, appropriate reactivity, and high strength to weight ratio,^[173-174] it is a prime candidate to be present in an MPEA for medical applications. Other refractory metals including Nb, Ta and Hf also possess good biocompatibility.^[175] Hence, Ti-based MPEAs TiNbTaZrMo and TiTaHfM (where M = Nb, NbZr or MoZr) were investigated and the former surpassed the corrosion resistance of the conventionally employed Ti₆Al₄V implant alloy in SBF and the latter showed reduced ion release in AS when containing Zr and Nb. Analyses in microbial environments have demonstrated the deterioration of TiZrNb and FeCoCrNiMo_{0.1} MPEAs due to enhanced localized corrosion aggravated by sulfate reducing bacteria.^[172, 176] Corrosive investigations of MPEAs in these complex and highly specialized electrolytes are currently in their infancy and require further research to deem the respective applications appropriate.

Most of the corrosion research on MPEAs to date has focused on simpler aqueous electrolytes as outlined above. In turn, effects on corrosive behaviors because of differing microstructures due to heat treatment or compositional changes accomplished by targeted element addition have generally been investigated in electrolytes of H₂SO₄ and NaCl. When electrodeposited CrMnFeCoNi MPEA coatings on copper were investigated for corrosion resistance in simulated sea water, heat treatment resulted in films with homogeneous distribution, improved growth and enhanced corrosion resistance compared to the as-deposited coatings.^[177] In their study on grain size influence on the corrosion behavior of CrMnFeCoNi in 0.5 M H₂SO₄, Jin et al.^[178] annealed the MPEA specimen at different temperatures for 1 h to compare between the variants. According to the increase in the heat treatment temperature, the as-cast state, fine-grained (FG), medium-grained (MG) and coarse-grained (CG) variants were analyzed. The results demonstrate that for the FG sample rapid ion dissolution due to abundant grain boundaries leads to fast passive film formation. However, the FG passive film is unstable, and passive film stability increases with grain size. Interestingly, the highest amount of protective Cr oxides was found on the MG and not the CG sample, highlighting that larger grain sizes are desirable but the balance between fast

passivation and film stability needs to be considered. In contrast, results by Don et al.^[179] on the influence of heat treatment on the corrosion behavior of laser powder bed fusion (PBF-LB) produced AlCrMnFeCoNi MPEAs underline the difficulty of finding the appropriate heat treatment which may generate divergent microstructures. Their sample exacerbated from the as-cast state to the heat-treated state at 850°C with a pronounced increase in pitting corrosion in 0.6 M NaCl and 0.5 M H₂SO₄ because of microcracks and chemical segregation. After heat treatment at 1150°C, the MPEA's corrosion behavior improved compared to the as-cast state and exhibited improved strength and ductility.

CrFeCoNi-based MPEAs with additions of other elements such as Al, Cu, Mo, or Mn have been extensively studied whereas the most employed system encompasses Mn and is sometimes referred to as the Cantor alloy.^[24, 180-184] As a point of reference, the corrosion behavior of an MPEA is typically compared to a conventional alloy. For example, Luo et al.^[101] compared the passive film properties and corrosion behavior of CrMnFeCoNi in 0.1 M H₂SO₄ to 304L SS. Despite microstructural and compositional similarities – both alloys contain passivating elements Cr and Ni – their corrosive response differed. The selective dissolution of Fe is in synergy with the formation of a Cr-rich passive film on 304L SS and surpassed the corrosion resistance of the MPEA for which the authors reported similar dissolution of all elements and the formation of a defective passive film. After corrosion in 0.05 M H₂SO₄ Marcus et al.^[131] examined the thickness and composition of the formed passive layer with XPS and ToF-SIMS. To circumvent the complications that arise with 2p core level spectra of transition metals, such as interfering Auger transitions, the group analyzed the 3p core level spectra. This approach determined a layered structure of the passive film comprising of a Cr-, Fe- and Co-rich outer oxide layer and a Cr-, Mn-rich inner oxide layer. Our own study looked at a comparison of passive film thickness and composition between corrosion of CrMnFeCoNi in 0.1 M H₂SO₄ and 0.1 M NaCl.^[185] In NaCl, the CrMnFeCoNi succumbs to severe pitting corrosion and generally performs poorer than SS. It has been suggested multiple times that the alloying of Mn, added to improve phase stability and mechanical properties, may cause poor corrosion performance.^[23-24, 79, 186] A study by Torbati-Sarraf et al.^[24] focused on the effect of Mn on the corrosion behavior of CrFeCoNi in 0.1 M NaCl through XPS investigation, and found that the Mn containing MPEA forms a more defective as well as less corrosion resistant passive film. In 0.1 M H₂SO₄, the influence of Mn on the corrosion properties of CrFeCoNi showed that Mn suppresses initial passivation and deteriorates passive film stability.^[23] Omission of Mn seems to improve the corrosion performance of the typical CrFeCoNi-based MPEA. Alloying only three elements leads to CrCoNi and FeCrNi MPEAs which both exhibit excellent mechanical properties.^[18, 187] Corrosion studies of CrCoNi showed that the MPEA exhibits superior corrosion resistance over 304 SS and CrMnFeCoNi in H₂SO₄ and NaCl electrolytes.^[25] In NaOH media, however, it is not as resistant as 304 SS due to its increased

Cr dissolution. The equimolar FeCrNi MPEA resembles the industrially employed Fenicro® alloy. While Fenicro® is highly corrosion resistant and does not succumb to intergranular corrosion due to its additions of Mo and Si, studies on the FeCrNi MPEA remain scarce. Compared with CrCoNi, however, FeCrNi may pose a more feasible option, as Co typically comes with a high ethical and economical cost. [188-190]

Generally, the corrosion properties and surface characteristics have been investigated with electrochemical methods where cyclic potentiodynamic polarization and electrochemical impedance spectroscopy found predominant use. Analyses of the electrolyte have been conducted after electrochemical measurement as well as on-line. [102, 164, 191-192] On-line metal dissolution was followed by atomic emission spectroelectrochemical (AESEC) methods, where the electrolyte is simultaneously transferred by pumps into an inductively coupled-mass spectrometry (ICP-MS) or optical emission spectroscopy (ICP-OES) instrument to quantify dissolved metal ions. Surface properties such as structure, composition, and film thickness have been examined ex-situ via transmission electron microscopy (TEM), X-ray photoelectron spectroscopy (XPS), X-ray diffraction analysis (XRD), time of flight-secondary ion mass spectrometry (TOF-SIMS) and atomic force microscopy (AFM). [131, 192-195] Characterization methods employed within the scope of this work will be discussed in the following Chapter 5.

5 Applied Characterization Methods

5.1 Electrochemical Characterization of the Corrosion Behavior

The analysis of electrochemical processes is based on measurements that enable the control and monitoring of the energy and flow of electrons, i.e., the potential and current.^[196] To adjust and measure variables, a high impedance potentiostat is needed to prevent undesirable current flow.^[197] With a potentiostat or galvanostat the electrochemical system may be perturbed in a controlled manner to extract information from the resulting current or potential, respectively. Many modern instruments, often called electrochemical workstations, can switch between potentiostatic operation (applying a potential, measuring current) and galvanostatic operation (applying a current, measuring potential). The current I through an electrochemical system

$$I = \frac{dQ}{dt} \quad 5.1$$

corresponds to the amount of electrons because Q is a multitude of the elementary charge $e = 1.602 \times 10^{-19}$ C. Q is linked by Faraday's law (Equation (4.26)) to the amount of converted substances.^[196-197]

5.1.1 Polarization Measurements

A typical corrosion experiment starts with monitoring the open circuit potential (OCP) as it is often required as a reference point for other measurements. The OCP represents the potential difference between the WE and the RE while no current is flowing between the WE and the AE.^[198] Depending on the stability, the OCP may change over time due to, e.g., corrosion, chemical reactions at the electrode surface or other changes at the electrolyte/electrode interface. To investigate the corrosive behavior of a material, the current-potential relationship is studied over broad ranges of applied potentials.^[109]

In potentiodynamic polarization measurements, a potential range is scanned at a fixed rate between set values. For linear potentiodynamic polarization a starting and a terminating potential are selected, whereas for cyclic polarization an apex potential is set between the starting and final potential (as shown in Figure 5.1). To avoid non-faradaic currents from capacitor charging and to maintain steady-state conditions, scan rates range from 0.1 mV s^{-1} to 1 mV s^{-1} are preferred.^[109] The resulting current is recorded.

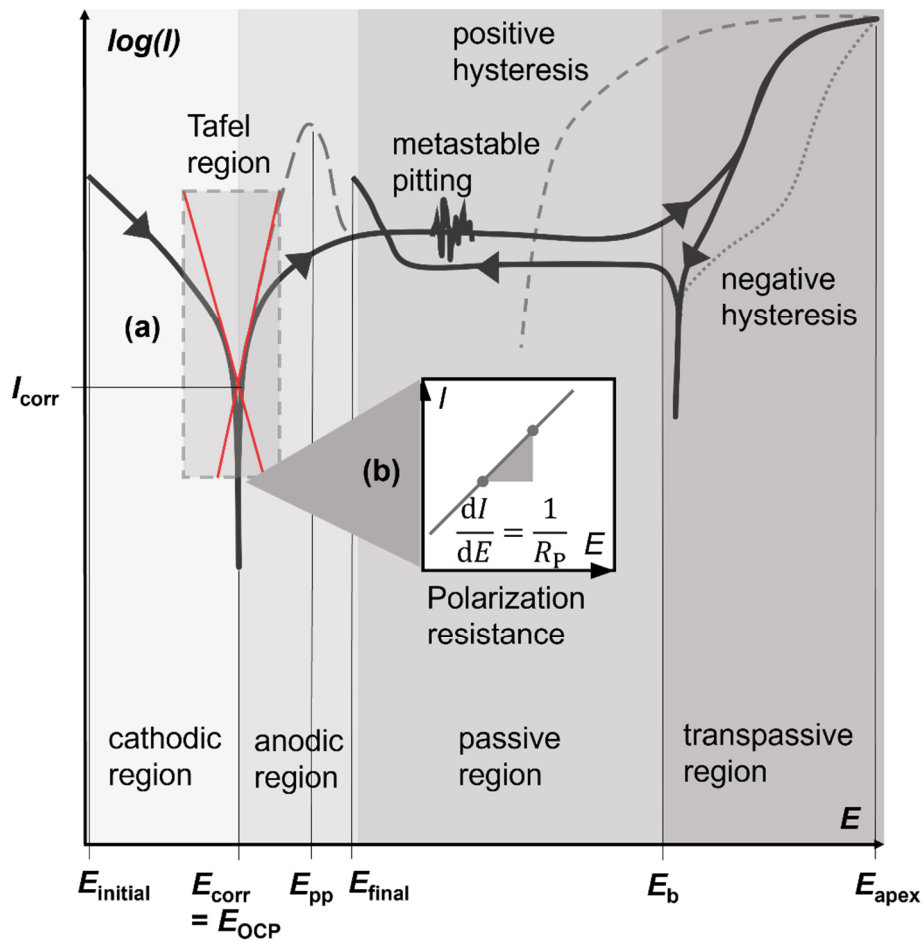


Figure 5.1. Generic cyclic potentiodynamic polarization diagram with current (logarithmic scale) plotted versus the applied potential. Respective electrochemical parameters and characteristics that can be retrieved from a CPP are highlighted.

To record the current-potential relationship in the Tafel region, potentials need to be sufficiently far from the OCP, typically $\pm 50 - 70$ mV vs. OCP.^[109] At these potentials either the cathodic (I_c) or anodic (I_a) current predominate the net current. The whole scan is then run within a range of -250 mV to $+250$ mV vs. OCP which accounts for the fact that the OCP may shift during the measurement due to oxide reduction, metal dissolution, or passivation.^[109] Figure 5.1a shows the Tafel region of a generic potentiodynamic polarization. In the diagram the cathodic and anodic region generally expand over more than a magnitude in current, and thus allow for extrapolation and fitting. Research has shown that the extrapolation of the cathodic region is generally more practical and sensible to deduce the corrosion current and Tafel slope β_c .^[199] The anodic portion, especially in corrosion-prone systems, may be affected by dissolution or oxide film formation, leading to different corrosion current densities.^[109] Most software packages of commercially available electrochemical workstations offer fitting of the Tafel polarization region through non-linear least squares fitting of the Wagner-Traud equation (Equation (5.2)).^[200]

$$j_{\text{net}} = j_{\text{corr}} \left[e^{\left(\frac{2.3(E-E_{\text{corr}})}{\beta_a} \right)} - e^{\left(\frac{2.3(E-E_{\text{corr}})}{|\beta_c|} \right)} \right] \quad 5.2$$

This fitting approach should be applied when both, the cathodic and anodic regions are under activation control, as non-Tafel like behavior produces non-sensible values.^[109] Corrosion current density values are rendered from the recorded net current density j_{net} and reside in between the cathodic and anodic extrapolation values.

Similar to the Tafel polarization, linear polarization resistance (LPR) is recorded close to OCP. Here, the potential scan range is kept narrower, approximately ± 30 mV vs. OCP, to measure within a potential region where the current behavior is linear.^[109] Figure 5.1b shows the linear behavior in current response for an LPR measurement where the slope is the polarization resistance R_p .

$$R_p = \frac{dE}{dI} \quad 5.3$$

The corrosion current density may also be extracted from these scans by employing the Stern-Geary equation (Equation (5.4)), when the Tafel slopes are known.^[201]

$$j_{\text{corr}} = \frac{\beta_a \beta_c}{(\beta_a + \beta_c) 2.3 R_p} \quad 5.4$$

By combining Equations (5.2) and (5.4), Mansfeld^[201] showed that the Tafel slopes may be extracted through Equation (5.5) from polarization analysis close to OCP when R_p and E_{corr} are known.

$$j_{\text{net}} = \frac{\beta_a \beta_c}{(\beta_a + \beta_c) 2.3 R_p} \left[e^{\left(\frac{2.3(E-E_{\text{corr}})}{\beta_a} \right)} - e^{\left(\frac{2.3(E-E_{\text{corr}})}{|\beta_c|} \right)} \right] \quad 5.5$$

Further polarization to higher anodic potentials yields valuable qualitative and quantitative information on the electrochemical behavior of the electrode material under investigation. Characteristics that can be drawn from these measurements are summarized in Figure 5.1 and encompass the corrosion potential (E_{corr}), primary passivation potential (i.e., active dissolution, E_{pp}), active/passive transition, passive region (ΔE), metastable pitting/metastable localized corrosion (including crevice corrosion), breakdown/pitting/pit nucleation potential (E_b), transpassive region (the literature typically assumes OER and passive film dissolution),^[202-204] re-passivation potential (E_{rp}).

For cyclic potentiodynamic polarization (CPP) studies, the scan is reversed upon reaching the pre-defined apex potential where linear potentiodynamic polarization (LPP) otherwise terminates. Typically, measured currents in CPP or LPP are recorded and displayed on the logarithmic scale and the changes in current ranges are automatically switched by the instrument. The resulting hysteresis as indicated in Figure 5.1 provides further information on localized corrosion (positive hysteresis) and re-passivation (E_{rp}). A negative hysteresis is typically indicative of a stable system. LPP or CPP both provide the data necessary for Tafel

extrapolation and LPR as can be seen in Figure 5.1a and b. However, Tafel polarization and LPR are generally non-destructive, as the electrode is not perturbed far from its OCP, allowing for repeated measurements and long-term monitoring.^[109] LPP and CPP, on the other hand, render significantly changed electrode surfaces due to passivation and corrosion. Drawing from potentiodynamic polarization measurements, the material may also be investigated potentiostatically at certain potentials to, e.g., induce passivation or dissolution.

When employing faster scan rates, potentiodynamic polarization may be termed either linear sweep (LSV) or cyclic voltammetry (CV) depending on whether the scan is conducted in a linear or cyclic fashion. LSV or CV experiments are typically conducted to elucidate reaction mechanisms and kinetics of dissolved reagents.^[205] In this work, CV measurements were mainly employed in connection with scanning electrochemical microscopy analyses on which more information is disclosed in Chapter 5.2.2.

5.1.2 Electrochemical Impedance Spectroscopy

Electrochemical impedance spectroscopy (EIS) is another non-destructive electrochemical technique used to analyze linear time-invariant systems.^[206] A periodic perturbation excitation of the system under investigation is achieved by applying a small-amplitude sinusoidal signal (ac voltage or current) superimposed on a respective dc signal (typically OCP) over a broad range of frequencies (commercially available instruments offer ranges from 1 MHz to 10 μ Hz).^[207-208] The electrochemical impedance Z is a complex quantity that depends on frequency f , and accordingly EIS is a transfer function method that measures an output signal (ac voltage or current) to an input signal (ac voltage or current) (see Equation (5.6)).^[208] The measurement of the output signal is complemented by calculating the transfer function using equivalent circuits that resemble the electrical behavior of the electrode under study.

$$Z(\omega) = \frac{\tilde{E}(\omega)}{\tilde{I}(\omega)} = \frac{\Delta E e^{i\phi}}{I_0 e^{i\phi}} = |Z|(\cos \phi + i \sin \phi) = Z' + i Z'' \quad 5.6$$

Here, ω is the angular frequency related to the frequency f by $\omega = 2\pi f$, $\phi = \omega t$ is the phase angle (phase shift between input and output signal), $i = \sqrt{-1}$, and $|Z| = \Delta E / I_0$ is the magnitude. \tilde{V} and \tilde{I} are phasors which are complex time-invariant numbers that represent the amplitude and phase of a sinusoidal function.^[207-208]

Electrical, electrochemical, and physical processes of an electrochemical system exhibit different time behaviors which may be classified into three types of perturbation response.^[208] At high frequencies, fast processes due to the kinetics of faradaic reactions are observed. Within medium frequencies, the charging/discharging of the EDL or other surface layers at the electrolyte/electrode interface reside. Slower physical processes such as mass transport phenomena are located at low frequencies. The associated time constants of these processes may be deconvoluted by EIS analysis.^[208] In an electrochemical system, the real

part Z' represents the frequency-dependent resistance which impedes current flow and exhibits a phase shift of $\phi = 0^\circ$. The imaginary part Z'' represents the reactance of the system when current flow is impeded either by capacitors ($\phi = 90^\circ$) or inductors ($\phi = -90^\circ$), respectively.^[207-208] Due to the different time constants, EIS may enable the analysis of different electrochemically relevant events in one experiment.^[207]

The measurements are interpreted by fitting an electrical equivalent circuit (EEC) model to the experimental data. The EEC typically comprises resistors, capacitors, inductors and often more complicated elements such as the constant phase element (CPE).^[208] As passive films formed on metal electrodes are inherently defective, the CPE is employed in EECs to model a non-ideal capacitor. The impedance of a CPE is given by

$$Z_{\text{CPE}} = \frac{1}{(i\omega)^\alpha Q_{\text{CPE}}}, \quad 5.7$$

where Q_{CPE} (the subscript is included to avoid confusion with the charge, Q) contains the capacitance information of the CPE and is given in F s^{m-1} .^[208] The exponent m represents the degree of deviation from ideal capacitor behavior and may range from $m = 0$ (resistor) to $m = 1$ (capacitor).^[209] If the CPE behaves as an inductor, $m = -1$.^[210] As the ideal capacitor has a phase shift of $\phi = 90^\circ$, the deviation θ of the CPE is related to the phase by

$$\theta = 90^\circ(1 - m) \quad 5.8$$

For reliable electrochemical impedance spectra, the system under investigation must be linear (the use of a small perturbation should ensure that input and output signals have the same frequency), causal (the output is dependent on the input signal), stable (the system returns to its original state when perturbation ceases) and finite (the impedance of the system tends to constant values when $\omega \rightarrow 0$ and $\omega \rightarrow \infty$).^[207-208] The Kramers-Kronig relation relies on these four criteria and allows to calculate Z' from Z'' and vice versa and consequently enables the detection of errors due to the interdependence of the real and imaginary parts of impedance.^[211]

EIS data for electrochemical systems are typically represented either by Bode or Nyquist plots.^[207] The spectrum displayed in the Bode plot presents two curves vs. $\log(f)$, the magnitude of impedance $|Z|$ and the phase shift ϕ . Bode representations facilitate matching electrochemical processes to the respective frequencies. For Nyquist representations, the imaginary part of the impedance is plotted as a function of its real part ($-Z' = f(Z'')$). Both axes should be drawn to depict the same range.^[208] Figure 5.2 shows the generic Bode (a) and Nyquist (b) diagrams for the electrical equivalent circuit (c) employed to analyze the EIS spectra in this work.

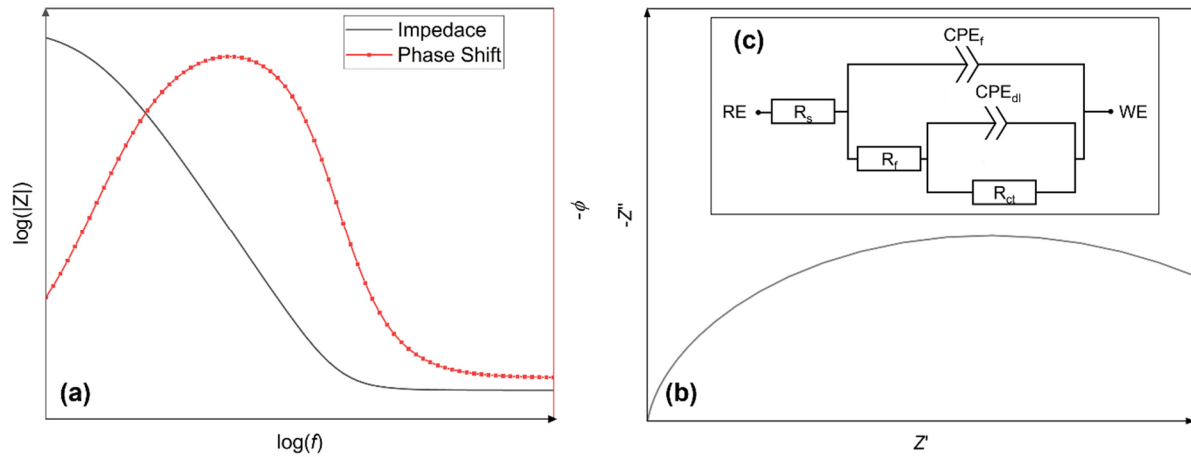


Figure 5.2. Generic (a) Bode and (b) Nyquist diagrams for the electrical equivalent circuit in (c).

5.2 Surface Characterization by Scanning Probe Microscopy

Scanning probe microscopy uses a pointed sensor to scan a surface and to build an image from the sequentially recorded data points. The sensor can be a force sensor in atomic force microscopy (AFM), a capacitive sensor in scanning Kelvin force microscopy (SKPFM) or an amperometric microelectrode in scanning electrochemical microscopy (SECM). Scanning electron microscopy (SEM), on the other hand constitutes a special form of scanning probe microscopy, where a focused electron beam probe is scanned over the sample surface.

5.2.1 Atomic Force Microscopy

The AFM imaging technique is based on monitoring the deflection of a plate spring (termed cantilever) while it is scanned over a substrate surface. Typically, the cantilever consists of a silicon wafer coated with a specific metal (e.g., Pt, Cr, Al). The cantilever is fixed on a holder at one end. At the other end it has a small lever (the plate spring) with a sharp tip that faces the sample (see Figure 5.3).

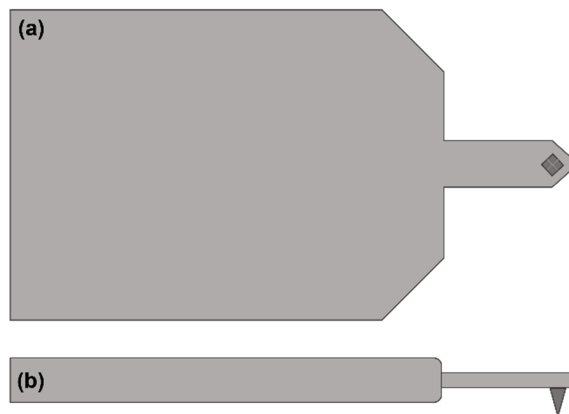


Figure 5.3. Schematic of a cantilever plate spring with its holder from (a) the top and (b) the side view.

The sharp tip enables the local monitoring of force interactions (attractive or repulsive) that result in bending of the lever. The bending of the lever is detected by the deflection of a laser beam that is oriented onto the tip of the lever. The reflected laser beam hits a photodetector, typically a photodiode with four quadrants to monitor vertical and lateral deflection of the lever, that converts the incident laser beam into an electrical signal (see Figure 5.4).^[212-213] A typical AFM image reflects the topography (height) of the investigated surface. In addition electrostatic, mechanical, and magnetic properties can also be scanned.^[212] The force that the cantilever spring experiences can be expressed by Hooke's law

$$F = -kz \quad 5.9$$

where k is the force constant of the cantilever and z is the distance of deflection relative to the equilibrium position. The shorter and thicker a cantilever, the higher will be its force constant and resonance frequency ω_0 which is also called the natural frequency of the oscillator.^[212, 214]

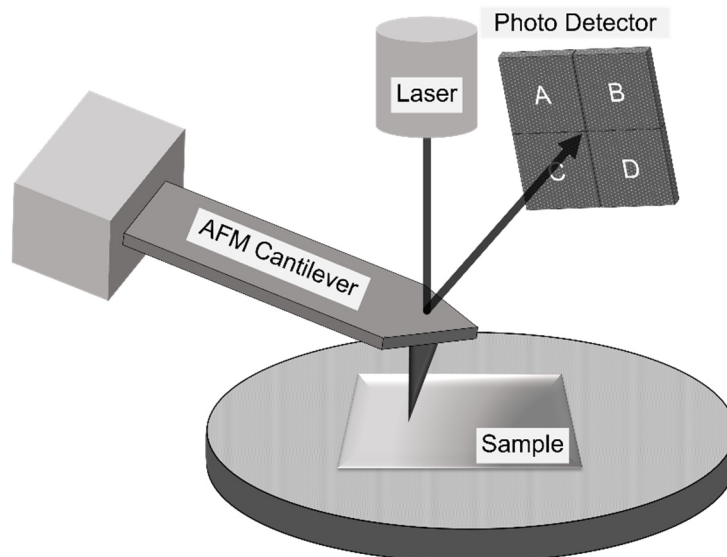


Figure 5.4. Schematic of the detection of the deflection of the cantilever by a reflection of a laser beam onto a split photodiode.

The translation of the tip during imaging is made by means of piezoelectric motors which expand or retract by applying a voltage and enable sub-nanometer precise positioning.^[215] Further stepper motors enable coarse positioning of the tip over the sample.

Images may be recorded in different modes which include contact, force modulation, non-contact, intermittent contact, and force spectroscopy modes. Figure 5.5 shows a force-distance curve and schematically presents the range of operation of each mode.^[212] Two regions are identified in the diagram. Upon approaching the sample from faraway (approx. a few 100 nm), the tip enters an attractive interaction region due to capillary and van-der-Waals forces, which reach a minimum at a certain distance (see Figure 5.5). After the minimum, the tip-sample interaction enters the repulsive region due to electrostatic forces.^[213] Both the contact and force modulation mode act in the repulsive region where the cantilever tip never leaves the sample surface.^[212] While the contact mode is either conducted at constant height

or constant force, the force modulation mode is the dynamic version of the former. These two modes may suffer from lateral deflections and may destroy the interrogated surface due to the close contact. On the contrary, in the non-contact mode, the cantilever oscillates within the attractive part. This mode is rarely used because capillary forces due to condensed thin water films under ambient conditions may pull the cantilever tip into contact resulting in erroneous signals.^[212]

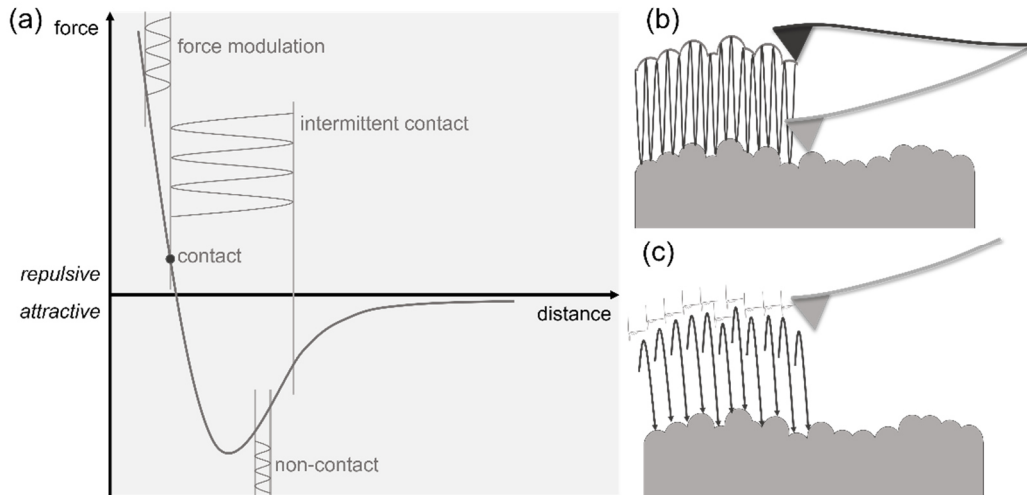


Figure 5.5. (a) Force interaction between the cantilever tip and sample surface as a function of distance. (b) Intermittent contact or tapping mode with a setpoint amplitude. (c) Force spectroscopy or quantitative imaging mode where a force curve is recorded at each pixel. Adapted with permission from ^[212]. Copyright 2017, The Authors.

In this work, the intermittent contact mode was employed as the main method in ambient conditions and force spectroscopy as the main method for in-situ imaging. The drawbacks of the contact and non-contact modes are overcome in the intermittent contact mode (IC), sometimes referred to as tapping mode, where the cantilever is oscillated and operated between the repulsive and attractive region and lightly taps the surface periodically (as depicted in Figure 5.5).^[212, 216] The distance, z , of the oscillating cantilever is given by

$$z = A \cos(\omega_0 t + \phi) \quad 5.10$$

where A is the amplitude, ω_0 is the resonance frequency, t is the time and ϕ is the phase shift between the excitation and the oscillation signal.^[214, 216] Respectively, the IC mode is either operated at a setpoint frequency, phase, or amplitude. The height is then scanned, while the position of the cantilever is adjusted via the piezoelectric motor through feedback systems so that the setpoint is maintained. To avoid interference due attractive forces acting on the tip, cantilevers with force constants of 21 to 78 N/m are employed for the IC mode.^[212]

In force spectroscopy, a full force-distance curve is recorded at each pixel of the scan, providing local information on tip-sample interactions while recording topographic images. Typically, the instrument records the extension and retraction force-distance curve.^[212] Two examples are displayed in Figure 5.6, one in ambient conditions (Figure 5.6a) and one in 0.1 M NaCl (Figure 5.6b), of a Cr/Pt coated silicon cantilever tip approaching a polished CrCoNi

surface. This mode is especially useful for measuring in-situ as the cantilever can be retracted as far as required and the damping of the cantilever vibration due to the liquid does not interfere with the measurement.

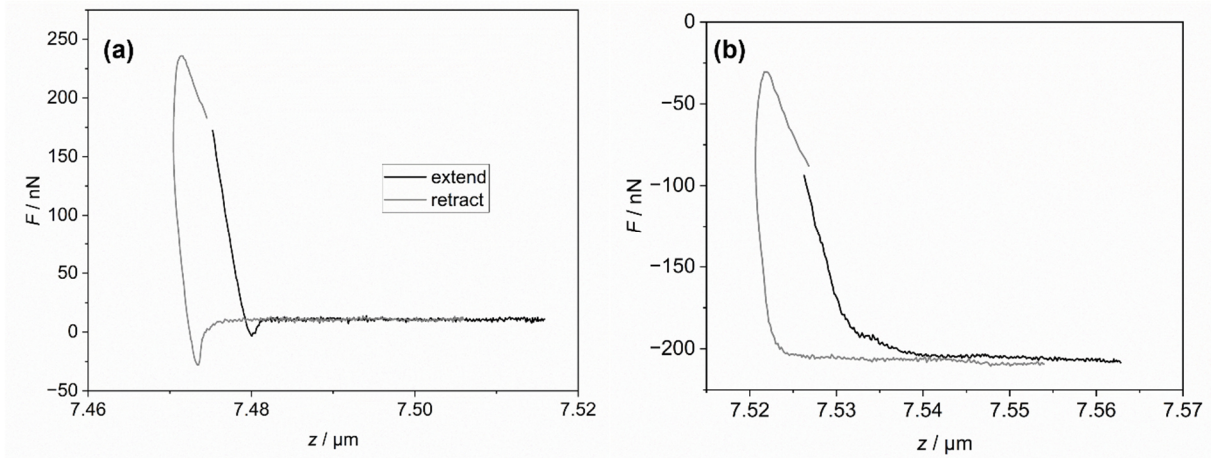


Figure 5.6. (a) Force curves of a Cr/Pt coated silicon cantilever ($k = 40 \text{ N m}^{-1}$) approaching a polished CrCoNi surface at $25 \text{ }^\circ\text{C}$ in air. (b) Force curves of a Cr/Pt coated silicon cantilever ($k = 40 \text{ N m}^{-1}$) approaching a polished CrCoNi surface at $25 \text{ }^\circ\text{C}$ in 0.1 M NaCl.

SKPFM as a form of atomic force microscopy, employs conductive cantilever probes to scan on top of the topography the electrical properties of a conductive sample surface. The method is based on the macroscopic Kelvin method, invented by Lord Kelvin in 1898.^[217] The Kelvin method measures the contact potential between two metal samples which are brought in close proximity to form a plate capacitor.^[218] A common mode for SKPFM measurements is the lift mode, or hover mode.^[217] In this mode, the topography of the surface is recorded in the IC mode on the first scan. The retrieved height information is then employed to guide the cantilever according to the topographic contour on the second scan but at an offset of 10 - 100 nm (see Figure 5.7).^[217] The lift mode possesses the ability to measure the electrostatic force decoupled from long or short range forces that could otherwise act on the tip.^[217]

In analogy to the Kelvin method, in SKPFM the tip potential U_{tip} of the conductive cantilever is applied through an external circuit. U_{tip} consists of a dc component U_{dc} and an ac component U_{ac} .^[219] U_{ac} is typically modulated at the resonance frequency ω_0 of the cantilever. Differences between the surface potential ϕ and U_{tip} during the scan lead to a capacitive force F_{cap} which will act on the cantilever. Due to U_{tip} being modulated by U_{ac} , F_{cap} is also modulated and causes the cantilever to oscillate with amplitude A_{tip} which can be measured.^[219] In the lift mode, the feedback from the topography scan is used to adapt U_{dc} of the cantilever to minimize its oscillation A_{tip} . The applied potential U_{tip} of the cantilever is equal to the surface potential when $A_{\text{tip}} = 0$. Hence, the scanned U_{tip} information from the lift mode scan results in a surface potential difference $\Delta\phi$ image. Figure 5.7 summarizes the acquisition of an SKPFM scan.^[219]

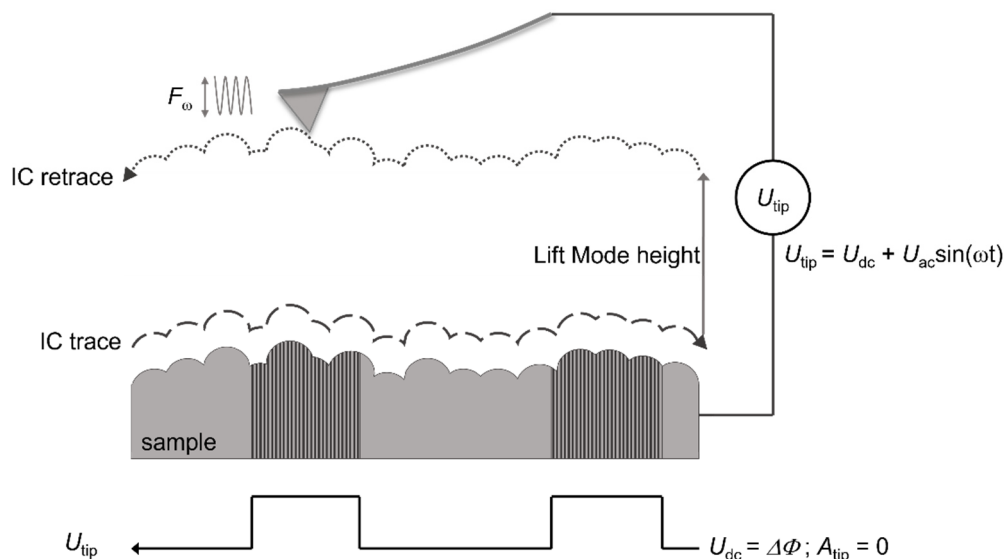


Figure 5.7. Schematic of the SKPFM lift mode showing the recording of the topography in the IC mode (IC trace) and the IC retrace used to record the surface potential difference $\Delta\phi$. Adapted with permission from [219]. Copyright 2016, The Authors.

5.2.2 Scanning Electrochemical Microscopy

SECM is an in-situ SPM technique that employs a microelectrode (ME; also referred to as tip) to probe the electrochemical reactivity of an immersed surface. Apart from topographic information, SECM predominantly provides a tool to map the rate of electrochemical reactions of a sample surface.^[220] SECM instruments are commercially available and typically consist of four major components, a bipotentiostat, a positioning system for the ME probe, an electrochemical cell and the control and data acquisition system. To control and measure the current and potential of the ME and sample independently, the SECM is equipped with a bipotentiostat. The ME is nanometer to micrometer-sized electrode of disk-shaped geometry to probe the surface.^[220-221] Both ME shape and geometry determine the image resolution. Employing an ME as the probe holds the advantages of small steady-state currents (nano- and picoampere-range), short response times, negligible ohmic drop and the possibility to clean by mechanical polishing.^[221] The three-dimensional positioning of the ME above the sample surface is accomplished through stepper- and piezoelectric motors, analogous to AFM. The electrochemical cell holds the electrolyte solution which typically consists of a supporting electrolyte as well as a redox mediator and is designed in such a way that the surface of interest can be mounted from the bottom as depicted in Figure 5.8. Furthermore, the set up allows to fix the auxiliary electrode far away from the ME to avoid interfering reactions.^[222]

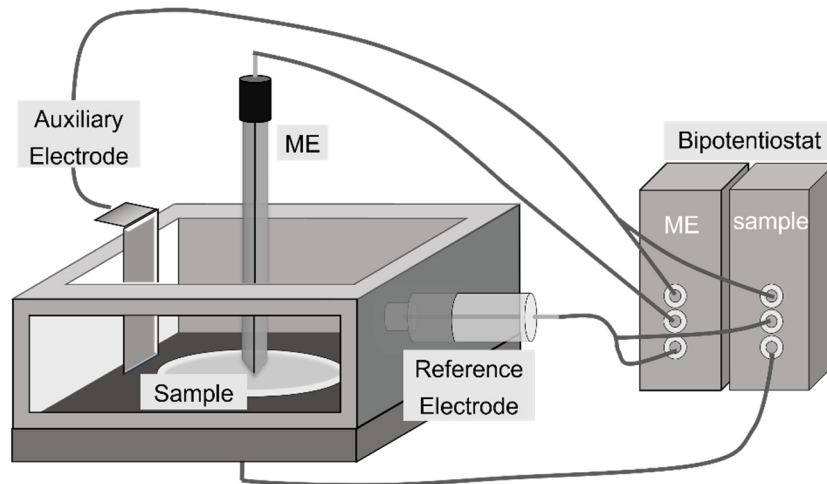


Figure 5.8. Set-up of an SECM cell with the respective electrodes and connections to the bipotentiostat.

Important parameters in SECM entail the measured current response to an applied potential which is generally designated by a lower-case i but the reported current is commonly normalized and designated with an upper-case I . Indices are added to indicate tip or sample (substrate) current i_T and i_S , respectively. Normalization of the tip current i_T is achieved by dividing the measured i_T by the steady-state bulk current i_∞ in the same solution. The sample or substrate current is denoted by i_S . Another normalized quantity is the tip-substrate distance, L_{T-S} which is given by dividing the distance z between tip and substrate by the ME radius r .^[220] Figure 5.9a shows two approach curves in an i_T - z plot and Figure 5.9b shows the same curves as normalized current I_T vs. distance L_{T-S} . The steady-state bulk current of the ME is measured far away from the substrate surface ($z > 10r$) and is given by

$$i_{T,\infty} = 4nFDcr \quad 5.11$$

where n is the number of exchanged electrons, F is the Faraday constant, D is the diffusion coefficient of the redox species and c is the concentration.^[220]

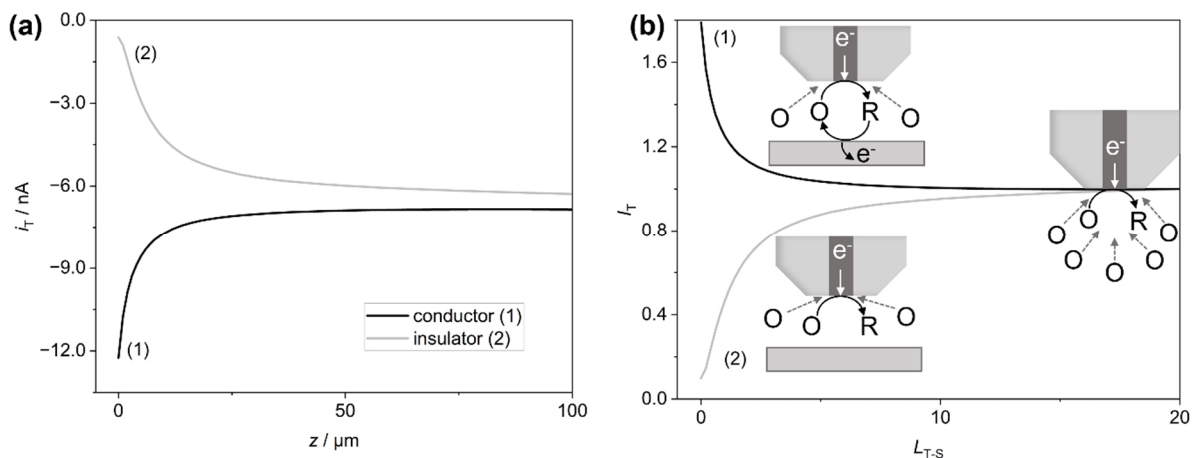


Figure 5.9. (a) Approach curves of a Pt ME ($r = 5 \mu\text{m}$) towards (1) a gold sample and (2) an epoxy surface in 0.1 M KCl with 5 mM $\text{K}_3[\text{Fe}(\text{CN})_6]$ as the redox mediator, depicting the absolute currents measured. (b) Same as (a) in normalized quantities.

There are two commonly employed modes in SECM imaging, the feedback mode, and the generation/collection mode.^[220, 222] The feedback mode is the most frequently utilized mode.^[220] When the redox mediator is dissolved in the electrolyte in its oxidized form O, biasing the probe to a respective reduction potential (deduced by CV) reduces O to R and a respective faradaic current at the ME results. At distances $z > 10r$, O can diffuse freely to the ME tip and the steady-state bulk current is observed.^[220] If the tip approaches an inert region, e.g., the epoxy resin of an embedded sample, diffusion of O to the tip becomes increasingly hindered and i_T decreases, corresponding to negative feedback (Figure 5.9a, insulator). In contrast, if the tip approaches a conducting surface, e.g., a gold sample, R can be oxidized back to O by the sample and i_T increases, corresponding to positive feedback (Figure 5.9b, conductor).^[220] Positioning the tip close enough to the surface allows to measure the tip current in the negative and positive feedback regime and generates images that show electrochemically active regions on a substrate surface.

In the generation/collection mode, the redox active compound is generated at one interface and collected at the other. The mode can be carried out in either the substrate generation/tip collection mode (SG/TC) or the tip generation/substrate collection mode (TG/SC).^[220] The latter mode finds predominant use in kinetic measurements and local surface modifications through, e.g., deposition or etching.^[223-224] The SECM is a versatile analytical tool and other modes comprise e.g., the redox competition mode where the tip and surface compete for the same redox species which finds use in catalytic activity and corrosion screening or the potentiometric mode which uses potentiometric probes, e.g., for monitoring local pH variations.^[225-227]

Due to the high corrosion resistance of the MPEAs studied within this work, imaging of electrochemically active sites was mostly impossible. The surfaces formed protecting passive films that generally showed no weak points during SECM imaging. For this reason, the SECM was employed to conduct tip-substrate voltammetry (TSV) where the ME was polarized at a constant potential and held at a fixed position to detect certain emerging redoxactive species while the sample was scanned potentiodynamically.

5.2.3 Scanning Electron Microscopy

SEM represents a special case of scanning probe microscopy where instead of a solid probe, a focused electron beam scans the sample surface. To date, SEM is one of the most essential and widely employed techniques for materials characterization due to its ease of use, rapid imaging and its ability to determine local elemental composition.^[228] It provides information on the surface structure, composition, and bulk material defects at the sub-micrometer to nanometer scale. Typical magnifications are around 200000x, meaning that resolutions of 1 nm can be achieved which corresponds to beam energies of 20 to 30 kV.

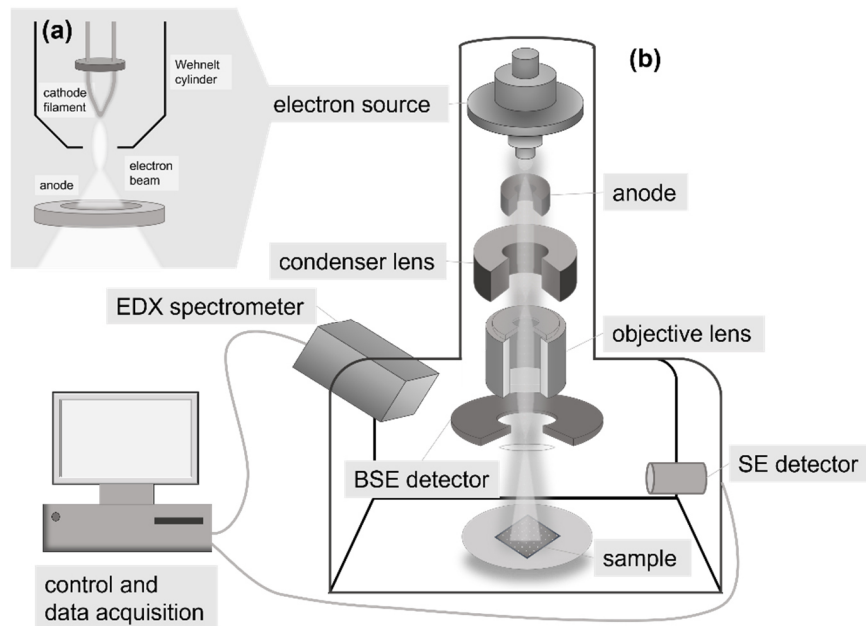


Figure 5.10. Schematic of an SEM set-up. (a) Close-up of the electron source. (b) Complete SEM set-up.^[229]

An SEM consists of three major components, the electron column, the sample chamber, and the control and data acquisition unit (Figure 5.10b). The electron column comprises the electron source that generates the beam, termed electron gun, electromagnetic lenses that demagnify and focus the electron beam to a small diameter electron probe and scan coils that move the probe across the surface to procure the SEM image.^[228] The electron gun on top of the column generally generates electrons either by thermionic emission or field emission.^[229] For thermionic emission a metal filament (e.g., W or LaB₆) called the cathode is placed at a high negative potential (corresponding to the reported beam energy) and heated to a high enough temperature by a current so that electrons can overcome the work function of the cathode and leave the surface (see Figure 5.10a). The potential difference between the anode which is grounded at zero potential and the cathode accelerates the emitted electrons through a hole in the anode. The emission of electrons sets the surrounding Wehnelt cylinder at a more negative potential than the filament. This resulting negative bias in turn replenishes emitted electrons on the filament and ensures that the electrons are emitted from the tip of the filament. A field emission gun employs a very small single crystal wire with a sharp tip instead of a filament as the cathode. This enables the generation of a strong electric field at the cathode tip, reducing the energy barrier of electron emission. Down the column the electron beam is demagnified by condenser lenses, the number of electrons and convergence angle of the beam are controlled by apertures and the beam is finally focused by an objective lens.^[229]

Both the electron column and the sample chamber are operated under vacuum conditions to avoid scattering of the beam electrons.^[229] The electron beam penetrates the sample by a few microns and its interaction with sample atoms generates three signals that can be detected. When the electrons are scattered elastically, backscattered electrons (BSE)

result which are of the same energy as the incident beam and are detected to produce images of topographic and qualitative compositional information.^[230] Upon inelastic scattering, secondary electrons (SE) are emitted from the sample which are lower in energy and once detected produce topographic images.^[230] The inelastic scattering leaves behind an ionized atom with an electron vacancy in a core shell. An outer shell electron may fill the vacancy and this process releases energy in the form of an X-ray photon. The emitted photons are element-specific as the electron transition between any two shells is unique to an element. The detection of the emitted X-rays results in a spectrum and typically an elemental map may be recorded.^[231]

A conventional SEM typically has two stationary detectors, one for BSE and one for SE. BSE and SE signals can only be distinguished by energy. As most BSE are scattered upwards and scattering probability decreases towards the sides, the BSE detector is placed directly below the objective lens as shown schematically in Figure 5.10b.^[229] The SE detector is mounted from the side and brought close to the sample surface. Depending on the instrument, the X-ray detector is either also stationary or mobile so that the operator can adjust the distance between the detector and sample surface which is typically around 20 mm. The X-ray detector is an energy dispersive spectrometer and hence gives the measurement the name energy dispersive spectroscopy (EDS or EDX).^[232]

5.3 Quantitative Surface and Electrolyte Characterization

5.3.1 X-Ray Photoelectron Spectroscopy

X-ray photoelectron spectroscopy (XPS) employs X-rays which irradiate the sample surface. Typically, laboratory instruments work with the Al $K\alpha$ line with a photon energy of 1486.6 eV.^[233] XPS is a surface sensitive technique and examines the electrons ejected from core levels upon absorption of an X-ray photon. The resulting photoelectron spectrum represents the electronic structure of the elements contained at and close to the sample surface. Depending on the material under investigation, the energy of the incident X-ray photons and the emission angle (typically $< 60^\circ$), the information depth of XPS reaches a few nanometers.^[233] The measured kinetic energy E_k of the photoelectrons is related to their binding energies E_B by Equation (5.12). Qualitative and quantitative information are provided on the chemical state of the atoms which is influenced by their chemical environment.^[233] XPS was used in Chapters 7.1.2 and 7.2.2 to elucidate the surface compositions and surface composition changes of the MPEAs due to corrosion.

Conventional XPS measurements are run under an ultra-high vacuum (UHV), which excludes liquid or gaseous samples. Nevertheless, methods exist, where XPS are collected at near ambient pressure which allow in-situ monitoring of electrochemical processes.^[234-235] An XPS instrument constitutes an X-ray source, a monochromator (e.g., quartz crystal), electron

energy analyzer and a data acquisition and processing system. Figure 5.11 shows a schematic illustration of a generic XPS spectrometer whereas the X-ray source is magnified to demonstrate its components.^[236]

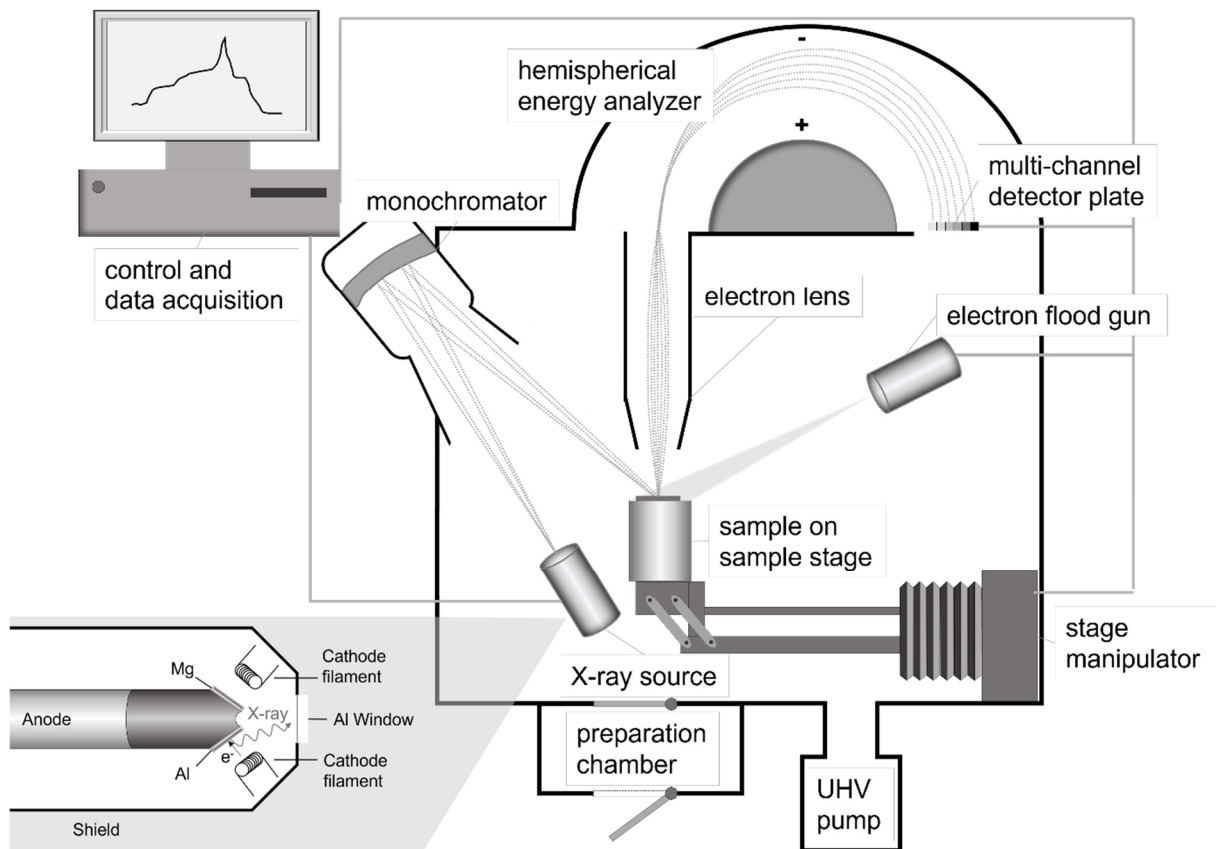


Figure 5.11. General set-up of an X-ray photoelectron spectrometer with a close-up of the X-ray source in the left hand corner.

In XPS, X-ray photons are generated by bombarding the anode which is a metallic solid, typically Al or Mg, with electrons from a thermionic source (cathode) as discussed for the SEM in Chapter 5.2.3. Depending on the anode material, energies of 1486.6 eV and 1253.6 eV can be generated by Al and Mg, respectively. Due to the high energy and intensity of the Al $K\alpha$ X-ray, minimal energy spread, effective heat conduction and the ease of manufacture as well as the inherent robustness, Al anodes are commonly used.^[237] An XPS spectrum displays the intensity of emitted photoelectrons versus the energy either in form of the kinetic energy E_K or the binding energy E_B which are interrelated by

$$E_B = h\nu - E_K - \phi \quad 5.12$$

where $h\nu$ is the photon energy and ϕ is the instrument specific work function.^[233] From Equation (5.12) it becomes clear that E_B is an intrinsic property of the examined material, whereas E_K depends on the energy of the X-ray source.^[233] The characteristic photoelectron peaks in XPS spectra are formed by photoelectrons that reached the detector without inelastic scattering (loss in E_K). Electrons that succumb to inelastic scattering, lose energy, and will contribute to the background of the spectrum. To label the element specific peaks, the

spectroscopists' notation is used.^[233] The peaks are labelled by n_l_j where n is principal quantum number (given by integers), $l = n - 1$ is the orbital angular momentum (given by integers, and denoted s, p, d, etc.), and $j = |l+s|$ is the total angular momentum with s being the spin angular momentum (either $s = + 1/2$ or $s = - 1/2$).

The ejection of an electron from a core level as shown in Figure 5.12a is recorded in XPS. The process ionizes the atom which can relax by X-ray fluorescence (Figure 5.12b) or Auger emission (Figure 5.12c). For first-row transition metals as studied in this thesis, Auger emission peaks in XPS spectra can complicate the XPS analysis due to the overlap of AES and XPS peaks.^[131]

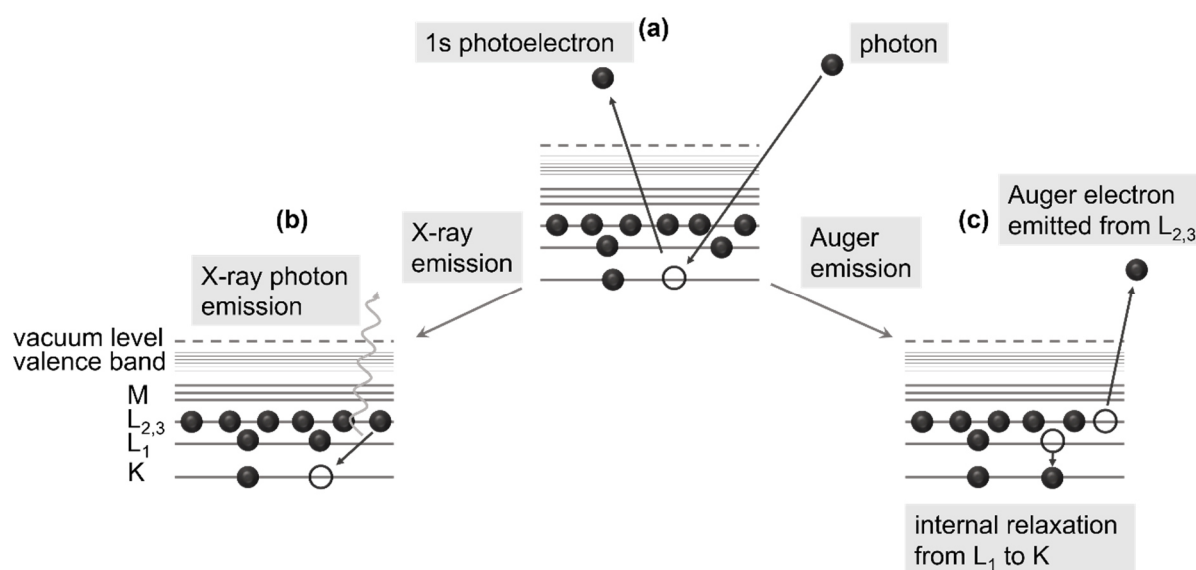


Figure 5.12. Illustration of (a) emission of photoelectrons, (b) emission of X-rays and (c) emission of an Auger electron as the result of an incident electron hitting the sample surface.^[233]

The analysis of the 2p XPS spectra of the first-row transition metals is further complicated by shake-up satellites, plasmon loss and multiplet splitting effects.^[238] Shake-up satellites arise due to emitted photoelectrons exciting valence electrons.^[239] This excitation is observed in XPS spectra by structures appearing at binding energies above the actual photoelectron peak. Satellite peaks may be evaluated if they are well separated from the main peak and of identifiable intensity.^[239] The spectrum evaluation is complicated when satellite peaks introduce asymmetry to the main photoelectron peak. Plasmon loss is generally observed for clean metallic surfaces where outgoing photoelectrons interact with conduction band electrons, leading to a loss in E_K and thus, an apparently higher E_B .^[239] The peaks that arise merely complicate XPS spectra. Transition metals are known to possess unpaired electrons. Due to the emission of an electron, the unpaired electron within the core level can interact with unpaired valence electrons. This interaction results in multiplet splitting and is observed, e.g., for Cr(III), Mn(II) and Fe(III).^[238] To circumvent the complications with 2p XPS spectra of transition metals, this work focused on analyzing the respective 3p level peaks which while less sensitive do not overlap with Auger emission peaks.^[131]

5.3.2 Inductively Coupled Plasma Mass Spectrometry

Inductively coupled plasma mass spectrometry (ICP-MS) is an analytical technique that allows to measure elemental species qualitatively and quantitatively.^[240] Most commonly the technique is employed to analyze the composition of fluids (liquid and gaseous) and its high sensitivity enables the analysis of trace elements in the range of ng L^{-1} , i.e., ppb. The inductively coupled plasma is the ionization source for the analytes which are then passed to the enclosed mass spectrometer (see Figure 5.13).^[240] The plasma is generated by passing argon gas through a quartz torch which resides in an induction coil. A radio frequency, typically 27.1 MHz or 40.6 MHz, is applied to the induction coil, resulting in an electromagnetic field at the top of torch.^[241] With a tesla coil a spark is applied that initiates the stripping of electrons from the argon atoms. The resulting argon cations and electrons are then trapped in the magnetic field and subsequently accelerated in closed circular paths.^[241] Some electrons collide with neutral argon atoms which removes electrons, and a chain reaction is established. These collisions generate the plasma flame which is of a high temperature of approximately 6000 to 10000 K. The plasma which consists of neutral and positively charged argon atoms and electrons persists as long as the radio frequency is applied.^[241]

Once the plasma is established, the analyte can be introduced for ionization. Via pumps the liquid sample is converted into an aerosol in the nebulizer. Droplets that are larger than $10\ \mu\text{m}$ are removed from the aerosol in the spray chamber before introducing it into the plasma. Within the plasma flame, the droplets undergo rapid de-solvation, vaporization, atomization and ultimately ionization which is ensured by the high plasma temperature.^[240] The ICP generates the ionized analyte under atmospheric pressure. Extraction of the plasma which, after ionization, now also contains analyte ions is accomplished through a sampling cone orifice into a low-pressure expansion chamber.^[241] The plasma accelerates and expands quicker than the local speed of sound which is termed supersonic expansion and leads to jet formation. The jet is then extracted through a skimmer cone by an extraction lens that is essentially a negatively charged metal tube to accelerate and move forward the positive ions while repelling electrons.^[241] The resulting ion beam of positively charged ions enters the ion optics. This device comprises further electrostatic lenses that act as ion energy filters and guide the analyte ion beam to the mass spectrometer. Here, a quadrupole mass filter (QMF) consisting of four rod electrodes utilizes time-variant electric fields to separate the analyte ions by their mass/charge ratio.^[242] The electric field within the QMF represents a selective mass window and is adjusted by applying a potential with dc and ac components. Only ions with the respective mass/charge ratio have the correct trajectory to pass the QMF and reach the detector. Another mass window is selected by re-adjusting the applied potential while the ac/dc ratio is kept constant.^[240] Via external calibration, the concentrations of elements within the

sample can be quantified. ICP-MS analyses of corrosion electrolytes have been widely used to clarify metal and alloy dissolution.^[101, 243-244] In this thesis the electrolytes after corrosion were quantified for the dissolved metal ion concentrations.

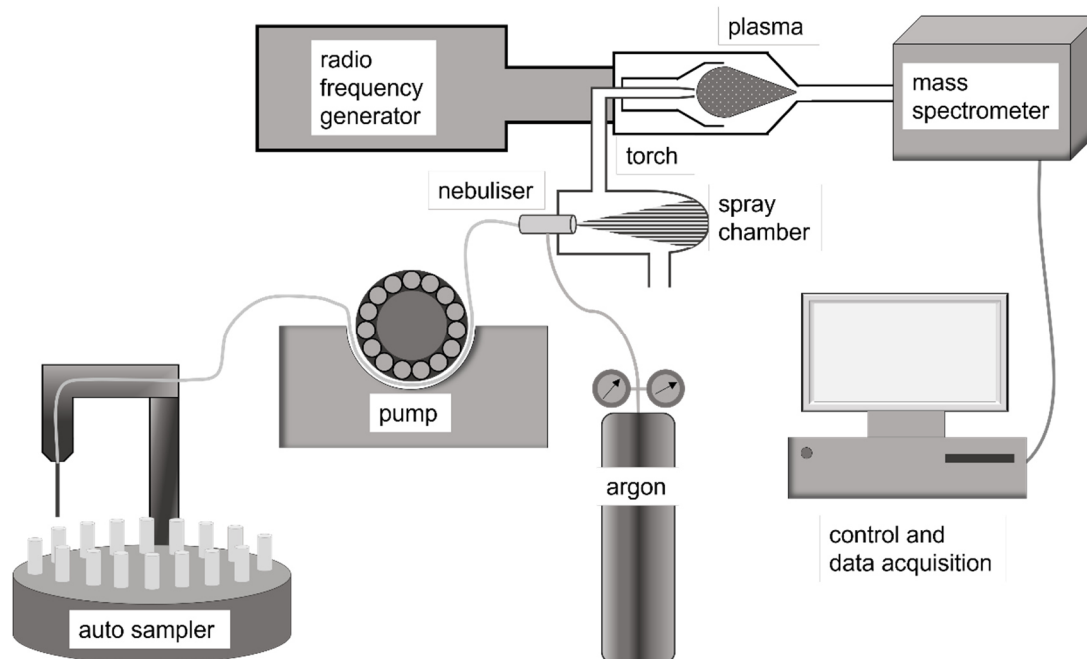


Figure 5.13. Schematic setup of an ICP-MS instrument.

6 Experimental

6.1 Chemicals

All chemicals employed during the preparation and analyses of the specimens are listed in Table 6.1 and Table 6.2. The supplier and purity grade of all commercially acquired metallic specimens can be found in Chapter 6.2. The aqueous solutions were prepared at room temperature, using deionized water (Evoqua, USA) with a conductivity of 18.2 M Ω . If not stated otherwise, all chemicals were used without further purification and were of analytical grade.

Table 6.1. Preparation of Metal Interfaces.

Product	Formula	Supplier
diamond paste (3 μ m/1 μ m)	C	ATM Qness GmbH, Germany
diamond lubricant	-	ATM Qness GmbH, Germany
colloidal silicon dioxide	SiO ₂	ATM Qness GmbH, Germany
acetone	(CH ₃) ₂ CH ₂ O	ChemSolute, Germany
ethanol	CH ₃ CH ₂ OH	ChemSolute, Germany
EpoFix Resin	Oxirane mixture	Struers, Germany
EpoFix Hardener	Amine mixture	Struers, Germany
alumina (3 μ m/1 μ m)	Al ₂ O ₃	ATM Qness GmbH, Germany

Table 6.2. Electrochemistry and Surface Characterization.

Product	Formula	Supplier	Grade
sodium chloride	NaCl	ChemSolute, Germany	99%
sulfuric acid	H ₂ SO ₄	ChemSolute, Germany	98%
sodium hydroxide	NaOH	ChemSolute, Germany	99.5%
potassium iodide	KI	ChemSolute, Germany	99.5%
nitric acid	HNO ₃		65%
hydrochloric acid	HCl	ChemSolute, Germany	37%
chromium dichromate	K ₂ Cr ₂ O ₇	abcr, Germany	99%
Cr(VI) solution	K ₂ CrO ₄	ChemSolute, Germany	50g L ⁻¹
chromium(III) chloride hexahydrate	CrCl ₃ · 6H ₂ O	ChemSolute, Germany	98%
rhodium solution	Rh	Certipur Merck, Germany	1 g L ⁻¹
ICP-multi element standard IV	Including: Cr, Fe, Mn, Co, Ni	Certipur Merck, Germany	1 g L ⁻¹
Sea salts	-	Sigma-Aldrich, USA	-
hydrogen peroxide	H ₂ O ₂	ChemSolute, Germany	30%
potassium chloride	KCl	ChemSolute, Germany	99.5%
potassium ferricyanide	K ₃ (Fe(CN) ₆)	ChemSolute, Germany	99%

6.2 Materials

MPEA Samples. The MPEAs CrMnFeCoNi and CrCoNi were manufactured in equiatomic ratios via vacuum induction melting by the Laplanche group at Ruhr-University, Bochum, Germany.^[18, 245] For the five component MPEA, the respective pure metals (in elemental form, >99.9 wt%) were melted in an alumina crucible under argon atmosphere (high purity, Ar 99.998 vol%) in a Leybold Heraeus IS 1/III vacuum induction furnace operating at 5-20 kW. The furnace was evacuated to 3 mbar and subsequently filled with Ar to reach a pressure of 500 mbar prior to melting. An ingot was cast by pouring the melted MPEA mixture into a cylindrical zirconia coated steel mold. Afterwards the as-cast ingot was homogenized at 1200°C for 48h in an evacuated and sealed quartz tube to eliminate undesirable oxidation. Finally, the heat-treated ingot was reduced in diameter in seven steps via rotary swaging at room temperature with a HMP R6-4-120-21S four-die swaging machine (HMP Umformtechnik GmbH, Pforzheim, Germany) from 40 mm to 16.5 mm.^[245] The three component MPEA was fabricated in an

identical fashion, except that a MgO crucible was employed for casting.^[18] Table 6.3 summarizes the elemental compositions measured by the Laplanche group as presented in^[18, 246].

Table 6.3. Chemical compositions of CrMnFeCoNi and CrCoNi as reported in^[18, 246].

MPEA	Cr	Mn	Fe	Co	Ni	O	S	C
CrMnFeCoNi	19.41	20.10	20.56	20.26	19.58	0.033	0.009	0.051
CrCoNi	32.53	0.09	0.95	33.30	32.85	0.226	0.004	0.019

Pure Metals. Pure metal specimen of Cr, Co and Ni were acquired in 7.5mm (Cr) and 5 mm (Co, Ni) thick sheets (HMW Hauner GmbH & Co. KG, Germany) that were cut into 15 mm x 15 mm square coupons. The metals were of $\geq 99.9\%$ purity, according to the manufacturer.

AISI 304. Apart from the MPEA and pure metal samples, AISI 304 stainless steel as a widely used alloy system was employed as a reference material in this work. Received as 1.2 mm thick annealed sheets, the austenitic stainless-steel sheets (AISI 304, Goodfellow Cambridge Ltd. United Kingdom) were cut into smaller size sheets of 15 x 15 mm dimensions. The corresponding chemical composition is compiled in Table 6.4 as it has been reported in^[247].

Table 6.4. Chemical composition of AISI 304 as reported in^[247].

AISI 304	Fe	Cr	Ni	Mn	C	S, P, N, Si
at%	69.88	19.46	7.46	0.96	0.16	$\ll 2$

Auxiliary Electrodes. For electrochemical measurements inert metals were used to function either as a source or sink of electrons, i.e., auxiliary electrode (AE). High purity wires of Au and Pt (Goodfellow, 99.9% each) were acquired and coiled up to immerse a large surface area of the AE in the electrolyte.

6.3 Preparation of Metal Interface

Metal and Alloy Surfaces. The metal and alloy specimens all underwent the preparation methods indicated in the following. Depending on the investigation method some alloy surfaces were subjected to further polishing and cleaning steps. First, the surfaces were wet-ground

consecutively with SiC paper (600 to 4000 grit, ATM GmbH, Germany) and then polished with diamond paste on respective polishing clothes (3 to 1 μm ATM GmbH, Germany). The polishing clothes were each reserved for one size of diamond paste and one alloy species to avoid contamination. The 1 μm polishing step was the final one for most investigations, especially the general electrochemical and SECM investigations. For investigations with the AFM, the 1 μm polishing step was followed by another polishing step with a 0.05 μm SiO_2 suspension (ATM GmbH, Germany) to ensure a smoother surface. After the final polishing step, the samples were washed in deionized water and acetone in an ultrasonic bath (Elmasonic P) for 5 min each at 80 kHz to remove any residual polishing particles and organic contaminations. The clean surfaces were dried in an oil-free compressed air stream in the final step.

Embedding. For SECM and in-situ AFM measurements the samples were embedded in a two-component epoxy resin (Technovit Epox Resin and Technovit Epox Hardener regular, Kulzer GmbH, Germany). The embedded specimens were ground and polished as stated above and rinsed in deionized water in the ultrasonic bath. However instead of rinsing them in acetone, ethanol was employed to avoid dissolution of the epoxy resin.

Microelectrode. Before any SECM measurements, the microelectrode (ME) was carefully and subsequently polished on separate polishing cloths (ATM GmbH, Germany) with first 0.3 μm and then 0.05 μm Al_2O_3 (ATM GmbH, Germany). In between polishing steps, the ME was thoroughly rinsed with DI-water and finally rinsed in acetone in an ultrasonic bath (Elmasonic P) for at 80 kHz 10 min.

6.4 Instrumentation for General Electrochemical Investigations

Electrochemistry. All general electrochemical investigations were conducted with a Gamry Reference 600+ (Gamry Instruments, C3 Prozess- und Analysentechnik, Germany) using the Gamry Framework data acquisition software (version 7.8.2) at room temperature. For the electrochemical testing which predominantly comprised cyclic potentiodynamic polarization (CPP), open circuit potential, potentiostatic polarization and electrochemical impedance spectroscopy measurements, a three-electrode set-up was utilized. Within this set-up the alloy surfaces were functioning as the WE which was polarized versus a Ag/AgCl/3 M NaCl reference electrode (ALS Co. Ltd., Japan) and either Au or Pt were employed as the AE. The reference electrodes were regularly controlled against a master Ag/AgCl/3M NaCl electrode to ensure accurate measurements. According to the manufacturer the potential of the Ag/AgCl/3M NaCl electrode corresponds to $E^0 = 0.195 \text{ V vs. RHE}$ (at 25°C).^[248] If not otherwise stated, all presented electrochemical potentials within this work are referenced to the Ag/AgCl/3M NaCl electrode.

Prior to measuring, the cells were sealed and purged with N₂ for 30 min and kept under a N₂ atmosphere during measurements to ensure reproducibility and to exclude interfering redox reactions. Before the electrochemical experiments were conducted, samples were cathodically conditioned at - 1.00 V for 10 min, to remove oxides formed on the surfaces. CPP measurements were run at a scan rate of 1 mV s⁻¹ from - 0.25 V vs. OCP to 1.50 V. The scans were reversed before 1.50 V if the current density reached 5 mA cm⁻². EIS measurements were generally performed in the frequency range from 100000 Hz down to 0.1 Hz and with an applied ac voltage of 10 mV and a dc voltage at OCP. The Gamry EChem Analyst software (version 7.8.2) was utilized to analyze the EIS data and fit the equivalent electrical circuits (EEC).

Inductively Coupled Mass Spectrometry. The ICP-MS analyses were executed using the iCAP Q ICP-MS (Thermo Fischer Scientific, Germany) coupled to an ESI SC 4 DX Fast autosampler (Elemental Scientific, USA) and the Qtegra™ software (Thermo Fischer Scientific, version 2.10.4345.64). In accordance with the guidelines of the manufacturer, the MS-system was tuned daily. To allow for, e.g., drift corrections, an external standard of a 10 µg L⁻¹ Rhodium solution (Merck, 1000 mg L⁻¹ Certipur, Germany) was mixed on-line into the samples at a mixing ratio of approx. 1:10 via the autosampler. For the quantitative analysis of the electrolyte samples after electrochemical measurements, a multi-element standard was used for external calibration (ICP-multi element standard IV (Certipur), Merck, Germany). For preparing the standards as well as the sample dilution, Type I reagent-grade water (18.2 MΩ cm) obtained from a Milli-Q-System (MerckMillipore, Germany) as well as HNO₃ (65 % p.A. (Chemsolute), Th. Geyer, Germany (double sub-boiled)) were used prior to the analysis. Metal concentrations were obtained in mg L⁻¹ and subsequently converted to molar concentrations.

UV-Vis Spectroscopy. UV-Vis measurements were conducted to measure the Cr(VI)- and Cr(III)-contents within the electrolytes after electrochemical measurements. The spectrometric measurements were performed by means of a Jenway™ 7315 spectrometer (Bibby Scientific, United Kingdom), employing quartz glass cuvettes. Figure 6.1 shows the UV-Vis spectrum of a Cr(VI) solution with $c(\text{Cr(VI)}) = 20 \text{ mmol L}^{-1}$ with the maximum at $\lambda = 373\text{nm}$. The working wavelength $\lambda = 373 \text{ nm}$ was used for determination of Cr(VI) concentrations.

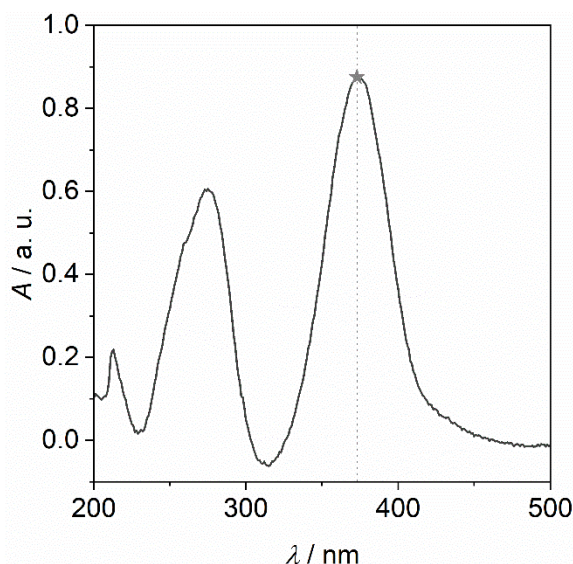


Figure 6.1. UV-Vis spectrum of a Cr(VI) solution with $c(\text{Cr(VI)}) = 20 \text{ mmol L}^{-1}$ showing the maximum absorbance at $\lambda = 373 \text{ nm}$.

For the quantitative analysis, a CrO_4^{2-} stock solution was prepared by dissolving $\text{K}_2\text{Cr}_2\text{O}_7$ in water. The stock solution was adjusted to pH 14 and utilized for external calibration. A separate Cr(VI) standard, for which a 50 g L^{-1} K_2CrO_4 in H_2O solution was diluted, was employed to ensure the accuracy of the calibration. Furthermore, to ensure successful conversion of Cr(III) to Cr(VI), a Cr(III) standard was prepared by dissolving $\text{CrCl}_3 \cdot 6\text{H}_2\text{O}$. It was oxidized by adding hydrogen peroxide H_2O_2 in excess and adjusting the pH to 14. The solutions were then heated until the green solution turned bright yellow and gas formation ceased (Equation (6.1)). The reaction produces powerful oxidants (OH^\cdot , O_2^{2-} and O_2^\cdot), and most likely proceeds via a Fenton-like mechanism.^[249-250]

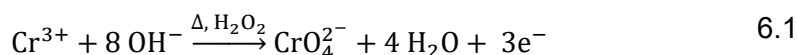


Figure 6.2 shows a calibration curve and the respective determinations of the Cr(III) and Cr(VI) standards.

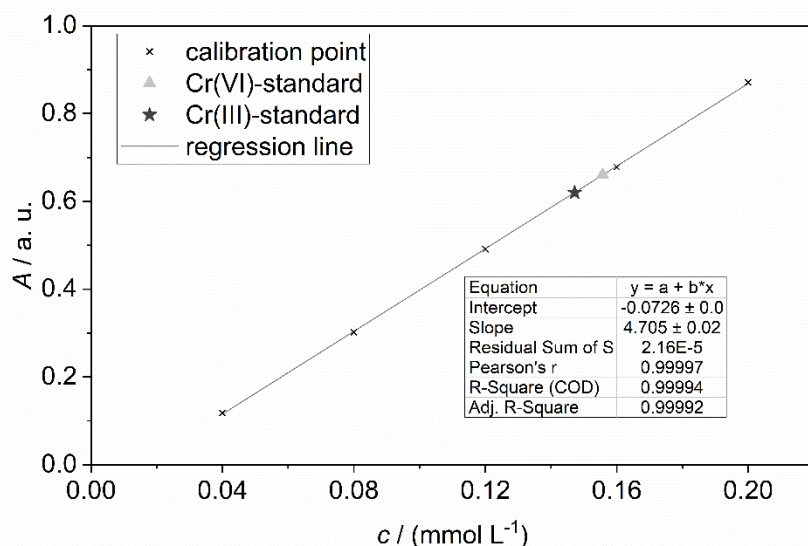


Figure 6.2. Calibration curve showing the absorbance A versus the Cr(VI) concentration c . The respective standards are indicated.

After respective dilution, the electrolyte samples were alkalized with 3 M NaOH to pH 14, monitored with pH paper. Cr(VI) concentrations were determined without an oxidation step. To determine Cr(III)-contents, another sample solution was oxidized as described above. The cooled mixtures were then diluted as needed. The resulting Cr(VI)-contents represented the total Cr content and were used to determine the sum of the original Cr(III) and Cr(VI) content. From this value the original Cr(III) content was obtained as the difference between the total Cr content and the original Cr(VI) content.

6.5 Instrumentation Used for Alloy Surface Characterization

Atomic Force Microscopy. A NanoWizard 4 (Bruker Nano GmbH, Germany – formerly known as JPK instruments) was utilized to study the metal surfaces after polishing and corrosion studies. The typical images provided topographic data and were recorded with a resolution of 512×512 pixels in the intermittent contact mode at scan frequencies of 0.4 to 1.0 Hz depending on the surface roughness. A Tap300-G Cantilever (Budget Sensors, NanoAndMore GmbH, Germany) was used. This silicon cantilever has a conductive Cr/Pt-coating and a nominal spring constant of 40 N m^{-1} . Offline analyses were carried out with the JPK Data Processing Suite software (version 6.1.88). Image flattening was achieved by applying the first order least square polynomial function to remove image tilt and the vertical z-offset between the single line scans.

In-situ Atomic Force Microscopy. Similar to the ex-situ AFM measurements, a Tap300-G cantilever with the NanoWizard 4 instrument and the acquired data were processed with the JPK Data Processing Suite. For the electrochemical cell, a JPK-manufactured electrochemical cell was used which comprised of a Pt-wire as the auxiliary electrode and a Ag/AgCl in 3 M KCl reference electrode. The in-situ measurements were coupled to a CPP

scan that was independently performed using a Gamry Reference 600+ under the conditions stated previously. To monitor the evolution of local corrosion sites, the CPP scan was paused at characteristic potentials such as the OCP, the passive and transpassive region. In contrast to the ex-situ AFM measurements, the topographical images were recorded with the JPK-specific Quantitative Imaging mode (QI™ mode) which determines force curves at each pixel (512 x 512) of the scan region (100 x 100 μm).

Scanning Kelvin Probe Force Microscopy. For SKPFM scans, intermittent contact mode topographical image collection had to be set up first with the NanoWizard to adjust the primary settings of the instrument. Only afterwards could the SKPFM mode be set up and adjusted. Once adjusted, the cantilever tip was lifted to a predefined height of 30 - 50 nm, and to determine the surface potential of the underlying topographical profile an ac voltage of 1.0 V was applied. The reported values are potential differences since no absolute reference was deployed in the SKPFM analyses. Offline analyses were conducted in a similar fashion with the same software as for the AFM images.

Scanning Electrochemical Microscopy. SECM imaging was performed with a modular M470 (Bio-Logic SAS, France). The electrochemical cell (μ-TriCell, Biologic SAS, France) comprised a Pt-plate as the AE and a Ag/AgCl/ 3M NaCl reference electrode as described previously. For imaging the metal surfaces had to be embedded in epoxy to fit into the cell. For the ME, a fused silica-based Pt-disk electrode (BioLogic, SAS, France) was used with $r = 5 \mu\text{m}$ and $RG = 10$. The measurements were recorded with the M470 software (version 1.47.5951) and offline analyses were performed with MIRA (version 8.1).

To image the alloy interface, a base electrolyte of 0.1 M KCl with 5 mM KI as the mediator was utilized. Prior to any image recording, the cleanliness of the electrolyte and oxidation potentials were monitor via cyclic voltammetry. Approach curves were then run to determine the ME-sample distance and ensure that the sample was plane. The images were recorded in the feedback mode, where the ME was held 5 μm above the sample surface and polarized at 0.6 V to oxidize the iodide to triiodide (Equation (6.2)).^[251]



Tip-Substrate Voltammetry. The same set-up was employed as specified in SECM imaging description with the additional usage of a Gamry Reference 600+ to run a CPP scan while holding the ME at a constant potential to monitor the evolution of O₂. The as-delivered M470 set-up would not allow for such a measurement. Before monitoring any evolved O₂, cyclic voltammetry and approach curves were run to ensure the correct selection of applied potentials and to set a constant distance of ~ 5μm between the ME and sample surface,

respectively. Prior to the measurement, the solution was sparged with N₂ to remove dissolved oxygen from the electrolyte. The ME was then held potentiostatically at - 0.65 V vs. Ag/AgCl/3M NaCl to reduce evolved oxygen. The CPP scans were acquired as described above from an initial potential of - 0.25 V vs. OCP to a final potential of 1.50 V vs. OCP at a scan rate of 1 mV s⁻¹. The scan was also reversed, if the current density reached a value of 5 mA cm⁻² before the indicated apex voltage.

Scanning Electron Microscopy. A Phenom XL Desktop-scanning electron microscope was used to perform most of the electron microscopy imaging (secondary electron [SE], or back scattered electron [BSE] mode) and energy dispersive X-ray spectroscopy (EDX) data. The instrument was operated at 15 kV, other parameters were automatically adjusted by the instrument. For SEM images obtained for the long-term corrosion analysis in Chapter 7.3, a VEGA3 TESCAN system equipped with an EDX detector operated at 20 kV was used to record the scanning electron microscopy (SEM) images (in the SE mode) and EDX data.

X-Ray Photoelectron Spectroscopy. X-Ray Photoelectron Spectra of the anodically passivated alloy surfaces were recorded with a commercial spectrometer (SPECS Surface Nano Analysis GmbH, Germany). To acquire the spectra a monochromatic Al K α source ($h\nu = 1486.76$ eV) and a PHOIBOS 150 hemispherical analyzer combined with a 1D-CMOS detector were employed. The angle between the analyzer and the X-ray source was 55° and the photoelectron emission angle was 0°. Charge compensation was achieved by a flood gun (FG22/35) that emitted a beam of low energy electrons (3.5 eV, 75 μ A) onto the sample. For the collected 3p core-level and survey spectra, the analyzer was operated in the fixed analyzer transmission (FAT) mode with pass energies of 20 eV and 50 eV, respectively. Instrumental calibration and specification were accomplished by measuring a cleaned and sputtered Ag sample. Using SPECS relative sensitivity factors (RSF; see Table 6.5), the acquired spectra were fitted with CasaXPS (version 2.3.22PR1.0). The energy scales of the spectra were calibrated via the C 1s peak to 284.8 eV. Peak fitting was performed by applying a Shirley-type background and a Gaussian-Lorentzian ratio GL(30).

Experimental

Table 6.5. Summary of SPECS specific relative sensitivity factors of relevant elements for an angle of 55° between an Al K α X-ray source and the analyzer adjusted to the carbon C 1s photoelectrons.

Number	Element	Transition	SPECS RSF
6	C	1s	1.00
8	O	1s	2.77
16	S	2p	1.73
		2p _{1/2}	0.58
		2p _{3/2}	1.14
24	Cr	2p	10.96
		2p _{1/2}	3.73
		2p _{3/2}	7.23
		3p	1.24
		3p _{1/2}	0.42
		3p _{3/2}	0.82
25	Mn	2p	12.83
		2p _{1/2}	4.36
		2p _{3/2}	8.47
		3p	1.51
		3p _{1/2}	0.51
		3p _{3/2}	0.99
26	Fe	2p	14.84
		2p _{1/2}	5.05
		2p _{3/2}	9.79
		3p	1.77
		3p _{1/2}	0.60
		3p _{3/2}	1.16
27	Co	2p	16.92
		2p _{1/2}	5.76
		2p _{3/2}	11.16
		3p	2.04

Experimental

		3p _{1/2}	0.70
		3p _{3/2}	1.34
28	Ni	2p	19.06
		2p _{1/2}	6.48
		2p _{3/2}	12.58
		3p	2.34
		3p _{1/2}	0.80
		3p _{3/2}	1.54

7 Corrosion of MPEAs CrMnFeCoNi and CrCoNi in Aqueous Solutions

To study the corrosion behavior of the two MPEAs CrMnFeCoNi and CrCoNi in aqueous media, a multitude of analytical methods have been employed. Typical corrosion studies commence with the investigation of the electrochemical responses of the material in electrolytes with common ions (here Cl^- and SO_4^{2-}) by means of cyclic potentiodynamic polarization (CPP). The resistance of an alloy towards corrosion strongly depends on its passive film characteristics. Therefore, surface specific analyses by means of electrochemical impedance spectroscopy (EIS), X-ray photoelectron spectroscopy (XPS), scanning electron microscopy (SEM), and atomic force microscopy (AFM) were conducted to investigate the protective passive layer. Corrosive metal dissolution could be quantified through inductively coupled mass spectrometry (ICP-MS).

In this work, the corrosive behaviors of CrMnFeCoNi and CrCoNi were analyzed in two electrolyte systems. The most extensively studied solutions to evaluate corrosion performance contain NaCl as this salt can be found in many environments.^[252] Hence, the first part of this chapter examines the corrosion characteristics of MPEAs in NaCl solutions with $c(\text{NaCl}) = 0.1 \text{ M}$ in Chapter 7.1. Another frequently studied solution encompasses H_2SO_4 .^[253] Chapter 7.2 deals with the corrosion of CrMnFeCoNi and CrCoNi in $0.1 \text{ M H}_2\text{SO}_4$, presenting the electrochemical features of the MPEAs in an acidic environment and under the influence of SO_4^{2-} ions. Finally, due to the good durability of both alloys in $0.1 \text{ M H}_2\text{SO}_4$, long-term investigations were conducted in $1 \text{ M H}_2\text{SO}_4$ to deduce the stability of the alloys over extended times of immersion. The comparison of the corrosion behavior between CrMnFeCoNi and CrCoNi in 0.1 M NaCl and $0.1 \text{ M H}_2\text{SO}_4$ have been published in Applied Surface Science.^[X2]

7.1 Behavior in NaCl Solution

NaCl can be found in abundance in our environment. While its most apparent sources include seawater, the Earth's crust, and salt wells, it is a primary salt in body fluids of living organisms and an indispensable material in industrial production.^[254] Since two thirds of extracted NaCl are used in the chemical industry as electrolysis starting material to produce Cl_2 and NaOH, the salt is of economic importance. The other third finds applicability in, e.g., the food, dye, and detergent industries.^[252] Another use encompasses chemical and biological laboratories where NaCl is an essential compound serving a multitude of purposes.^[255] In the corrosion context, NaCl is a typical electrolyte studied due to its omnipresence whereas the concentrations under study differ and go as high as 3.5 wt.-% which resembles the NaCl concentrations in seawater.^[256] As discussed in Chapter 4.4, Cl^- ions are known to be corrosively aggressive,

being initiators of pitting corrosion as well as accelerators to other local corrosion phenomena such as crevice corrosion.^[257-258] Due to the low cost of NaCl extraction from natural deposits or seawater, it poses a highly economically feasible electrolyte component in the field of electrochemical energy. Properties such as its high conductivity, thermal stability and safety render it an even more suitable candidate.^[254] While an increasing interest in employing NaCl as an electrolyte in electrochemical energy technology exists, its corrosive nature toward novel electrode materials such as MPEAs needs to be investigated. Furthermore, considering the use of MPEAs in other contexts such as structural materials or coatings, their susceptibility to corrosion needs also to be analyzed in the presence of Cl⁻ to evaluate their safe use. Hence, this chapter will present and compare the corrosion performances of CrMnFeCoNi and CrCoNi in 0.1 M NaCl. To provide a point of reference, the data obtained for the MPEAs will be compared to AISI 304 stainless steel.

7.1.1 General Electrochemical Behavior

Dissolving NaCl in de-ionized water renders a close to neutral electrolyte. In the studies conducted within this work, the produced 0.1 M NaCl solution had a pH of 6.25. In neutral electrolytes the prevailing anodic and cathodic reactions are



as discussed in Chapter 4. To investigate the general electrochemical behavior of the MPEAs, CPP scans (Chapter 5.1.1) were conducted. Figure 7.1a shows the CPP scan for AISI 304 as an exemplary corrosion-resistant alloy, whereas Figure 7.1b depicts the respective Tafel region of the scan. From the CPP, it can be deduced that AISI 304 passivates spontaneously, as no E_{pp} is discernible.^[259] The following passive region ΔE , where the current density j remains constant with increasing potentials, ranges from E_{corr} at -0.27 V to 0.43 V. From 0.31 V up to the breakdown potential E_b at 0.43 V, j fluctuates suggesting metastable pitting on the surface, i.e., the initiation and immediate re-passivation of small pits.^[260] With E_b , initiated pits grow and do not re-passivate. At this point j increases sharply suggesting rapid breakdown of the passive film and transpassive metal dissolution primarily from pits that grow and nucleate.^[259-260] The scan was reversed upon reaching the current density threshold of 5 mA cm⁻². The apex potential was set at 1.5 V vs. OCP, however the strong transpassive dissolution caused j to reach its threshold value before the apex potential. Reversing the potentiodynamic scan results in higher j at the same potentials in the reverse scan compared to the forward scan (positive hysteresis). In the corrosion literature, this is the prime indication for the occurrence of localized corrosion in the form of pitting and/or crevice corrosion. The enclosed area may provide predictions upon the severity/extend of pitting/crevice corrosion.^[259] At -0.03 V the reversed scan crossed the forward scan which is known as the re-passivation

potential E_{rp} . As this cross-over point extends over 0.6 V since the apex potential, AISI 304 presents rather poor re-passivation characteristics in the Cl-medium, potentially due to the severity of pitting and crevice corrosion.

Through extrapolation of the cathodic and anodic curves within the Tafel region as illustrated in Figure 7.1b, $j_{corr} = 8.91 \times 10^{-7} \text{ A cm}^{-2}$ and $E_{corr} = -0.28 \text{ V}$ were determined. To apply Tafel extrapolation to voltammetric data, the anodic and cathodic portions need to be under activation control.^[199] This means that for either the cathodic or anodic reaction to take place, a certain amount of activation energy must be supplied. In this case the typical rate-determining process is a charge transfer process.^[261] The symmetry of the of the anodic and cathodic branch is a further indicator of the prevalent electrochemical reactions at E_{corr} . With $|\beta_c| \gg \beta_a$, the corrosion of AISI 304 in NaCl is cathodically controlled, meaning that in neutral 0.1 M NaCl the oxygen reduction reaction (Equation (7.2)) will limit the overall corrosion process at E_{corr} .^[261]

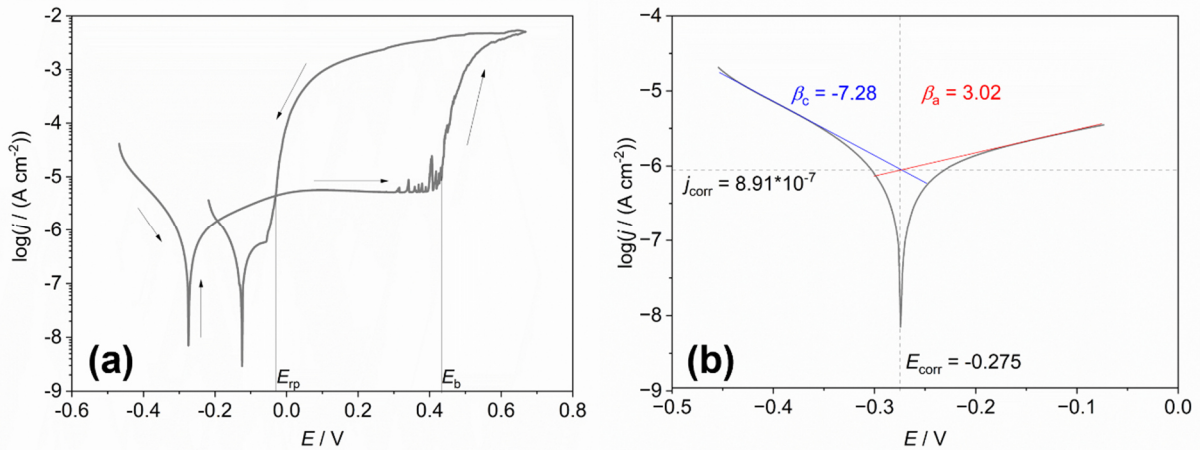


Figure 7.1. (a) CPP scan of AISI 304 in 0.1 M NaCl recorded at 1 mV s^{-1} vs. Ag/AgCl/3M NaCl. (b) The respective Tafel region of the CPP scan in (a) with cathodic (blue, β_c) and anodic fits (red, β_a). The diagram in (a) is adapted with permission from own publication^[185] published by Elsevier B.V. under the terms of the CC BY 4.0 license. Copyright 2022, The Authors.

Figure 7.2a represents the CPP diagram of CrMnFeCoNi which shows a comparable j response to AISI 304. This similarity may be due to the presence of the same alloying elements. While the MPEA encompasses Cr, Mn, Fe, Co, and Ni in equimolar concentrations (at.% = 20%), AISI 304 contains apart from Fe (at.% = 69.88%), Cr (at.% = 19.46%), Ni (at.% = 7.46%) and Mn (at.% = 0.96%). Only Co is not present in AISI 304. In strong contrast, however, the concentrations of Fe and Ni are 3.5 and 2.5 times lower, respectively, and the concentration of Mn is 20 times higher in the MPEA. The identical concentrations of Cr may potentially be one of the reasons for the similar behavior as this is the main element added to alloys to enhance corrosion resistance.^[253] It is assumed that Cr addition leads to the formation of Cr(III) species such as Cr_2O_3 within the passive film which protects the alloy underneath from further dissolution.^[262] The high Mn content in CrMnFeCoNi decreases its corrosion resistance but is added to enhance the mechanical properties. As shown by Torbati-Saraf et

al.^[24] and Wang et. al.^[263], the effect of Mn on the corrosion resistance of CrMnFeCoNi related MPEAs decreases the corrosion resistance in NaCl and H₂SO₄. The main reason behind the increased corrosion susceptibility arises due to the presence of Mn in the alloy matrix which according to the Point Defect Model facilitates the formation and migration of oxygen vacancies in the passive film.^[24] While CrMnFeCoNi also passivates spontaneously, no stable passive region is discernible. After E_{corr} , j steadily increases. Upon further inspection of the CPP, no clear E_b is identifiable. Nevertheless, from $E_{\text{corr}} = -0.19$ V to approx. 0.12 V, the same slope change in j with increasing E can be observed which then increases further with a different slope above 0.12 V. For that reason, two theoretical linear fits were drawn onto the CPP diagram to illustrate this slope in j . The intersection of the two lines marks the onset potential (E_b) of the transpassive region at 0.12 V which is lower than for AISI 304. As with AISI 304, metastable pitting for CrMnFeCoNi can be observed approx. 0.1 V before and after E_b . Before the apex potential of 1.5 V vs. OCP could be reached, the scan was reversed at the threshold of $j = 5$ mA cm⁻². On the reversal scan, j -values are higher at the same potentials than on the forward scan, forming a positive hysteresis. This in turn indicates localized corrosion on the MPEA surface in the form of pitting. The reversal scan crosses the forward scan at $E_{\text{rp}} = -0.15$ V which is very close to E_{corr} and its low potential suggests poor re-passivation. In comparison, the cathodic and anodic branch of the Tafel region in Figure 7.2b look quite symmetrical, indicating a mixed control by anodic and cathodic reactions at E_{corr} .^[261]

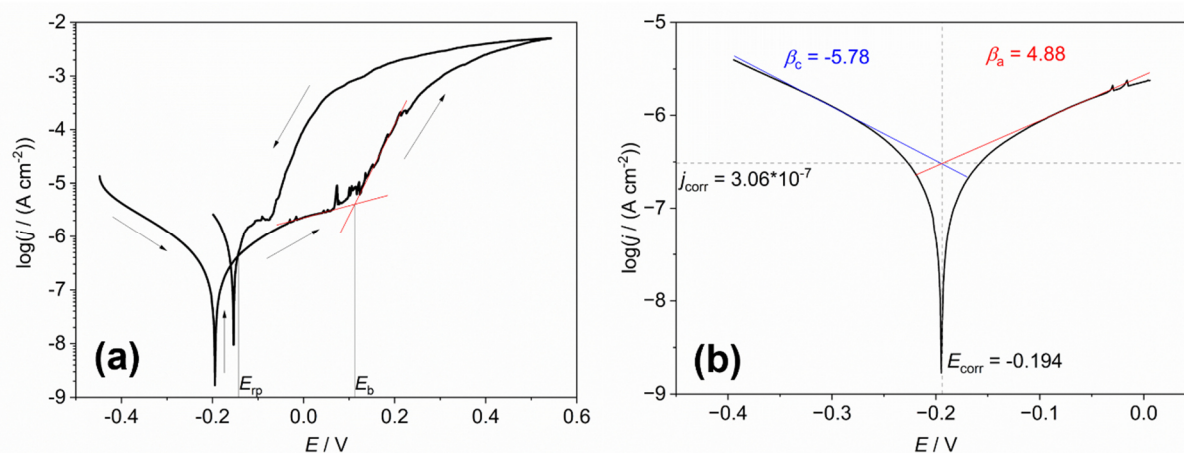


Figure 7.2. (a) CPP scan of CrMnFeCoNi in 0.1 M NaCl recorded at 1 mV s⁻¹ vs. Ag/AgCl/3M NaCl. (b) The respective Tafel region of the CPP scan in (a) with cathodic (blue) and anodic fits (red). The diagram in (a) is adapted with permission from own publication^[185] published by Elsevier B.V. under the terms of the CC BY 4.0 license. Copyright 2022, The Authors.

The CPP for CrCoNi in Figure 7.3a reveals a different electrochemical behavior compared to AISI 304 and CrMnFeCoNi. Nevertheless, CrCoNi also shows spontaneous passivation at potentials positive of its $E_{\text{corr}} = -0.11$ V. The most apparent differences observed between CrCoNi and the two other materials is the absence of pitting indicators. Neither metastable pitting through fluctuating j nor positive hysteresis are monitored. While its passive region shows a slight increase in j with increasing potential, the slope is low compared to

CrMnFeCoNi. However, no clear E_b is identifiable from the CPP scan. Again, linear fits of the passive and transpassive region were used to determine $E_b = 0.60$ V. Even though the potentiodynamic scan was also reversed upon reaching $j = 5$ mA cm⁻², it reached higher potentials (1.36 V vs. OCP), indicating a higher surface stability than for AISI 304 and CrMnFeCoNi. Upon reversal, the j -values are lower than on the forward scan forming a negative hysteresis and indicating good re-passivation properties. Since the current densities are initially lower on the reversed scan, the crossing with the forward scan at $E_{cr} = 0.58$ V is not a point of re-passivation but rather a point where to some extent cathodic reactions may become faster. Such reactions include O₂, oxide and metal ion reduction. The re-passivation of the surface in the reversal scan is indicated by the apparent constant current density while the potential is decreasing. The stable current densities may also be a sign of limited diffusion of O₂ and dissolved metal cations to be reduced.^[264] Compared to CrMnFeCoNi and AISI 304, where the current densities increase sharply in the transpassive region, this is not observed for CrCoNi and its transpassive region extends over a range of 0.6 V. Finally, to determine E_{corr} and j_{corr} , Tafel extrapolation was conducted. From Figure 7.3b it been deduced that the cathodic slope is only slightly larger than the anodic slope implying that reactions at E_{corr} are under mixed control.^[261]

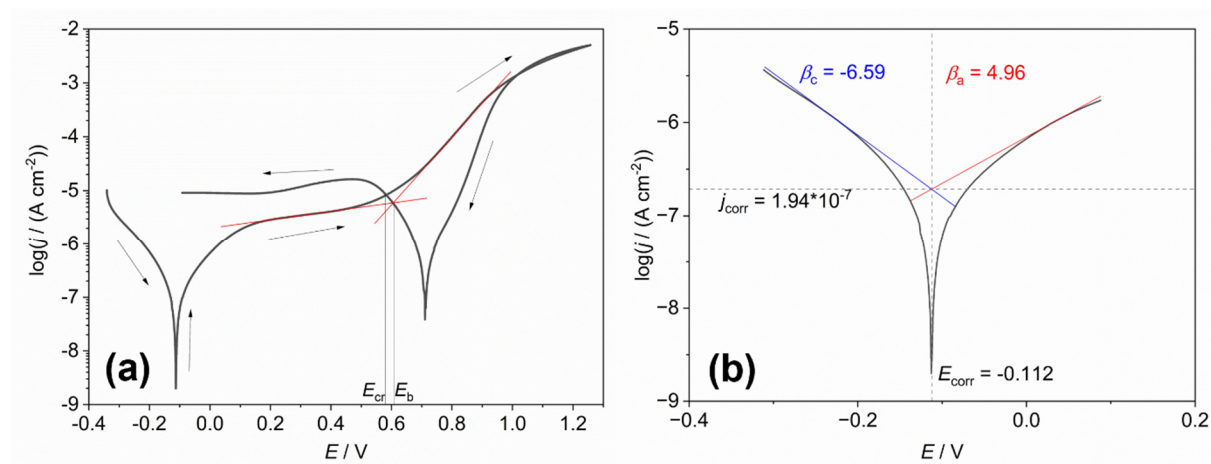


Figure 7.3. (a) CPP scan of CrCoNi in 0.1 M NaCl recorded at 1 mV s⁻¹ vs. Ag/AgCl/3M NaCl. (b) The respective Tafel region of the CPP scan in (a) with cathodic (blue) and anodic fits (red). The diagram in (a) is adapted with permission from own publication^[185] published by Elsevier B.V. under the terms of the CC BY 4.0 license. Copyright 2022, The Authors.

To ensure reproducibility, all electrochemical measurements were conducted at least 3 times. Table 7.1 summarizes the resulting average values with their standard deviation for the electrochemical parameters of AISI 304, CrMnFeCoNi and CrCoNi in 0.1 M NaCl. While the E_{corr} , E_{rp} and ΔE values are quite consistent, other values spread more. The main reason for this lies within the nature of the experiments. Despite all efforts of establishing the same protocol for all measurements, i.e., polishing and cleaning the sample surface, purging the electrolyte with N₂ and keeping the cell under a N₂ environment during the CPP, deviations may still occur resulting in the observed spreading of measured parameters. Overall, however,

the electrochemical data obtained through CPP measurements indicate that CrCoNi exhibits superior corrosion resistance over AISI 304 and CrMnFeCoNi. To further understand this superiority, the passive films were analyzed.

Table 7.1. Summary of the average electrochemical parameters with their standard deviations determined through the CPP measurements of the three samples in 0.1 M NaCl.

	AISI 304	CrMnFeCoNi	CrCoNi
$E_{\text{corr}} / \text{V}$	-0.31 ± 0.03	-0.17 ± 0.03	-0.14 ± 0.08
$j_{\text{corr}} / \text{A cm}^{-2}$	$(5.14 \pm 3.27) \times 10^{-7}$	$(2.79 \pm 3.10) \times 10^{-7}$	$(4.45 \pm 2.84) \times 10^{-7}$
β_c	-8.77 ± 1.32	-5.75 ± 0.44	-6.62 ± 0.38
β_a	4.36 ± 1.18	7.77 ± 4.63	4.15 ± 0.72
$\Delta E / \text{V}$	0.38 ± 0.09	-	0.51 ± 0.09
E_{rp} / V	-0.04 ± 0.01	-0.14 ± 0.00	0.65 ± 0.03
E_b / V	0.32 ± 0.24	0.08 ± 0.02	0.57 ± 0.2

7.1.2 Passive Film Characteristics

To understand the passive film composition, thickness, and protectiveness, XPS and EIS were carried out. While XPS offers information on the passive layer composition, EIS represents a means of evaluating the passive film protectiveness. Both methods enable the calculation of film thicknesses. First, the native passive films on the bare polished surfaces of the alloys were investigated by means of XPS. Since EIS is an electrochemical method, the measurement of the native passive film was conducted so that after a stable OCP was obtained, the EIS spectrum was recorded. For the passive film investigations, the alloys were anodically passivated at potentials within the passive region of the CPP scans presented in Chapter 7.1.1 followed by another EIS and XPS analysis.

Figure 7.4 displays the survey XPS spectra of the native CrMnFeCoNi and CrCoNi surfaces. It illustrates an essential obstacle which renders the analysis of the 2p spectra of first row transition metals and their oxides a challenging and complex task. This obstacle mainly includes the overlap of Auger emission and photoemission peaks. In particular, this is true for the Co LMM, Ni LMM and Fe LMM which overlap with the Fe 2p, Mn 2p and Co 2p peaks, respectively. The effect is most obvious when inspecting the survey spectrum of CrCoNi where seemingly an Fe 2p and an Mn 2p peak are present which of course are the Co LMM and Ni LMM Auger peaks. As discussed by Biesinger et al.,^[238] even the interpretation of the Cr, Mn, Fe, Co and Ni 2p spectra on their own are highly complicated due to multiplet splitting, asymmetric peaks, peak broadening, spectral overlap and plasmonic effects. The combined

analysis of all five promises to be error-prone and potentially questionable without suitable standard samples.

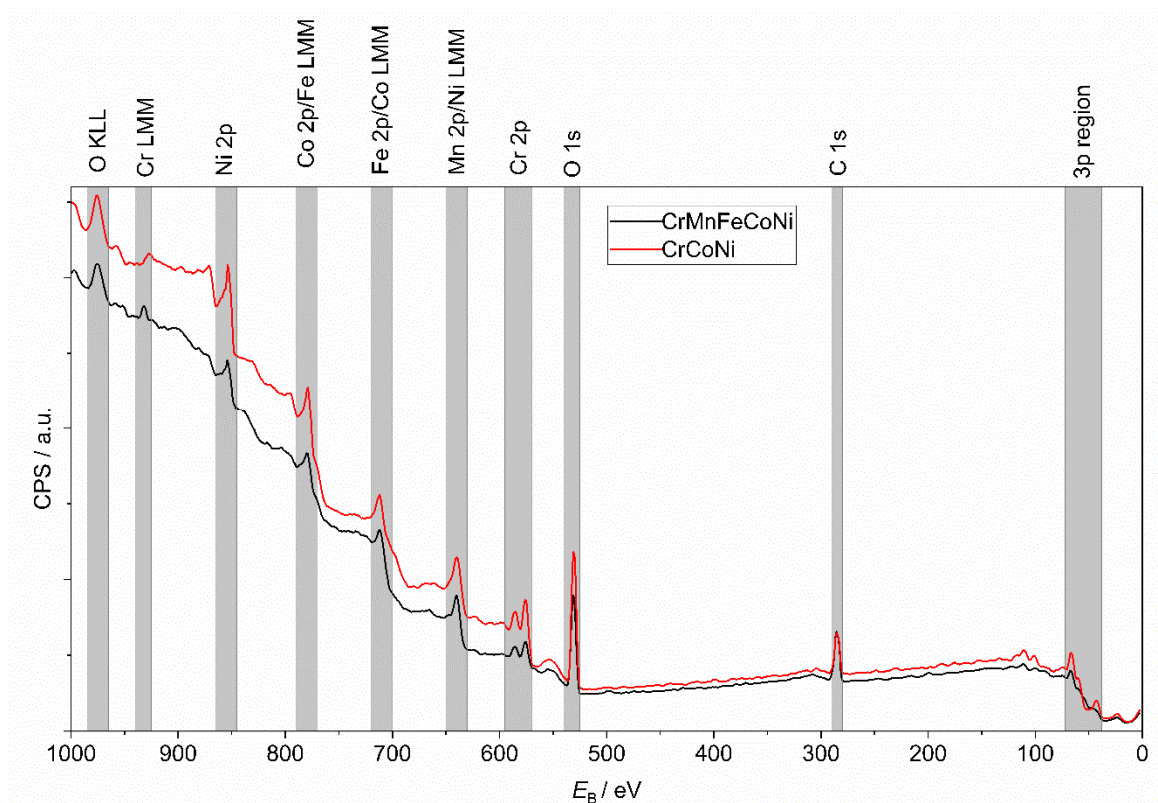


Figure 7.4. XPS 2p survey spectra of the native CrMnFeCoNi and CrCoNi surfaces with the respective metal 2p peak and interfering Auger LMM transition peak allocations.

Previous studies that employed XPS for the passive film analysis of MPEAs heavily relied on the E_B of potentially present oxidation states, but did not necessarily address the complexity of the spectra.^[101, 265-266] Typically, qualitative statements are made and the O 1s spectrum is utilized to elucidate whether the respective oxide, hydroxide species, or bound H₂O may be present. In their study, Marcus et al.^[69] address the additional complexity of overlapping photoemission peaks with Auger transition peaks of MPEAs. To avoid erroneous interpretations, they utilized another approach employing the less sensitive 3p core level peak spectra at lower E_B . Interestingly, another prior study of Al_xCrFeCoNi MPEAs also recorded the 3p spectra of the corroded specimens,^[267] however, no reason is given as to why the 2p core level peak spectra were circumvented. For this work, the 3p core level peaks were analyzed as demonstrated by Marcus et al.^[69] In order to quantify the individual components of the oxide layer on the native and electrochemically treated alloy surfaces, the 3p core level peaks with binding energies ranging between 38.0 eV and 72.0 eV were used.

Figure 7.5 summarizes the 3p survey spectra for the native alloy surfaces. The resulting spectra are in good agreement with the findings by Marcus et al.^[69] Specifically, going from lower to higher E_B , the Cr 3p were fitted with two components, Cr_{ox} ($E_B = 43.5$ eV) and Cr_{met} ($E_B = 41.3$ eV). The Mn 3p peaks of its metal and oxide component are situated at $E_B = 46.5$ eV

and 48.0 eV. The following signals for the Fe 3p core level electrons of both AISI 304 and the native CrMnFeCoNi surfaces could not solely be fitted by an oxide and a metal peak, but needed the introduction of a third peak, representing the differentiation of Fe²⁺ and Fe³⁺ species whereas the respective E_B 's are Fe_{met} ($E_B = 52.1$ eV), Fe²⁺ ($E_B = 53.3$ eV) and Fe³⁺ ($E_B = 55.3$ eV).^[268] Recent work highlights the controversy of differentiating of Fe²⁺ and Fe³⁺ species in the Fe 3p spectra.^[269] However, satisfactory peak fitting could not be achieved without considering both oxidation states of Fe for both, AISI 304 and CrMnFeCoNi. As discussed above, due to the compositional complexity and the presence of multiple first-row transition metals, a systematic analysis of the Fe oxide species was not possible. Hence, the consideration of the two Fe oxidation states seemed a viable option. The Co 3p peaks are composed of a metallic and oxide component at $E_B = 58.5$ eV and 59.8 eV, respectively. Previous studies on stainless steels and the MPEA CrMnFeCoNi have demonstrated that beneath the passive oxide layer, Ni enriches in its metallic form.^[69, 270-271] Due to its clear spin-orbit splitting with Ni 3p_{3/2} ($E_B = 66.0$ eV) and Ni 3p_{1/2} ($E_B = 68.0$ eV), the Ni 3p core level peak is assumed to be fully metallic.^[69]

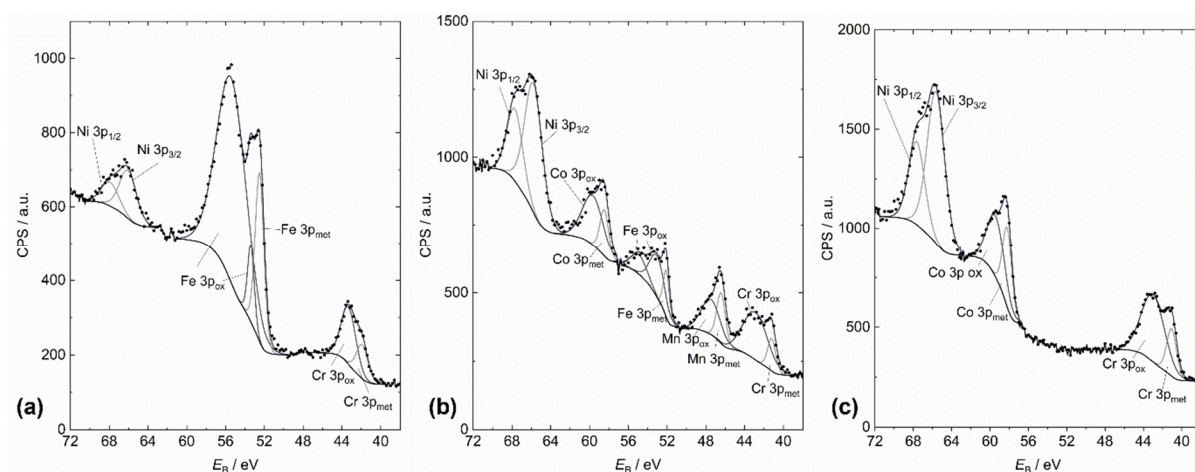


Figure 7.5. XPS 3p survey spectra of (a) AISI 304, (b) CrMnFeCoNi and (c) CrCoNi in the native state. The oxide and metal peaks are indicated by the respective labels. Adapted with permission from own publication^[185] published by Elsevier B.V. under the terms of the CC BY 4.0 license. Copyright 2022, The Authors.

Through fitting of the 3p spectra (see Appendix 2 for fitting parameters), the relative proportions in atomic percent of the oxide and metal contribution toward the surface composition could be determined. Accordingly, Figure 7.6 illustrates the surface compositions of the native alloy surfaces. For the two MPEAs, Cr-oxide is the major component of the passive film. Due to the initially higher Cr content in the bulk alloy, Cr oxide comprises 70 % of the passive layer for CrCoNi while for CrMnFeCoNi it is 38%. In the conventional alloy AISI 304 for which Cr-oxide only constitutes 15%, Fe-oxide is the major passive film component with 85%. As Ni is assumed to remain metallic, it is the dominant component of the metallic signals of all three alloys. This is in agreement with the ToF-SIMS analysis of the CrMnFeCoNi passive film by Marcus et al.^[69] who have demonstrated by depth profiling a modified metallic

layer enriched in Ni beneath the passive film. Looking at the oxide to metal ratio of all surface metal species, AISI 304 exhibits the highest ratio of 2.9:1, CrCoNi has the lowest ratio of nearly 1:1, CrMnFeCoNi is positioned in between with 1.3 : 1.

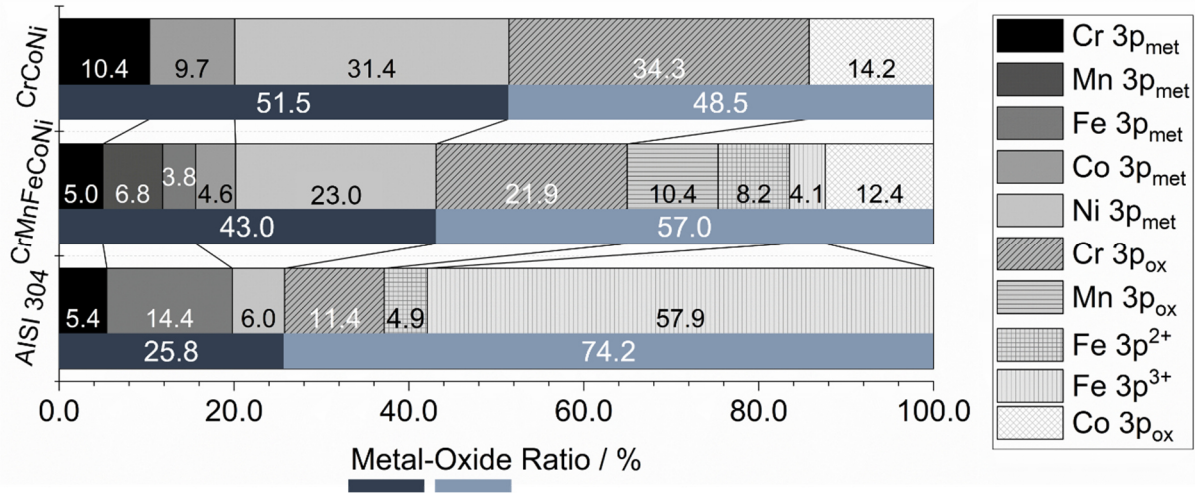


Figure 7.6. Surface compositions of the three alloys in the native state with the respective mole fraction of metallic and oxide metal species. The metal to oxide ratio is highlighted by the dark and light blue bars, respectively. Adapted with permission from own publication^[185] published by Elsevier B.V. under the terms of the CC BY 4.0 license. Copyright 2022, The Authors.

After anodic passivation in 0.1 M NaCl at $E_{\text{pass}} = 0.15$ V, 0.01 V and 0.32 V for AISI 304, CrMnFeCoNi and CrCoNi, respectively, the oxide components of the 3p core level peaks increase and the metal component peaks decrease in intensity. Figure 7.7 shows the respective 3p spectra. As a general observation, the Ni 3p peak decreases with passivation due to the growth of the oxide layer, supporting the assumption that it is present in its metallic state. Comparing AISI 304 and CrMnFeCoNi, only two component peaks Fe_{met} and Fe_{ox} are observed in the XPS spectrum after anodic passivation in NaCl.

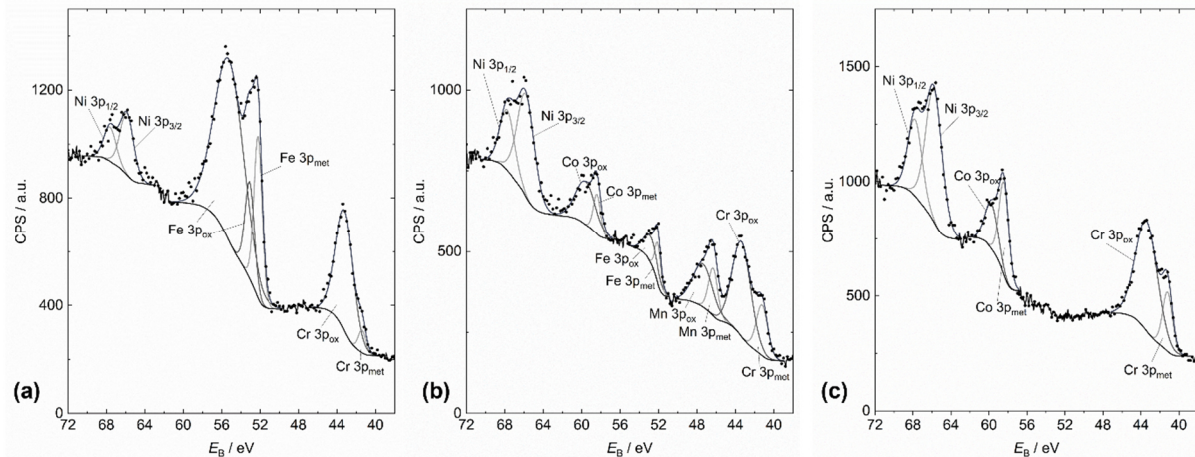


Figure 7.7. XPS 3p survey spectra of (a) AISI 304, (b) CrMnFeCoNi and (c) CrCoNi after anodic passivation in 0.1 M NaCl. The oxide and metal peaks are indicated by the respective labels. Adapted with permission from own publication^[185] published by Elsevier B.V. under the terms of the CC BY 4.0 license. Copyright 2022, The Authors.

The growth of the passive oxide layer after the anodic passivation in 0.1 M NaCl becomes apparent when looking at the derived surface compositions in Figure 7.8. Compared to the composition of the bare surface, the oxide fraction on the CrCoNi surface increases by

6.1%. AISI 304 demonstrates a similar increase of 6.5%. For CrMnFeCoNi, the oxide components only increase by 2.1% which correlates with its poorer performance in the polarization tests. Nevertheless, CrCoNi still presents the lowest oxide to metal ratio with 1.2:1, while for CrMnFeMnCoNi it remains nearly unchanged with 1.4:1. For AISI 304 the ratio surmounts to 4.2:1. Interestingly, the increase in oxide to metal ratio for all three alloys is mainly due to the growth of Cr-oxides. While the determined surface compositions may suggest the assumption of thicker films on AISI 304 compared to the MPEAs, it does not correlate with better corrosion resistance as has been demonstrated previously in the polarization studies, where CrCoNi clearly exhibits the superior resistance towards corrosive deterioration.

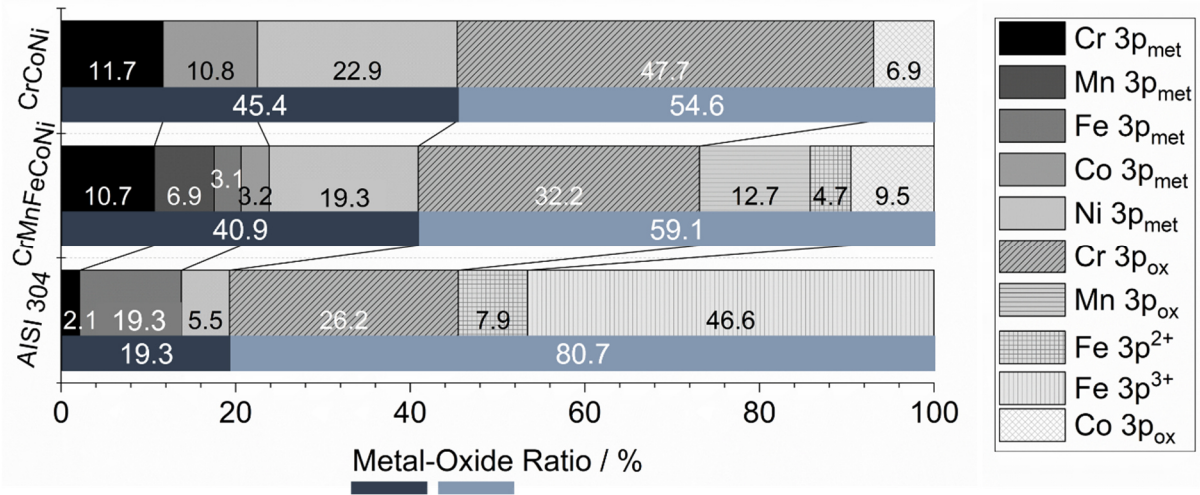


Figure 7.8. Surface compositions of the three alloys after anodic passivation in 0.1 M NaCl with the respective mole fractions of metallic and oxide metal species. The metal to oxide ratio is highlighted by the dark and light blue bars, respectively. Adapted with permission from own publication^[185] published by Elsevier B.V. under the terms of the CC BY 4.0 license. Copyright 2022, The Authors.

It becomes evident that the oxides slightly dominate the metallic components at the topmost layer after passivation in NaCl, suggesting the growth of a thin passive film. Oxide layer thicknesses of CrMnFeCoNi after electrochemical treatment in 0.05 M H₂SO₄ ranged between 1.4 and 2 nm, according to Marcus et al.^[69] Assuming a continuous and homogeneous oxide layer on the alloys, passive layer thicknesses were calculated by employing Equations (7.3) to (7.5).

$$I_X^{\text{met}} = k\sigma_X\lambda_X^{\text{met}}D_X^{\text{met}}T_X\exp\left(-\frac{d_{\text{oxide}}}{\lambda_Y^{\text{ox}}}\right) \quad 7.3$$

$$I_Z^{\text{ox}} = k\sigma_Z\lambda_Z^{\text{ox}}D_Z^{\text{ox}}T_Z\left[1 - \exp\left(-\frac{d_{\text{oxide}}}{\lambda_Z^{\text{ox}}}\right)\right] \quad 7.4$$

$$d_{\text{oxide}} = \ln\left(\frac{I_Z^{\text{ox}}\lambda_Y^{\text{met}}D_X^{\text{met}}}{I_Y^{\text{met}}\lambda_Z^{\text{ox}}D_Z^{\text{ox}}} + 1\right) * \lambda_Y^{\text{ox}} \quad 7.5$$

The parameters in Equations (7.3) to (7.5) encompass the intensity I_Z^Y of emitted photoelectrons from the core level Z in matrix Y (met or ox), k is a specific spectrometer

constant, the photoionization cross-section σ , the inelastic mean free path (IMFP) λ_Z^Y , the transmission function T_X of the PHOIBOS analyzer (considered as constant over the small employed energy range), the density D_Z^Y of element Z in matrix X/Y and the oxide layer thickness d_{oxide} .^[69] Furthermore, $D_Z^Y = \frac{\rho_Y}{M_Y} x_Z^Y$ where ρ_Y is the density of matrix Y, M_Y is the molecular weight of matrix Y and x_Z^Y is the atomic percentage of element Z in matrix Y. For CrMnFeCoNi, the homogeneous oxide layer was assumed to comprise Cr, Mn, Fe and Co oxides whereas the modified alloy layer underneath was accounted by containing Cr, Mn, Fe, Co and Ni. For CrCoNi, only Cr and Co oxides were assumed for the oxide layer and Cr, Co, and Ni for the metallic underlying alloy layer. The oxide densities used for the calculations, the photoionization cross-sections and IMFPs can be found in Appendix 3. IMFPs were calculated according to the TTP-2 formula,^[272] and double checked with the NIST database.^[273]

Table 7.2 outlines the respective oxide layer thicknesses d_{oxide} of the native and passivated state of CrCoNi and CrMnFeCoNi. As stated before, the layers were expected to be thin, especially for transition metals, and within the nanometer-range. While the oxide layer on CrMnFeCoNi increases in thickness by 30%, it increases by 60% for CrCoNi upon anodic passivation, supporting the previous finding of higher corrosion resistance for CrCoNi. Nevertheless, the results should be treated carefully, as porosity of the passive film cannot be excluded.

Table 7.2. Surface layer thicknesses of CrMnFeCoNi and CrCoNi determined for the native state and the after anodic passivation in 0.1 M NaCl.

	CrMnFeCoNi	CrCoNi
	nm	nm
Native	2.81	2.46
NaCl	3.65	3.93

In contrast to the XPS measurements, which are conducted under high vacuum, EIS experiments typically involve a complete electrochemical cell, in which the specimen operates as the working electrode. Here, the alloy surfaces were stabilized in the 0.1 M NaCl electrolyte for 30 min before the EIS was recorded. As outlined in Chapter 5.1.2, EIS enables to monitor electrical, electrochemical, and physical processes of an electrochemical system as they exhibit different time behaviors.^[208]

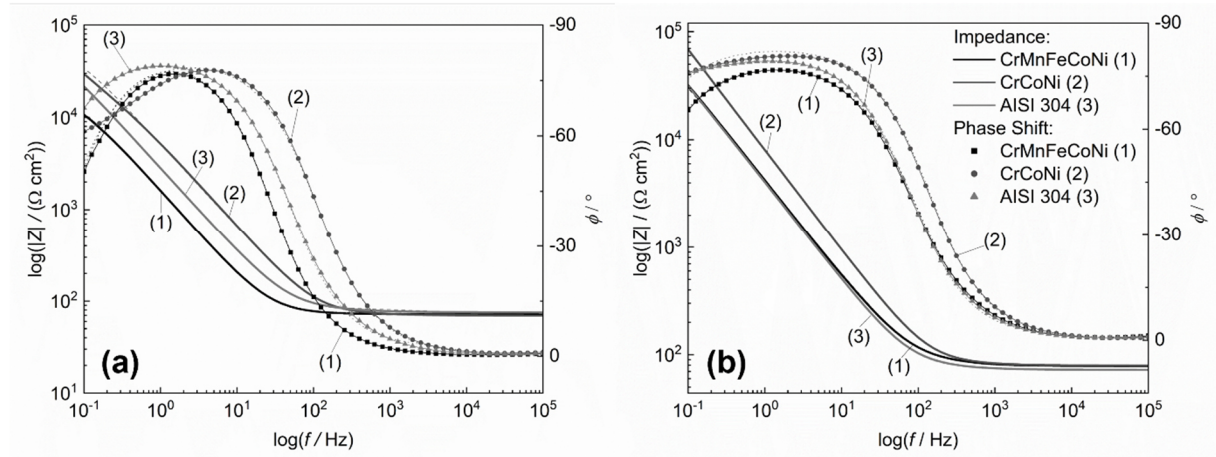
Figure 5.2c depicts the electrical equivalent circuit (EEC) used to fit the impedance data and identify the respective processes on the alloy surfaces in 0.1 M NaCl. The circuit was also used to fit the EIS data obtained for 0.1 M H₂SO₄ in Chapter 7.2.2. First employed by Joiret et al.^[274] to analyze oxide films on Fe which were modelled by capacitors, Orazem et al.^[275]

exchanged the capacitance element with a constant phase element (CPE) to study oxide films formed on ASTM A416 steel. The EEC shown in Figure 5.2c was also employed in other MPEA studies to analyze the properties of their oxide films.^[266, 276] In this work a high-quality fit was acquired through obtaining χ^2 values below 10^{-3} orders of magnitude during Kramers-Kronig analysis.^[101] The model in Figure 5.2c comprises a resistor R_s for the electrolyte resistance in series with a parallel combination CPE_f and resistor R_f which represent the heterogenous and potentially porous nature of the dielectric passive film.^[275] In series with R_f , a parallel combination of CPE_{dl} for the electrical double layer and a resistor R_{ct} for charge transfer processes that need to pass the EDL follows. Generally, the passive film resistivity was considered to be normal to the electrode surface.^[275]

Figure 7.9 presents the Bode plots and the fitted curves after the OCP (Figure 7.9a) and anodic passivation (Figure 7.9b) in 0.1 M NaCl. The respective data are summarized in Table 7.3. At high frequencies the impedance response of the electrolyte can be observed, which resides at approx. $70 \Omega \text{ cm}^2$ for all three alloys and does not change after anodic passivation. As the phase angle ϕ approaches 0° in this domain, the observed impedance corresponds to an ideal resistor and represents the electrolyte resistance.^[208] The mid-frequency range shows a linear decrease and increase in phase angle ϕ and impedance Z . The decreasing or increasing phase angle indicates the change in the predominant process from an ideal resistor at high frequency to capacitor-like behavior at low frequencies. The gradient of the impedance modulus is another indicator for the change from resistive to capacitive behavior. While $\text{grad}|Z| = 1$ represents an ideal capacitor, $\text{grad}|Z|$ for the studied alloys remains below unity, confirming non-ideal capacitor behavior of the passive layer.^[277] The pseudo-capacitive nature of the passive films is further supported by the minima in phase angle which do not reach $\phi = -90^\circ$ as it would be the case for an ideal capacitor. AISI 304 and CrCoNi have similar minimum phase angles of -78° and -79° , respectively. CrCoNi exhibits a lower $\phi = -81^\circ$ after passivation, suggesting the most homogeneous passive film for the three-component MPEA. CrMnFeCoNi shows the same and highest phase angle in both scenarios, $\phi = 77^\circ$. The broadening of the phase angle signal after passivation indicates the growth of the passive film for all three alloys.^[278] However, CrCoNi shows the most significant increase in its passive film stability. At low frequencies ($f = 0.1 \text{ Hz}$), the modulus of impedance correlates with to the polarization resistance of an alloy and both are an indicator of its corrosion resistance.^[279] The polarization resistance R_p is derived as the sum of R_s , R_{ct} and R_f .^[265] From Figure 7.9, it can be seen that CrCoNi exhibits the highest $|Z|$ at $f = 0.1 \text{ Hz}$ and its R_p also exceeds that of CrMnFeCoNi (see Table 7.3).

Table 7.3. EIS data for (1) CrCoNi and (2) CrMnFeCoNi after OCP and anodic passivation in 0.1 M NaCl where m and n are the exponents of CPE_f and CPE_{dl} , respectively.

OCP								
	R_s	R_{ct}	R_f	R_p	CPE_{dl}	n	CPE_f	m
	$[\Omega \text{ cm}^2]$	$[\Omega \text{ cm}^2]$	$[\Omega \text{ cm}^2]$	$[\Omega \text{ cm}^2]$	$[\text{S s}^n \text{ cm}^{-2}]$		$[\text{S s}^m \text{ cm}^{-2}]$	
(1)	69.60	6.91×10^4	3.02	6.92×10^4	1.94×10^{-5}	0.92	1.68×10^{-5}	0.90
(2)	71.25	2.04×10^4	1.25	2.05×10^4	9.49×10^{-5}	0.94	1.58×10^{-5}	0.90
Anodic Passivation								
(1)	79.46	4.14×10^5	4.24	4.14×10^5	1.27×10^{-5}	0.93	9.81×10^{-6}	0.93
(2)	78.60	1.26×10^5	3.24	1.26×10^5	3.45×10^{-5}	0.89	1.24×10^{-5}	0.86


 Figure 7.9. Bode plots of the three alloys after (a) OCP and (b) anodic passivation in 0.1 M NaCl recorded at OCP and an AC voltage of 10 mV. Adapted with permission from own publication^[185] published by Elsevier B.V. under the terms of the CC BY 4.0 license. Copyright 2022, The Authors.

The derived oxide layer thicknesses d_{oxide} of the alloys from EIS data were obtained through Equation (7.6).

$$C_f = \frac{\varepsilon \varepsilon_0}{d_{\text{oxide}}} \quad 7.6$$

Here, C_f is the capacitance at frequency f_{max} , ε_0 is the permittivity of vacuum and ε is the relative permittivity of the oxide layer which was assumed to be 30.^[266, 280-281] As the alloys EIS data of the alloys were fitted with $CPEs$ to represent the imperfect nature of the formed passive layer, the respective capacitances were calculated from CPE_f at f_{max} which corresponds to the frequency at the largest phase angle employing Equation (7.7).^[247, 282]

$$C_f = CPE_f (2\pi f_{\text{max}})^{m-1} g \quad 7.7$$

$$g = 1 + 2.88(1 - m)^{2.375} \quad 7.8$$

where m is the CPE exponent which represents the degree of deviation from ideal capacitor behavior ($m = 0$ (resistor) to $m = 1$ (capacitor)).^[209] In close relation to the XPS-derived film thicknesses (see Table 7.2), the passive films derived by EIS (see Table 7.4) are about 1 nm

thicker after passivation compared to the initial OCP state. CrCoNi revealed the thickest film after passivation with 3.2 nm.

Table 7.4. Summary of capacitances and oxide layer thicknesses of CrMnFeCoNi and CrCoNi in 0.1 M NaCl determined by EIS.

	C_i	δ_{oxide}
OCP	(F cm ⁻²)	nm
CrMnFeCoNi	1.28 x 10 ⁻⁵	2.08
CrCoNi	1.23 x 10 ⁻⁵	2.16
Pass		
CrMnFeCoNi	9.12 x 10 ⁻⁶	2.91
CrCoNi	8.20 x 10 ⁻⁶	3.24

On stainless steels oxide layer thicknesses have been studied extensively in different electrolytes,^[247, 283] and respective measurements have not been repeated in this work. However, the values obtained for the MPEAs are comparable to what has been reported in the literature where oxide layer thicknesses of AISI 304 range from 1 to 3 nm.^[270]

7.1.3 Corrosion Mechanism in Chloride-Containing Electrolyte

Considering that corrosion describes the deterioration through metal dissolution from the exposed surface, it is vital in corrosion studies to analyze the electrolyte after corrosion and inspect the attacked surfaces. The data on the passive films and their properties provide information on the materials corrosion resistance. The electrochemical measurements show that CrCoNi exhibits superior corrosion resistance compared to CrMnFeCoNi and AISI 304. To further elucidate the prevailing corrosion mechanisms and possible preferential metal dissolution, ICP-MS, AFM and SEM studies were conducted after CPP measurements. While ICP-MS was employed to quantify the dissolved metal species after CPP in the electrolytes, AFM and SEM images of the MPEA surfaces were recorded to elucidate localized corrosion mechanism.

Table 7.5 outlines the absolute metal concentrations in solution after the corrosion of the alloys through CPP in 0.1 M NaCl. Figure 7.10 summarizes the molar metal distributions more visually in percent to allow for better comparison between the alloys and their bulk metal mole fraction. From the concentrations in Table 7.5, it can be seen that the highest concentration of total dissolved metals is measured for AISI 304 with $c = 484.52 \mu\text{mol L}^{-1}$. This is followed by CrMnFeCoNi with $c = 364.11 \mu\text{mol L}^{-1}$ whereas the lowest concentration of dissolved metal cations during the CPP is found for CrCoNi with $c = 120.57 \mu\text{mol L}^{-1}$. Looking back at the CPP results, one may assume that the strongest metal dissolution should be

observed for CrMnFeCoNi. However, AISI 304 showed a much more extensive hysteresis, indicating stronger pitting and crevice corrosion on the stainless steel. Furthermore, the corrosion susceptibility of protective oxide film in Cl⁻-containing media is widely known.^[284] The formation of FeCl_{ads}⁻ species, e.g., is assumed to accelerate Fe dissolution from steels,^[285] which is supported by the high Fe concentration found for AISI 304. Figure 7.10 facilitates the assessment of metal dissolution tendencies. Inspecting the concentration of dissolved metal cations for CrCoNi, it is apparent, that the metal ion concentrations in the electrolyte are proportional to the mole fraction of the metals in the bulk alloy. CrMnFeCoNi, on the other hand, displays predominant dissolution of Mn, which may be attributed to the ability of Mn to stabilize at a multitude of oxidation states.^[263] Contrarily, Fe is found in the electrolyte at only 11%, suggesting that it partakes in the formation of the passive film. While the XPS results indicate an increase in Fe oxide after anodic passivation, Cr oxides increase to a larger extent within the oxide layer. This suggests that in the ICP-MS results, lower Cr concentrations are to be expected which is not the case. In this context, it should be considered that in the CPP, the reversal scan initiates re-passivation of the surface where Fe may be a key component in re-passivating the surface. It is known that the interplay of Fe, Ni and Cr leads to secondary passivation of certain steels at high potentials.^[286] Such an interaction may be active in this instance leading to the observed distributions. A comparison of the MPEA dissolution tendencies with AISI 304, shows that different dissolution and passivation mechanisms must be active. For AISI 304, a higher concentration of Fe and slightly lower concentration of Cr are dissolved when compared to their bulk mole fraction in the alloy, indicating that the ratio of Fe to Cr may interfere with the passivation of the alloy. Caution should be practiced in this context, as the metals and passive films may not solely dissolve due to electrochemical processes. Chemical dissolution and mechanical rupture of the passive film may further contribute toward the dissolved metal species.^[287] Finally, as ICP-MS measurements are conducted by acidifying the analyte solutions (i.e., electrolytes) with HNO₃, all metal species should be detected. This includes metal hydroxides which are typical corrosion products that are only minimally soluble in water, but which will dissolve upon acidification.

Table 7.5. Concentrations of dissolved metals after CPP in 0.1 M NaCl.

	[Cr]	[Co]	[Ni]	[Fe]	[Mn]	[Total]
	[$\mu\text{m L}^{-1}$]	[$\mu\text{m L}^{-1}$]	[$\mu\text{m L}^{-1}$]	[$\mu\text{m L}^{-1}$]	[$\mu\text{m L}^{-1}$]	[$\mu\text{m L}^{-1}$]
AISI 304	78.31 ± 4.31		48.99 ± 2.39	346.87 ± 25.53	9.39 ± 0.60	484.52
CrMnFeCoNi	65.82 ± 3.82	84.23 ± 7.06	79.87 ± 6.74	40.72 ± 1.38	93.47 ± 11.28	364.11
CrCoNi	39.75 ± 1.48	37.49 ± 7.02	43.33 ± 2.46	-	-	120.57

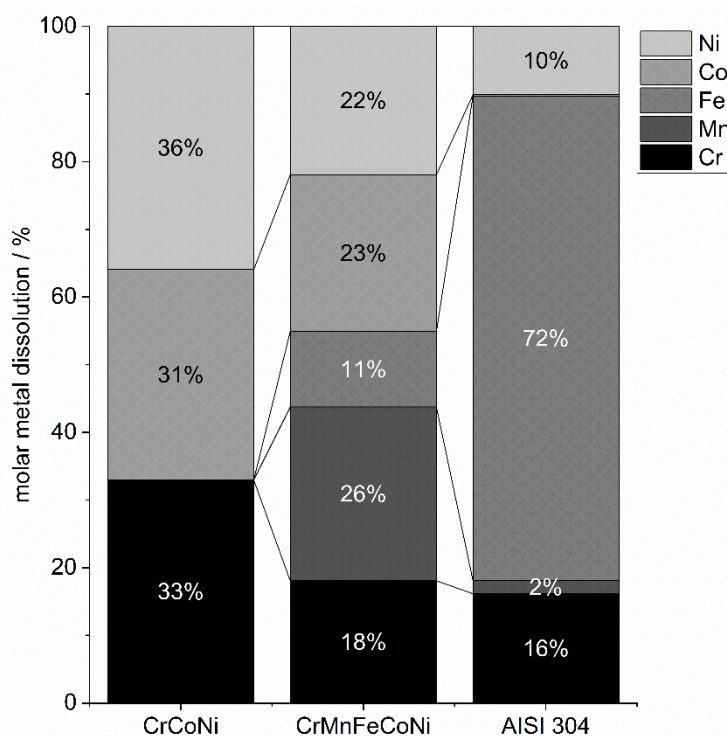


Figure 7.10. Molar fraction of dissolved metal ions in the 0.1 M NaCl electrolyte after CPP. Data are based on respective metal concentrations in Table 7.5. Adapted with permission from own publication^[185] published by Elsevier B.V. under the terms of the CC BY 4.0 license. Copyright 2022, The Authors.

From the CPP, it can be deduced that CrMnFeCoNi and AISI 304 succumb to localized corrosion in the form of pitting and/or crevice corrosion. For CrCoNi, however, the electrochemical data does not provide qualitative information on its corrosion mechanism. To understand how the surface morphologies changed in accordance with the prevalent corrosion mechanism, AFM and SEM images were recorded of the pre- and post-corrosion state through CPP.

Figure 7.11 and Figure 7.12 show the surface morphologies of CrMnFeCoNi before and after corrosion, respectively. Figure 7.11a and b show the AFM and SKPFM maps of the same CrMnFeCoNi surface after polishing. The polishing lines are clearly visible on the untreated surface and an inclusion of Cr-/Mn-oxide smaller than 2 μm was captured. The inclusions are a product of the manufacturing process and could not be circumvented. Figure 7.12a and b show the SEM images in the BSE and SE modes, respectively. In the BSE mode the inclusions are darker, due to their lighter mass and the concomitant decrease in back scattering ability. The SE mode offers a topographical view of the surface in a lower magnification compared to the AFM maps. Grains and twins as a result of the applied heat and deformation treatment of the alloy are well resolved in the SEM images. The SEM images further confirm the presence of a single phase and the solid solution state of CrMnFeCoNi.

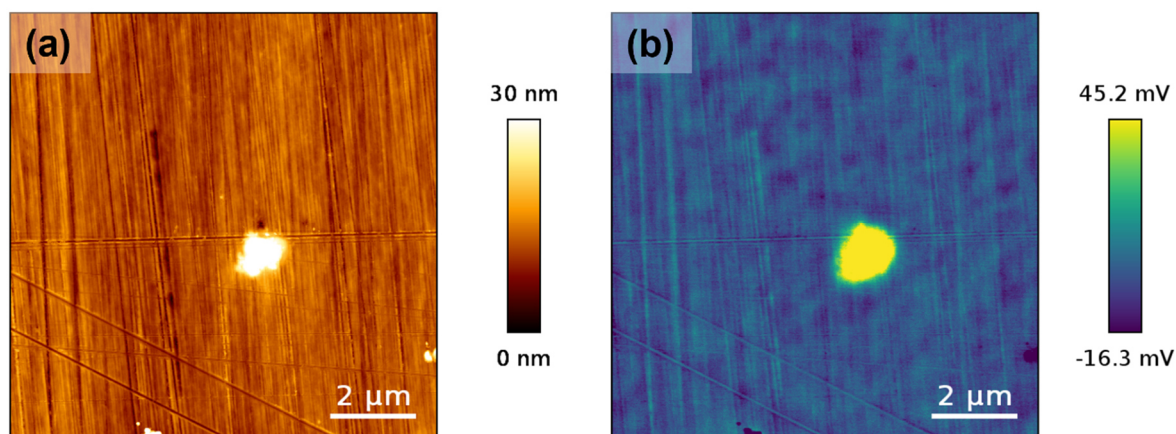


Figure 7.11. (a) AFM topography of a polished CrMnFeCoNi surface and (b) SKPFM potential map of the same polished CrMnFeCoNi surface. Adapted with permission from own publication^[185] published by Elsevier B.V. under the terms of the CC BY 4.0 license. Copyright 2022, The Authors.

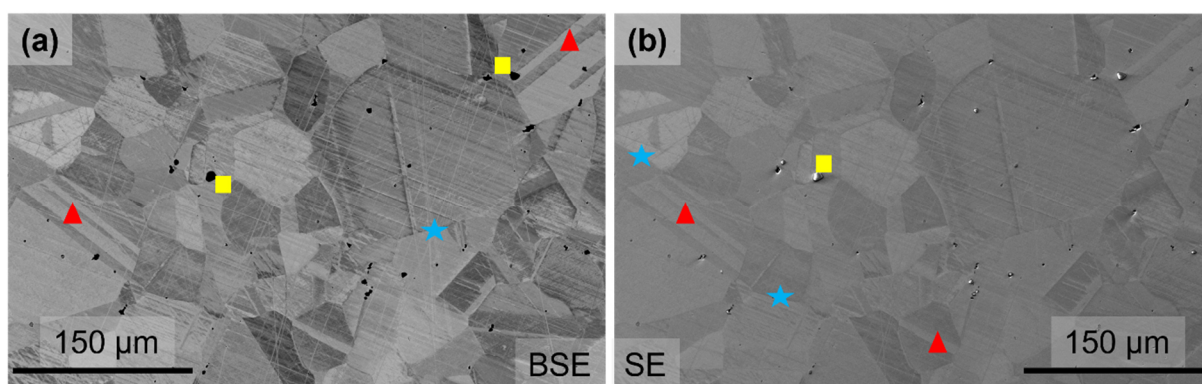


Figure 7.12. SEM images of a polished CrMnFeCoNi surface in (a) BSE and (b) SE mode. The symbols highlight grain boundaries (blue star), twin structures (red triangle), and intact inclusions (yellow square).

After corrosion through CPP in 0.1 M NaCl, the AFM and SEM images in Figure 7.13 confirm the corrosion of CrMnFeCoNi through pitting corrosion. While the AFM and SKPFM maps could only display sites of small pits ($d \approx 0.5 \mu\text{m}$), the SEM images show the extend of pitting on CrMnFeCoNi. In the potential map in Figure 7.13b, the potentials are lowest within the formed pits, indicating the formation of an oxide layer on the alloy matrix surrounding the cavity. Figure 7.14a and b show narrow and long pits with dimensions of roughly $5 \mu\text{m} \times 30 \mu\text{m}$. Figure 7.14c and d, on the other hand, show a large pit, that is probably the result of pit nucleation and agglomeration and has a diameter of more than $300 \mu\text{m}$. This pit also represents the hollowing nature of pit growth by some original metal surface still hovering above the pit.

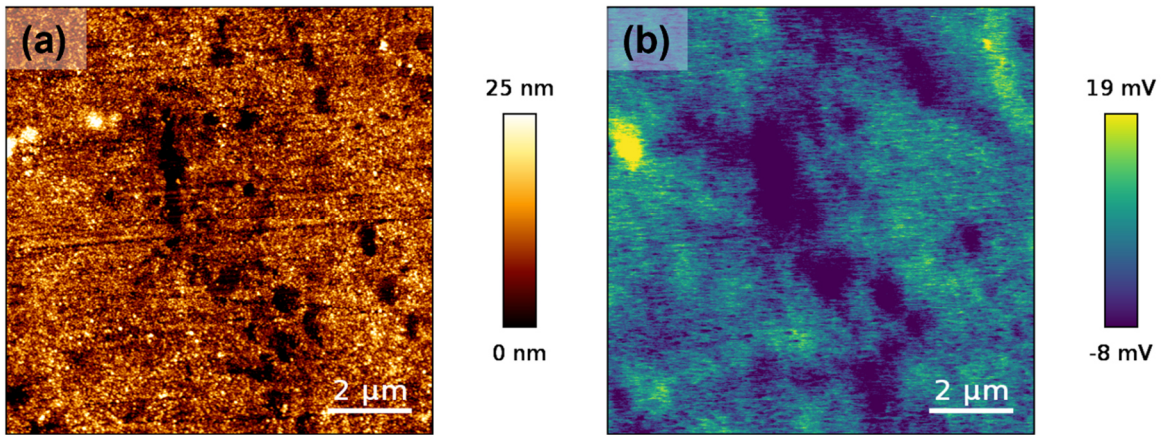


Figure 7.13. (a) AFM topography of a CrMnFeCoNi surface corroded in 0.1 M NaCl and (b) SKPFM potential map of the same corroded CrMnFeCoNi surface showing the growth of pits. Adapted with permission from own publication^[185] published by Elsevier B.V. under the terms of the CC BY 4.0 license. Copyright 2022, The Authors.

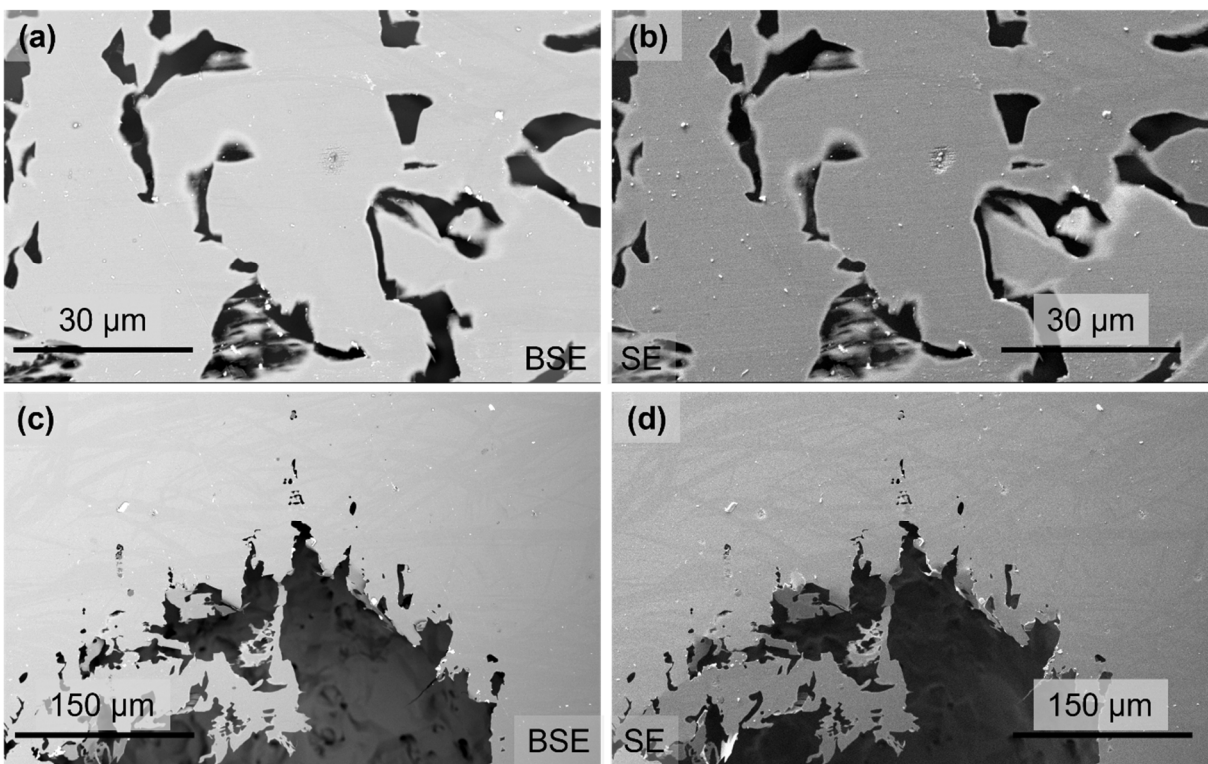


Figure 7.14. SEM images of different pit morphologies on CrMnFeCoNi as a result of its corrosion in 0.1 M NaCl. (a) and (b) show many smaller pits in the BSE and SE mode, respectively. (c) and (d) show a large pit in the BSE and SE mode, respectively, with some of the original MPEA surface overarching the cavity.

As with CrMnFeCoNi, the polished surfaces of CrCoNi clearly show the polishing lines in the AFM and SKPFM maps in Figure 7.15a and b. For CrCoNi the inclusions are also a product of the manufacturing process and are composed of Cr-oxides. A slightly larger inclusion was captured for the CrCoNi surface with a diameter of $d = 4 \mu\text{m}$. Figure 7.16a and b illustrate the BSE and SE images of CrCoNi. The presence of a single phase and the solid solution state of CrCoNi are confirmed. In contrast to CrMnFeCoNi, CrCoNi possesses more inclusions and twin structures. Furthermore, its grains are slightly smaller. In a corrosion context, this usually increases corrosion susceptibility.^[278]

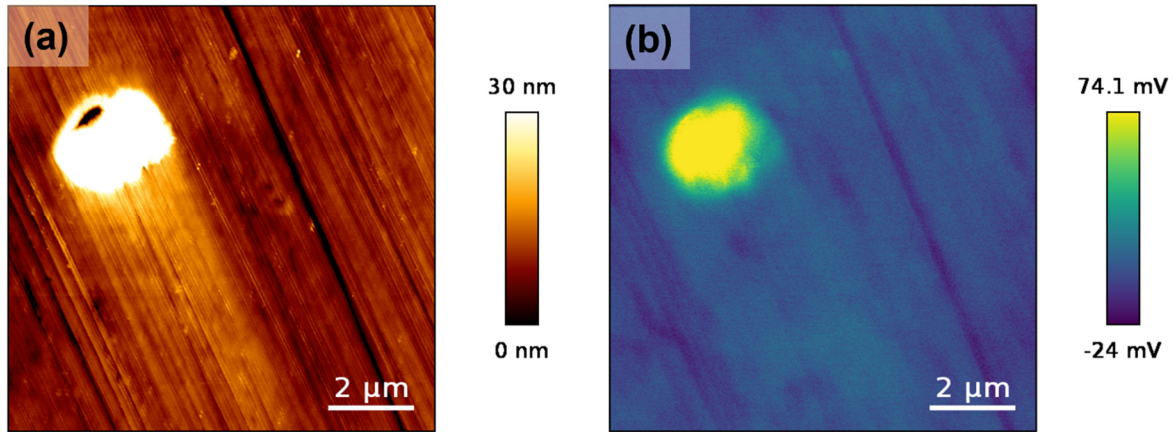


Figure 7.15. (a) AFM topography of a polished CrCoNi surface and (b) SKPFM potential map of the same polished CrCoNi surface. Adapted with permission from own publication^[185] published by Elsevier B.V. under the terms of the CC BY 4.0 license. Copyright 2022, The Authors.

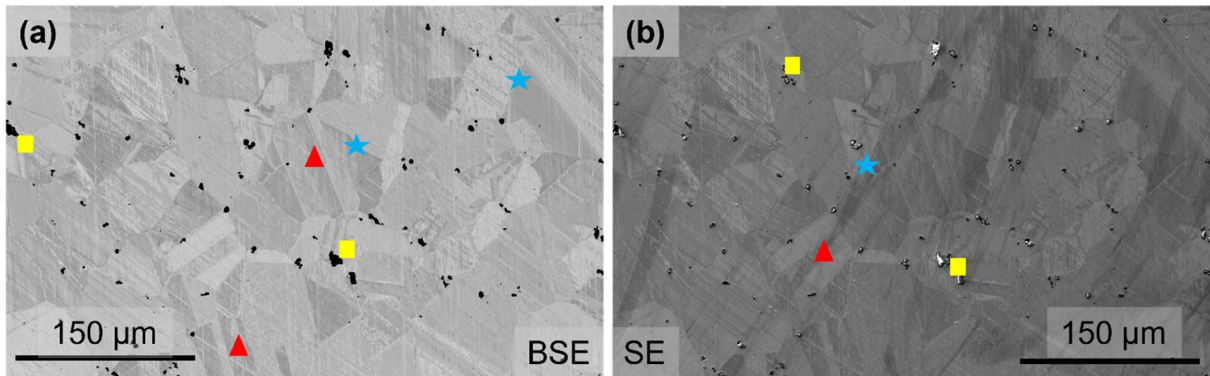


Figure 7.16. SEM images of a polished CrCoNi surface in (a) BSE and (b) SE mode. The arrows highlight grain boundaries (blue star), twin structures (red triangle), and intact inclusions (yellow square).

However, the polarization measurements suggest that CrMnFeCoNi is more susceptible to corrosion in 0.1 M NaCl. The dissolved metals recorded for CrCoNi are due to intergranular corrosion of the MPEA. Figure 7.17 shows the AFM and SKPFM maps of the corroded grain boundaries. The potential in the SKPFM is higher within the grain boundaries which may indicate the accumulation of oxides at the grain boundaries, leading to passivation at those sites and the observed high corrosion resistance. The SEM images in Figure 7.18 show the intergranular corrosion of CrCoNi at different magnifications.

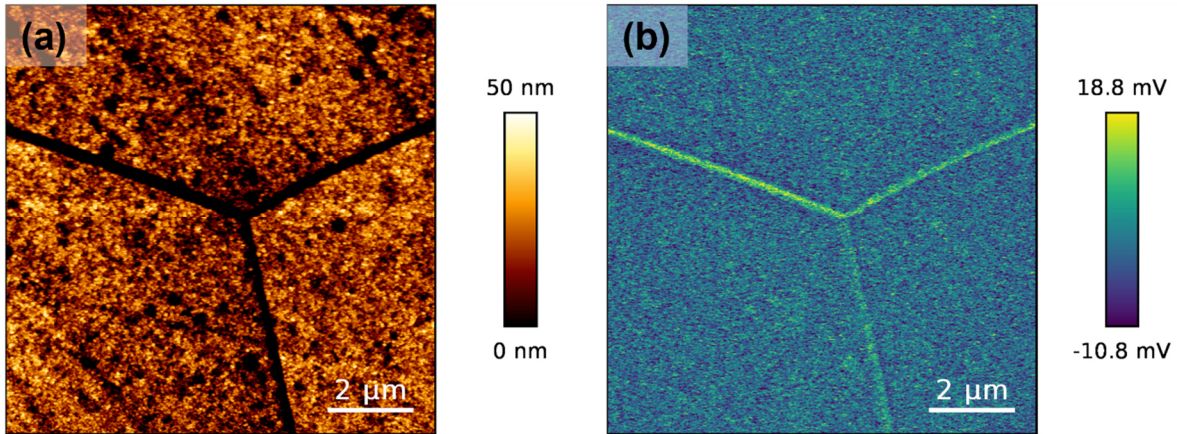


Figure 7.17. (a) AFM topography of a CrCoNi surface corroded in 0.1 M NaCl and (b) SKPFM potential map of the same corroded CrCoNi surface showing the corrosive attack at grain boundaries. Adapted with permission from own publication^[185] published by Elsevier B.V. under the terms of the CC BY 4.0 license. Copyright 2022, The Authors.

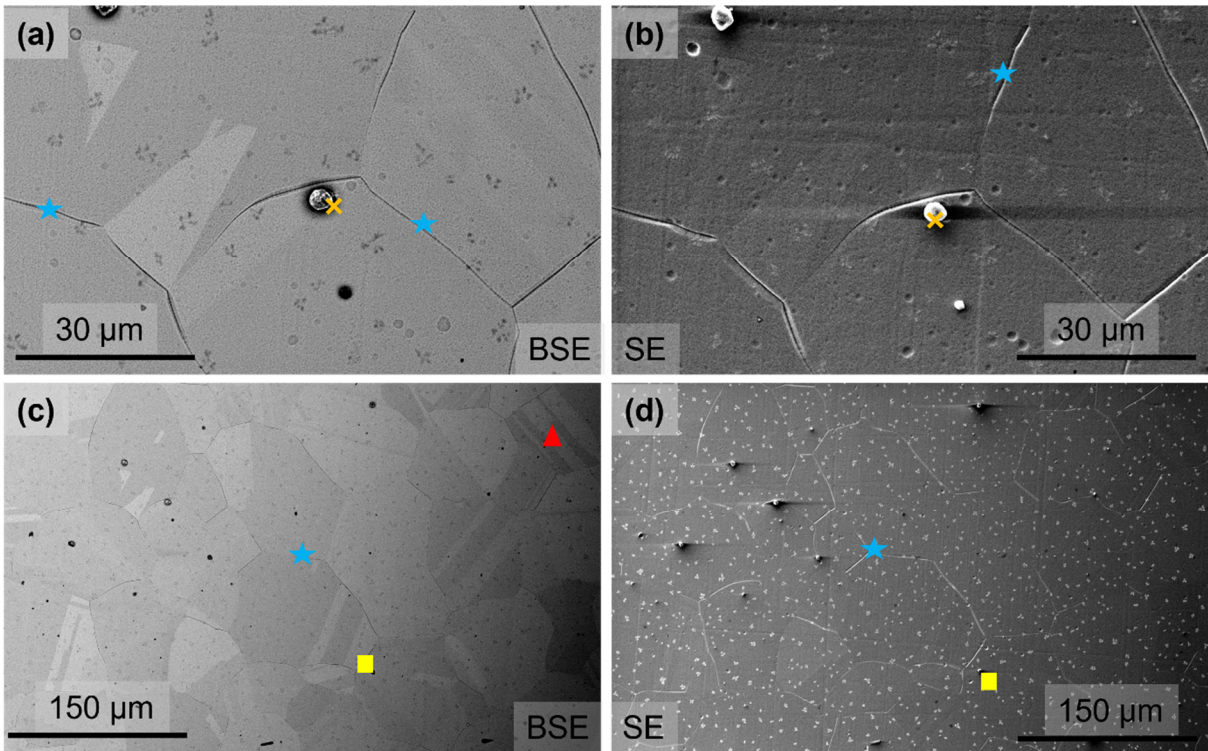


Figure 7.18. SEM images at different magnification of CrCoNi as a result of its corrosion in 0.1 M NaCl. (a) and (b) show the intergranular corrosion (blue star) at a higher magnification in BSE and SE modes, respectively. (c) and (d) show the extend of the intergranular corrosion on a larger CrCoNi surface area in BSE and SE modes, respectively, with some residual electrolyte dried on the surface (orange cross). Inclusions remain intact (yellow square) after corrosion. The diagrams in (b) and (d) are adapted with permission from own publication^[185] published by Elsevier B.V. under the terms of the CC BY 4.0 license. Copyright 2022, The Authors.

The corrosion behavior of the MPEAs in 0.1 M NaCl comprises different passivation and corrosion mechanisms for the two alloys. While CrMnFeCoNi passivates mainly through the formation of a passive film enriched in Cr-, Fe- and Co-oxides, Mn preferentially dissolves and EIS data suggest a heterogeneous passive film. These results are confirmed when looking at the main corrosion mechanism of pitting corrosion on CrMnFeCoNi. The five-component MPEA compares well to AISI 304. In contrast, CrCoNi forms passive films enriched in Cr-

oxides which protect the alloy from further corrosion as can be derived from EIS measurements. The non-ideal capacitor behavior of CrCoNi may be a result of the intergranular corrosion. SKPFM maps show, however, that CrCoNi is capable of re-passivating these corrosion sites which ultimately underlines its superiority in corrosion resistance compared to CrMnFeCoNi and AISI 304.

7.2 Behavior in H₂SO₄ Solution

H₂SO₄ is another commonly employed electrolyte in corrosion studies. Considering that industrial processes related to coal combustion emit SO₃,^[288] H₂SO₄ can form in the environment and lead to corrosive deterioration of materials.^[289] Generally H₂SO₄ is a key product and reactant in the chemical industry playing a vital role in the manufacture of inorganic and organic compounds.^[252] Furthermore, it is utilized in batteries and it finds applications as an electrolyte in acidic OER catalysis.^[290] Hence, the investigation of corrosion resistance toward H₂SO₄ is of vital importance to render the use of a material safe and also economically feasible. Examples of MPEA corrosion studies in H₂SO₄ electrolytes have been given in Chapter 4.5. In the following, the corrosion resistance of CrMnFeCoNi and CrCoNi will be investigated in 0.1 M H₂SO₄.

7.2.1 General Electrochemical Behavior

This chapter will investigate the electrochemical behavior and corrosion properties for the MPEAs in 0.1 M H₂SO₄ in comparison to AISI 304 as a point of reference. In the acid electrolyte, the primary corrosion reaction will be:



In contrast to NaCl, AISI 304 does not passivate spontaneously in H₂SO₄ as depicted in the CPP in Figure 7.19a. After $E_{\text{corr}} = -0.40$ V, the increase in current density before dropping indicates active metal dissolution whereas the resulting peak in current density coincides with the primary passivation potentials E_{pp} which resides at -0.27 V. Its $j_{\text{corr}} = 3.07 \times 10^{-5}$ A cm⁻² is two orders of magnitude higher than in NaCl, which corroborates with the active metal dissolution following E_{corr} . Within the subsequent passive region that extends over $\Delta E = 1.06$ V, the current density responses are not completely constant but slightly decrease and rise, reaching the lowest value at $E = 0.36$ V. Furthermore, a secondary passivation is observed from 0.96 V to 1.36 V. Secondary passivation is the result of the interaction of Ni, Fe and Cr in the passive film formation.^[286] The scan was reversed upon reaching the apex potential of 2.00 V vs. OCP. This is in contrast to the CPP measurement in NaCl, where for all alloys the scans were reversed upon reaching the current density threshold of $j = 5$ mA cm⁻². The negative hysteresis upon scan reversal indicates good re-passivation characteristics whereas the point

of the reversed and forward scan cross-over is at $E_{cr} = 0.27$ V which, however, does not indicate re-passivation as discussed for CrCoNi in 0.1 M NaCl. The CPP suggests the general corrosion of AISI 304. Looking at the Tafel region in Figure 7.19b the electrochemical reactions at E_{corr} are predominantly under cathodic activation control as $\beta_c > \beta_a$.

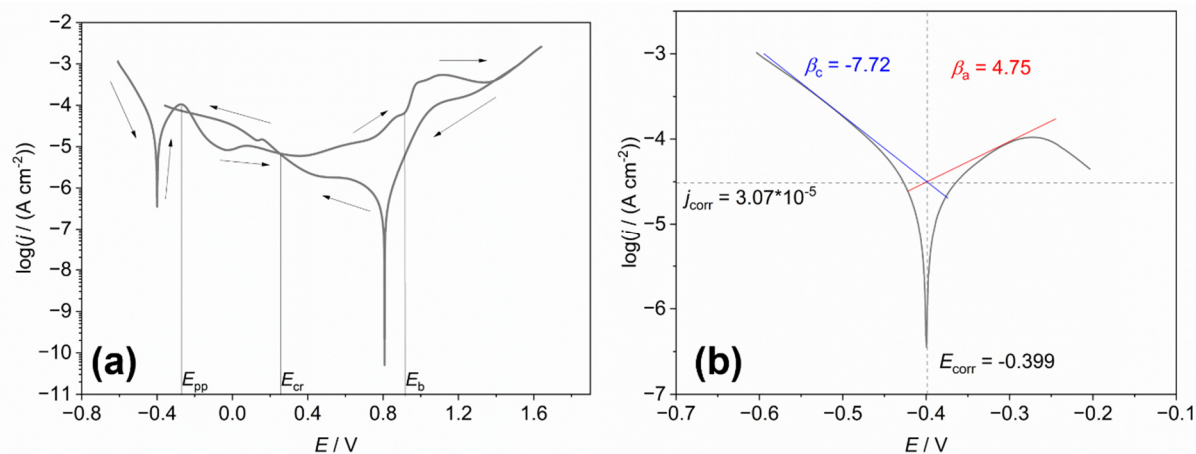


Figure 7.19. (a) CPP scan of AISI 304 in 0.1 M H_2SO_4 at 1 mV s^{-1} vs. Ag/AgCl/3M NaCl. (b) The respective Tafel region of the CPP scan in (a) with cathodic (blue) and anodic fits (red). The diagram in (a) is adapted with permission from own publication^[185] published by Elsevier B.V. under the terms of the CC BY 4.0 license. Copyright 2022, The Authors.

In Figure 7.20a, CrMnFeCoNi exhibits the most pronounced current density peak at $E_{pp} = 0.19$ V, suggesting active metal dissolution upon potential increase from E_{corr} onward. The high Mn content in the bulk alloy may be the cause of the extensive increase in j at E_{pp} . Wang et al.^[263] have demonstrated that the addition of Mn to CrFeCoNi increased the current densities at the E_{pp} . Through Tafel extrapolation as depicted in Figure 7.20b, $j_{corr} = 6.01 \times 10^{-5} \text{ A cm}^{-2}$ and $E_{corr} = -0.38$ V were determined. In correlation to the observed active metal dissolution, j_{corr} is an order of magnitude higher than for the corrosion tested in NaCl. Nevertheless, its passive region also ranges over $\Delta E = 1.06$ V as observed for AISI 304. In contrast to AISI 304, no secondary passivation was observed for CrMnFeCoNi. In further comparison to AISI 304, however, CrMnFeCoNi demonstrates better re-passivation characteristics upon scan reversal after reaching the apex potential of 1.5 V vs. OCP. Its j values on the reversed scan remain below the forward scan values until the scans cross close to j_{corr} . Another observation that differentiates the electrochemical behavior of CrMnFeCoNi from AISI 304 and CrCoNi are the multiple j peaks in the reversal scan. Typically, these peaks are analyzed as anodic/cathodic transitions, which in this case would mean an anodic to cathodic, cathodic to anodic and anodic to cathodic transition.^[259] While these peaks appear reproducibly, the investigations within this work could not clarify the mechanism behind their occurrence. In contrast to AISI 304, the Tafel region in Figure 7.20b suggests that the predominant electrochemical reactions at E_{corr} are under anodic activation control as $\beta_a > \beta_c$ which entails metal dissolution as shown in reaction 7.1. This result corroborates with the high j at E_{pp} .

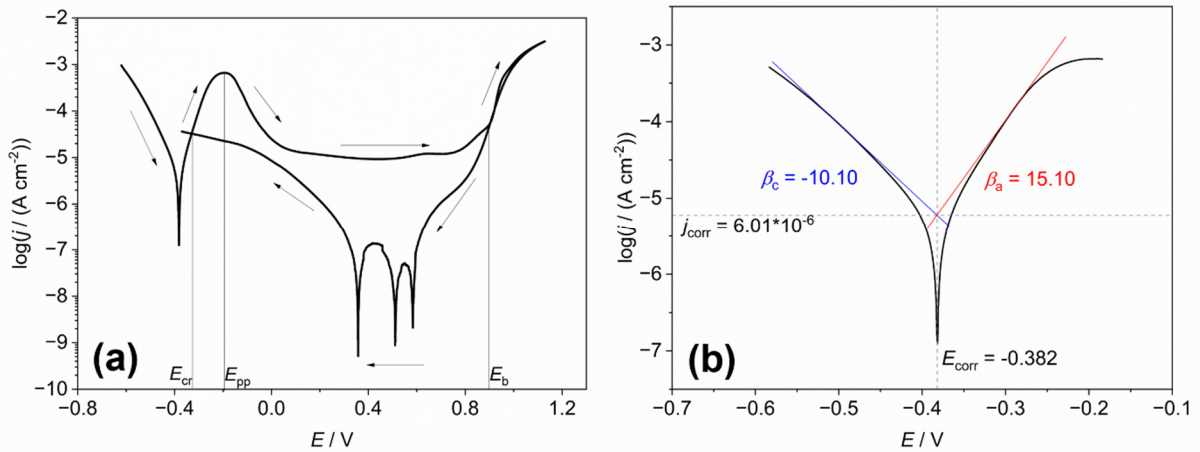


Figure 7.20. (a) CPP scan of CrMnFeCoNi in 0.1 M H₂SO₄ at 1 mV s⁻¹; potentials given vs. Ag/AgCl/3M NaCl. (b) The respective Tafel region of the CPP scan in (a) with cathodic (blue) and anodic fits (red). The diagram in (a) is adapted with permission from own publication^[185] published by Elsevier B.V. under the terms of the CC BY 4.0 license. Copyright 2022, The Authors.

The CPP for CrCoNi shows the lowest extent of active metal dissolution in Figure 7.21a. While the current density increases after $E_{\text{corr}} = -0.30$ V for CrCoNi, the current density at E_{pp} reaches a maximum of $j_{\text{pp}} = 2.06 \times 10^{-5}$ A cm⁻². AISI 304 and CrMnFeCoNi reached maximum current densities of j_{pp} (AISI 304) = 1.62×10^{-4} A cm⁻² and j_{pp} (CrMnFeCoNi) = 6.50×10^{-4} A cm⁻². In comparison, CrCoNi passivates faster than the other two alloys. Furthermore, its passive region ranges over $\Delta E = 1.10$ V, within which j initially decreases from -0.22 V to 0.20 V. At more positive potentials, it remains constant until $E_b = 0.88$ V. As with the other alloys, CrCoNi shows a negative hysteresis upon scan reversal at the apex potential of 1.5 V vs. OCP and the current density in the reverse scan remains below the forward scan, indicating excellent re-passivation characteristics. A cross-over of forward and reversed scan occurs at $E_{\text{cr}} = -0.28$ V. Similar to AISI 304, the Tafel region in Figure 7.21b suggests that the electrochemical reactions at E_{corr} are predominantly under cathodic activation control as $\beta_c > \beta_a$.

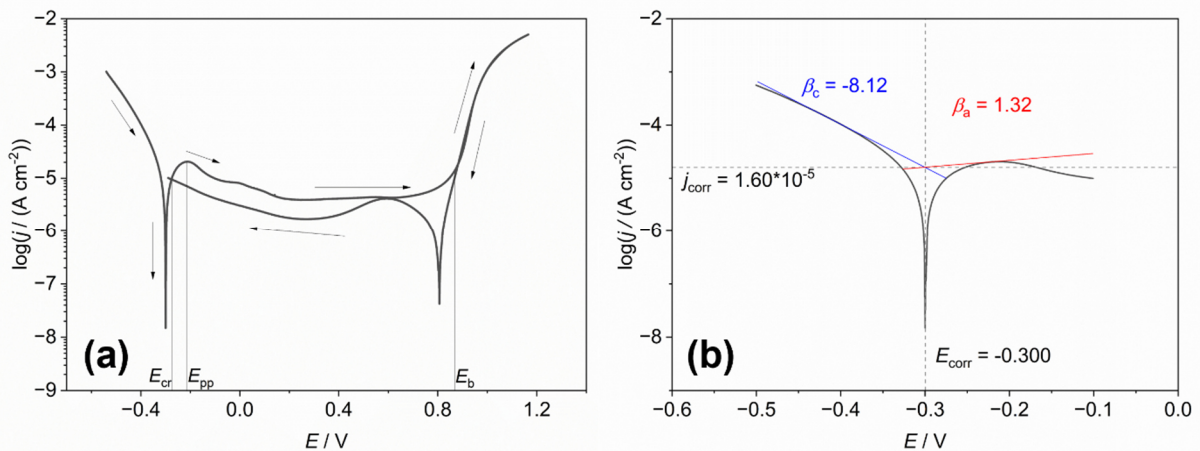


Figure 7.21. (a) CPP scan of CrCoNi in 0.1 M H₂SO₄ at 1 mV s⁻¹; potentials given vs. Ag/AgCl/3M NaCl. (b) The respective Tafel region of the CPP scan in (a) with cathodic (blue) and anodic fits (red). The diagram in (a) is adapted with permission from own publication^[185] published by Elsevier B.V. under the terms of the CC BY 4.0 license. Copyright 2022, The Authors.

Table 7.6 below summarizes the average electrochemical data with the respective standard deviations obtained through CPP analysis. Typically, at least three measurements were conducted to ensure reproducibility. Nevertheless, as was described in Chapter 7.1.1, fluctuations may still occur. Looking at the data, it becomes apparent that CrCoNi also exhibits superior corrosion resistance in 0.1 M H₂SO₄ over CrMnFeCoNi and the conventional alloy AISI 304 which is predominantly supported by the low j at E_{pp} , largest passive region and most stable current density on the reversal scan. To further understand this superiority in corrosion resistance, analyses of the passive film were conducted according to an analogous scheme used in 0.1M NaCl.

Table 7.6. Summary of the average electrochemical parameters with their standard deviations determined through the CPP measurements of the three alloys in 0.1 M H₂SO₄.

	AISI 304	CrMnFeCoNi	CrCoNi
E_{corr} / V	-0.30 ± 0.26	-0.37 ± 0.02	-0.29 ± 0.01
$j_{corr} / A\ cm^{-2}$	$(2.09 \pm 1.70) \times 10^{-5}$	$(5.54 \pm 0.63) \times 10^{-6}$	$(1.65 \pm 0.06) \times 10^{-5}$
β_c	-6.03 ± 3.32	-9.63 ± 1.50	-8.00 ± 0.11
β_a	5.58 ± 1.58	16.26 ± 1.01	2.51 ± 1.03
$\Delta E / V$	1.06 ± 0.23	1.06 ± 0.05	1.10 ± 0.01
E_{cr} / V	0.27 ± 0.03	-0.32 ± 0.01	-0.28 ± 0.0
E_b / V	0.91 ± 0.01	0.88 ± 0.03	0.88 ± 0.0
E_{pp} / V	-0.27 ± 0.0	-0.19 ± 0.02	-0.22 ± 0.01

7.2.2 Passive Film Characteristics

As describe in Chapter 7.1.2, XPS analyses was used to analyze the passive film compositions. Instead of the typical 2p spectra, 3p spectra were recorded and evaluated to overcome problems such as overlap of photoemission and Auger peaks, multiplet splitting and asymmetric peaks that arise for 2p core electron peaks of first row transition metals. The spectra of the native surfaces are presented in Figure 7.5 in Chapter 7.1.2 for comparison. The alloys were also anodically passivated in 0.1 M H₂SO₄ at 0.15 V, 0.25 V and 0.40 V for AISI 304, CrMnFeCoNi and CrCoNi, respectively.

Figure 7.22 depicts the 3p core level spectra for all three alloys. The intensities measured after the anodic passivation in H₂SO₄ are similar to the native surfaces for all three alloys, while the oxide signals increase. Figure 7.5 summarizes the 3p spectra for the native alloy surfaces. The resulting spectra for the passive films formed in 0.1 M H₂SO₄ are in good agreement with the findings by Marcus et al.^[69] In analogy to the fitting of the passivated

surface in 0.1 M NaCl, the Cr 3p signal was fitted with 2 components, Cr_{ox} ($E_B = 43.5$ eV) and Cr_{met} ($E_B = 41.3$ eV). The Mn 3p peaks of metallic and oxide components are situated at $E_B = 46.5$ eV and 48.0 eV. As with native surface of CrMnFeCoNi and AISI 304, both needed to be fitted by two oxide peaks for Fe²⁺ ($E_B = 53.3$ eV) and Fe³⁺ ($E_B = 55.3$ eV), respectively, apart from the Fe_{met} peak ($E_B = 52.1$ eV). Reasoning for this approach is given in Chapter 7.1.2. Finally, the Co 3p peak is also composed of a metallic and oxide component at $E_B = 58.5$ eV and 59.8 eV, respectively. While all elements form their respective oxides, Ni is assumed to remain metallic and enriched in a modified metallic layer beneath the passive oxide film. Its 3p core level peaks correspond to Ni 3p_{3/2} ($E_B = 66.0$ eV) and Ni 3p_{1/2} ($E_B = 68.0$ eV).

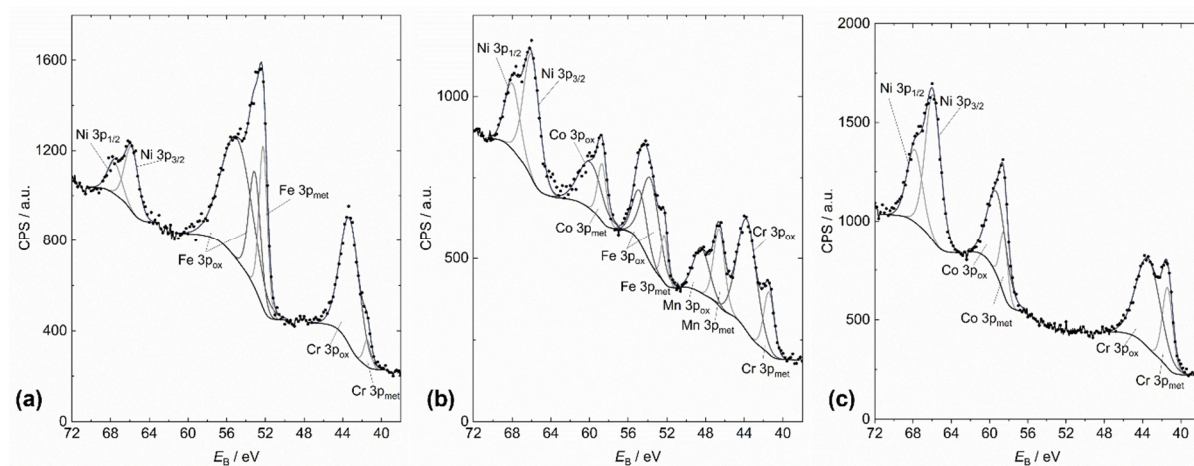


Figure 7.22. XPS 3p survey spectra of (a) AISI 304, (b) CrMnFeCoNi and (c) CrCoNi after anodic passivation in 0.1 M H₂SO₄. The metallic peaks are indicated by the labels and the corresponding the light grey lines and the oxide peaks by the dark grey lines. Adapted with permission from own publication^[185] published by Elsevier B.V. under the terms of the CC BY 4.0 license. Copyright 2022, The Authors.

As with the spectra presented in Chapter 7.1.2, fitting of the 3p survey spectra allowed the extraction of the relative proportions in atomic percent of the oxide and metal contribution toward the surface composition. For comparison, Figure 7.4 presents the surface compositions of the native alloy surfaces. Compared to the native surface, the surface composition of CrCoNi is higher in Cr- and Co-oxide, where the oxide percentage increased by 9.0% after passivation. This may be due to the higher Co-oxide ratio, which previously decreased for CrCoNi when passivated in 0.1 M NaCl. The overall oxide to metal ratio for CrCoNi after passivation in H₂SO₄ surmounts to 1.4:1. CrMnFeCoNi also experiences a higher increase in oxide components of 6.0% on its surface after anodic passivation in H₂SO₄ compared to NaCl. While its fraction of Cr-oxide is lower than after passivation in NaCl, the fraction in Fe-oxide increased. This also leads to a higher oxide to metal ratio of 1.70:1. While AISI 304 still presents the highest oxide-to-metal composition ratio (3.8:1), it is lower than after anodic passivation of AISI 304 in NaCl.

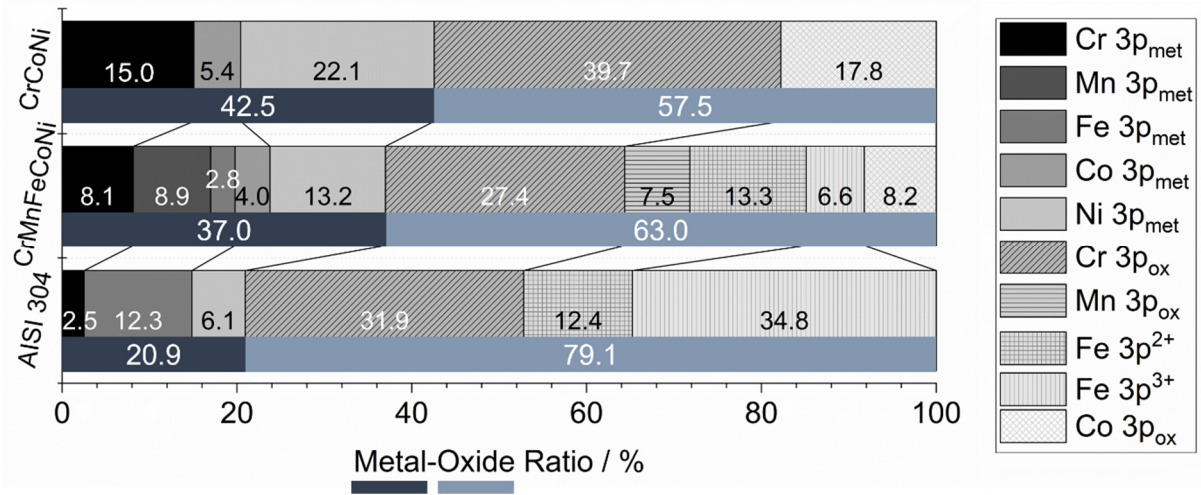


Figure 7.23. Surface compositions of the 3 alloys after anodic passivation in 0.1 M H₂SO₄ with the respective mole fractions of metallic and oxide species. The metal to oxide ratio is highlighted by the dark and light blue bars, respectively. Adapted with permission from own publication^[185] published by Elsevier B.V. under the terms of the CC BY 4.0 license. Copyright 2022, The Authors.

Further investigations of the XPS spectra showed, that after anodic passivation in 0.1 M H₂SO₄, S 2p peaks for metal sulfates were detected at $E_B = 168.9$ eV. Figure 7.24 shows the respective S 2p_{3/2} and S 2p_{1/2} spectra. This finding suggests that SO₄²⁻ may contribute toward the passivation of the metals and it should be considered that it may contribute toward the oxide components. In fact, it is generally accepted that porous films due to anodic polarization in H₂SO₄, incorporate SO₄²⁻ within their bulk structure.^[291] This further indicates that analyzing the O 1s alone, cannot reveal all relevant details about the surface composition of passive films obtained in SO₄²⁻ containing electrolyte solutions.

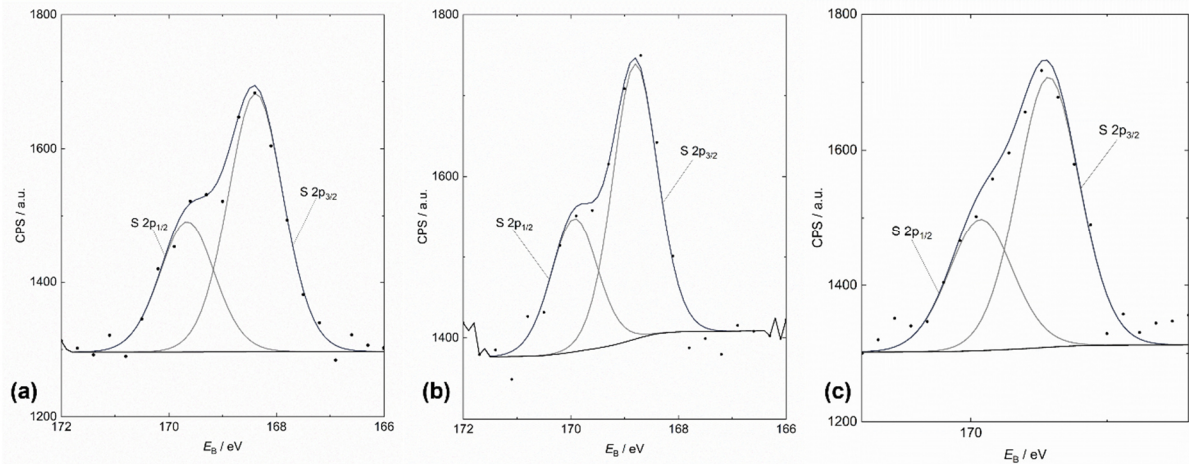


Figure 7.24. S 2p XPS spectra of (a) AISI 304, (b) CrMnFeCoNi and (c) CrCoNi after anodic passivation in 0.1 M H₂SO₄. Adapted with permission from own publication^[185] published by Elsevier B.V. under the terms of the CC BY 4.0 license. Copyright 2022, The Authors.

The amount of oxide species is higher than that of the metallic components after corrosion. This trend is slightly stronger after passivation in H₂SO₄ compared to passivation in 0.1 M NaCl. This suggests either a thicker or denser passive layer. Again, assuming a continuous and homogeneous oxide layer on the alloys after passivation, passive layer

thicknesses were calculated by using Equations (7.3) to (7.5) (Chapter 7.1.2). The resulting thicknesses are outlined in Table 7.7. Interestingly, the passive layer thickness for CrMnFeCoNi is nearly identical to that after passivation in NaCl. Since, CrMnFeCoNi showed poorer corrosion resistance within NaCl electrolyte, a denser passive film may have formed during passivation in H₂SO₄. On the other hand, CrCoNi reveals a thinner passive film after the anodic treatment in H₂SO₄. However, the alloy has demonstrated comparable corrosion resistance in both electrolytes based on the electrochemical data from CPP, suggesting that a denser passive layer may have been formed.

Table 7.7. Surface layer thicknesses of CrMnFeCoNi and CrCoNi determined through XPS for the native state and after anodic passivation in 0.1 M H₂SO₄.

	CrCoNi	CrMnFeCoNi
	nm	nm
Blank	2.46	2.81
H₂SO₄^{Pass}	3.22	3.69

Compared to the ultra-high vacuum XPS measurements, EIS is conducted on the alloy surfaces while they are still in contact with the corrosive medium. As in Chapter 7.1.2, the alloy surfaces were first left to stabilize at OCP for 30 min in 0.1 M H₂SO₄, in to order to record the impedance of the “native” state in the acidic electrolyte. For the passivated surfaces, the EIS were recorded after 30 min of anodic passivation. Figure 7.25 shows the respective EIS spectra. First comparing the initial EIS after OCP in H₂SO₄ in Figure 7.25a with that of NaCl in Figure 7.9a, discloses poorer passivation in H₂SO₄ in the form of a lower $Z(0.1 \text{ Hz})$ and a higher minimum phase angle of $\phi = -65^\circ$ for CrMnFeCoNi and AISI. CrCoNi reaches a minimum phase angle of $\phi = -80^\circ$ and similar impedance $Z(0.1 \text{ Hz}) = 27300 \Omega \text{ cm}^2$ as obtained in Figure 7.9a after OCP in 0.1 M NaCl. For CrMnFeCoNi and AISI 304, the low phase angle and low impedance correlate with the observation of active metal dissolution positive of E_{corr} . This applies especially to CrMnFeCoNi, as the Tafel extrapolation showed that the electrochemical corrosion reactions at E_{corr} are under anodic activation control.

Upon the anodic passivation, the solution resistance at high frequencies remains constant for all alloys as shown Figure 7.25b. Moreover, $Z(0.1 \text{ Hz})$ increases and the phase angles decrease also for all alloys upon passivation. Overall, CrMnFeCoNi displays the poorest passivation behavior based on the EIS spectra. While its phase angle reaches $\phi = -70^\circ$ and slightly broadens, it suggests that even though the capacitor-like behavior increased upon passivation, a less protective passive film has formed than in NaCl. AISI 304 shows a similar passivation behavior to CrMnFeCoNi. Despite its impedance increasing at low frequency by

one order of magnitude, its phase angle only reaches $\phi = -75^\circ$, representing poor capacitor-like behaviour and with that a more defective passive film. In analogy to its corrosion resistance in 0.1 M NaCl, CrCoNi displays a phase angle of $\phi = -83^\circ$ and its impedance at low frequency doubled in magnitude. These results again confirm the superior corrosion resistance of CrCoNi compared to CrMnFeCoNi and AISI 304 in 0.1 H₂SO₄.

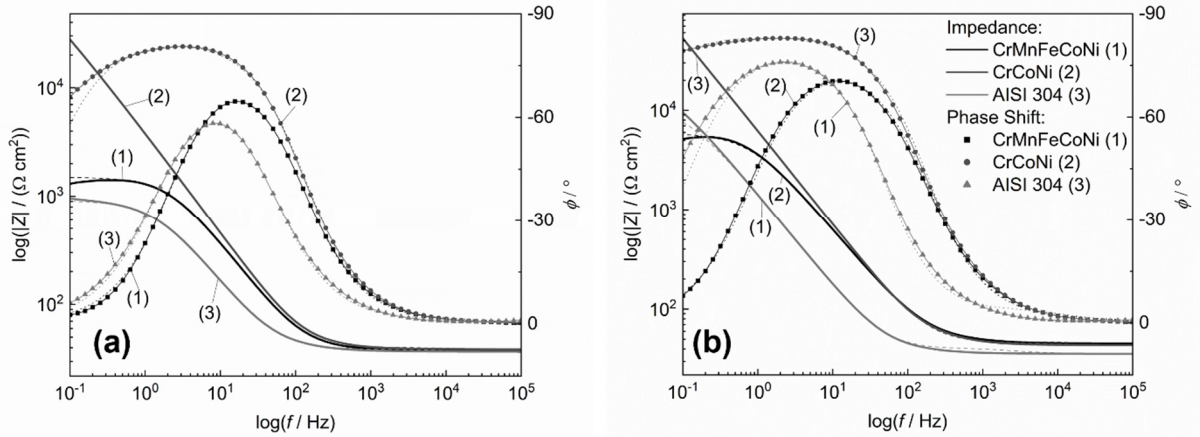


Figure 7.25. EIS Bode diagrams of the three alloy after (a) OCP and (b) anodic passivation in 0.1 M H₂SO₄ recorded at DC voltage of 0 V vs. OCP and an AC voltage of 10 mV. Adapted with permission from own publication¹⁸⁵ published by Elsevier B.V. under the terms of the CC BY 4.0 license. Copyright 2022, The Authors.

To obtain the respective electrochemical impedance parameters, the spectra in Figure 7.25 were fitted with the EEC in Figure 5.2c. The data can be found in Table 7.8. In analogy to the determination of the oxide layer thickness through the passive film capacitance (Equation (7.6)), the CPE_f element for the passive films was first converted into capacitance C_f through Equation (7.7) which takes into account the non-ideal nature of the passive capacitance. In correlation to the XPS-derived passive layer thicknesses, CrCoNi revealed a slightly thinner film than CrMnFeCoNi after passivation in H₂SO₄ as outlined in Table 7.9. Nevertheless, the impedance spectra clearly indicate a more defective film on CrMnFeCoNi, indicating that passive layer thickness alone cannot rationalize corrosion resistance.

Table 7.8. EIS data of (1) CrCoNi and (2) CrMnFeCoNi after OCP and anodic passivation in 0.1 M H₂SO₄ where m and n are the exponents of CPE_f and CPE_{dl} , respectively

OCP								
	R_s	R_{ct}	R_f	R_p	CPE_{dl}	n	CPE_f	m
	[$\Omega \text{ cm}^2$]	[$\Omega \text{ cm}^2$]	[$\Omega \text{ cm}^2$]	[$\Omega \text{ cm}^2$]	[$\text{S s}^n \text{ cm}^{-2}$]		[$\text{S s}^m \text{ cm}^{-2}$]	
(1)	38.67	6.38×10^4	2.53	6.39×10^4	3.09×10^{-5}	0.94	1.72×10^{-5}	0.90
(2)	37.18	1.47×10^3	2.12	1.51×10^3	4.42×10^{-5}	0.91	1.71×10^{-5}	0.92
Anodic Passivation								
(1)	43.74	5.49×10^5	5.00	5.49×10^5	1.87×10^{-5}	0.94	1.05×10^{-5}	0.92
(2)	44.97	5.91×10^3	3.33	5.96×10^3	2.50×10^{-5}	0.90	1.51×10^{-5}	0.86

Table 7.9. Summary of capacitances and oxide layer thicknesses of CrMnFeCoNi and CrCoNi in 0.1 M H₂SO₄ determined by EIS.

	C_f	d_{oxide}
OCP	[F cm ⁻²]	[nm]
Cantor	1.21 x 10 ⁻⁵	2.19
CrCoNi	1.30 x 10 ⁻⁵	2.05
Pass		
Cantor	8.45 x 10 ⁻⁶	3.14
CrCoNi	8.69 x 10 ⁻⁶	3.06

7.2.3 Corrosion mechanism

While XPS and EIS are valid methods to evaluate passive layer composition, properties and thickness, the results show that caution should be practiced in the interpretation. From the electrochemical results (CPP and EIS), it becomes evident that CrCoNi is the more corrosion resistant MPEA. However, the passive layer thicknesses from XPS and EIS suggest thicker films on CrMnFeCoNi. Even though thicker passive films may suggest more protective films, this rationale does not consider defects in the passive layer. Hence, the analysis of dissolved metal concentrations and the resulting surface morphology were conducted to further support the interpretation of corrosion behavior of the investigated metal. The corrosion through CPP in NaCl revealed pitting and crevice corrosion for the CrMnFeCoNi and intergranular corrosion for CrCoNi. AISI 304 corrodes similarly to CrMnFeCoNi.

Table 7.10 outlines the metal ion concentrations in the H₂SO₄ electrolyte after CPP which were quantified through ICP-MS. In general, looking at the total metal ion concentrations, CrCoNi exhibits the lowest dissolution rate of metal ions with $c = 105.02 \mu\text{mol L}^{-1}$ which is comparable to the values found in NaCl. CrMnFeCoNi reveals the highest dissolved metal ion concentration after its CPP in H₂SO₄ with $c = 161.03 \mu\text{mol L}^{-1}$ while the dissolved metal concentration of AISI 304 lies in between the MPEAs with $c = 141.89 \mu\text{mol L}^{-1}$. This result correlates with the observed active metal dissolution at E_{pp} , which is highest for CrMnFeCoNi (see Figure 7.20a). To better compare the dissolved metal ions, Figure 7.26 displays the dissolution tendencies of the alloy components in mole fraction, while Table 7.10 provides the respective absolute concentrations. Figure 7.26 shows that CrCoNi dissolves largely uniformly, as the dissolved metal ion concentrations resemble the elemental composition of the respective alloy. Deviations from the equimolar bulk alloy concentrations are evident in the slightly higher and lower concentrations of Ni- and Co-ions. In comparison to the CrCoNi dissolution behavior in NaCl, the results are very similar. For CrMnFeCoNi, the dissolution

tendencies of the constituting elements are also comparable to the behavior in NaCl. The total amount of dissolved metal ions is more than two-fold higher after CPP in NaCl than H₂SO₄. Fe-ions are found at the lowest concentrations in H₂SO₄. The relative amount of Cr-ions is higher in H₂SO₄ than that of other metal ions. The dissolved relative amount of Cr increased for all three alloys in H₂SO₄ compared to NaCl, suggesting a correlation to the acidity of the electrolyte. Inspecting the Pourbaix diagram of Cr at 25°C (Figure 4.5) reveals that at a pH < 3.5,^[105] Cr dissolves as Cr³⁺, while at pH = 6.25 (pH of 0.1 M NaCl), Cr preferentially forms Cr₂O₃. While XPS shows that Cr-oxides have formed on the surface, the initial active metal dissolution observed in the CPP diagrams may be due to an increased dissolution of Cr.

Table 7.10. Concentrations of dissolved metals after CPP in 0.1 M H₂SO₄.

	Cr	Co	Ni	Fe	Mn	Total
	[$\mu\text{m L}^{-1}$]	[$\mu\text{m L}^{-1}$]	[$\mu\text{m L}^{-1}$]	[$\mu\text{m L}^{-1}$]	[$\mu\text{m L}^{-1}$]	[$\mu\text{m L}^{-1}$]
AISI 304	31.59 ± 1.63		12.94 ± 1.08	95.30 ± 8.77	2.06 ± 0.13	141.89
CrMnFeCoNi	34.93 ± 2.56	36.72 ± 1.47	37.53 ± 1.67	15.38 ± 5.59	36.46 ± 1.41	161.03
CrCoNi	35.97 ± 2.56	30.40 ± 6.38	38.75 ± 3.09			105.12

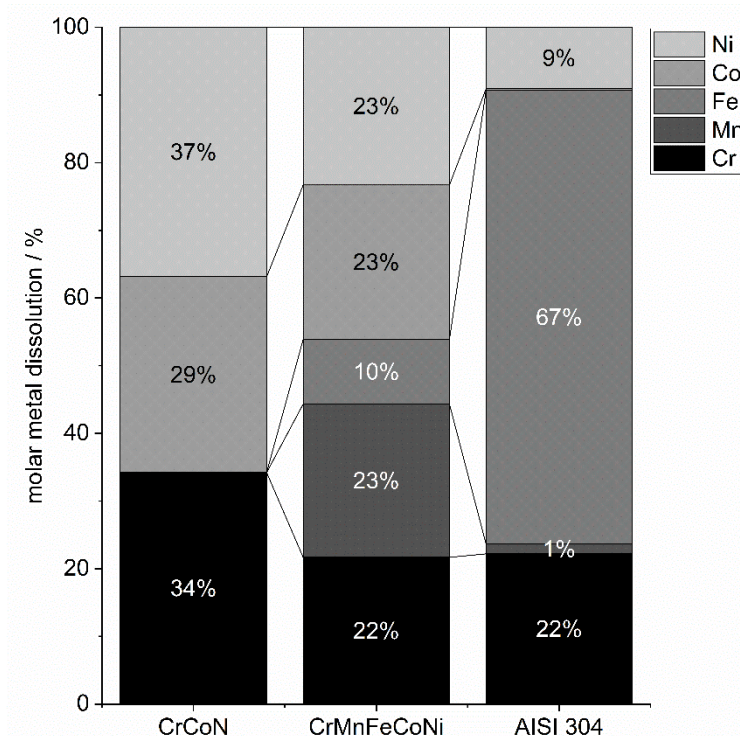


Figure 7.26. Metal distribution in the 0.1 M H₂SO₄ electrolyte after CPP based on the respective metal concentrations as presented in Table 7.10. Adapted with permission from own publication^[185] published by Elsevier B.V. under the terms of the CC BY 4.0 license. Copyright 2022, The Authors.

Examining the surface morphologies after CPP in H_2SO_4 confirms that a different corrosion mechanism than pitting occurs on the CrMnFeCoNi alloy. Figure 7.27 displays the AFM and SKFM maps of CrMnFeCoNi after its CPP in H_2SO_4 . The topographic image in Figure 7.27a shows some residual electrolyte that crystallized on the surface and a small cavity. The crystallized electrolyte salts can be better identified in the SKPFM map in Figure 7.27b. The small cavity in Figure 7.27 is not a pit, but the result of a dissolved inclusion. This becomes more evident when inspecting the respective SEM images in Figure 7.28a to d. Figure 7.28c and d serve to give a broader overview. They clearly show the dissolution of inclusions and further reveal some form of preferential dissolution around the inclusion sites. The SEM images in Figure 7.28a and b demonstrate that every inclusion experiences this form of corrosion. From Figure 7.28c and d it seems that smaller inclusions predominantly dissolve in combination with metal attack around the inclusion site. As the SKPFM image of the native surface in Figure 7.11 shows, there is a large potential difference between the inclusions and surrounding metal matrix. This can potentially lead to galvanic corrosion which would explain this preferential dissolution behavior.

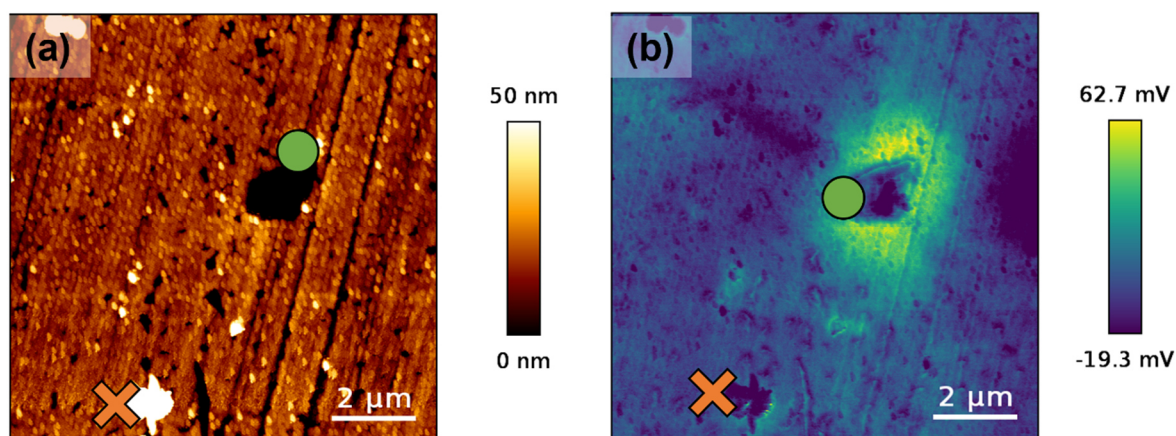


Figure 7.27. (a) AFM topography of a CrMnFeCoNi surface after CPP in 0.1 M H_2SO_4 and (b) SKPFM potential map of the same corroded CrMnFeCoNi surface with a corroded inclusion site (green circle) and residual electrolyte (orange cross). Adapted with permission from own publication^[185] published by Elsevier B.V. under the terms of the CC BY 4.0 license. Copyright 2022, The Authors.

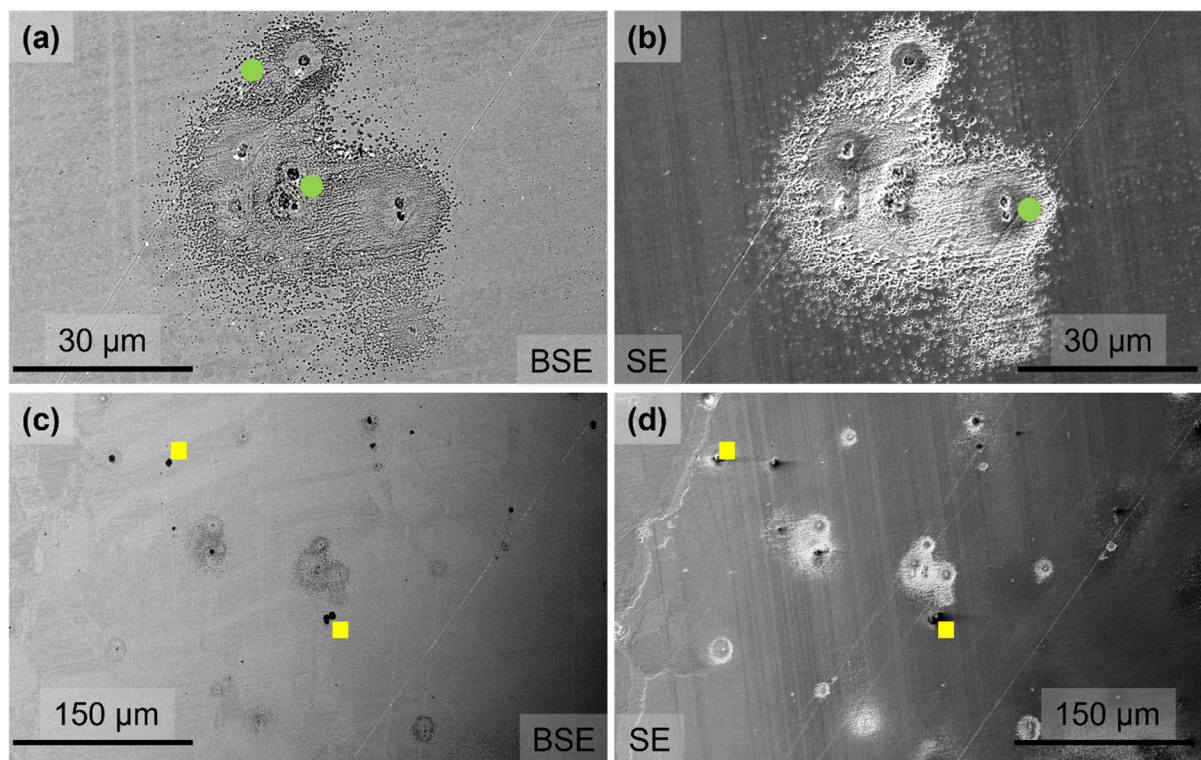


Figure 7.28. SEM images of different localized corrosion morphologies around inclusions on CrMnFeCoNi after CPP in 0.1 M H₂SO₄. (a) and (b) the corrosion of and around inclusions (green circle) in the BSE and SE mode (c) and (d) show the extend of this form of galvanic corrosion at a lower magnification in the BSE and SE mode revealing that some larger inclusions remain intact (yellow square). The diagrams in (b) and (d) are adapted with permission from own publication^[185] published by Elsevier B.V. under the terms of the CC BY 4.0 license. Copyright 2022, The Authors.

The minimal differences in oxide layer thicknesses, similar results in electrochemical behavior, especially, the oxide layer properties determined through EIS and the nearly identical dissolution tendencies suggest that the same corrosion mechanism observed in NaCl occurs on CrCoNi in H₂SO₄ as in NaCl. The AFM and SKPFM maps in Figure 7.29 confirm, that intergranular corrosion takes place on CrCoNi. The attacked grain boundaries are not as deep and wide in H₂SO₄ as in NaCl. This may potentially be due to SO₄²⁻ partaking in the passivation of the alloys. As with the SKPFM maps obtained after corrosion in NaCl, the potential maps in Figure 7.29b show higher signals within the grain boundaries indicating the accumulation of oxide at the grain boundaries. The increased surface potentials suggest re-passivation at those sites and support the observed high corrosion resistance. The SEM images in Figure 7.30a to d show the intergranular corrosion of CrCoNi at different magnifications. Both figures show smaller cracks on the grains, which are due to dried residual electrolyte that gets further dehydrated when introduced to the vacuum of the SEM and cracks.

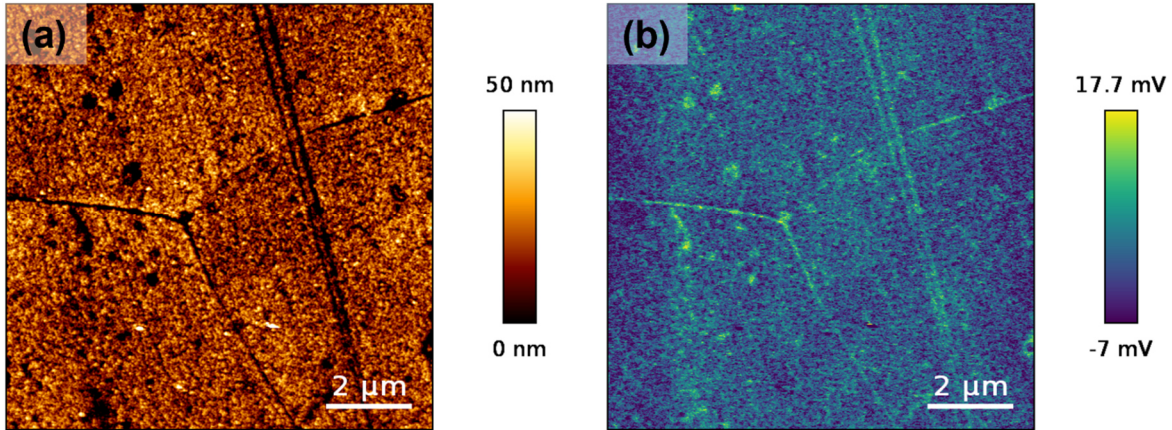


Figure 7.29. (a) AFM topography of a CrCoNi surface corroded in 0.1 M H_2SO_4 and (b) SKPFM potential map of the same corroded CrCoNi surface showing the corrosive attack at grain boundaries. Adapted with permission from own publication^[185] published by Elsevier B.V. under the terms of the CC BY 4.0 license. Copyright 2022, The Authors.

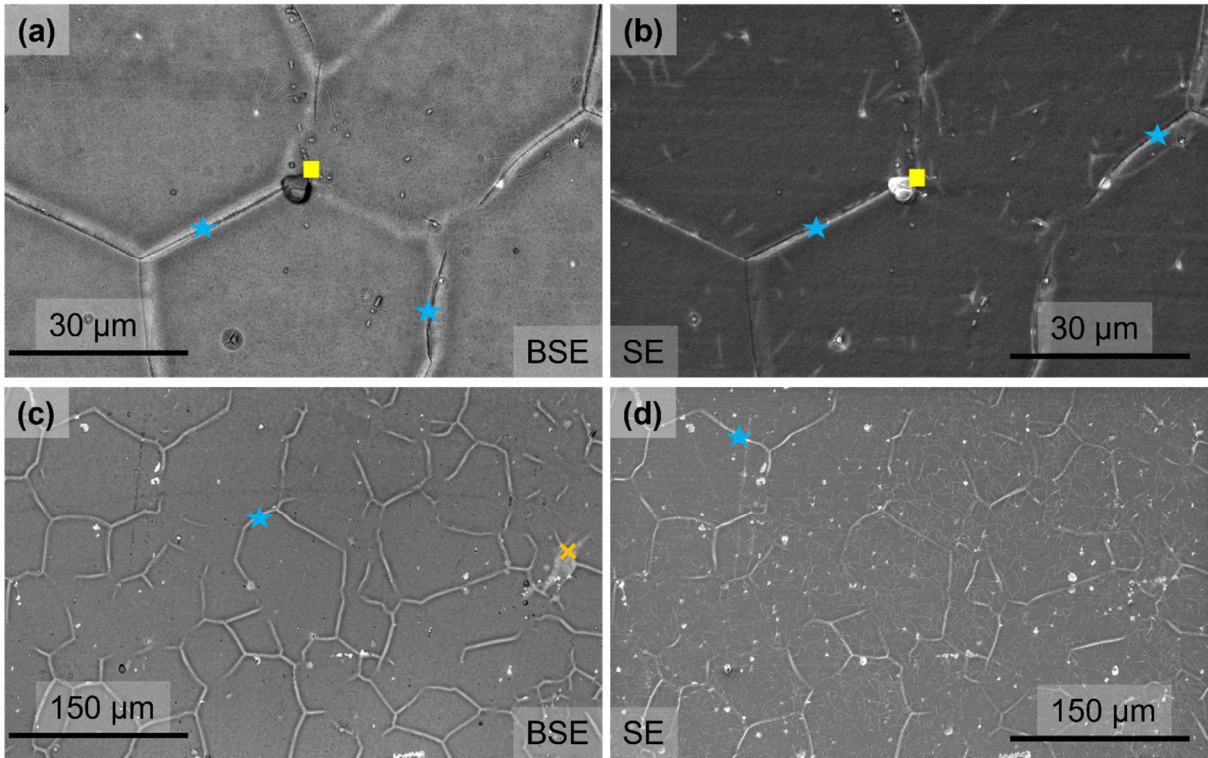


Figure 7.30. SEM images of different magnification of CrCoNi as a result of its corrosion in 0.1 M H_2SO_4 . (a) and (b) show the intergranular corrosion (blue star) at a higher magnification in the BSE and SE mode. (c) and (d) show the extent of the intergranular corrosion on a larger CrCoNi surface area in the BSE and SE mode. Some residual electrolyte dried on the surface (orange cross). Inclusions remain intact after corrosion (yellow square). The diagrams in (b) and (c) are adapted with permission from own publication^[185] published by Elsevier B.V. under the terms of the CC BY 4.0 license. Copyright 2022, The Authors.

The corrosion behavior of the MPEAs in 0.1 M H_2SO_4 also encompasses different passivation and corrosion mechanism for the two alloys. CrMnFeCoNi passivates mainly through the formation of a passive film enriched in Cr and Fe. While Mn preferentially dissolves during corrosion in NaCl, such a tendency is not observed in H_2SO_4 . Here, Mn, Co, and Ni predominantly dissolve compared to the other two metals in the same experiment. The EIS data of CrMnFeCoNi suggest the formation of a heterogeneous passive film in H_2SO_4 , despite

the determination of a thicker passive layer than for CrCoNi through XPS and EIS data. CrMnFeCoNi exhibits a better corrosion resistance in H₂SO₄ compared to NaCl, as evidenced by the lower metal ion concentrations and relatively intact surface morphologies after CPP. The predominant corrosion mechanism for CrMnFeCoNi discloses a form of galvanic corrosion of and around its inclusions. CrMnFeCoNi corrodes similarly to AISI 304 as it was also concluded from the tests in NaCl solutions.

In contrast, CrCoNi corrodes in a nearly identical manner in both studied electrolytes. Its passive films are enriched in Cr-oxides and Ni preferentially dissolves in NaCl and in H₂SO₄. Furthermore, the non-ideal capacitor behavior of the passive film on CrCoNi is likely the result of the intergranular corrosion which is also the main mode of corrosion in both media. The main difference between the electrolytes may lie in the presence of SO₄²⁻ in the passive layer which could enhance the corrosion resistance. The examinations in both electrolytes clearly show that CrCoNi exhibits the higher corrosion resistance of the two MPEAs.

7.3 Long-term Corrosion in 1 M H₂SO₄

Since both MPEAs, CrCoNi and CrMnFeCoNi exhibit excellent and good corrosion resistance, respectively, their long-term stability in 1 M H₂SO₄ was investigated. The long-term corrosion behavior of MPEAs was investigated by immersion tests in 1 M H₂SO₄ over 4 weeks. The corrosion process and progress were monitored by OCP, EIS and SEM measurements. The change in surface composition was qualitatively examined with XPS.

While typical corrosion studies investigate the electrochemical behavior of a metal or alloy through polarization and impedance tests as shown in Chapter 7.1 and 7.2, these are generally short termed, lasting from a few minutes to a few hours at most. Despite the possibility of extrapolation, such experiments cannot always be employed to evaluate a materials long-term performance. Nevertheless, long-term corrosion experiments remain relatively scarce in corrosion science research and are essentially non-existent for newer materials such as MPEAs.

Since the open circuit potential (OCP) or corrosion potential, is generally a good indicator of the materials corrosion resistance, it is the first parameter that was investigated for the MPEAs' long-term stability. Figure 7.31a and b show the respective OCP transients for CrMnFeCoNi and CrCoNi, respectively. For CrMnFeCoNi, the general trend shows a decrease in OCP over the time of immersion, indicating that the MPEA becomes less corrosion resistant.^[292] After 1 day of immersion, however, the OCP initially increases, indicating some form of passivation. Surpassing day 2, however, reveals an exponential decay in OCP, as indicated by the red line. After 21 days, this decay seems to remain relatively constant, suggesting that corrosion processes slow down over the time of immersion. The plot for CrCoNi in Figure 7.31b illustrates the opposite behavior. Up to day 7, the OCP increases rapidly. The

overall increase in OCP may be described by limited exponential growth of the passive layer as indicated by the red line in Figure 7.31b. In contrast to CrMnFeCoNi this indicates the formation of stable protective passive film on CrCoNi when exposed to 1 M H₂SO₄ over a period of 4 weeks.

Comparing the OCPs of the two MPEAs shows that CrMnFeCoNi exhibits marginally lower OCPs ranging from -312 mV within the first 2 days of immersion down to -388 mV in the fourth week, indicating a lower resistance towards corrosive deterioration in H₂SO₄. CrCoNi, on the other hand, exhibits OCPs in the range of 150 mV upon initial immersion up to 325 mV within the fourth week. As previous results in Chapter 7.2 showed, CrMnFeCoNi experiences the strongest active metal dissolution at E_{pp} of the CPP measurement and the respective Tafel region revealed that its corrosion reactions are limited by anodic activation polarization.

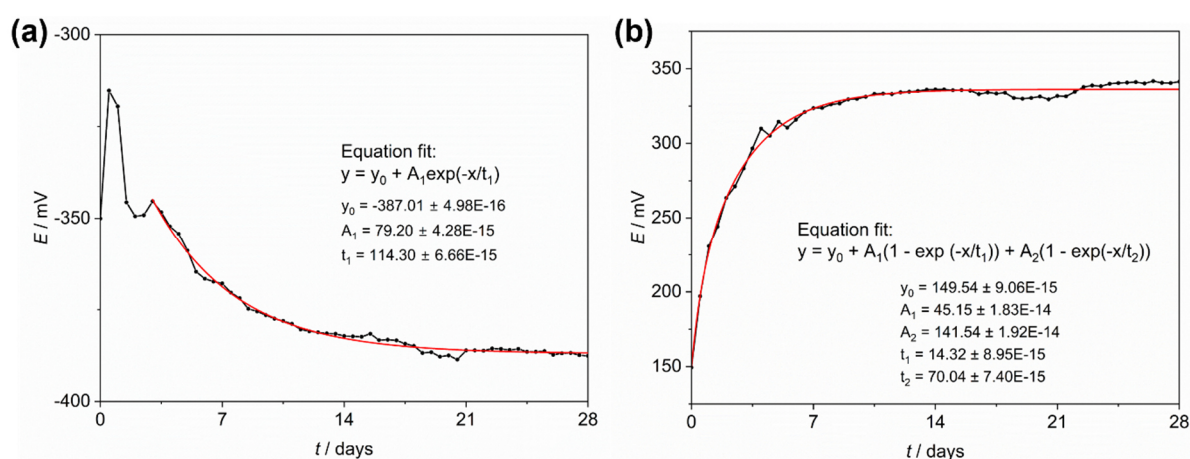


Figure 7.31. The OCP transients of (a) CrMnFeCoNi and (b) CrCoNi in 1 M H₂SO₄ over the immersion period of 28 days.

To investigate the passive film properties, impedance spectra were recorded in addition to the OCP every day. The data are presented in the form of maps that illustrate the change in impedance and phase shift of the scanned frequency range over the time of immersion. Figure 7.32 shows the impedance and phase shift maps of CrMnFeCoNi and the presented EIS-results coincide with the change in OCP outlined in Figure 7.31. The impedance at low frequency of CrMnFeCoNi initially increases until day 2 of immersion to 2 k Ω cm² which in turn coincides with the observed increase in OCP. The phase shift maximum concomitantly exhibits the highest phase shift after the same time of immersion, reaching $\phi = -76.2^\circ$. This non-ideality in capacitive behavior has already been observed in the analysis of the EIS spectra of CrMnFeCoNi in 0.1 M H₂SO₄ (see Figure 7.25). In contrast to the CrCoNi alloy (see below), no point of stabilization is recognizable neither in the impedance nor in the phases. The impedance and phase shift responses decrease in magnitude over the time of immersion over the low and mid frequency domain, indicating the severe deterioration of the MPEA in 1 M H₂SO₄. After 3 weeks of immersion, a sudden sharp drop in impedance and phase shift can

be observed in Figure 7.32. While the OCP remains constant after 3 weeks, the reason for this imminent decrease in impedance is unknown. The phase shift response reached $\phi = -50^\circ$ after 2.5 weeks indicating that the formed passive film does not exhibit a capacitor-like behavior. This is likely due to the continued dissolution of the surface. The EIS-results suggest that for CrMnFeCoNi no stable passive film protects the alloy against corrosion.

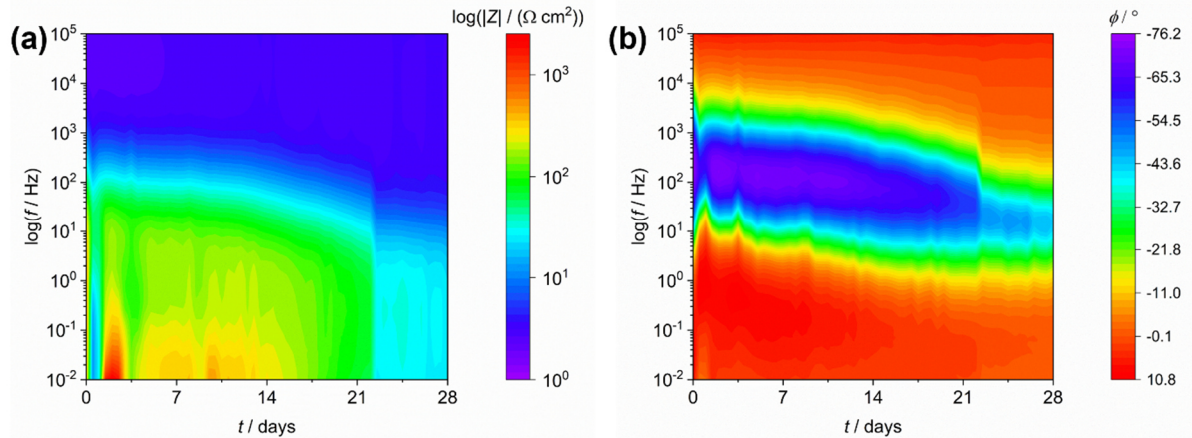


Figure 7.32. EIS data of immersion of CrMnFeCoNi in 1 M H₂SO₄ for 28 days represented as maps to display the change in (a) impedance and (b) phase shift with time over the applied frequencies.

Looking at Figure 7.33, the impedance and phase shift maps of CrCoNi in 1 M H₂SO₄ show a stable system that does not change over its time of immersion. It should be mentioned that initially during the first week, the impedance at low frequency stabilizes from 342 k Ω cm² to 530 k Ω cm². The phase shift maxima at medium frequency stabilizes from initially $\phi = -84^\circ$ to $\phi = -87.5^\circ$ after 3 weeks. Both results indicate the formation of a protective passive film with nearly perfect capacitor-like behavior. Apart from the first stabilization period, the impedance response for CrCoNi remains constant over the whole frequency range during the time of immersion, confirming a stable protective passive layer on the alloy surface that strengthens with prolonged immersion in 1 M H₂SO₄.

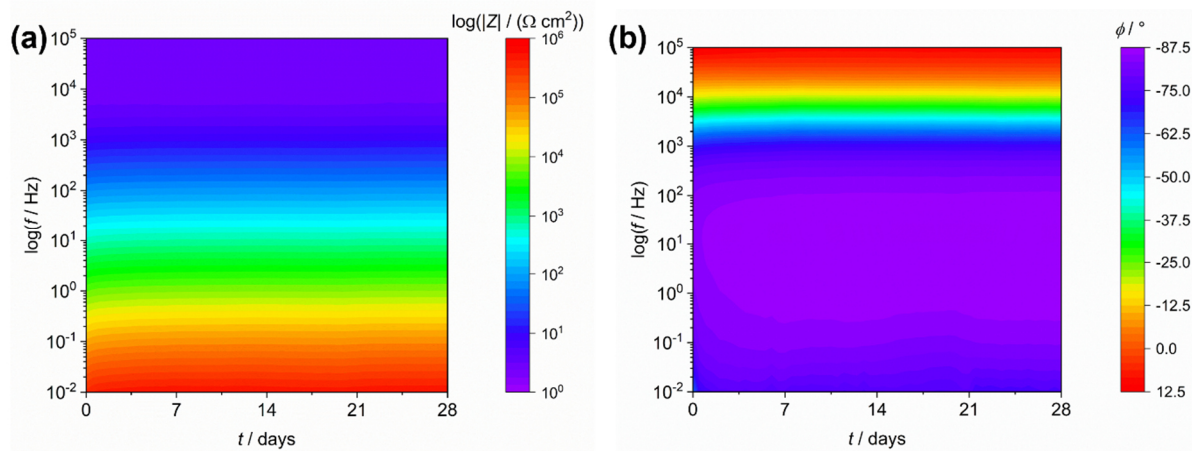


Figure 7.33. EIS data of immersion of CrCoNi in 1 M H₂SO₄ for 28 days displays the change in (a) impedance and (b) phase shift with time over the applied frequency range.

The bar graph plots in Figure 7.34a and b illustrate the relative mole fractions of dissolved metal ions for CrMnFeCoNi and CrCoNi in 1 M H₂SO₄. The results for CrMnFeCoNi show that Cr, Mn, Co, and Ni dissolve to a similar extent. In contrast to the ICP-MS analysis conducted for the 0.1 M H₂SO₄ electrolyte after CPP, Fe preferentially dissolves in this long-term immersion experiment. For CrCoNi, the analysis of dissolved metal species in 1 M H₂SO₄ rendered concentrations close to the limit of detection (LOD) of the instrument, which suggests a highly corrosion-resistant surface. Compared to the results of forced corrosion through CPP in 0.1 M H₂SO₄, Cr dissolves to a significantly lower extent under OCP conditions in 1 M H₂SO₄. As with the results of the CPP in 0.1 M H₂SO₄, Ni dissolves preferentially.

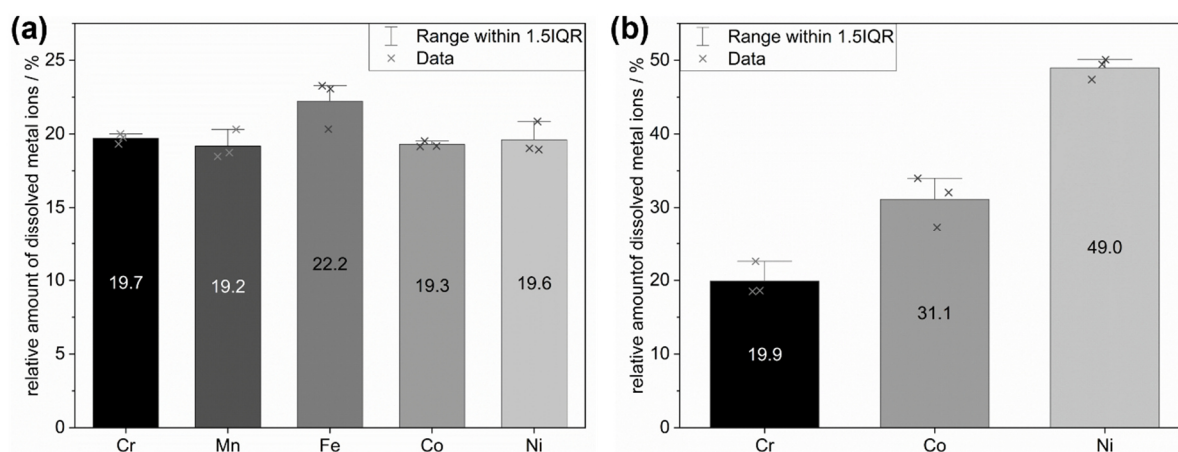


Figure 7.34. Relative amount of dissolved metal ions based on their concentrations in the 1 M H₂SO₄ electrolyte after 28 days of immersion for (a) CrMnFeCoNi and (b) CrCoNi.

As discussed in Chapter 7.1.2, the analysis of the 2p peak of first row transition metals is highly complicated and error-prone. Nevertheless, the 2p peak spectra of the individual metals offer qualitative information on the surface composition of the two MPEAs after the exposure to 1 M H₂SO₄.

Figure 7.35 displays the 2p spectra of CrMnFeCoNi at different stages of corrosion in 1 M H₂SO₄. The top row of spectra was obtained from the native surface composition. While a metal component may be clearly identifiable for all five metals, only the Cr and Ni spectra of the native surface seem viable for fitting. The 2p spectra of Mn, Fe and Co overlap among others with the Co LMM, Ni LMM and Fe LMM, respectively, rendering the fitting of these highly complicated. The middle row of the spectra in Figure 7.35 shows the data obtained after 1 week of corrosion. It becomes evident that a passive layer was formed that is mainly composed of metal oxides. The oxide formation on the surface seems to lead to a decrease in signal intensity, as identified from the signal-to-noise ratio. This trend continues for the third row in Figure 7.35 recorded after 4-weeks of immersion where the metal peaks completely disappear. While this suggests that a thick oxide layer must have formed on the CrMnFeCoNi surface, EIS results indicate a continually corroding alloy. Another reason for the decrease in signal intensity lies within the surface roughening as a result of corrosion which reduces the

average take-off angle of the photoelectron.^[293] This suggests that while a thick passive layer of oxides may have formed on the surface of the MPEA, it must be rough, porous and defective which leads to the observed continued corrosion and the decrease in photoelectron intensities with an increased immersion time.

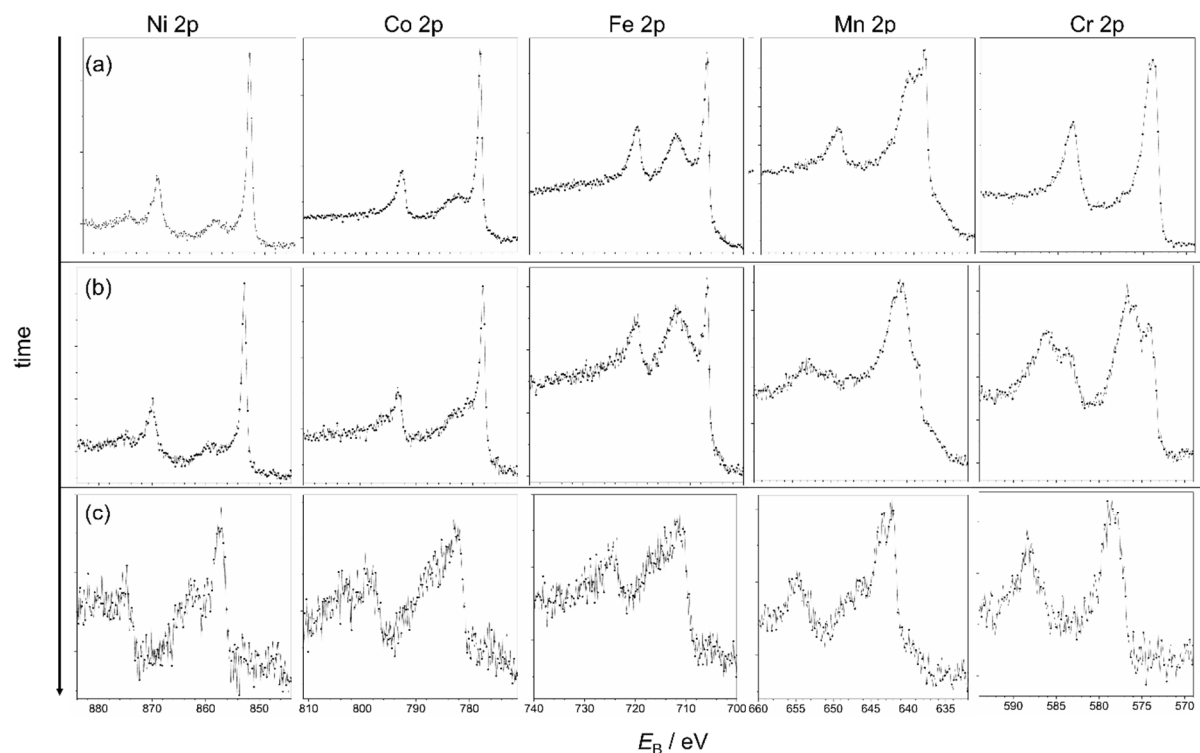


Figure 7.35. Change in 2p metal spectra of CrMnFeCoNi in (a) its native state, (b) after 1 week of immersion and (c) after 4 weeks of immersion in 1 M H_2SO_4 .

As with the XPS results obtained after the CPPs in 0.1 M H_2SO_4 in Chapter 7.2.2, sulfur could also be detected after corrosion in 1 M H_2SO_4 . The progressive increase in the S 2p signal intensity can be seen in Figure 7.36. The S 2p spectrum after 1 week could suggest the presence of metal sulfides and sulfates. However, the signal-to-noise ratio is quite low for a clear identification. Nevertheless, the spectrum changes with increasing time of immersion. The S 2p peak after 4 weeks of immersion is situated at 169 eV which it indicates that SO_4^{2-} has been incorporated into the oxide film. The two peaks fitted into the spectra, represent the S $2p_{3/2}$ and S $2p_{1/2}$ components with spin-orbit splitting of 1.15 eV. In contrast to the metal 2p spectra for CrMnFeCoNi in Figure 7.35, the S 2p increases in signal to noise ratio with the time of immersion.

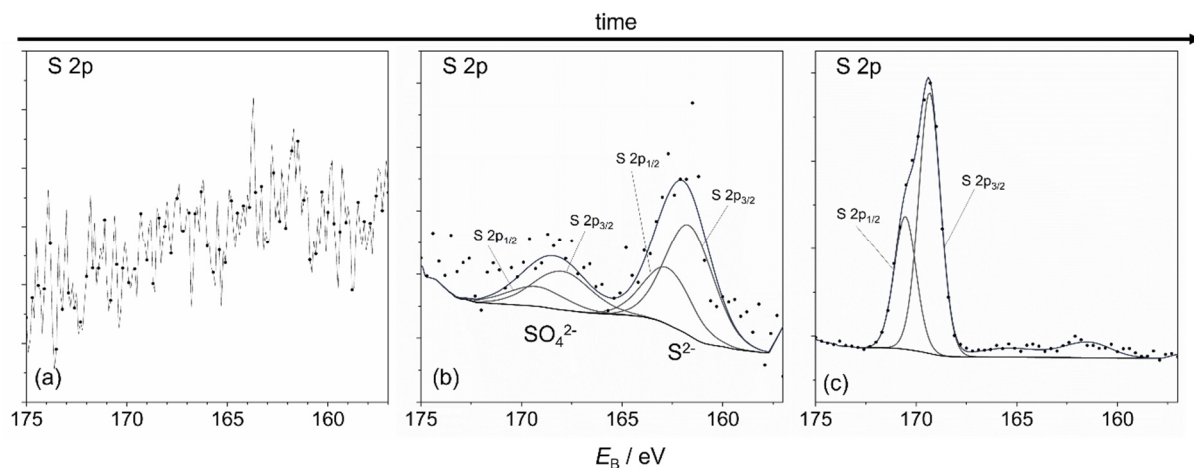


Figure 7.36. Development of S 2p XPS spectrum on CrMnFeCoNi with increasing immersion time of immersion at (a) the native state, (b) 1 week and (c) 4 weeks in 1 M H_2SO_4 .

Investigating the O 1s spectra for CrMnFeCoNi after the respective corrosion times in 1 M H_2SO_4 in Figure 7.37, a change in the detected oxygen species becomes evident. In the native state, the alloy surface is covered with metal oxides (529.9 eV), metal hydroxides (531.4 eV) and organic residue (532.8 eV). After 1 week of immersion, the organic residue peak vanishes, while the metal oxide and hydroxide signals increase. Instead of a change in the signal intensity of the oxide and hydroxide species, the peaks vanish after 4 weeks of immersion. In its place are two peaks at 532.3 eV and 533.5 eV which suggests the presence of SO_4^{2-} and water within the surface layer, respectively.

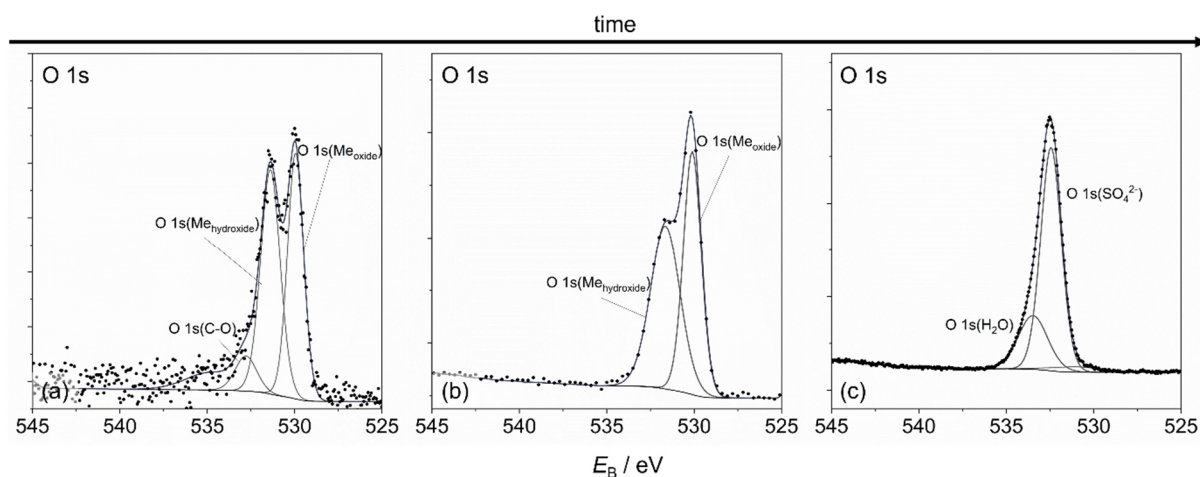


Figure 7.37. Development of O 1s XPS spectrum on CrMnFeCoNi with increasing time of immersion at (a) the native state, (b) 1 week and (c) 4 weeks in 1 M H_2SO_4 .

CrCoNi remains resistant towards corrosion in 1 M H_2SO_4 according to the electrochemical and ICP-MS results. In agreement with this finding, XPS measurements showed no noticeable change in the metal 2p spectra after one week of immersion. Hence, Figure 7.38 presents only the 2p spectra of the native CrCoNi surface and of samples after 4 weeks of immersion. The spectra of the native surface clearly show a contribution of metallic components for all three metals. The oxide species formed after 4 weeks of immersion

decrease the signal-to-noise ratios in the respective spectra. This allows only for insufficient fitting and lead to error-prone interpretation. Nevertheless, the spectra clearly show a growth of Cr-, Co- and Ni-oxides on the alloy surface after 4 weeks of immersion in 1 M H₂SO₄. While Ni generally has been assumed to remain metallic, the Ni 2p spectrum in Figure 7.38 clearly shows that Ni-oxide has formed after exposure to 1 M H₂SO₄. In comparison to Co and Ni, the Cr 2p spectrum exhibits no metallic Cr signals after corrosion. Although no change in surface composition was detectable after 1 week, there must have been a point of initial oxide growth on the MPEAs surface.

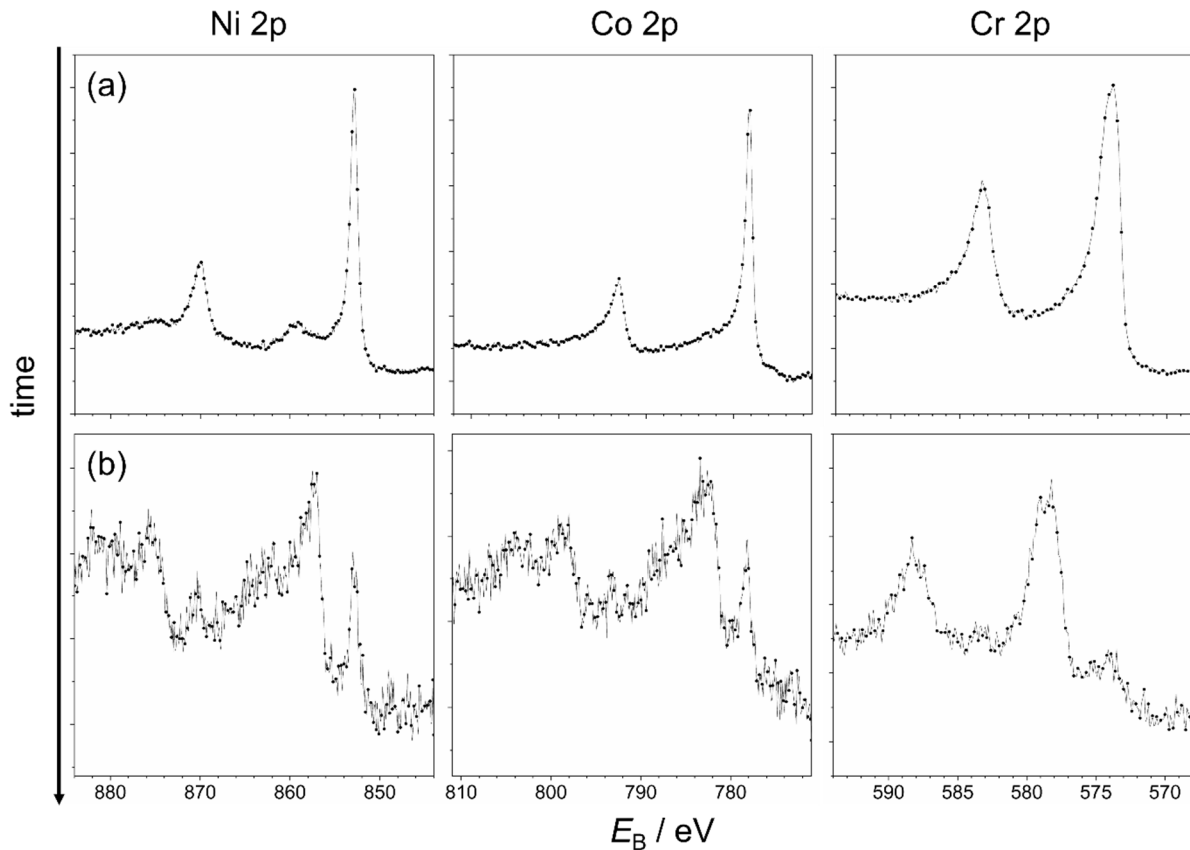


Figure 7.38. Change in 2p metal spectra of CrCoNi in its (a) native state and (b) after 4 weeks of immersion.

Similar to the metal 2p peaks, the increase in the S 2p signal as a result of SO₄²⁻ incorporation into the passive layer is observed only after 4 weeks. Figure 7.39 shows the S 2p spectra of the native and corroded CrCoNi alloy. The spectrum from the native sample is included to show the absence of sulfur before the corrosion experiment. Thus, the corrosion in H₂SO₄ leads to SO₄²⁻ incorporation into or adsorption onto the passive film. The presence of SO₄²⁻ has not been mentioned in prior MPEA studies where the surface compositions were also analyzed through XPS after corrosion in H₂SO₄.^[69, 101, 265] As the samples were lightly rinsed with de-ionized water after the corrosion measurement, SO₄²⁻ must adhere strongly enough to not be washed off.

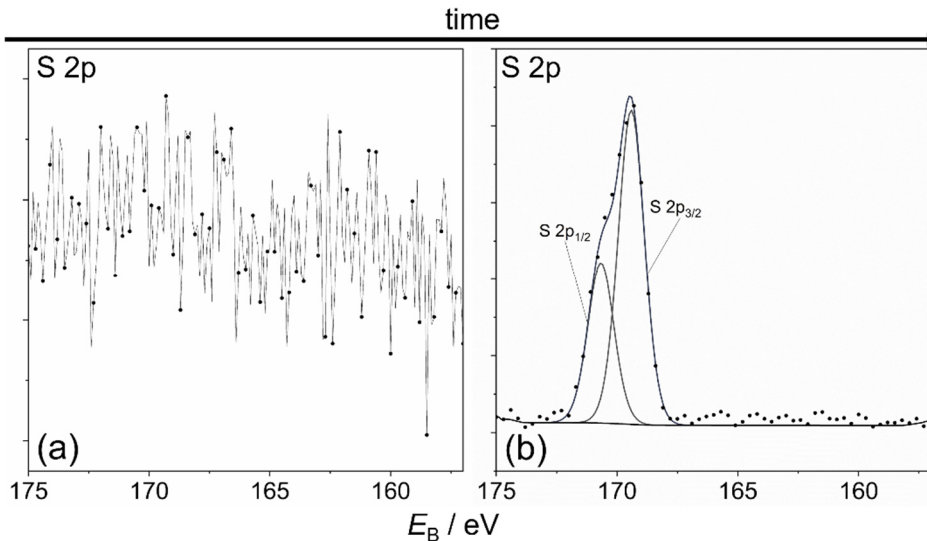


Figure 7.39. S 2p XPS spectra on CrCoNi after (a) before and (b) after 4 weeks of immersion in 1 M H_2SO_4 .

Even though no change in surface composition could be detected for CrCoNi in the metal 2p and S 2p spectra after 1 week of immersion, the O 1s spectra do show a change in surface composition after 1 week of immersion. The change in detected oxygen species is summarized in Figure 7.40. In the native state namely metal oxides (529.9 eV), metal hydroxides (530.9 eV) and organic residue (533.2 eV) make up the surface composition. After 1 week of immersion, the organic residue peak decreases in signal, while the metal oxide and hydroxide signals increase, indicating the growth of the passive layer. After 4 weeks of immersion the same O 1s spectra are very similar for CrCoNi and for CrMnFeCoNi. At 532.5 eV, the peak for SO_4^{2-} arises and at 533.6 eV the peak for water.

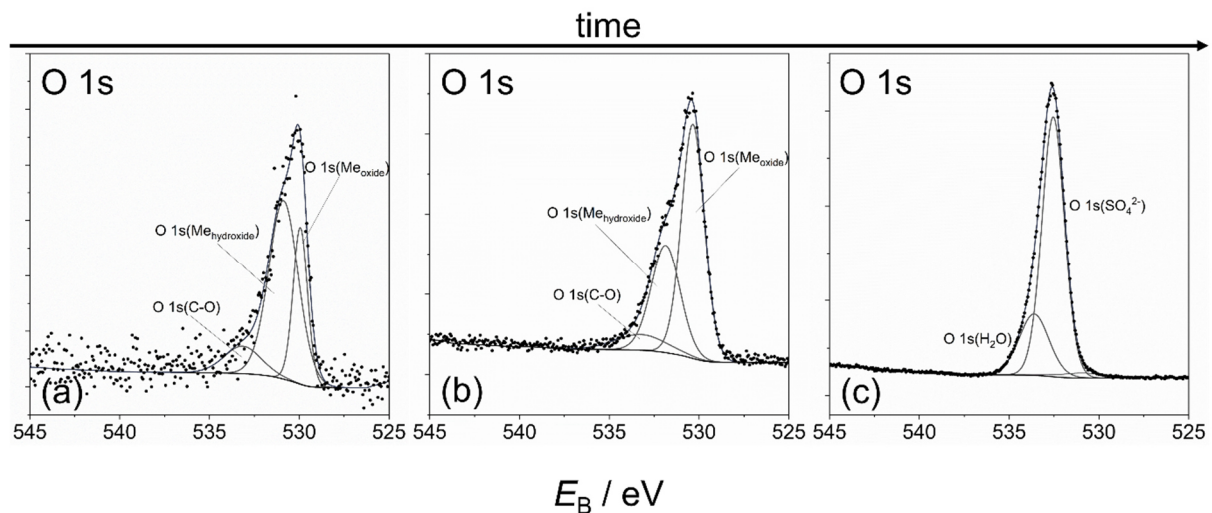


Figure 7.40. Development of O 1s XPS spectrum on CrCoNi with increasing time of immersion at (a) the native state, (b) 1 week and (c) 4 weeks in 1 M H_2SO_4 .

Finally, SEM images were recorded in the SE mode that demonstrate the surface topography of the CrMnFeCoNi and CrCoNi samples before and after the long-term corrosion tests in a 1 M H_2SO_4 electrolyte solution for 4 weeks (Figure 7.41 and Figure 7.42). The SEM

image of a polished CrMnFeCoNi surface in Figure 7.41a illustrates a smooth topography with the manufacture-born Cr- and Mn-oxide inclusions. The SE image in Figure 7.41b which was taken after 4 weeks of immersion in 1 M H₂SO₄ shows how severely CrMnFeCoNi succumbs to corrosion in this medium over long-term exposure. The respective EDX maps of the post corrosion surface represent all five metals. Furthermore, the maps of S and O could be generated suggesting a thicker oxide film and confirming the presence of the elements in the passive layer as the interaction volume of the electron beam with the sample can reach a thickness of more than 1 μm .^[294] The crater-like morphologies and the uneven spread of O and S support the previous finding that the formed passive film is rough, porous, defective and ultimately inefficient in protecting the MPEA from corrosive deterioration.

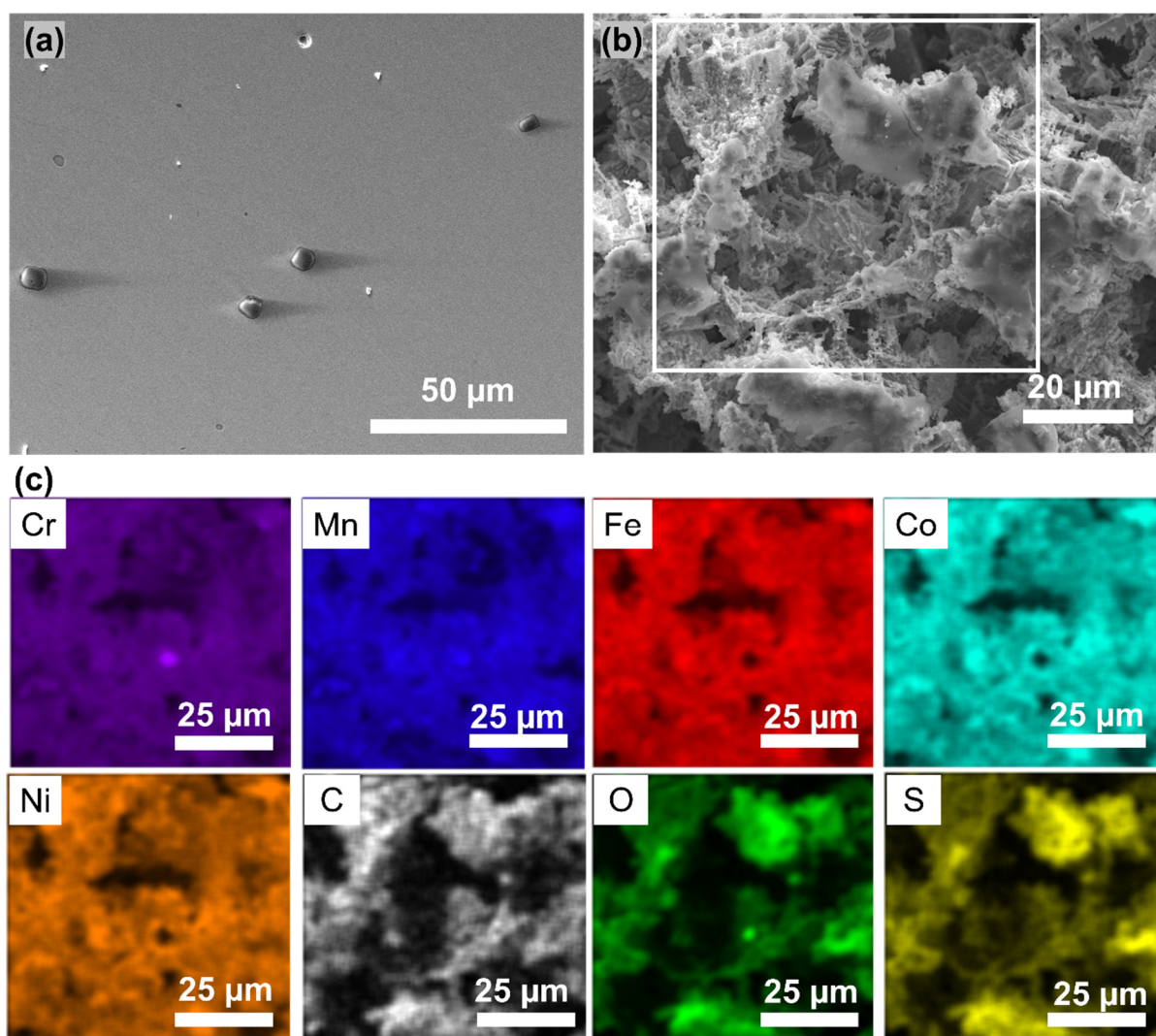


Figure 7.41. (a) SE image of the polished CrMnFeCoNi surface before long-term immersion. (b) SE image of the CrMnFeCoNi surface after 4 weeks of immersion in 1 M H₂SO₄. (c) EDX maps of the area shown in the frame of (b).

Figure 7.42a displays the polished pre-corrosion CrCoNi surface with its smooth topography and Cr-oxide inclusions as a point of reference for the post corrosion surface in Figure 7.42b. After the 4-week immersion in 1 M H₂SO₄, the inclusions are still present and intact, this is in contrast to the CrMnFeCoNi MPEA where the inclusions succumb to corrosive

dissolution due to galvanic coupling as shown after the CPP measurements in 0.1 M H₂SO₄ (see Chapter 7.2.3). The respective EDX maps of the post corrosion surface show the presence of all three MPEA metals. While the maps of S and O could also be generated, they both accumulate at specific sites. As the inclusions remain intact, the highest oxygen concentrations are detected there as indicated by the green arrows in Figure 7.42b and the respective O EDX map. After taking the CrCoNi sample out of the electrochemical cell, not all of the electrolyte has been washed of, as some SO₄²⁻ salts crystallized on the surface. This is indicated by the orange crosses in Figure 7.42b and in the S EDX map. In correspondence with the electrochemical results, the SEM images show that the CrCoNi specimen remains untarnished after a 4-week exposure to 1 M H₂SO₄.

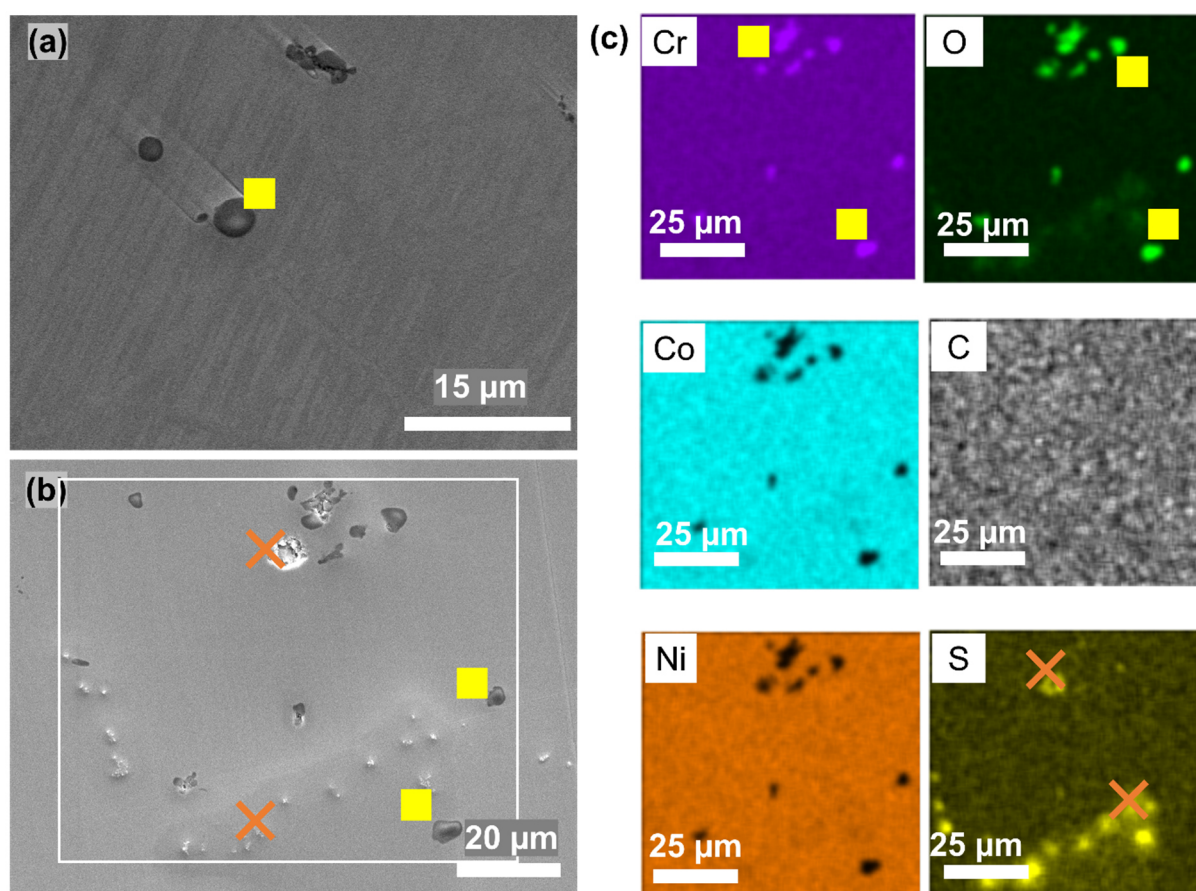


Figure 7.42. (a) SE image of the polished CrCoNi surface before long-term immersion. (b) SE image of the CrMnFeCoNi surface after 4 weeks of immersion in 1 M H₂SO₄ with intact inclusion (yellow square) and residual electrolyte (orange cross). (c) EDX maps of the area shown in the frame of (b).

7.4 Conclusion

The results presented in this chapter clearly show that the CrMnFeCoNi MPEA behaves similarly to AISI 304 when exposed to 0.1 M NaCl and H₂SO₄. Its corrosion resistance is slightly inferior to the stainless steel in the chloride-containing medium, which may be due to the high Mn content in the MPEA. The electrochemical behaviors of AISI 304 and CrMnFeCoNi are nearly identical in 0.1 M H₂SO₄. While the CrMnFeCoNi alloy seems to form a relatively thick

oxide film, the impedance data suggest a defective passive film that does not protect the alloy sufficiently from corrosion. In NaCl the MPEA corrodes mainly through pitting and crevice corrosion which due to their autocatalytic nature decrease the re-passivation capabilities of the alloy. In the 0.1 M H₂SO₄, CrMnFeCoNi shows improved corrosion resistance compared to NaCl and does not succumb to pitting. Some of the improved corrosion performance may be attributed to the incorporation or adsorption of SO₄²⁻ ions into or onto the passive layer, respectively. The presence of the anions in the surface composition has been shown by XPS. In the acidic electrolyte, the manufacture-born Cr- and Mn-oxide inclusions seem to introduce sites for galvanic corrosion. AFM and SEM images revealed the dissolution of the inclusions and increased corrosive surface breakdown around the inclusions. Avoiding the formation of such oxide inclusions during manufacturing may potentially increase the corrosion resistance of the alloy. Exposing CrMnFeCoNi to 1 M H₂SO₄ for up to 4 weeks shows that the MPEA cannot withstand corrosion in this medium. While upon initial immersion electrochemical data demonstrates the formation of a protective passive layer, this protection ceases after 2 days. Even though the system stabilizes in its OCP after 3 weeks, the impedance data suggest further degeneration of the passive film. The SEM images and EDX maps taken of the CrMnFeCoNi surface after 4 weeks demonstrate the severity of the corrosion in 1 M H₂SO₄. Neither the polarization in 0.1 M NaCl nor in 0.1 M H₂SO₄ had a great impact on the CrCoNi surface. In both electrolytes, CrCoNi experiences intergranular corrosion, however, the extent is minimal and its Cr-oxide inclusions remain intact. While the passive layer thicknesses are comparable to CrMnFeCoNi, the impedance data suggest a passive layer with higher homogeneity and compactness. When exposed to 1 M H₂SO₄ over 4 weeks, the protectiveness of the passive layer increased for CrCoNi as demonstrated by the change in OCP over time and the increase in impedance at low frequencies. After 1 week, a growth in metal oxide species can be observed through the XPS analyses of CrCoNi. Similar to CrMnFeCoNi, only the SO₄²⁻ and H₂O oxygen signals are detectable after 4 weeks of immersion, suggesting that the anion may contribute to the passivation of CrCoNi. When comparing the results of the two MPEAs, CrCoNi exhibited a superior corrosion resistance over CrMnFeCoNi as well as over conventional AISI 304 in the typical corrosion electrolytes NaCl and H₂SO₄. It also showed excellent resistance toward long-term exposure.

8 Electrochemical Behavior at High Anodic Potentials in Chloride-Containing Aqueous Media

In Chapter 7.1, it has been outlined that NaCl is chosen as a typical electrolyte in corrosion studies. Due to its abundance, high conductivity, and thermal stability, NaCl offers a highly economically feasible electrolyte for electrochemical water splitting.^[254] The previous studies in Chapter 7 have shown that CrMnFeCoNi and CrCoNi corrode by pitting and intergranular corrosion, respectively. At more positive potentials, the transpassive behavior can be controlled by passive film dissolution, oxygen evolution reaction and chlorine evolution reaction.^[295] Thus, 0.1 M NaCl electrolytes of different pH levels were employed to investigate the stability, electrochemical behavior and potential application for water splitting of CrMnFeCoNi and CrCoNi. The results for the transpassive behavior of CrCoNi in 0.1 M NaCl at pH 2 are published in *Angewandte Chemie International Edition*^[X3]. Furthermore, I employed the methodology of electrochemical atomic force microscopy (EC-AFM) imaging during CPP measurements in combination with pre- and post-corrosion SEM to contribute toward another publication in *Corrosion Science* as part of a cooperation with colleagues from AGH.^[X4]

8.1 Transpassivity and Oxygen Evolution Reaction

In corrosion and catalyst research, it has been established that the oxygen evolution reaction (OER) occurs in concomitance with metal dissolution when polarizing metallic electrodes at high anodic potentials within the transpassive region.^[296] Recent research even indicates an inescapable link between the OER and material dissolution which poses a challenge for determining stable and active electrocatalysts.^[297-300] Despite the contribution of both processes toward experimentally observed current densities at transpassive potentials, most studies of water splitting catalysts have either focused on the OER activity or the catalyst stability toward corrosion.^[243, 301-304] Considering this interrelation requires an evaluation of material performance under the aspects of catalytic activity *and* corrosive degradation processes.

As demonstrated in Chapter 5.1, typical corrosion studies encompass electrochemical studies such as polarization measurements (e.g., CPP) and electrochemical impedance spectroscopy (EIS) as well as ex-situ analyses of the electrode surface in the pre- and post-corroded states through methods such as XPS and SEM. The emergence of online atomic spectroelectrochemistry (ASEC) allowed for the real-time analysis of selective corrosive metal dissolution during polarization.^[102, 295] Such analyses typically employ a flow-type scanning droplet or capillary cell, connected to ICP atomic emission or mass spectrometers that enable the simultaneous quantification of corrosion products which may be directly related to the

measured current densities of the respective polarization measurement.^[305-310] By means of the ICP-MS coupled scanning flow cell, Cherevko and Mayrhofer et al.^[297] showed that noble metal catalysts such as Au and Pt dissolve considerably during polarization, even though the metals demonstrated good OER activities at low overpotentials when tested by transient and steady-state potential applications. In their real-time dissolution analysis of pure Cr in 0.1 M NaCl through ASEC, Choudhary et al.^[191] elucidated the direct dissolution of the Cr₂O₃ passive layer to Cr(VI) in the transpassive region. Despite its power of the simultaneous analysis of electrochemical data and corrosive metal dissolution, the detection and quantification of other stoichiometrically relevant electron transfer processes such as the OER remain complex. Nevertheless, Wen et al.^[311] were able to ascribe the anodic current contribution of the OER of a carbon-supported Ru-based catalyst through the application of ASEC and could differentiate its current contribution from other reactions (including catalyst degradation or carbon-support dissolution).

While some localization of corrosion monitoring is possible with the scanning flow-cell, scanning probe techniques such as electrochemical atomic force microscopy (EC-AFM), and scanning electrochemical microscopy (SECM) allow for the visualization of local corrosion events in the micro- to nanometer range. EC-AFM enables to monitor surface-related changes as a result of corrosion, including the imaging of pitting initiation and surface roughening as well as topographically detecting catalytic active sites (e.g., through bubble formation) for OER/ORR on electrocatalysts.^[312-315] These in-situ topographical changes are readily recorded through EC-AFM. However, the method is mostly insensitive to electron transfer reactions and cannot detect local compositional information. Operating an SECM in the sample-generation/tip-collection (SG/TC) mode by setting the probe potential to either oxidize or to reduce a compound that is generated at reactive sites on the sample (e.g., at grain boundaries or active local corrosion sites) allows to monitor corrosion processes in a chemically selective manner.^[316-318] An example constitutes the analysis of anodic sites on corroding coated carbon steel by means of SECM in the SG/TC mode by Souto et al.^[319] They were able to detect and monitor the emergence of Fe(II) and O₂ species, by selectively applying the corresponding oxidizing and reducing potentials.

In this chapter, tip-substrate voltammetry (TSV) in a SG/TC mode configuration was employed to detect the onset of the OER within the transpassive region of the MPEAs CrMnFeCoNi and CrCoNi in 0.1 M NaCl electrolytes. While a CPP, i.e., a voltammetric scan, was conducted at the MPEA sample electrodes, the SECM microelectrode (ME) was positioned above the sample to detect evolving oxygen.^[318, 320] To monitor the corrosion-induced surface changes with increasing positive potentials, EC-AFM was utilized to capture the respective changes in surface morphologies. In correlation to the ASEC approach, the electrolytes were collected after the TSV-SECM studies and metal concentrations were

quantified by means of ICP-MS. While 0.1 M NaCl was chosen as the base electrolyte to monitor the electrochemical behavior of the MPEAs at high anodic potentials, the influence of the pH was also investigated by adjusting the original pH of 6.25 to an acidic and alkaline pH of 2 and 12 with H₂SO₄ and NaOH, respectively.

8.2 Transpassive Behavior of CrMnFeCoNi

Various MPEA electrocatalysts have recently emerged with the surge in research interest in these novel materials for electrocatalytic OER application.^[321-324] To realistically assess their viability as OER electrocatalysts, metal dissolution as a competing process to the OER at the anode surface needs to be reported in addition to overpotentials and electrocatalytic activities.^[323, 325] In Chapter 7.1, it has been demonstrated that the CrMnFeCoNi alloy succumbs to pitting corrosion in 0.1 M NaCl and to selective corrosive attack around manufacture-born Cr-/Mn-oxide inclusion in 0.1 M H₂SO₄. While the ICP-MS quantifications indicate that the MPEA severely dissolves in both media compared to CrCoNi, the synergistic effect of alloying 5 transition metals in equimolar concentrations could potentially produce an electrode material capable of the OER in concomitance to corrosive dissolution, especially because Co and Ni are known elements often found in OER electrocatalysts.

8.2.1 Electrochemical Characteristics at pH 2

The TSV-SECM scan for CrMnFeCoNi in 0.1 M NaCl at pH 2 is depicted in Figure 8.1. While the potential program of a CPP is applied to the MPEA surface, the ME is held potentiostatically at the potential for the oxygen reduction reaction (ORR) during the whole experiment. Upon the onset of OER at the sample surface, the ME should detect the evolved oxygen which would lead to a rise in ME current. Bearing in mind that the IUPAC convention considers negative currents to be reduction currents, current rise in this context means an increase in the absolute current and a smaller numerical value. Before the TSV-SECM scan commences, the system is flushed with N₂ to remove dissolved oxygen. However, since these scans are conducted in ambient laboratory conditions, diffusion of oxygen from air into the cell during the experiment cannot be fully excluded. Hence, at the beginning of the TSV-SECM scan, some residual dissolved oxygen is reduced at the ME (Figure 8.1a). However, within the transpassive region of the MPEA no oxygen is detected at the ME.

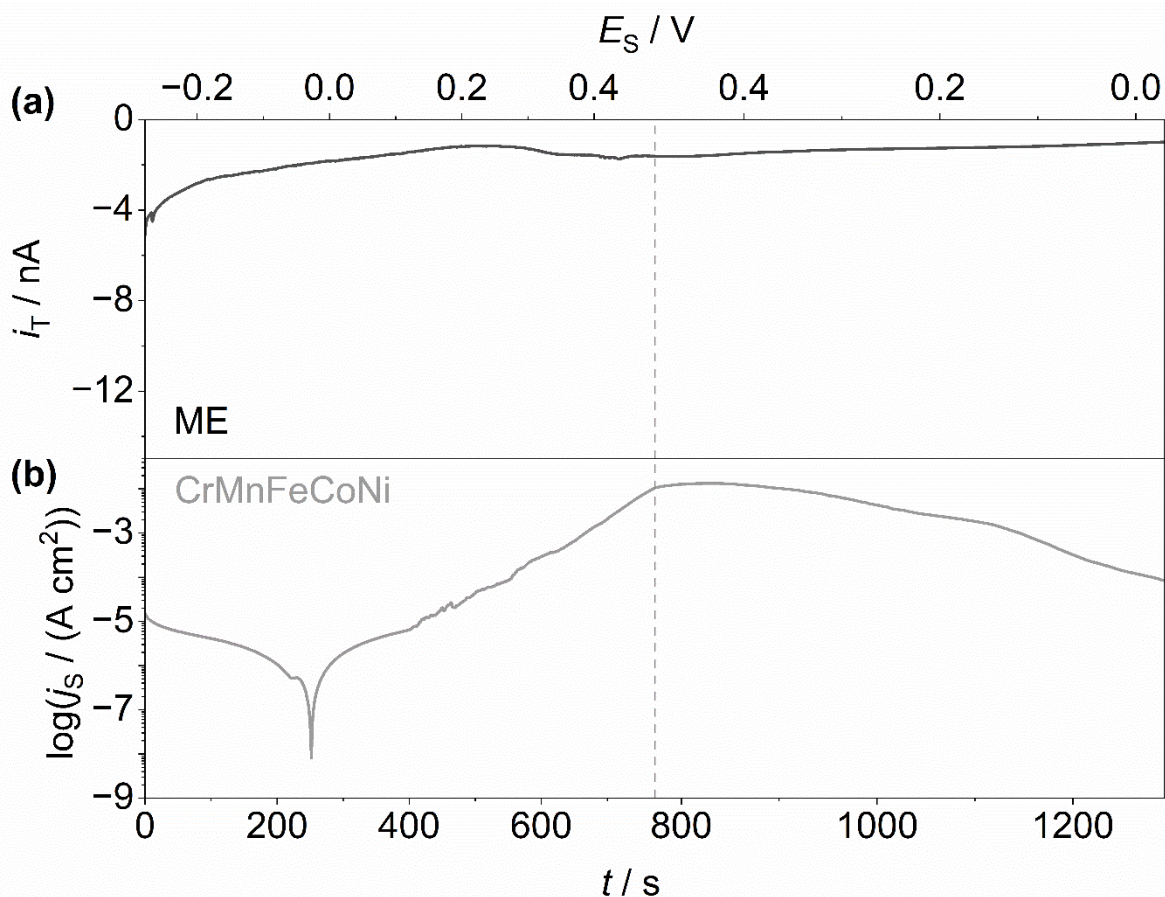


Figure 8.1. TSV-SECM of CrMnFeCoNi in 0.1 M NaCl at pH 2 with (a) the ME (Pt disc electrode $r = 5 \mu\text{m}$, $E_T = -0.65 \text{ V}$) current response toward the OER at the sample and (b) the CPP of the CrMnFeCoNi sample at 1 mV s^{-1} . Potentials are reported vs. Ag/AgCl/3M NaCl. Adapted with permission from own publication^[326] published by Wiley-VCH GmbH under the terms of the CC BY 4.0 license. Copyright 2024, The Authors.

8.2.2 Influence of pH

Figure 8.2 shows the TSV-SECM scan of CrMnFeCoNi in 0.1 M NaCl at pH 6.25. No ME response for the onset of the OER within the transpassive region of the MPEA is observed (Figure 8.2a). Compared to the TSV-SECM scan at pH 2 (Figure 8.1a), the ME current responses are lower in magnitude in Figure 8.2a. At pH 2, the ME current initially surmounts to $i_T = -5.1 \text{ nA}$ and eventually stabilizes around $i_T = -1.3 \text{ nA}$. Contrarily in pH 6.25, the ME current starts at $i_T = -0.4 \text{ nA}$ and increases to up to $i_T = -1.3 \text{ nA}$ positive of $E_S = 0.31 \text{ V}$. While one of the reasons could be the OER at the sample, this increase in ME current could also be due to diffusion of oxygen from air. Moreover, since the main mode of corrosion is pitting corrosion which does not cease upon the CPP scan reversal, the rise in ME current could also be a result of an increase in H^+ reduction (see Equation (4.2), Chapter 4). As described in Chapter 4.4, pitting and crevice corrosion lead to a local decrease in pH due to metal dissolution (see Figure 4.8 and Figure 4.9). If pits grow and propagate, they can become large enough to influence the local electrolyte composition experienced by the ME. By applying the ORR potential of -0.65 V , H^+ may also be reduced and hence the ME signal slightly increases.

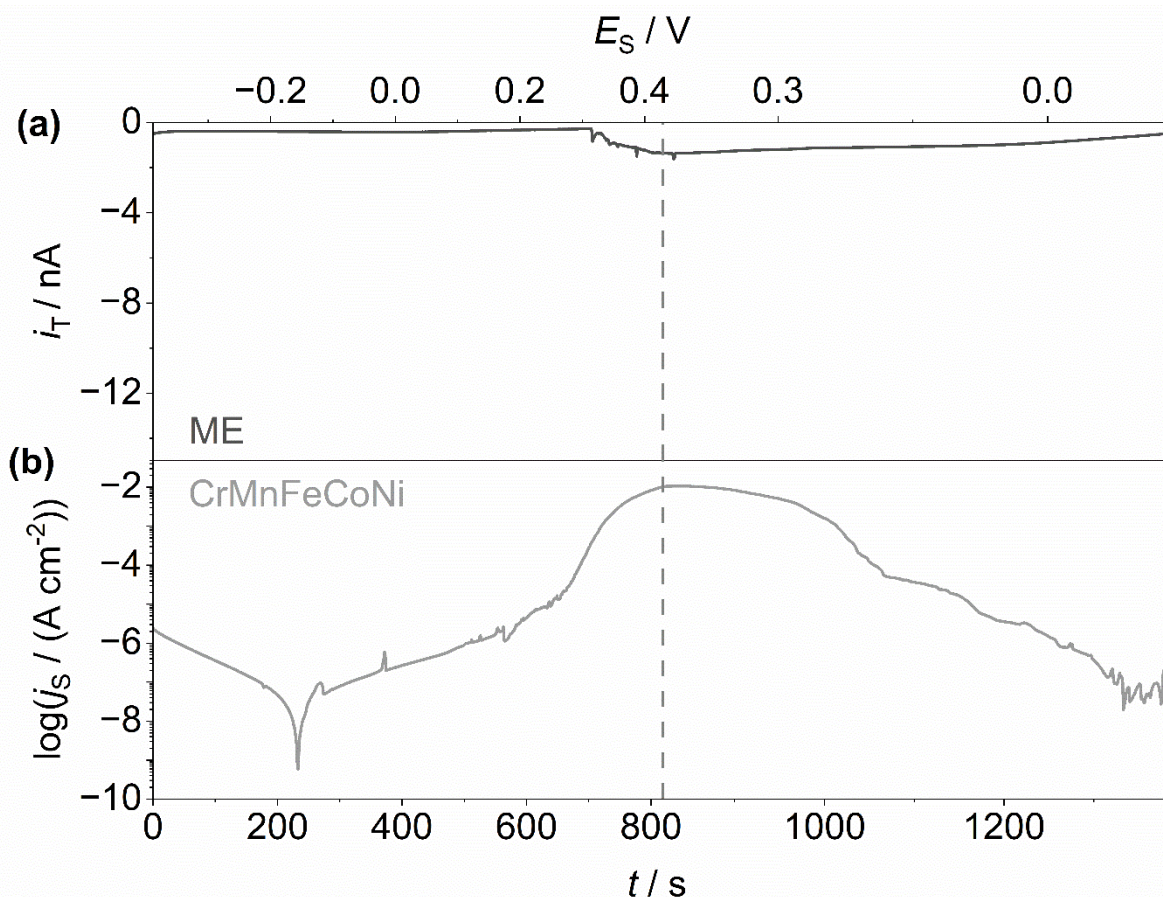


Figure 8.2. TSV-SECM of CrMnFeCoNi in 0.1 M NaCl at pH 6.25 with (a) the ME (Pt disc electrode $r = 5 \mu\text{m}$, $E_T = -0.65 \text{ V}$) current response toward the OER at the sample and (b) the CPP of the CrMnFeCoNi sample at 1 mV s^{-1} . Potentials are reported vs. Ag/AgCl/3M NaCl.

In 0.1 M NaCl at pH 12, the ME response is comparable to that in the pH 6.25 electrolyte (see Figure 8.3). As with the other two media, no sharp OER signal is observed in the ME current response (Figure 8.3a). Nevertheless, the ME current also slightly increases with increasing polarization potential from initially $i_T = -0.4 \text{ nA}$ to -0.9 nA at the apex potential. During the reversed scan, the ME current first decreases but then increases again to $i_T = -1.2 \text{ nA}$ at $E_s = 0.34 \text{ V}$. This may be due to pitting corrosion which initiates at higher potentials in alkaline NaCl than in a neutral electrolyte. The sharp increase in sample current upon E_b , suggests rapid pit growth. This rapid growth will result in localized high concentrations of dissolved metal ions, which can quickly form insoluble metal hydroxides in the alkaline environment. The observed decrease in ME current, may be due to this imminent increase in metal hydroxides. While the pits continually grow on the reversed scan, more room develops for the metal hydroxides to diffuse to and other evolved species such H^+ may be detected by the ME, leading to the small signal increase observed at $E_s = 0.34 \text{ V}$.

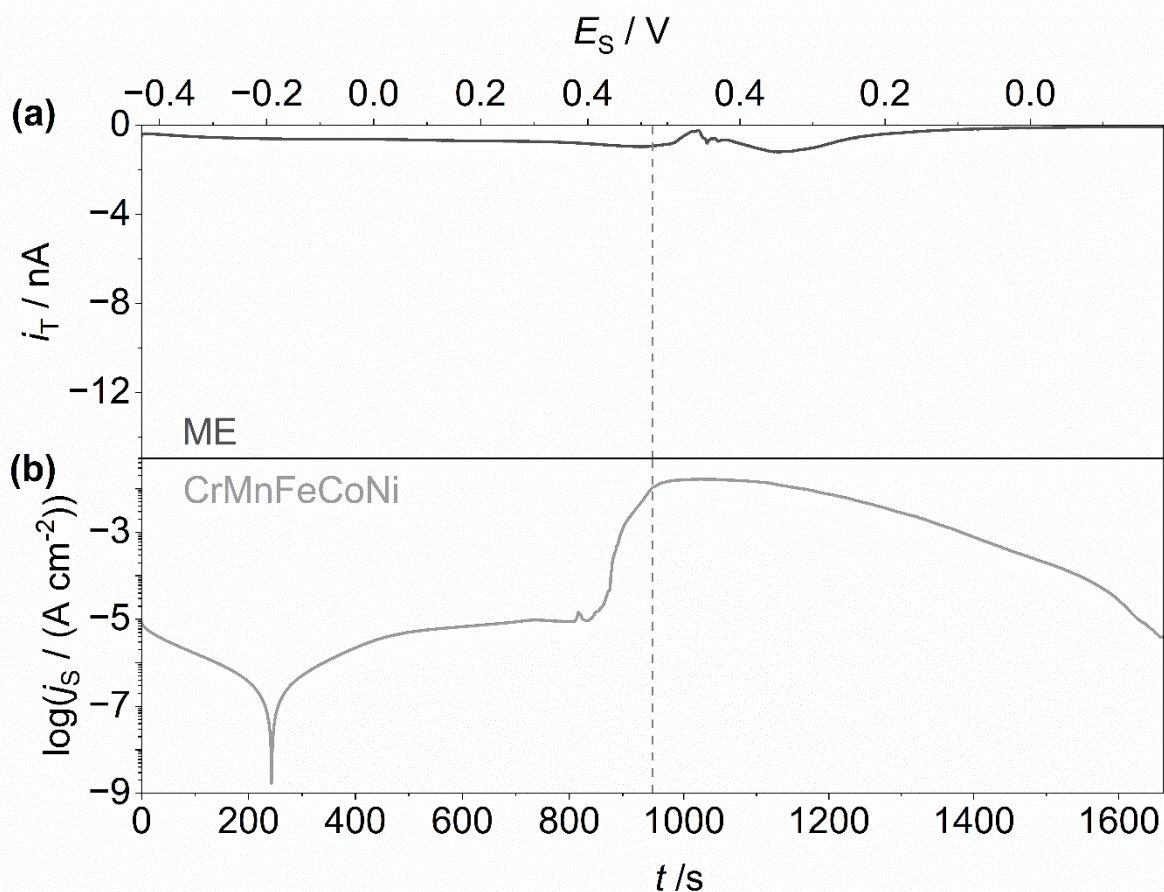


Figure 8.3. TSV-SECM of CrMnFeCoNi in 0.1 M NaCl at pH 12 with (a) the ME (Pt disc electrode $r = 5 \mu\text{m}$, $E_T = -0.65 \text{ V}$) current response toward the OER at the sample and (b) the CPP of the CrMnFeCoNi sample at 1 mV s^{-1} . Potentials are reported vs. Ag/AgCl/3M NaCl. The diagram is adapted with permission from own publication^[327] published by Wiley-VCH under the terms of the CC BY 4.0 license. Copyright 2024, The Authors.

While the TSV-SECM in all three pH levels of the NaCl electrolyte suggest that no considerable OER is occurring in combination with metal dissolution, slightly increasing ME reduction currents in pH 6.25 and pH 12 in the transpassive region could indicate that minimal concentrations of oxygen evolve. To elucidate whether the OER took place, the electrolytes were quantified through ICP-MS after the TSV-SECM. The determined metal ion concentrations were then converted into equivalent charges Q_{ICP} through utilizing Faraday's law (Equation (8.1)). In accordance with the Pourbaix diagrams of the metals, the number of exchanged electrons n_e at all pH levels are assumed to be $n_e = 3, 2,$ and 2 for Cr, Co, and Ni, respectively. For Mn and Fe, the number of exchanged electrons is assumed to be $n_e = 2$ in pH 2 and 6.25, and $n_e = 3$ in pH 12.

$$Q_{\text{ICP}} = (c_{\text{Cr,ICP}}n_{\text{Cr}} + c_{\text{Mn,ICP}}n_{\text{Mn}} + c_{\text{Fe,ICP}}n_{\text{Fe}} + c_{\text{Co,ICP}}n_{\text{Co}} + c_{\text{Ni,ICP}}n_{\text{Ni}})FV \quad 8.1$$

Retrieving the expended charge $Q_{\text{e-chem}}$ of the CPP scan through integration (Equation (8.2)), allows the comparison of the ICP-MS result for metal dissolution and the overall chemical reactions taking place on the CrMnFeCoNi surface. In Equation (8.2), t_1 and t_2 correspond the time of the beginning of the scan and the end, respectively.

$$Q_{e-\text{chem}} = \int_{t_1}^{t_2} I(t) dt \quad 8.2$$

Table 8.1 summarizes the charges and shows that in all three media, $Q_{e-\text{chem}}$ and Q_{ICP} are identical, indicating that solely metal dissolution contributes towards the transpassive currents of CrMnFeCoNi. To allow for comparison between samples of different sizes, the charges were normalized by the corresponding geometrical surface area of the sample. Despite the presence of OER active elements, no OER occurs on CrMnFeCoNi in different 0.1 M NaCl media of different pH.

Table 8.1. Derived charges from the electrochemical CPP $Q_{e-\text{chem}}$ and ICP-MS Q_{ICP} measurements and the respective ratio.

pH	$Q_{e-\text{chem}}$ [As cm ⁻²]	Q_{ICP} [As cm ⁻²]	$Q_{\text{ICP}}/Q_{e-\text{chem}}$ [%]
2	2.95 ± 0.55	2.96 ± 0.59	100.39
6.25	2.53 ± 0.55	2.55 ± 0.58	100.76
12	2.98 ± 0.72	2.96 ± 0.78	99.32

8.2.3 Local Dissolution Behavior

The results of the TSV-SECM scan for CrMnFeCoNi in combination with the ICP-MS quantification of dissolved metal species show that CrMnFeCoNi exhibits only corrosion reactions at high anodic potentials. While previous results in Chapter 7.1 suggest pitting corrosion in 0.1 M NaCl and localized galvanic corrosion around inclusions in 0.1 M H₂SO₄, the data provides no information about the onset of these reactions. To monitor the surface deterioration during the forward scan of the CPP scan, EC-AFM was conducted. Here, the potentiodynamic scans were paused at characteristic potentials and the surface topography was recorded before the scan was continued.

The EC-AFM images in 0.1 M NaCl at pH 2 are depicted in Figure 8.4. The polarization curve indicates the points where the respective EC-AFM topographies were recorded. From previous investigation in 0.1 M H₂SO₄ in Chapter 7.2, it is known that the CrMnFeCoNi alloy exhibits active metal dissolution after the OCP. This activity and the concomitant formation of pits and corrosion products rendered the EC-AFM surface imaging prone to artifacts. Figure 10.1 in the Appendix 4 shows the respective light microscopy images before and during the polarization and illustrates the interference of formed corrosion product as a result of pitting after point b. Even the topography in Figure 8.4i which represents the initial CrMnFeCoNi surface in air already shows small pits at grain boundaries as indicated by the arrows. From

points a to d in Figure 8.4, the surface morphology does not change noticeably. It does, however, become noisier within the transpassive region (Figure 8.4d). A magnified EC-AFM topography image in Figure 8.4e was recorded of the pits at the grain boundaries as indicated in Figure 8.4d, which shows that they are indeed cavities and not a repeating artifact. The decreasing signal-to-noise ratio observed in all AFM topographies must be a result of continued corrosive dissolution. While the position of the cantilever was not changed during the polarization scan to allow for comparison and to enable the identification of corrosion-related surface changes, Figure 8.4f illustrates the same CrMnFeCoNi surface after the polarization scan. Here, the selective galvanic corrosion around inclusions can be seen. The respective magnification in Figure 8.4g shows the effect more clearly.

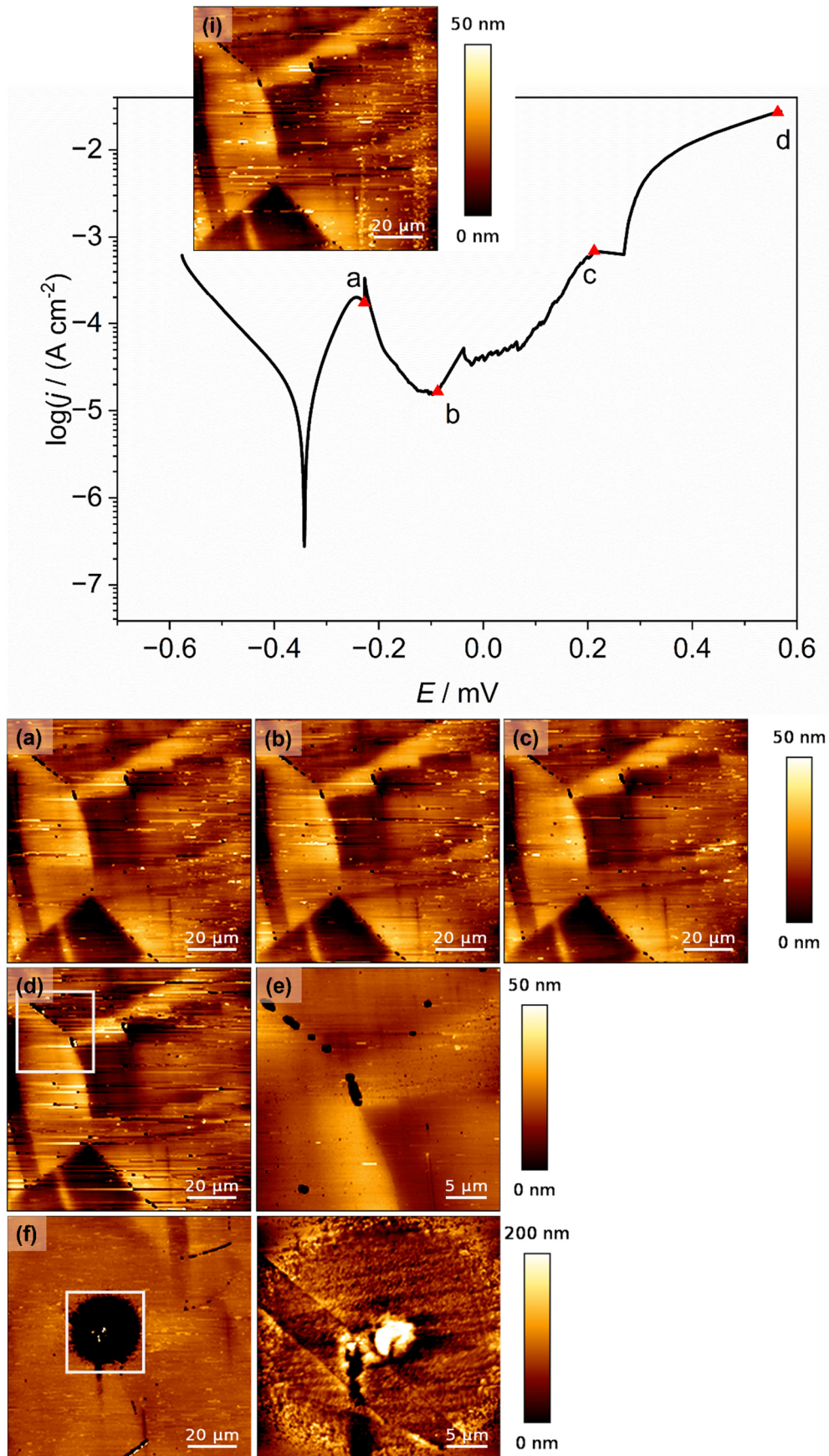


Figure 8.4. EC-AFM topographies of CrMnFeCoNi in 0.1 M NaCl at pH 2 recorded at the respective points: (i) initial surface in air, (a) after OCP, (b) passive region, (c) transpassive region, (d) high transpassive region, (e) magnification of (d), (f) corroded inclusion and (g) magnification of (f). The CPP scan was conducted in intervals at 1 mV s^{-1} . Potentials are reported vs. Ag/AgCl/3M NaCl.

While the progression of corrosion with applied potential was difficult to monitor in pH 2, the scan in pH 6.25 shows the occurrence and growth of pitting on the CrMnFeCoNi surface more clearly. In the initial AFM image in Figure 8.5i, twin structures and grain boundaries are distinctly identifiable. While the scan area was not changed during the polarization scan, the imminent diffusion of corrosion products due to pit initiation and manifestation after point b up to point c (see Figure 10.2 in Appendix 4) required the exchange of the electrolyte due to the corrosion products floating in the solution and obstructing the optical detection of cantilever deflection. Due to this exchange, the EC-AFM topography is slightly shifted, as the AFM head had to be removed for the electrolyte exchange. Even though no pits are recorded in Figure 8.5c, the light microscope image shows pits all over the MPEA surface (see Figure 10.2 in Appendix 4). Upon the point d, pits suddenly appeared within the AFM scan area, and the polarization was paused to capture the topography in Figure 8.5d showing the presence of 4 pits. Within the transpassive region further pits grow which becomes evident when inspecting Figure 8.5e which shows the final EC-AFM image at high anodic potential. Monitoring the progression of corrosion of the CrMnFeCoNi in 0.1 M NaCl at pH 6.25, reveals that pits already form and grow at potentials where the resulting fluctuating current is typically attributed to metastable pitting. While metastable pitting suggests local formation and re-passivation of small pits, this is not observed of CrMnFeCoNi where the fluctuating currents between point a and d of the polarization in Figure 8.5 already signify the formation and growth of pits.

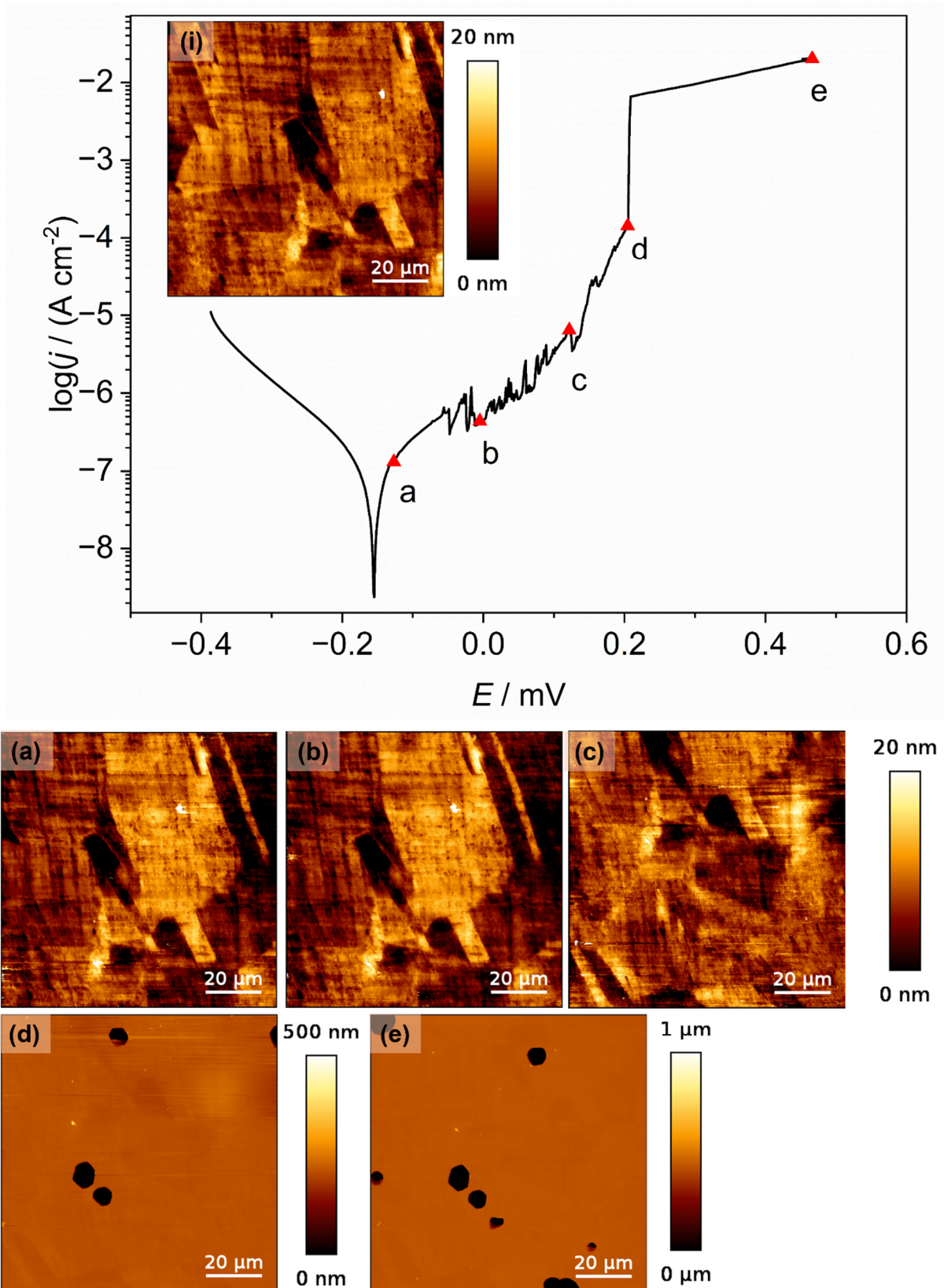


Figure 8.5. EC-AFM topographies of CrMnFeCoNi in 0.1 M NaCl at pH 6.25 recorded at the respective points: (i) initial surface in air, (a) after OCP, (b) passive region, (c) transpassive region, (d) high transpassive region, and (e) higher transpassive region. The CPP scan was conducted in intervals at 1 mV s^{-1} . Potentials are reported vs. Ag/AgCl/3M NaCl.

The corrosion process of CrMnFeCoNi in 0.1 M NaCl at pH 12 (Figure 8.6) is similar to that at pH 6.25. The initial topography clearly shows twin structures and grain boundaries (Figure 8.6i) which do not change in morphology until point b. However, pitting already commences after point a as can be seen by the light microscope images in Appendix 4. Due to the alkaline medium a high amount of insoluble corrosion products forms because of pitting corrosion which interferes with the laser system of the AFM. Hence, the electrolyte had to be exchanged before capturing the EC-AFM topography in Figure 8.6b. The diffusion of the corrosion products from the growing pit can be observed in Figure 10.3 in the Appendix 4. In comparison to pH 6.25, pits grow more rapidly in pH 12 leading to the formation of larger cavities. To monitor possible subtle morphologic changes, the EC-AFM images at point c and d were recorded at a higher magnification and indicate an increase in surface roughness upon reaching high anodic potentials in the transpassive region. Figure 8.6e was then captured again at the initial magnification demonstrating the presence of a pit that has been growing since point b.

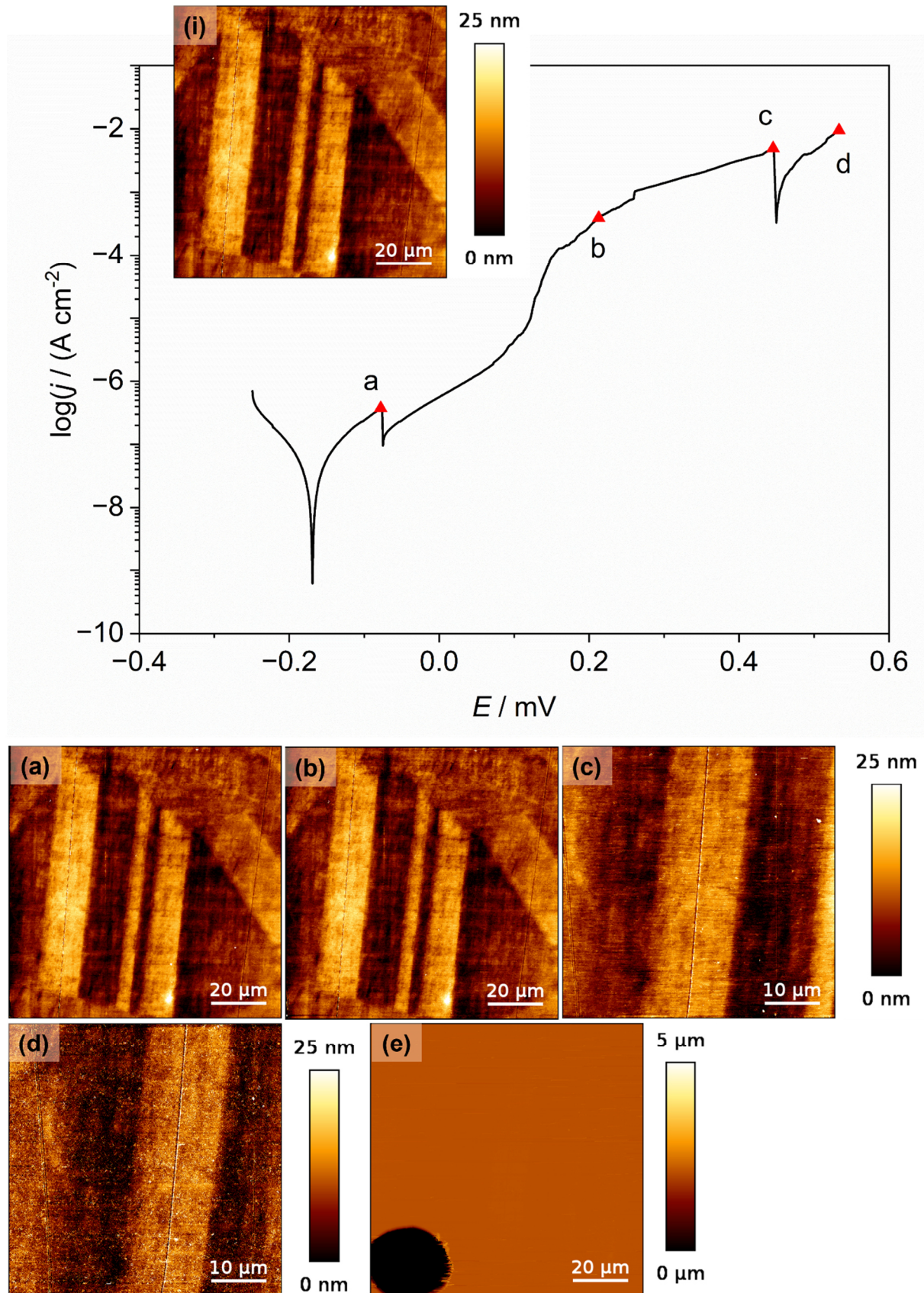


Figure 8.6. EC-AFM topographies of CrMnFeCoNi in 0.1 M NaCl at pH 12 recorded at the respective points: (i) initial surface in air, (a) after OCP, (b) passive region, (c) transpassive region and magnification of area indicated in (b), (d) high transpassive region, (e) same magnification as in (b) to show pit which grew since point (b). The CPP scan was conducted in intervals at 1 mV s^{-1} . Potentials are reported vs. Ag/AgCl/3M NaCl. The diagram is adapted with permission from own publication^[327] published by Wiley-VCH under the terms of the CC BY 4.0 license. Copyright 2024, The Authors.

Due to the severe metal dissolution in all three 0.1 M NaCl electrolytes, the monitoring of the changes in surface morphology proved complicated. Especially at pH 2, capturing EC-AFM images was disturbed by active metal dissolution. While formed pits could be monitored through EC-AFM at pH 6.25 and pH 12, the formed pits are so deep that the rest of CrMnFeCoNi surface could not be depicted with a suitable contrast (Figure 8.5e and Figure 8.6e). In combination with the results of Chapter 7 and the TSV-SECM and ICP-MS quantification, it becomes apparent that CrMnFeCoNi is not a very corrosion-resistant alloy and would be unsuitable to be considered as an OER electrocatalyst material.

8.3 Transpassive Behavior of CrCoNi

The results on the general electrochemical behavior in Chapter 7 have demonstrated that the corrosion-resistant properties of CrCoNi exceed CrMnFeCoNi in 0.1 M NaCl and 0.1 M H₂SO₄. Furthermore, long-term exposure to 1 M H₂SO₄ also does not deteriorate the alloys corrosion resistance. EIS results even indicate that the passive film becomes more protective over the duration of immersion in stagnant conditions. Quantifications of dissolved metal species after CPP through ICP-MS revealed minimal corrosive metal dissolution compared to CrMnFeCoNi and AISI 304, especially in 0.1 M NaCl (Chapter 7.1). The only apparent mode of corrosion that the alloy succumbs to is intergranular corrosion in both NaCl and H₂SO₄. In analogy to the previous investigation of CrMnFeCoNi toward the concomitance of OER and metal dissolution at high anodic potentials in Chapter 8.2, CrCoNi was also investigated through TSV-SECM. The progressive changes in surface morphology with increasing polarization potential were monitored through EC-AFM.

8.3.1 Electrochemical Characteristics at pH 2

At an acidic pH level, the OER proceeds through Equation (8.3).



Inspecting the TSV-SECM scan in Figure 8.7a, two distinctive peaks ($I_{T,1}$ and $II_{T,2}$) in the ORR current of the ME are observed at substrate potentials of $E_{S,1} = 1.00$ V and $E_{S,2} = 1.15$ V ($t_1 = 1206$ s and $t_2 = 1410$ s, respectively). The presence of the first reduction peak $I_{T,1}$ in the TSV ME response ($E_{S,1} = 1.00$ V) is an intriguing observation with excellent reproducibility. Considering that the tip-to-substrate distance of $z = 5$ μm in TSV-SECM creates a local thin layer cell (TLC), diffusion of species into and out of the TLC is hindered. During the OER, bubble formation may occur within the TLC which in turn would affect the ME response. Visual inspection of the TSV-SECM experiment through a side-view camera of the instrument revealed no perceivable bubble formation through OER. While the ME response increases at $E_{S,1}$, bubbles would cause a sharp drop of the ME current. Hence, bubble formation within the

TLC may be ruled out. The presence of the $I_{T,1}$ peak is further analyzed and discussed in Chapter 8.3.2. The increasing anodic polarization of the CrCoNi sample during the forward scan is expected to lead to the formation of a single peak at the ME that has a maximum current density close to the apex potential of the TSV-SECM scan in Figure 8.7b due to the finite transition time of O_2 from the CrCoNi surface to the ME. Looking at the ME response in Figure 8.7a, it can be seen that the peak current $I_{T,2}$ is minimally delayed to the maximum anodic current in Figure 8.7b. This delay is negligible against the time scale of the potential scan at the substrate with 1 mV s^{-1} .^[328] Upon reversal of the scan the CrCoNi surface re-passivates efficiently to much lower current densities of $j_s \approx 0.8 \mu\text{A cm}^{-2}$ than during the initial passivation with current densities of $j_s \approx 4.0 \mu\text{A cm}^{-2}$.

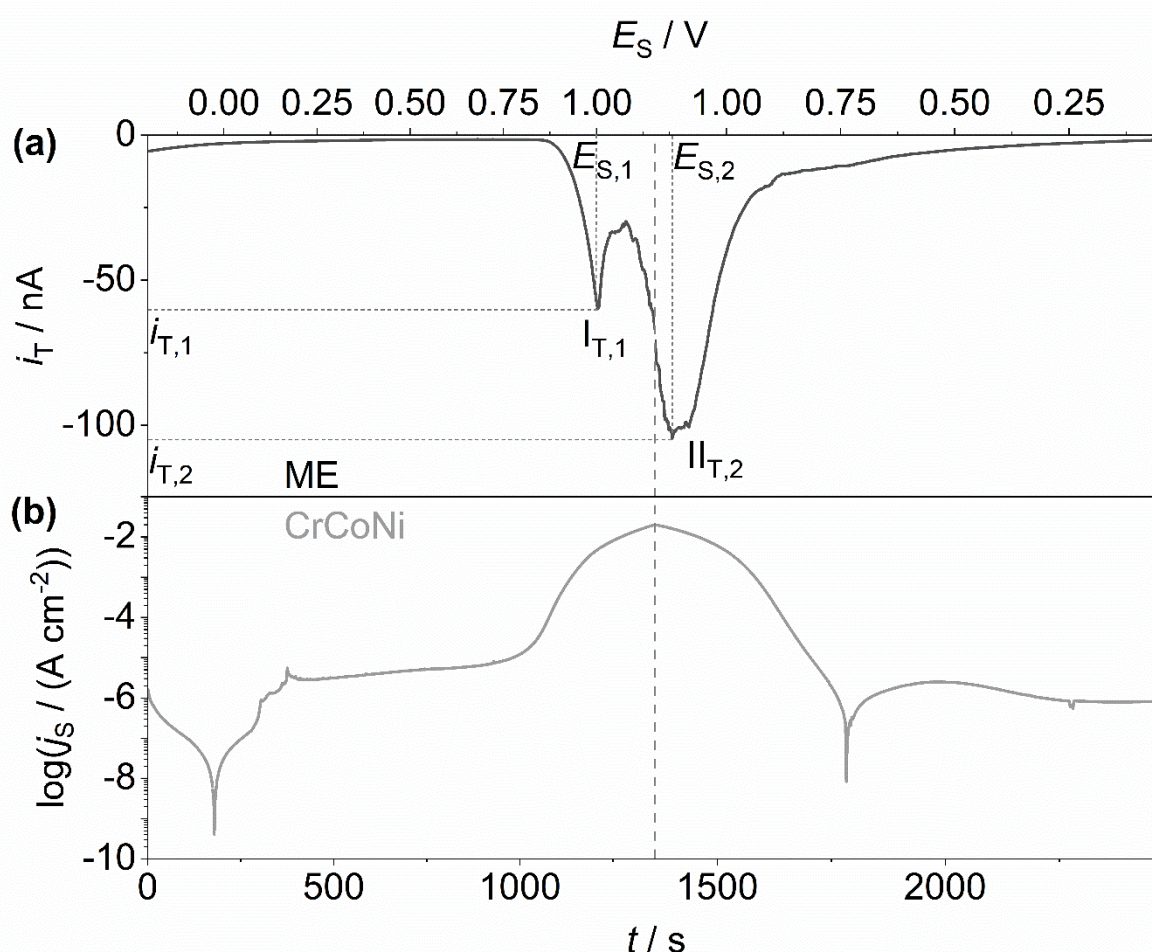


Figure 8.7. TSV-SECM of CrCoNi in 0.1 M NaCl at pH 2 with (a) the ME (Pt disc electrode $r = 5 \mu\text{m}$, $E_T = -0.65 \text{ V}$) current response toward the OER at the sample and (b) the CPP of the CrCoNi sample at 1 mV s^{-1} . Potentials are reported vs. Ag/AgCl/3M NaCl. Adapted with permission from own publication^[326] published by Wiley-VCH GmbH under the terms of the CC BY 4.0 license. Copyright 2024, The Authors.

8.3.2 Oxygen Evolution Reaction at High Anodic Potentials

For the evaluation of the OER on CrCoNi in 0.1 M NaCl at pH 2, it is essential to exclude other side reactions that may lead to the presence of the first ME current peak $I_{T,1}$ in Figure 8.7a. While the interference of bubble formation at $E_{S,1}$ has been excluded, dissolving metals could

be another reason that cause a respective current at the ME. The TSV-SECM results of the CrMnFeCoNi alloy under the same conditions, suggest that the reduction of Cr(III), Ni(II) and Co(II) to the respective metals does contribute significantly to the measured ME current. However, much higher potentials are applied to the CrCoNi sample in comparison to the CrMnFeCoNi MPEA, suggesting the possibility of the dissolved Cr, Co and Ni-species to assume higher oxidation states during the transpassive polarization. Pourbaix diagrams of the three metals indicate that at pH 2, Ni dissolves as Ni(II).^[329] Co also dissolves as Co(II) at pH 2 and could potentially be further oxidized to Co(III) at high anodic potentials.^[330] Cr dissolves as Cr(III) at pH 2 and is oxidized further to Cr(VI) upon applying high anodic potentials.^[105] The Pourbaix diagrams apply to pure metals and may serve only as a guideline. The oxidation states of the metals dissolving from an alloy will differ from the pure metals under otherwise identical conditions.^[104] TSV-SECM scans were recorded for the individual pure metals to examine whether similar responses can be observed as for CrCoNi.

Figure 8.8 shows the TSV-SECM experiment for pure Ni. No ME response towards the OER upon the CPP scan of the Ni specimen is observed. A slightly higher ME current is detected at the beginning of the TSV-SECM scan up to $E_s = 0.1$ V. While this occurs for all Ni TSV-SECM scans, it is still substantially lower than the ME currents for ORR observed for CrCoNi. As with CrMnFeCoNi, the dissolved Ni concentration was quantified through ICP-MS and converted into the corresponding charge through Faraday's law (Equation (8.1)). The respective theoretical charge Q_{ICP} was compared to the charge Q_{e-chem} of the CPP scan. The comparison reveals that the charge Q_{e-chem} is solely due to Ni dissolution. Table 8.2 summarizes the respective charges.

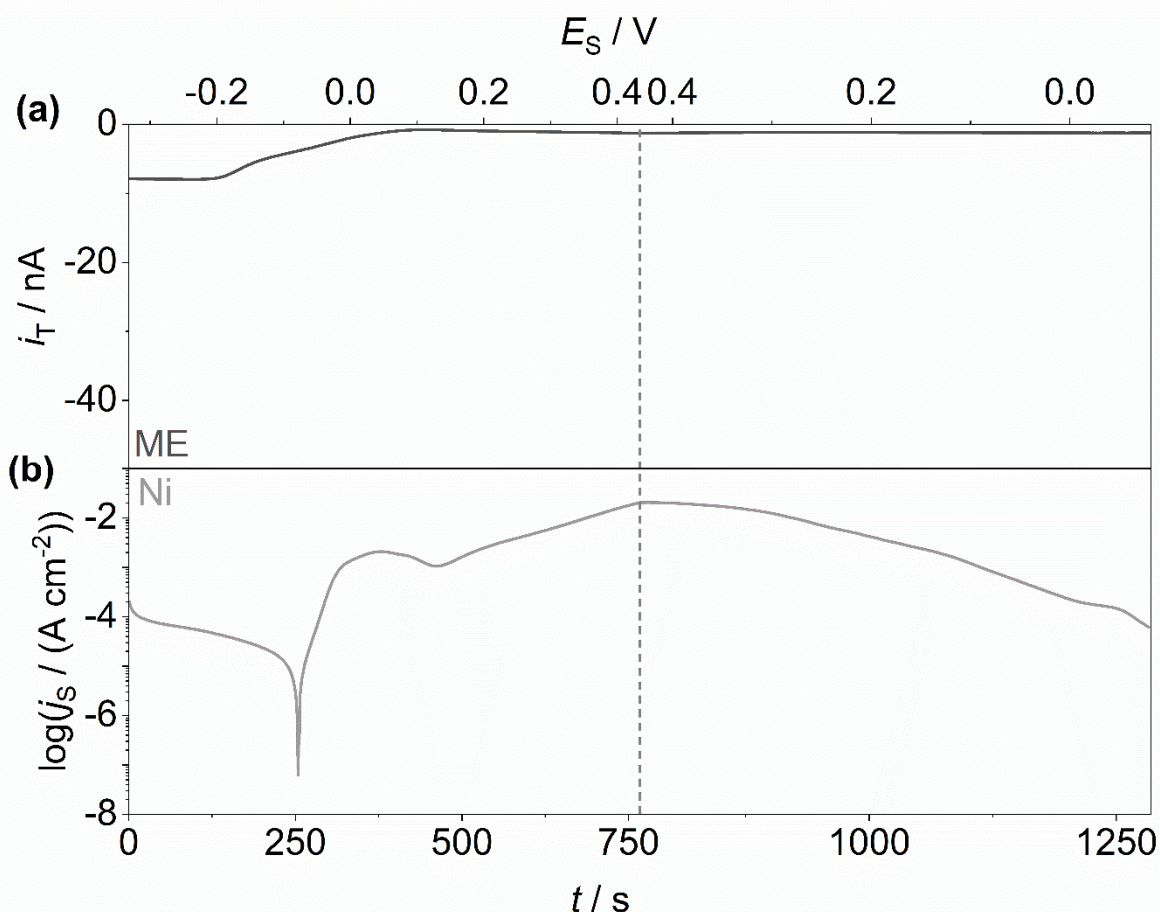


Figure 8.8. TSV-SECM of Ni in 0.1 M NaCl at pH 2 with (a) the ME (Pt disc electrode $r = 5 \mu\text{m}$, $E_T = -0.65 \text{ V}$) current response toward the OER at the sample and (b) the CPP of the Ni sample at 1 mV s^{-1} . Potentials are reported vs. Ag/AgCl/3M NaCl. Adapted with permission from own publication^[326] published by Wiley-VCH GmbH under the terms of the CC BY 4.0 license. Copyright 2024, The Authors.

Table 8.2. Measured Ni concentration in the electrolyte after CPP in 0.1 M NaCl at pH 2 and the derived charges from the electrochemical CPP $Q_{\text{e-chem}}$ and ICP-MS Q_{ICP} measurements.

Replicate	c_{Ni} [mmol L ⁻¹]	Q_{ICP} [As cm ⁻²]	Q_{Echem} [As cm ⁻²] ²	$Q_{\text{ICP}} / Q_{\text{Echem}}$
1	0.75	1.80	1.76	1.02
2	4.53	14.12	14.28	0.99

Figure 8.9 shows the TSV-SECM scan of pure Co. During the forward scan, no ME response is detectable. Only upon the CPP scan reversal, a ME response arises and ceases with the end of the scan. As the scan reversal for CrCoNi results in even lower current densities than on the forward scan, a contribution of anodic Co(II) dissolution and subsequent reduction at the ME within the applied potential range can be excluded. Before the Co TSV-SECM scan was reversed, the electrolyte turned dark black with increasing potential which disappeared completely upon scan reversal. While this unidentified reaction evokes an ME response it is not relatable to the observations made for the CrCoNi sample. Table 8.3 also summarizes the theoretical charge Q_{ICP} derived from ICP-MS quantification and the respective $Q_{\text{e-chem}}$ of the

CPP scan. The data in Table 8.3 show that the two retrieved charges do not correlate whereas Q_{echem} is approximately ten times higher than Q_{ICP} . This disparity may be due to the observed unidentified reaction upon scan reversal.

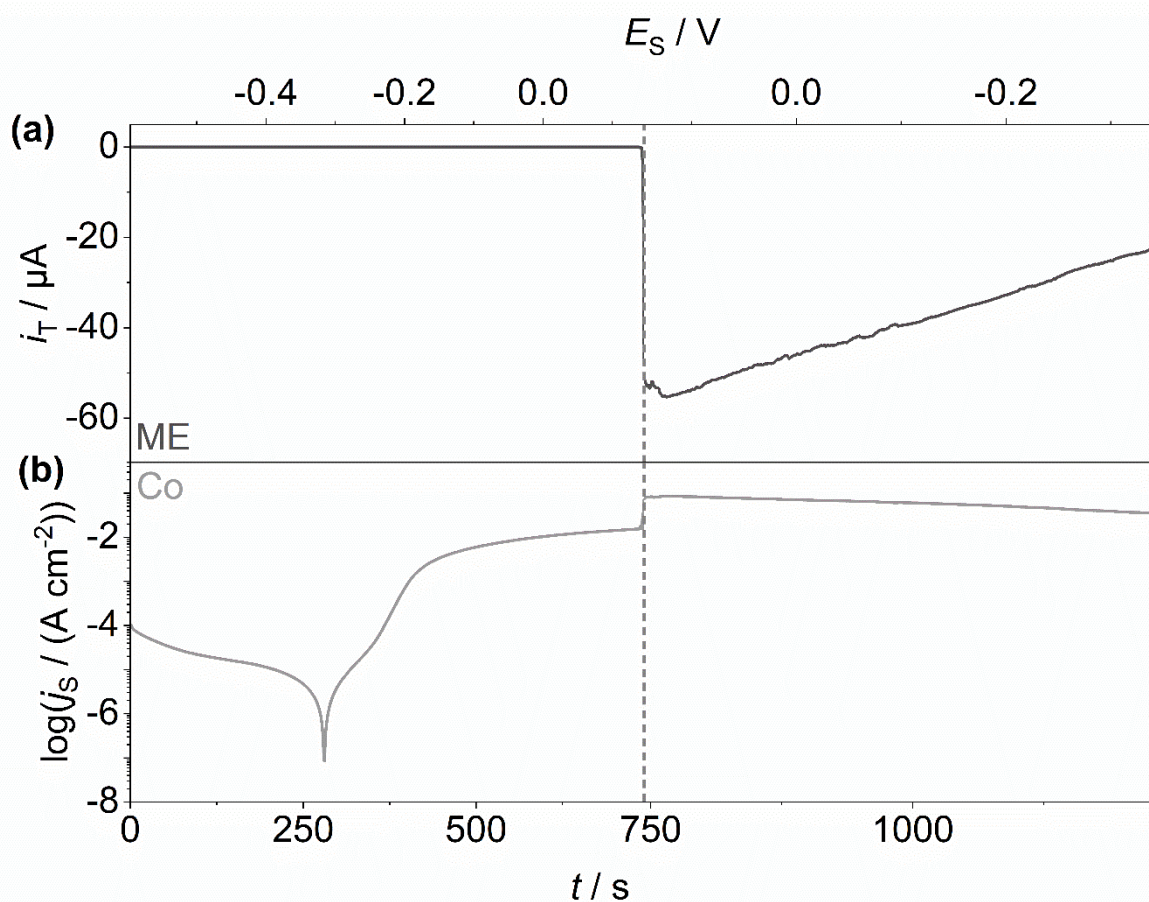


Figure 8.9. TSV-SECM of Co in 0.1 M NaCl at pH 2 with (a) the ME (Pt disc electrode $r = 5 \mu\text{m}$, $E_T = -0.65 \text{ V}$) current response toward the OER at the sample and (b) the CPP of the Co sample at 1 mV s^{-1} . Potentials are reported vs. Ag/AgCl/3M NaCl. Adapted with permission from own publication^[326] published by Wiley-VCH GmbH under the terms of the CC BY 4.0 license. Copyright 2024, The Authors.

Table 8.3. Measured Co concentration in the electrolyte after CPP in 0.1 M NaCl at pH 2 and the derived charges from the electrochemical CPP $Q_{\text{e-chem}}$ and ICP-MS Q_{ICP} measurements.

Replicate	c_{Co} [mmol L ⁻¹]	Q_{ICP} [As cm ⁻²]	Q_{Echem} [As cm ⁻²]
1	0.98	2.92	36.02
2	1.08	3.20	32.92

While the Ni and Co TSV-SECM show no similarities to the CrCoNi TSV-SECM scan, Cr, on the other hand, shows features identical to the ME response observed for CrCoNi. The respective TSV-SECM scan in Figure 8.10 demonstrates that pure Cr exhibits a similar behavior to CrCoNi with its ME current showing two maxima $I_{T,1}$ and $I_{T,2}$ that are shifted by $E_S = 0.15 \text{ V}$ to higher potentials compared to CrCoNi. Even though the reduction of Cr(III), Ni(II) and Co(II) could be excluded to account for the appearance of the two ME current peaks,

this similarity still holds the possibility that in addition to the reduction of oxygen, Cr(VI) ions may also be reduced at the ME.

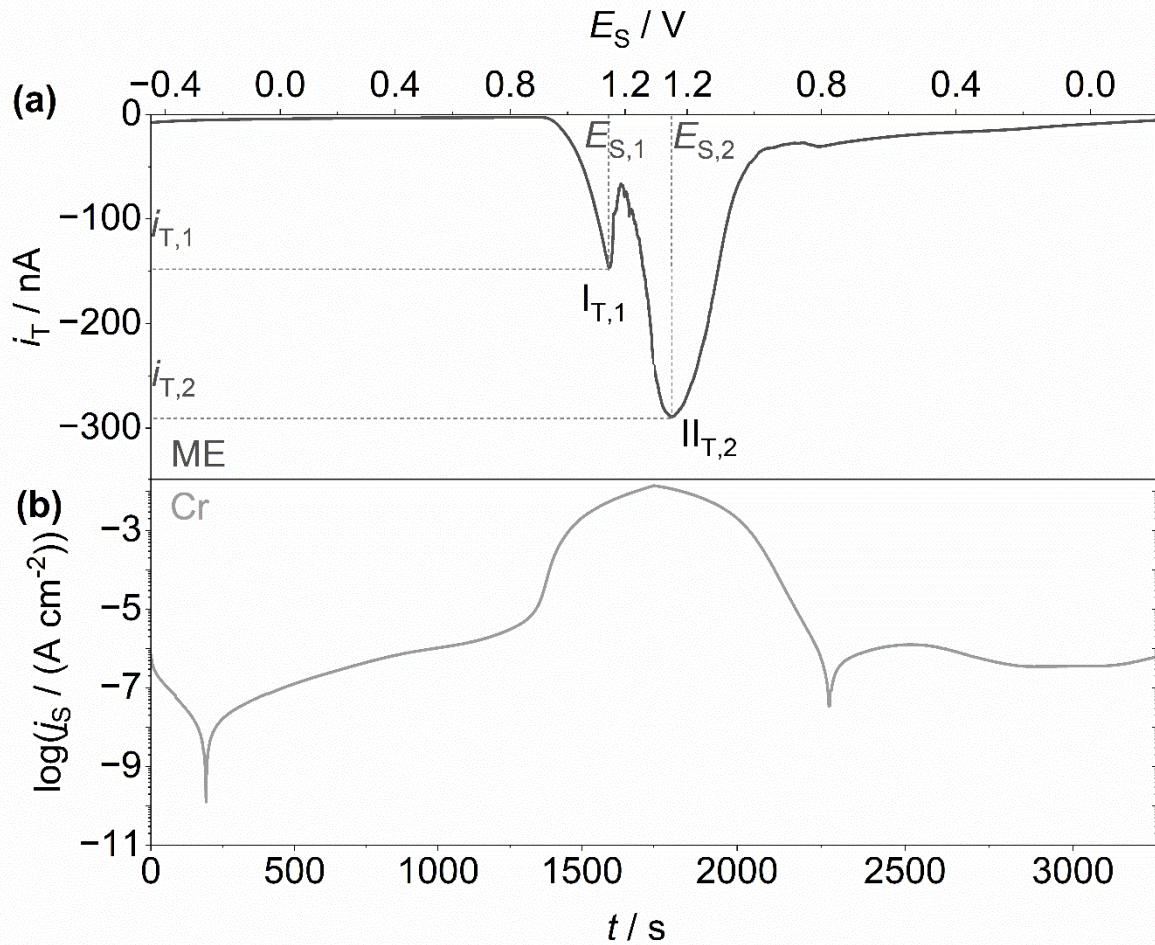


Figure 8.10. TSV-SECM of Cr in 0.1 M NaCl at pH 2 with (a) the ME (Pt disc electrode $r = 5 \mu\text{m}$, $E_T = -0.65 \text{ V}$) current response toward the OER at the sample and (b) the CPP of the Cr sample at 1 mV s^{-1} . Potentials are reported vs. Ag/AgCl/3M NaCl. Adapted with permission from own publication^[326] published by Wiley-VCH GmbH under the terms of the CC BY 4.0 license. Copyright 2024, The Authors.

To understand which electrochemical reactions prevail at the two peak potentials $E_{S,1}$ and $E_{S,2}$, the CrCoNi and Cr sample were chronoamperometrically polarized for 30 min at these potentials. For CrCoNi the chronoamperometric measurements in Figure 8.11 yield current densities of $j_S \approx 5 \text{ mA cm}^{-2}$ and $j_S \approx 20 \text{ mA cm}^{-2}$ at $E_{S,1} = 1.00 \text{ V}$ (Figure 8.11a) and $E_{S,2} = 1.15 \text{ V}$ (Figure 8.11b), respectively. On the pure Cr specimen, the current density increased to $j_S \approx 15 \text{ mA cm}^{-2}$ at $E_{S,2} = 1.30 \text{ V}$ (Figure 8.12b) from $\approx 6 \text{ mA cm}^{-2}$ at $E_{S,1} = 1.15 \text{ V}$ (Figure 8.12a). At $E_{S,1}$ both, CrCoNi and Cr display similar current densities. However, the current density of the CrCoNi surface stabilizes within the first few seconds of polarization at $E_{S,1}$ and remains constant over the duration of the measurement. Furthermore, the chronoamperometric measurement of the CrCoNi at $E_{S,1}$ constitutes the only case where the polarization results in initial capacitive charging. The subsequent constant current response indicates that a steady-state transport-limited reaction such as the OER transpires.^[331] For all other cases, i.e., both, polarizations of Cr and the polarization of CrCoNi at $E_{S,2}$, the current density increases with

time. This result suggests simultaneous surface dissolution and OER while the metal dissolution is most likely the predominant surface reaction.^[332] Compared to CrCoNi, the current density increase for pure Cr is more pronounced due to steeper slopes at both polarization potentials. Through integration of the resulting currents from the voltammetric scan of the TSV and chronoamperometric measurement the respective charges $Q_{e\text{-chem}}$ for CrCoNi and Cr were retrieved and are summarized in Table 8.5.

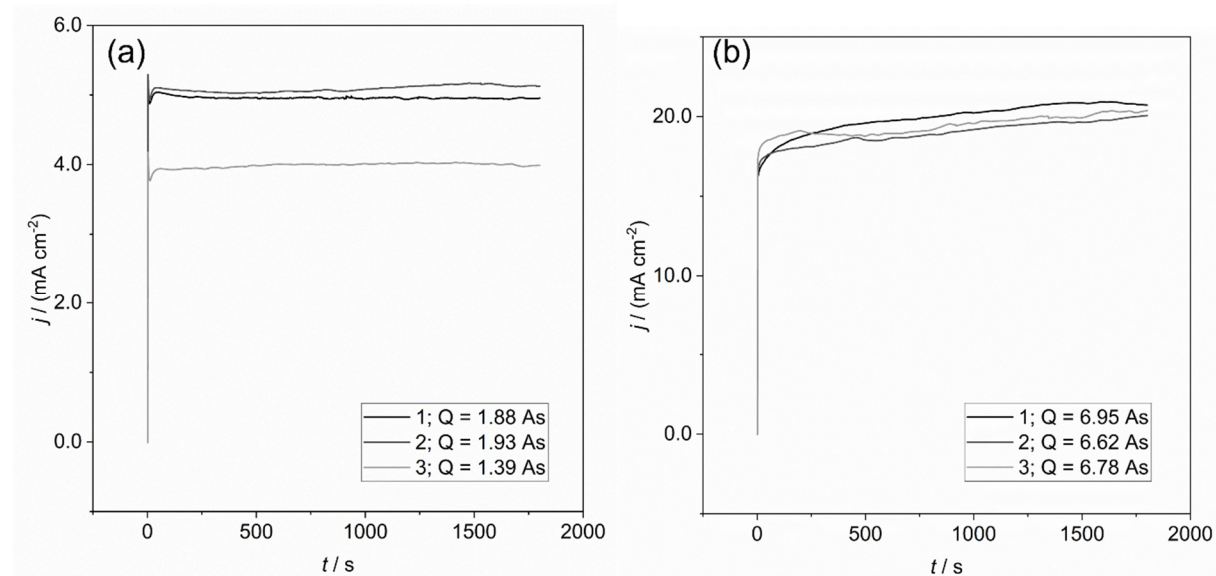


Figure 8.11. (a) Chronoamperometric measurement of CrCoNi in 0.1 M NaCl at pH 2 at $E_{s,1} = 1.0$ V vs. Ag/AgCl/3 NaCl and (b) chronoamperometric measurement of CrCoNi at $E_{s,1} = 1.15$ V vs. Ag/AgCl/3 NaCl. The respective charges (Q) are indicated in the legends and summarized in Table 8.5. Adapted with permission from own publication^[326] published by Wiley-VCH GmbH under the terms of the CC BY 4.0 license. Copyright 2024, The Authors.

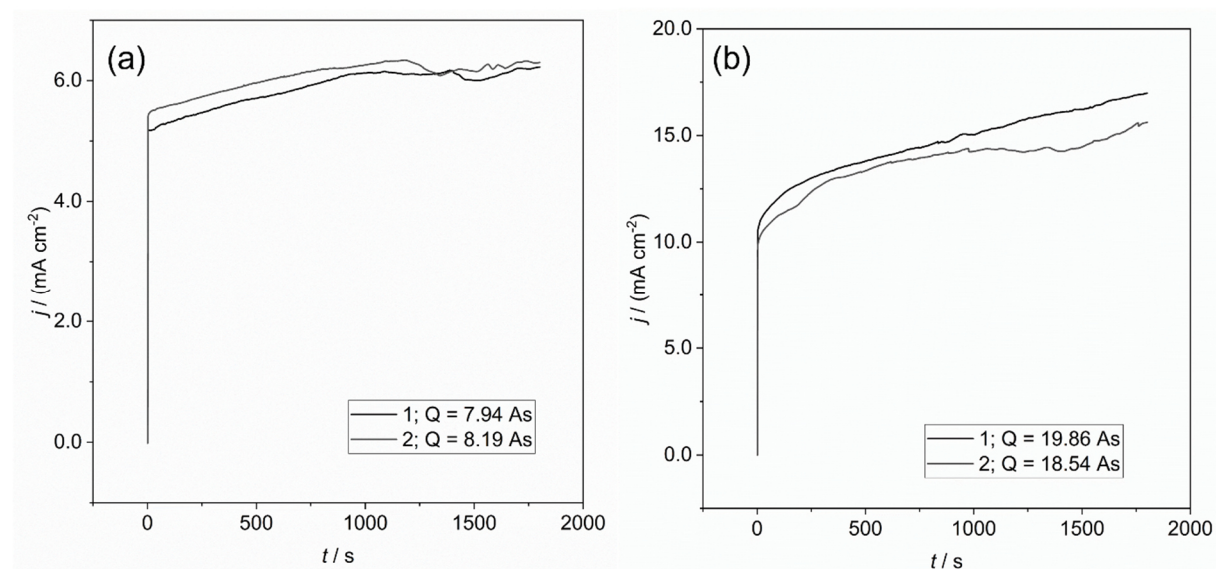


Figure 8.12. (a) Chronoamperometric measurement of Cr in 0.1 M NaCl at pH 2 at $E_{s,1} = 1.15$ V vs. Ag/AgCl/3 NaCl and (b) chronoamperometric measurement of Cr at $E_{s,1} = 1.30$ V vs. Ag/AgCl/3 NaCl. The respective charges (Q) are indicated in the legends and summarized in Table 8.5. Adapted with permission from own publication^[326] published by Wiley-VCH GmbH under the terms of the CC BY 4.0 license. Copyright 2024, The Authors.

In order to better account for the dissolution of Cr as Cr(III) and Cr(VI), UV-Vis spectroscopy of the respective hexavalent Cr(VI) aqua complex was conducted. The

electrolytes after the electrochemical TSV and chronoamperometric measurements were collected and the dissolved metal concentrations were then quantified through ICP-MS, whereas the differentiation of Cr(III) and Cr(VI) was achieved by UV-Vis spectroscopy. This is necessary for the conversion of the dissolved metal ion concentrations into a corresponding charge Q_{ICP} using Equation (8.1). While the number of exchanged electrons n_e can be assumed to be 2 for Ni and Co, the presence of Cr(III) and Cr(VI) requires the corresponding adjustment of $n_{e,Cr}$ to allow for the correct conversion of concentration into charge. Table 10.5 in Appendix 5 summarizes the UV-Vis absorbances and respective concentrations of Cr(III) and Cr(VI) in the electrolytes. Table 8.4 below presents the weighted averages of the exchanged electrons $n_{e,Cr}$ for Cr dissolution retrieved through UV-Vis quantification. Interestingly, after the TSV scan of CrCoNi, only Cr(III) is detected within the electrolyte. This could indicate that formed Cr(VI) during high anodic potentials is reduced back to Cr(III) during scan reversal. The results from the amperometric measurements show an increase in Cr(VI) from $E_{S,1}$ to $E_{S,2}$ for CrCoNi. In contrast, most of the dissolved Cr(VI) for pure Cr is not reduced to Cr(III) during the TSV-SECM scan. Furthermore, Cr preferentially dissolved as Cr(VI) at both peak potentials. With these results, Cr(VI) reduction at the ME cannot be fully excluded, hence CVs were recorded of dissolved K_2CrO_4 at different concentrations and the resulting ME CVs show that Cr(VI) is not reduced at the ME at -0.65 V (Figure 8.13).

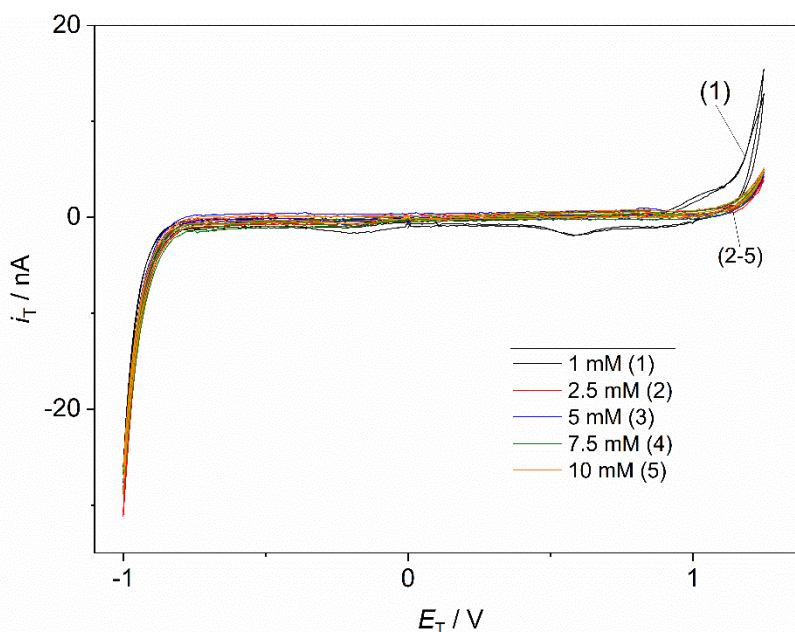


Figure 8.13. CV of K_2CrO_4 at the indicated concentrations in a base electrolyte of 0.1 M KCl at a Pt ME with $r = 5\mu\text{m}$ at a scan rate of 100 mV/s showing no reduction peak of Cr(VI) at -0.65 V vs. Ag/AgCl/3M NaCl.

This suggests that at both peaks, $I_{T,1}$ and $I_{T,2}$, oxygen is reduced at the ME. Since the OER may occur through oxidation of the metal oxides of the passive layer or through oxidation of adsorbed water (see discussion below), the two peaks could represent a shift in the OER reaction mechanism. It should be noted, that it was not investigated whether the OER intermediate product H_2O_2 has formed, and may have also been reduced at the ME.

Table 8.4. Summary of the weighted average numbers of exchanged electrons for Cr dissolution from CrCoNi and pure Cr with standard deviation for the respective experiments

sample	$n_{e,Cr(UV-Vis)}$
CrCoNi _{TSV}	3.00 ± 0
CrCoNi(I _{T,1})	4.37 ± 0.07
CrCoNi (II _{T,2})	5.16 ± 0.15
Cr _{TSV}	5.61 ± 0.03
Cr(I _{T,1})	5.84 ± 0.01
Cr(II _{T,2})	5.87 ± 0.06

Finally, the resulting Cr(III) and Cr(VI) concentrations were employed to determine the weighted average of exchanged electrons as shown in Equation (8.4) to obtain the respective charges through Faradays law (Equation (8.1)).

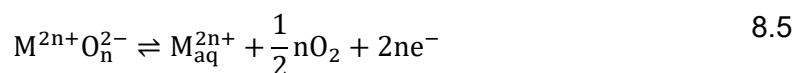
$$n_{Cr} = \frac{c_{Cr(III)}n_{Cr(III)} + c_{Cr(VI)}n_{Cr(VI)}}{c_{Cr,UV}} \quad 8.4$$

This way the theoretical charges Q_{ICP} of metal dissolution retrieved through ICP-MS quantification could be compared to the electrochemical charges Q_{e-chem} while the difference yields the charge Q_{O_2} expended on the OER. The corresponding results in Table 8.5 show that CrCoNi exhibits the highest Faradaic efficiencies ε_{FE} . Its highest $\varepsilon_{FE}(O_2) = 53\%$ is achieved for the TSV-SECM scan. The $\varepsilon_{FE}(O_2)$ value after chronoamperometry is slightly higher for polarization at $E_{S,1}$ than at $E_{S,2}$. The main disparity between the TSV-SECM scans and the chronoamperometric measurements may be the extend of anodic passivation. During the CPP scan, the passive layer grows within the passive regions, whereas the chronoamperometric polarizations were carried out directly at high anodic potentials. If the OER proceeds predominantly through the oxidation of passive layer oxides, the formation of a thicker oxide layer on the CrCoNi surface during TSV-SECM experiments may inhibit metal dissolution and consequentially boost the OER activity.

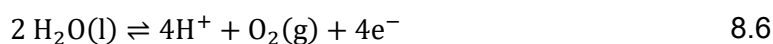
Table 8.5. Derived total charges from the electrochemical measurements ($Q_{e\text{-chem}}$) and ICP-MS (Q_{ICP}) measurements for CrCoNi and pure Cr after TSV-SECM and amperometric measurements with respective Faradaic efficiency ($\alpha(\text{O}_2)$) for the OER.

Sample	$Q_{e\text{-chem}}$ [As cm^{-2}]	Q_{ICP} [As cm^{-2}]	Q_{O_2} [As cm^{-2}]	$\alpha(\text{O}_2) =$ $Q_{\text{O}_2}/Q_{e\text{-chem}}$ [%]
CrCoNi _{TSV}	4.35 ± 0.35	2.02 ± 0.38	2.33 ± 0.38	53.46 ± 4.36
CrCoNi (I _{T,1})	8.95 ± 1.54	5.71 ± 0.90	3.23 ± 0.65	36.01 ± 1.35
CrCoNi(II _{T,2})	34.97 ± 0.85	25.35 ± 1.16	9.62 ± 1.77	27.46 ± 4.57
Cr _{TSV}	4.35 ± 0.20	2.65 ± 0.26	1.16 ± 0.06	30.62 ± 3.25
Cr(I _{T,1})	10.75 ± 0.24	8.78 ± 0.43	1.97 ± 0.20	18.37 ± 2.23
Cr(II _{T,2})	25.60 ± 1.24	20.44 ± 0.46	5.16 ± 0.78	20.11 ± 2.09

To obtain qualitative information on the potential OER reaction mechanisms, Tafel extrapolation of the respective anodic polarization region of the different metal surfaces was conducted.^[333] The diagram in Figure 8.14 displays the respective anodic Tafel slopes of CrCoNi and Cr. For comparison the anodic current densities of CrMnFeCoNi are also included. CrCoNi exhibits an anodic Tafel slope of 55 mV dec⁻¹ in 0.1 M NaCl, while pure Cr exhibits a slightly lower Tafel slope of 42 mV dec⁻¹. Both slopes suggest the participation of metal oxides of the passive film in the OER through the reaction in Equation (8.5).^[297-298]



The steeper slope of CrCoNi may be due to the presence of Co- and Ni-oxide/hydroxide in the passive layer. Even though both oxide species are utilized in OER electrocatalysis,^[334-335] the surface-specific studies on metal passivation of CrCoNi and CrMnFeCoNi in Chapter 7.1.2 suggest that Ni remains metallic.^[78, 192] Higher Tafel slopes may indicate the OER of adsorbed water. In the acidified NaCl electrolyte the respective OER is presented in Equation (8.6).^[297, 336]



In their study on OER catalyst stability, Cherevko et al.^[297] demonstrated a decrease in metal dissolution with an increase in Tafel slope. The slightly higher Tafel slope of CrCoNi may be a result of both mechanisms (via oxide and via adsorbed water) taking place due to the presence of Cr and Co oxides.^[299] However, as both OER and transpassive dissolution occur simultaneously,^[299-300] caution should be taken in interpreting these values. Especially, in the case of CrMnFeCoNi, the steep Tafel slope of 99 mV dec⁻¹ at relatively low potentials could suggest a high electrocatalytic activity. But the TSV-SECM data and the respective ICP-MS results in Chapter 8.2 indicate exclusive metal dissolution. Correspondingly, the steep anodic Tafel slope of CrMnFeCoNi is a result of severe metal dissolution, not of OER activity.

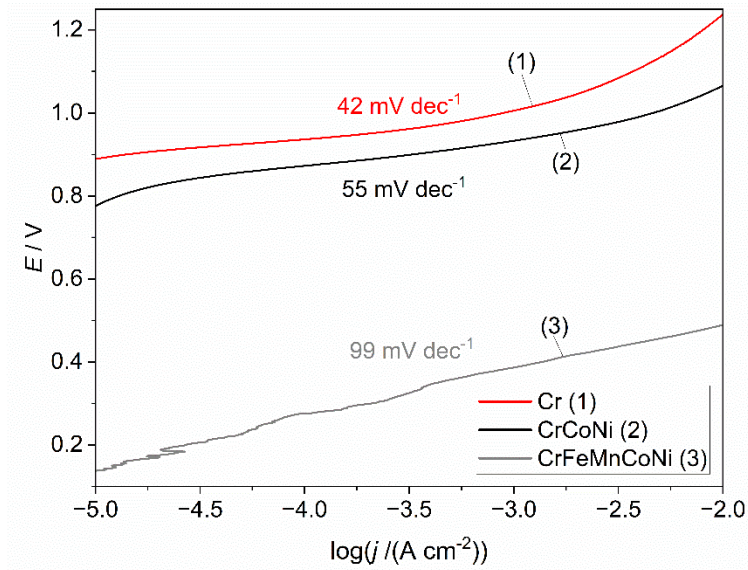
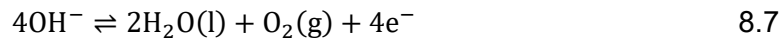


Figure 8.14. Anodic Tafel slopes for (1) Cr, (2) CrCoNi and (3) CrMnFeCoNi in 0.1 M NaCl at pH 2 obtained at a scan rate of 1 mV s^{-1} . The respective Tafel slopes are above the curves. The polarization potentials are recorded vs. Ag/AgCl/ 3M NaCl. Adapted with permission from own publication^[326] published by Wiley-VCH GmbH under the terms of the CC BY 4.0 license. Copyright 2024, The Authors.

8.3.3 Influence of pH

Changing the pH of the 0.1 M NaCl to 6.25, reveals a different TSV-SECM scan. The concomitant increase in OH^- concentration with increasing pH introduces the possibility of the OER to proceed through reaction (8.7).



The ME response shows the expected single peak $I_{\tau,1}$ for the OER at $E_{s,1} = 1.02 \text{ V}$ which is again slightly shifted into the reversed scan of the TSV-SECM diagram in Figure 8.15. The OER peak current is more than 10 times lower than at pH 2. However, this may also be due to deviations in the sample-tip-distance. The polarization curve of the CrCoNi substrate is comparable to the results in Chapter 7.2.1. While no clear passive region is evident in the forward scan, better re-passivation is observed during the reverse scan. The increase in pH of the 0.1 M NaCl from 2 to 6.25 suggests a decrease in the efficiency of the OER within the transpassive region.

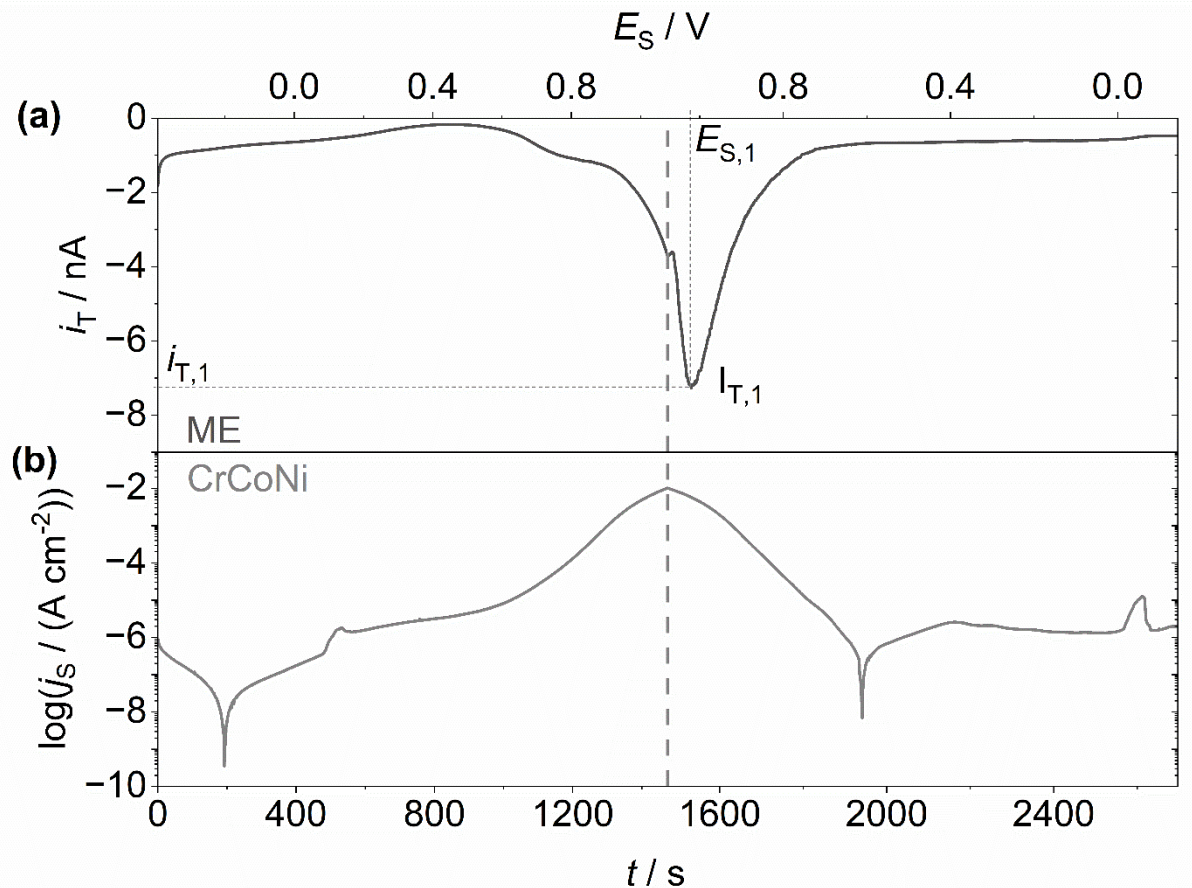


Figure 8.15. TSV-SECM of CrCoNi in 0.1 M NaCl at pH 6.25 with (a) the ME (Pt disc electrode $r = 5 \mu\text{m}$, $E_T = -0.65$ V) current response toward the OER at the sample and (b) the CPP of the CrCoNi sample at 1 mV s^{-1} . Potentials are reported vs. Ag/AgCl/3M NaCl.

However, increasing the pH of the electrolyte further leads to improved OER efficiency of the CrCoNi surface. Looking first at the polarization curve of the CrCoNi substrate in 0.1 M NaCl at pH 12 (Figure 8.16b), two current density plateaus are distinguishable in the forward scan of the CPP. The initial plateau occurs from 0.42 V to 0.63 V at $j_s = 12.0 \mu\text{A cm}^{-2}$ and the second plateau ranges from 0.76 to 0.98 V at $j_s = 922.7 \mu\text{A cm}^{-2}$. Inspecting the respective ME current response, it becomes evident that at pH 12 the OER in 0.1 M NaCl coincides with the second plateau. While the occurrence of another region of constant current density, despite increasing potential, is referred to as secondary passivation in the corrosion literature,^[301] this is clearly not the case in this instance. Since OH^- is readily available in the alkaline 0.1 M NaCl electrolyte, the second plateau in current density represents the limiting current density for OH^- oxidation to oxygen through Equation (8.7). The TSV-SECM scan shows a clear peak of the ME response that completely coincides with the respective limiting current density at the CrCoNi substrate. Once the current density increases again due to the application of even higher anodic potentials, the ME current drops sharply and then increases until the apex potential. The sharp drop in ME current and subsequent rise could be due to a change in the predominant anodic reaction from OER to metal dissolution, while the OER does not

completely cease. The formation of bubbles which could cause a sharp drop in the ME current response has not been observed.

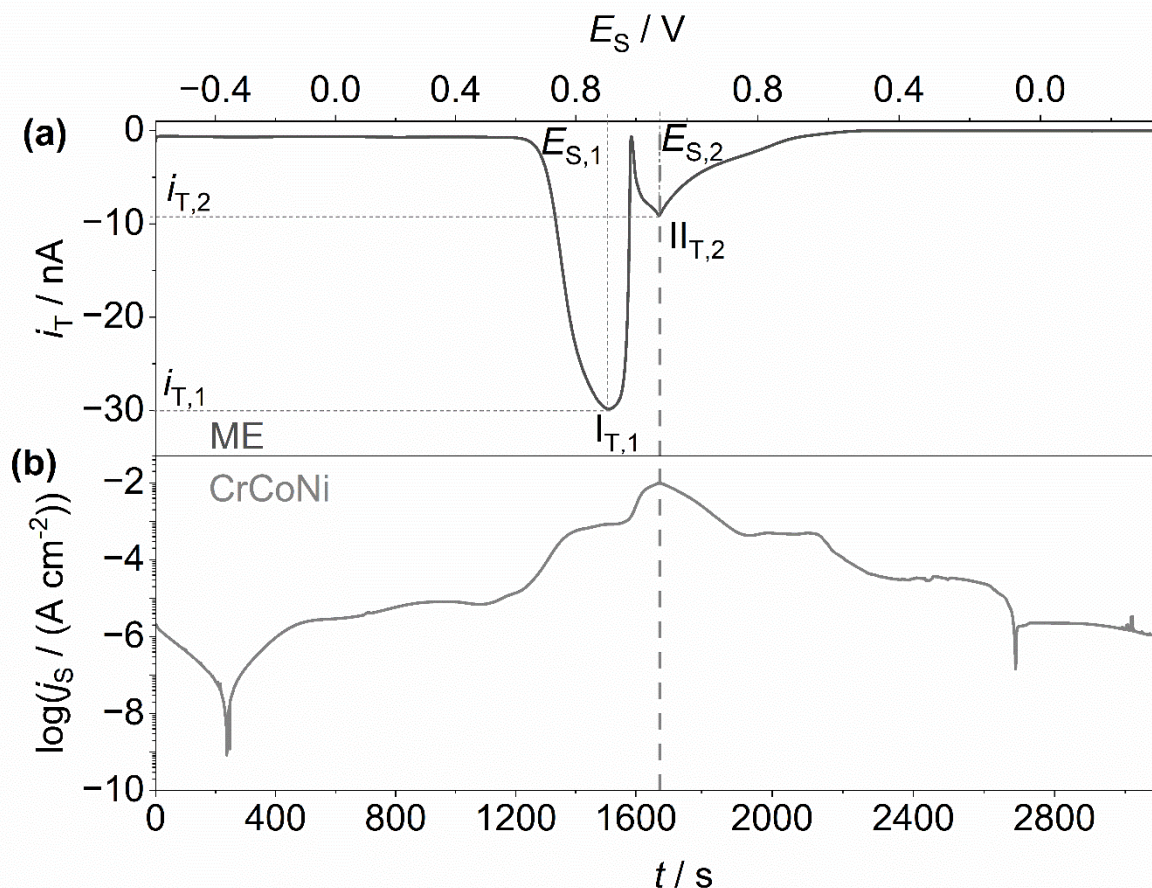


Figure 8.16. TSV-SECM of CrCoNi in 0.1 M NaCl at pH 12 with (a) the ME (Pt disc electrode $r = 5 \mu\text{m}$, $E_T = -0.65 \text{ V}$) current response toward the OER at the sample and (b) the CPP of the CrCoNi sample at 1 mV s^{-1} . Potentials are reported vs. Ag/AgCl/3M NaCl. The diagram is adapted with permission from own publication^[327] published by Wiley-VCH under the terms of the CC BY 4.0 license. Copyright 2024, The Authors.

While Pourbaix diagrams suggest that Cr predominantly forms Cr(III) at pH 6.25 and 12 at higher potentials, Cr(VI) is also a possible oxidation state. To deduce the oxidation state of the dissolved Cr-ions, the solutions were investigated by means of UV-Vis spectroscopy. The results show that after TSV-SECM only Cr(VI) is present in the electrolytes. Hence, for the conversion of the ICP-MS retrieved concentrations into charge Q_{ICP} , the number of exchanged electrons for Cr dissolution was assumed to be $n_{e,\text{Cr}} = 6$, while n_e for Co and Ni was assumed to be 2. The respective Cr-ion concentrations determined through UV-Vis spectroscopy are summarized in Table 10.5 in Appendix 6.

Table 8.6 below outlines $Q_{e\text{-chem}}$ and Q_{ICP} . As described above, the difference between the two charges may be attributed to the OER. The Faradaic efficiency in both electrolytes of $\delta_{\text{FE}}(\text{O}_2) = 36 \%$ and $\delta_{\text{FE}}(\text{O}_2) = 44 \%$ in pH 6.25 and 12, respectively, differ significantly. Compared to the $\delta_{\text{FE}}(\text{O}_2) = 53 \%$ in the acidic NaCl electrolyte, the OER efficiency of CrCoNi in 0.1 M NaCl exhibits a strong dependence on the pH of the electrolyte, while the close to neutral conditions seem to render the least efficient system for OER. While no substantial

passive region is observed for the MPEA at pH 6.25, the CPP presents distinct potential ranges where no changes in current are observed at pH 2 and 12. In turn this would indicate that the oxides of the passive film do participate in the OER.

Table 8.6. Derived total charges from the electrochemical measurements ($Q_{e\text{-chem}}$) and ICP-MS (Q_{ICP}) measurements for the CrCoNi TSV-SECM and amperometric measurements with respective Faradaic efficiency ($\varepsilon_{\text{FE}}(\text{O}_2)$) for the OER in 0.1 M NaCl at pH 6.25 and 12.

pH	$Q_{e\text{-chem}}$ [As cm ⁻²]	Q_{ICP} [As cm ⁻²]	Q_{O_2} [As cm ⁻²]	$\varepsilon_{\text{FE}}(\text{O}_2) =$ $Q_{\text{O}_2}/Q_{e\text{-chem}}$ [%]
6.25	1.71 ± 0.01	1.10 ± 0.06	0.61 ± 0.08	35.66 ± 4.18
12	1.69 ± 0.13	1.00 ± 0.09	0.77 ± 0.10	43.65 ± 4.11

The significance of the Tafel slope in the transpassive region has been discussed previously for the results in 0.1 M NaCl at pH 2 in Chapter 8.3.2. The anodic slope of CrCoNi was found to be 55 mV dec⁻¹ (Figure 8.14) which generally indicates the participation of metal oxides of the passive film in the OER through the reaction in Equation (8.5).^[297-298] However, the steep slope for CrMnFeCoNi indicates that the interpretation of such data needs to be treated with some caution. Nevertheless, Figure 8.17 shows the respective slopes for the transpassive current densities of CrCoNi in 0.1 M NaCl at pH 6.25 and pH 12. At pH 6.25, the Tafel slope of 120 mV dec⁻¹ would suggest the OER of adsorbed water. While in acidic media the OER proceeds through Equation (8.6), in neutral and alkaline media the OER proceeds through Equation (8.7).

Since pH 6.25 is below neutral, the OER could also proceed through Equation (8.6). While it is a complex task to determine which reaction leads to the evolution of oxygen in this medium, it must be noted that despite the high anodic Tafel slope, the lowest $\varepsilon_{\text{FE}}(\text{O}_2)$ was determined for this electrolyte. In contrast, the transpassive region of CrCoNi in the alkaline electrolyte presents three different anodic Tafel slopes. While the Tafel slope of 600 mV dec⁻¹ coincides with the OER peak in the ME response of the TSV-SECM scan and suggests that the OER proceeds through Equation (8.7), the other two slopes are significantly lower. Since the OER likely proceeds through the oxidation of adsorbed OH⁻, it seems plausible for the reaction in Equation (8.7) to be predominant in the alkaline medium. Despite their usefulness and ease of acquisition, the obtained Tafel slopes at high anodic potentials should be interpreted carefully, especially, considering that both the OER and metal dissolution contribute toward the measured current densities.

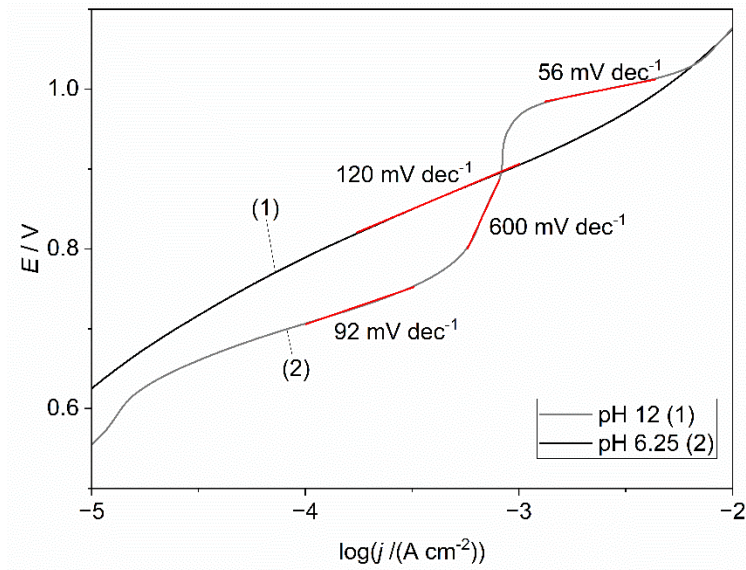


Figure 8.17. Anodic Tafel slopes for CrCoNi in 0.1 M NaCl at (1) pH 6.25 and (2) pH 12 obtained at a scan rate of 1 mV s^{-1} . The respective Tafel slopes are plotted next to the curves. The polarization potentials are recorded vs. Ag/AgCl/ 3M NaCl.

8.3.4 Local Dissolution Behavior

CrCoNi has demonstrated high corrosion resistance in both NaCl and H_2SO_4 . The results in Chapter 7 show that its mode of corrosion is intergranular corrosion. EC-AFM images were recorded during the forward scan of the CPP of CrCoNi to investigate the onset of intergranular corrosion. Figure 8.18 illustrates EC-AFM images of the CrCoNi MPEA during the polarization scan in 0.1 M NaCl at pH 2. While the topography in Figure 8.18i, shows the initial surface in air, the topographies recorded at points a to c show no changes, confirming the stable nature of the MPEA. At point d ($E = 0.87 \text{ V}$), intergranular corrosion can be monitored. While the progression to higher potentials does not severely deteriorate the CrCoNi surface as can be seen in Figure 8.18e, the extend of intergranular corrosion minimally increases. This result correlates with the findings of previous analyses that established the corrosion resistance of CrCoNi.

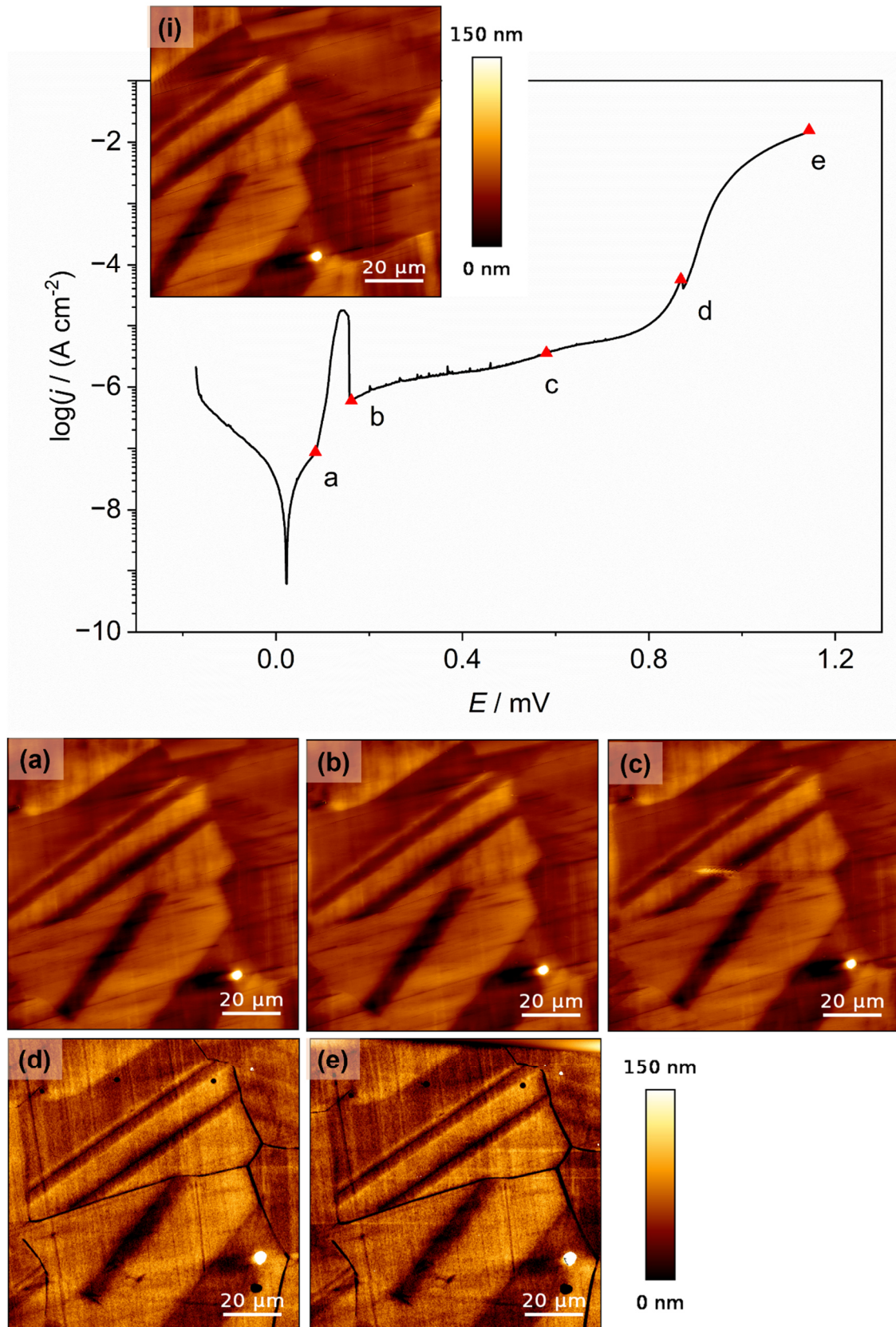


Figure 8.18. EC-AFM topographies of CrCoNi in 0.1 M NaCl at pH 2 recorded at the respective points: (i) initial surface in air, (a) after OCP, (b) passive region, (c) higher passive region, (d) transpassive region, and (e) higher transpassive region. The CPP scan was conducted in intervals at 1 mV s^{-1} . Potentials are reported vs. Ag/AgCl/3M NaCl. Adapted with permission from own publication^[326] published by Wiley-VCH GmbH under the terms of the CC BY 4.0 license. Copyright 2024, The Authors.

To further investigate the properties of the metal surface at different potentials, electrochemical impedance spectroscopy (EIS) was carried out from below the OCP up to transpassive potentials. The acquired EIS spectra are shown in Figure 10.4 to Figure 10.8 in Appendix 7. Based on similar electrochemical impedance studies on stainless steels,^[286, 337] the CrCoNi alloy displays a high corrosion resistance without undergoing an apparent secondary passivation in the transpassive regime at pH 2 when considering the respective polarization curve.^[338] The EIS spectra in Figure 10.4 to Figure 10.6 indicate a perfectly passivated metal surfaces while the magnitude of impedance reaches values of $|Z| = 0.25 \text{ M}\Omega \text{ cm}^2$ at 0.01 Hz in Figure 8.19 at polarizations below the transpassive region (-0.25 to 0.4 V). Inspecting the EIS spectra at transpassive polarizations (1.0 V and 1.15 V) in Figure 10.7 and Figure 10.8, an inductive loop in the Nyquist plots is recorded and the Bode plots suggest that currents are mainly impeded by the solution resistance, implying an increase in ion-conductivity of the oxide film.^[337] Moreover, inspecting the impedance at low frequencies (Figure 8.19), a significant decrease by four orders of magnitude in $|Z| = 0.25 \text{ M}\Omega \text{ cm}^2$ is measured at polarizations positive of 1.0 V. This may indicate a nearly resistance-free charge transfer at the CrCoNi electrode. Interpreted together with the EC-AFM results in Figure 8.18, the strong inductive response and low charge transfer resistance in the EIS data suggest fast kinetics for either metal dissolution, OER or both.^[339] The influences of the dissolution at the grain boundaries cannot be excluded to affect the EIS spectra.

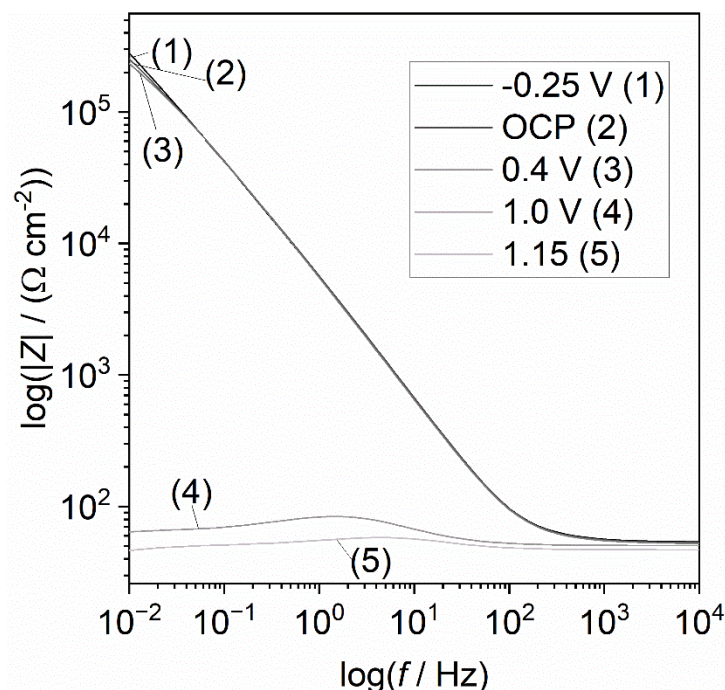


Figure 8.19. The impedance spectra of CrCoNi in 0.1 M NaCl pH 2 recorded at different dc voltages vs. Ag/AgCl/3 M NaCl showing the change of the CrCoNi surface reactivity with applied potential. Adapted with permission from own publication^[326] published by Wiley-VCH GmbH under the terms of the CC BY 4.0 license. Copyright 2024, The Authors.

Compared to pH 2, the topographical changes of CrCoNi through EC-AFM in pH 6.25 and pH 12 in Figure 8.20 and Figure 8.21 show that the onset of intergranular corrosion is shifted to approx. 1.0 V. In the acidic medium, intergranular corrosion sets in at 0.87 V. In contrast to the pH 2 electrolyte, a change in surface smoothness is noticeable in pH 6.25 and 12 starting at point e, which implies the onset of corrosion. While this preceding change in surface smoothness was not observed at pH 2, it may have been missed. Nevertheless, all EC-AFM measurements demonstrate that the corrosion mechanism does not change despite the change in pH of the electrolyte. Correlating the respective onsets of intergranular corrosion with the peak potential $E_{s,1}$ implies the concomitance of OER and transpassive metal dissolution of CrCoNi at high anodic potentials.

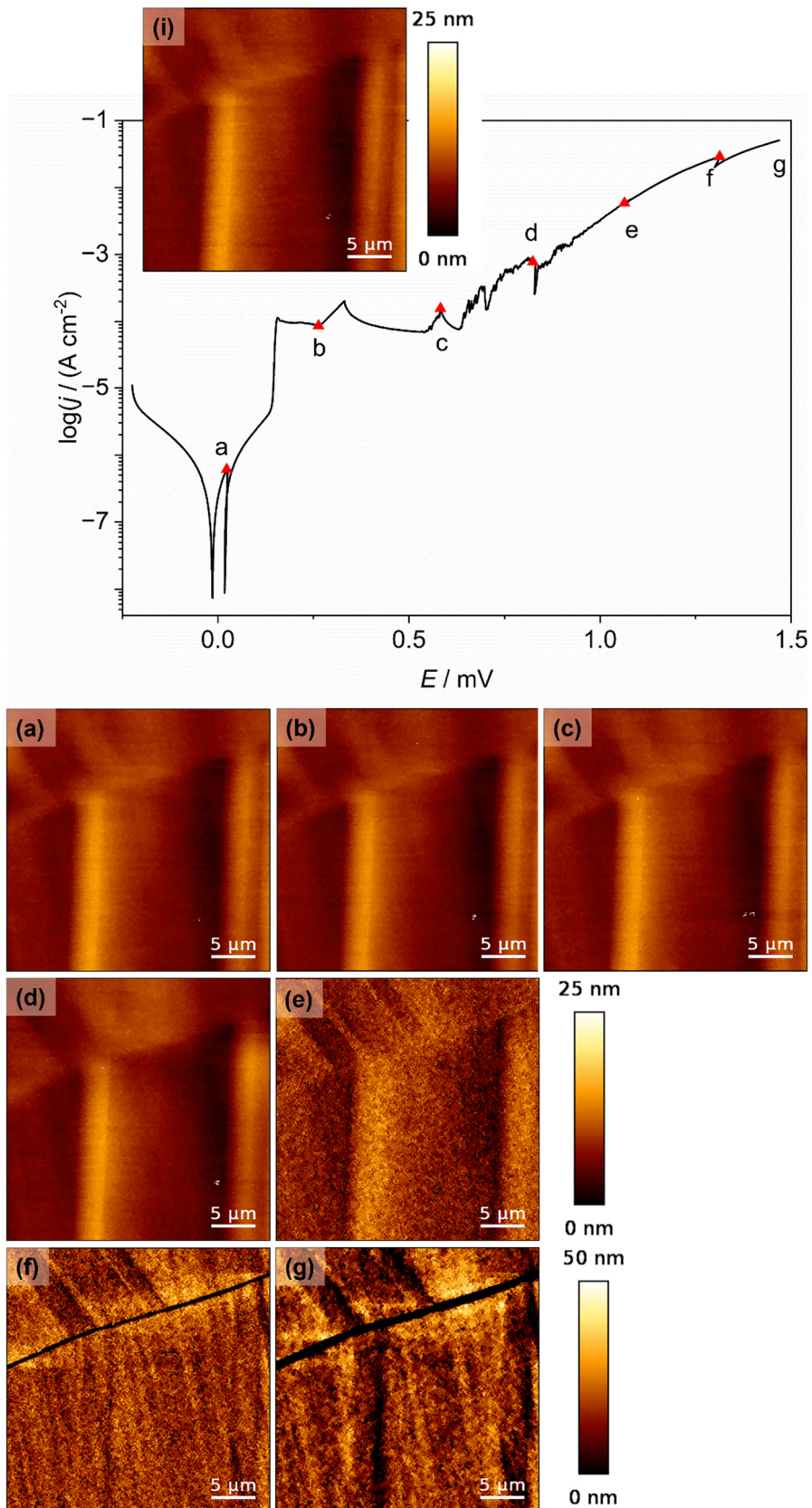


Figure 8.20. EC-AFM topographies of CrCoNi in 0.1 M NaCl at pH 6.25 recorded at the respective points: (i) initial surface in air, (a) after OCP, (b) passive region, (c) higher passive region, (d) transpassive region, (e) higher transpassive region with surface roughening, (f) higher transpassive region with intergranular corrosion and (g) higher transpassive region with progressed intergranular corrosion. The CPP scan was conducted in intervals at 1 mV s^{-1} . Potentials are reported vs. Ag/AgCl/3M NaCl.

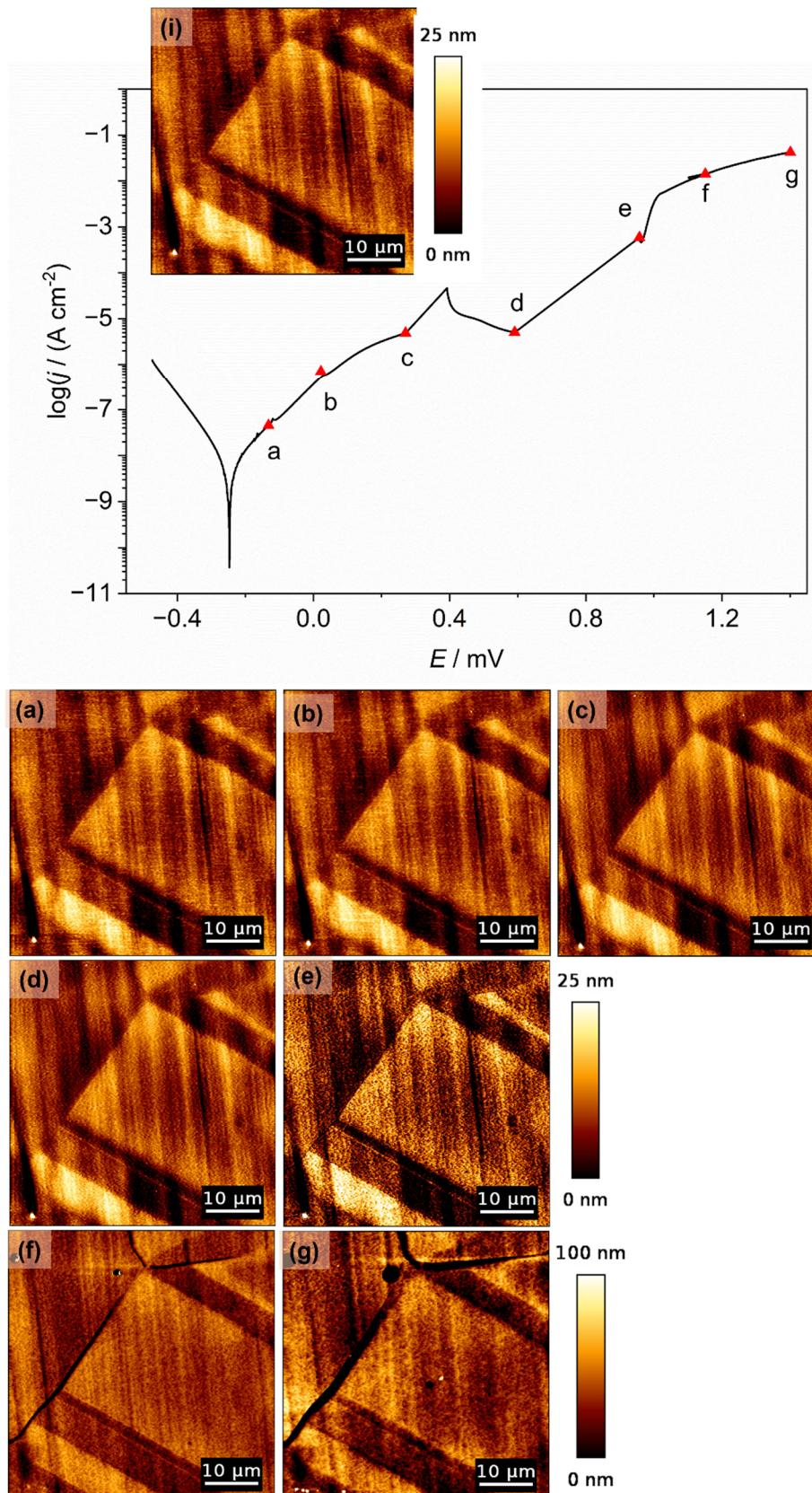


Figure 8.21. EC-AFM topographies of CrCoNi in 0.1 M NaCl at pH 12 recorded at the respective points: (i) initial surface in air, (a) after OCP, (b) passive region, (c) higher passive region, (d) transpassive region, (e) higher transpassive region with surface roughening, (f) higher transpassive region with intergranular corrosion and (g) higher transpassive region with progressed intergranular corrosion. The CPP scan was conducted in intervals at 1 mV s^{-1} . Potentials are reported vs. Ag/AgCl/3M NaCl. The diagram is adapted with permission from own publication^[327] published by Wiley-VCH under the terms of the CC BY 4.0 license. Copyright 2024, The Authors.

8.4 The Influence of High Anodic Potentials on CrCoNi compared to CrFeNi in simulated seawater

Since seawater is such an abundant resource, it may seem reasonable to consider its use for electrochemical applications for water splitting with corrosion-resistant MPEA electrodes. The high concentration of Cl^- ($c(\text{Cl}^-) = 0.6 \text{ M}$) deems seawater highly corrosive to most metals and alloys.^[340] However, the MPEA CrCoNi demonstrates excellent corrosion resistance in chloride-containing media as illustrated in Chapters 7.1 and 8.3 which renders the alloy a viable electrode material in seawater electrolysis. The increased use of Co in electronics and batteries,^[188] cause this metal to be relatively expensive in comparison.^[189] Co is mainly sourced in the Democratic Republic of Congo and often under unethical work conditions for miners.^[188, 190] To circumvent employing Co in the high concentrations as used for CrCoNi, another MPEA, FeCrNi, was investigated for its corrosion resistance and transpassive behavior in artificial seawater.

In Chapter 3, it has been described that the concept of MPEAs is in fact not novel. While simulations and improved technology allow for deeper investigations of the vast compositional space that the phase diagrams of MPEAs offer, alloys with similar composition to equi-molar CrFeNi have been used industrially for many years. Typically known as high-alloyed special steels, FeNiCr® and NiCroFer® are registered trademark alloys with high corrosion resistance and find application in highly oxidizing environments.^[341-342] FeNiCr® 28 exhibits good stability in seawater and encompasses approx. 30 % Ni, 26% Cr and 28% Fe while also comprising small amounts of Cu and Mo.^[341] Considering the definitions of MPEAs in Chapter 3, they designate such alloys as MPEAs. The equimolar CrFeNi MPEA employed to compare its electrochemical performance in artificial seawater with CrCoNi was manufactured in-house through arc-melting and subsequent heat treatment.

To evaluate the general corrosion behavior of CrCoNi and FeCrNi, the respective CPPs were recorded and are displayed in Figure 8.22 and Figure 8.23. First looking at the CPP of CrCoNi in Figure 8.22, E_{corr} is situated at -0.31 V while $j_{\text{corr}} = 2.31 \times 10^{-8} \text{ A cm}^{-2}$. Since no primary passivation peak appears, the MPEA passivates spontaneously in artificial seawater which is in agreement with results in 0.1 M NaCl . A passive region is discernible from $E = 0.04 \text{ V}$ to 0.31 V after the current density seems to increase in stages with minimal plateaus resulting at $E_{\text{p},1} = 0.56 \text{ V}$ and $E_{\text{p},2} = 0.78 \text{ V}$. While in 0.1 M NaCl at pH 12 similar features of constant current densities within the transpassive region were observed (see Figure 8.16), the small plateaus in artificial seawater range over 0.05 V only. This stabilization of current densities seems to be an event that may be related to the electrolyte pH because artificial seawater has an alkaline pH of 8.2. Furthermore, no sharp increase in current density is observed in the transpassive region of CrCoNi. Reversing the scan, as indicated by the arrows leads to lower current densities than on the forward scan, i.e., a negative hysteresis results,

suggesting stronger surface passivation upon the scan reversal. The cross over occurs at a higher potential ($E_{cr} = 0.35$ V) in artificial seawater, whereas the current densities in the reverse scan remain below current densities in the forward scan in NaCl electrolytes of lower concentration discussed in Chapter 7.1.

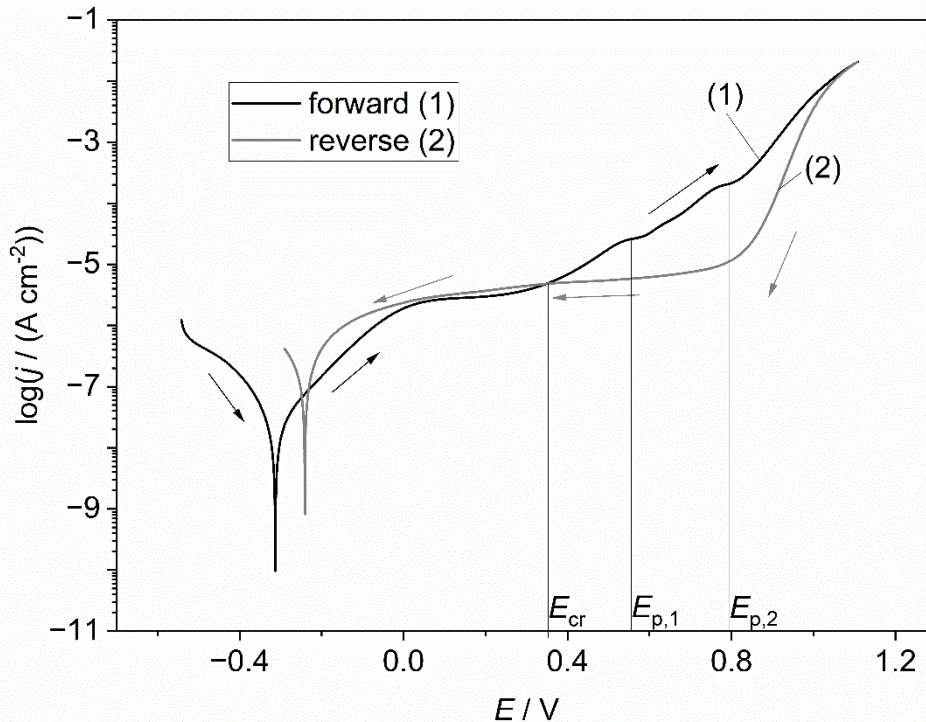


Figure 8.22. CPP scan of CrCoNi in artificial seawater recorded at 1 mV s^{-1} vs. Ag/AgCl/3M NaCl. Adapted with permission from own publication^[326] published by Wiley-VCH GmbH under the terms of the CC BY 4.0 license. Copyright 2024, The Authors.

At a first glance the CPP of the CrFeNi MPEA in Figure 8.23 reveals a different electrochemical behavior in artificial seawater than CrCoNi. CrFeNi also displays spontaneous passivation, but no clear passive region is distinguishable. However, the current densities rise at a low rate after the E_{corr} at $E = -0.22$ V up to $E = 0.73$ V, after which it decreases slightly until the $E_b = 0.92$ V. Upon E_b , the current densities increase steeply within the transpassive region, almost linearly. The positive hysteresis as a result of higher current densities in the reverse scan suggests that pitting corrosion may have occurred on the CrFeNi surface. In contrast to CrCoNi, a re-passivation occurs at $E_{rp} = 0.84$ V where the reversed and forward scan cross. In comparison to CrCoNi, CrFeNi exhibits inferior corrosion resistance due to the absence of a passive region and the respective indicators for pitting corrosion.

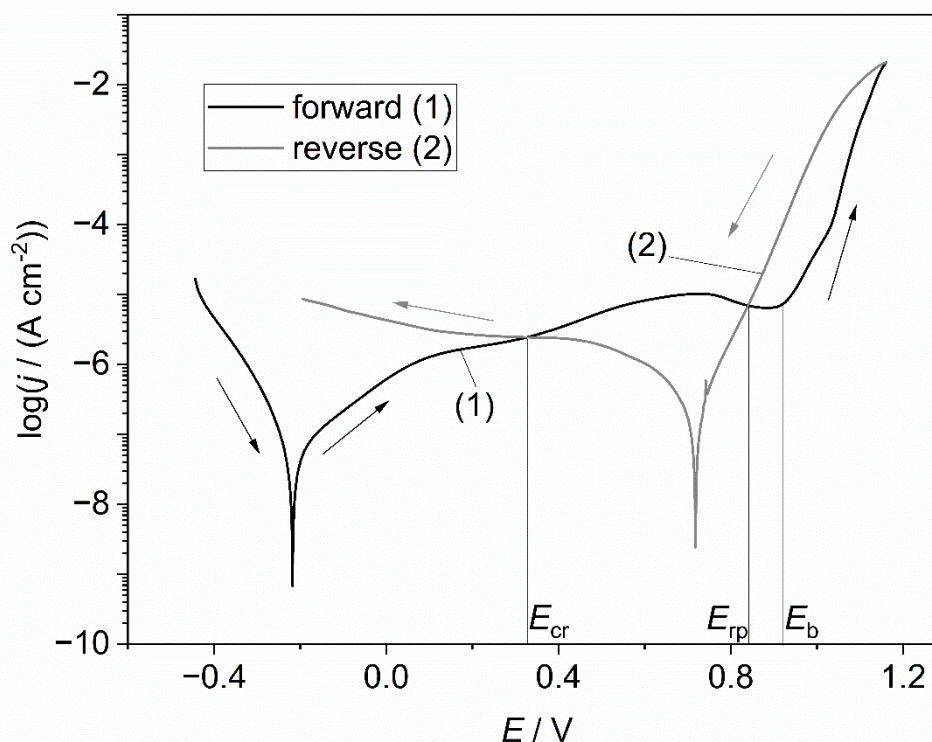


Figure 8.23. CPP scan of CrFeNi in artificial seawater recorded at 1 mV s^{-1} vs. Ag/AgCl/3M NaCl.

In analogy to the experiments conducted in Chapter 8.3, TSV-SECM scans were monitored to elucidate whether CrCoNi and CrFeNi may be potential electrode materials for water splitting in seawater. Figure 8.24 depicts the CPP graph of CrCoNi with the respective ME current response towards evolved oxygen. From the diagram it becomes apparent that the ME current begins to rise above $E = 0.76 \text{ V}$ which coincides with the second small plateau of the transpassive region. The ME current maximum concurs with the apex potential at $E_{S,1} = 1.1 \text{ V}$, and is minimally shifted to the reversed scan. This suggests that the OER peak potential $E_{S,1}$ may be higher than what was recorded in the TSV-SECM scan.

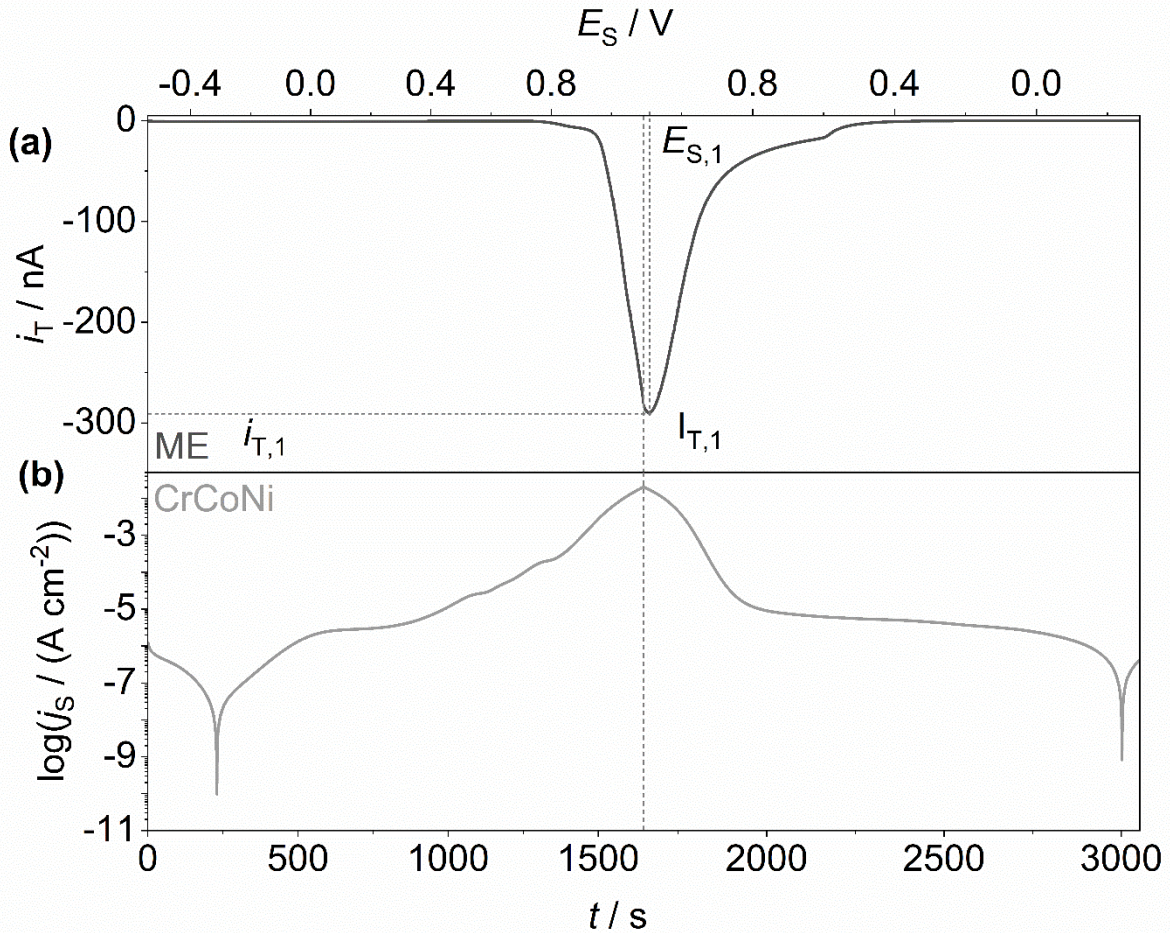


Figure 8.24. TSV-SECM of CrCoNi in artificial seawater with (a) the ME (Pt disc electrode $r = 5 \mu\text{m}$, $E_T = -0.65 \text{ V}$) current response toward the OER at the sample and (b) the CPP of the CrCoNi sample at 1 mV s^{-1} . Potentials are reported vs. Ag/AgCl/3M NaCl. Adapted with permission from own publication^[326] published by Wiley-VCH GmbH under the terms of the CC BY 4.0 license. Copyright 2024, The Authors.

The TSV-SECM scan for the CrFeNi MPEA is presented in Figure 8.25 and shows two OER peaks in the ME response. One before the apex potential at $E_{S,1} = 1.1 \text{ V}$ and one after the apex potential $E_{S,2} = 1.0 \text{ V}$. The noise observed in the ME response may be the result of either corrosion product diffusing from CrFeNi surface or gaseous oxygen bubbles that disturbed the ME current signal. However, bubble formation was not visible during the experiment and would most probably lead to more severe fluctuations in the ME current. In comparison to the TSV-SECM on CrCoNi, the detection of evolving oxygen sets in at $E = 1.0 \text{ V}$ for CrFeNi which is 0.24 V higher than for CrCoNi.

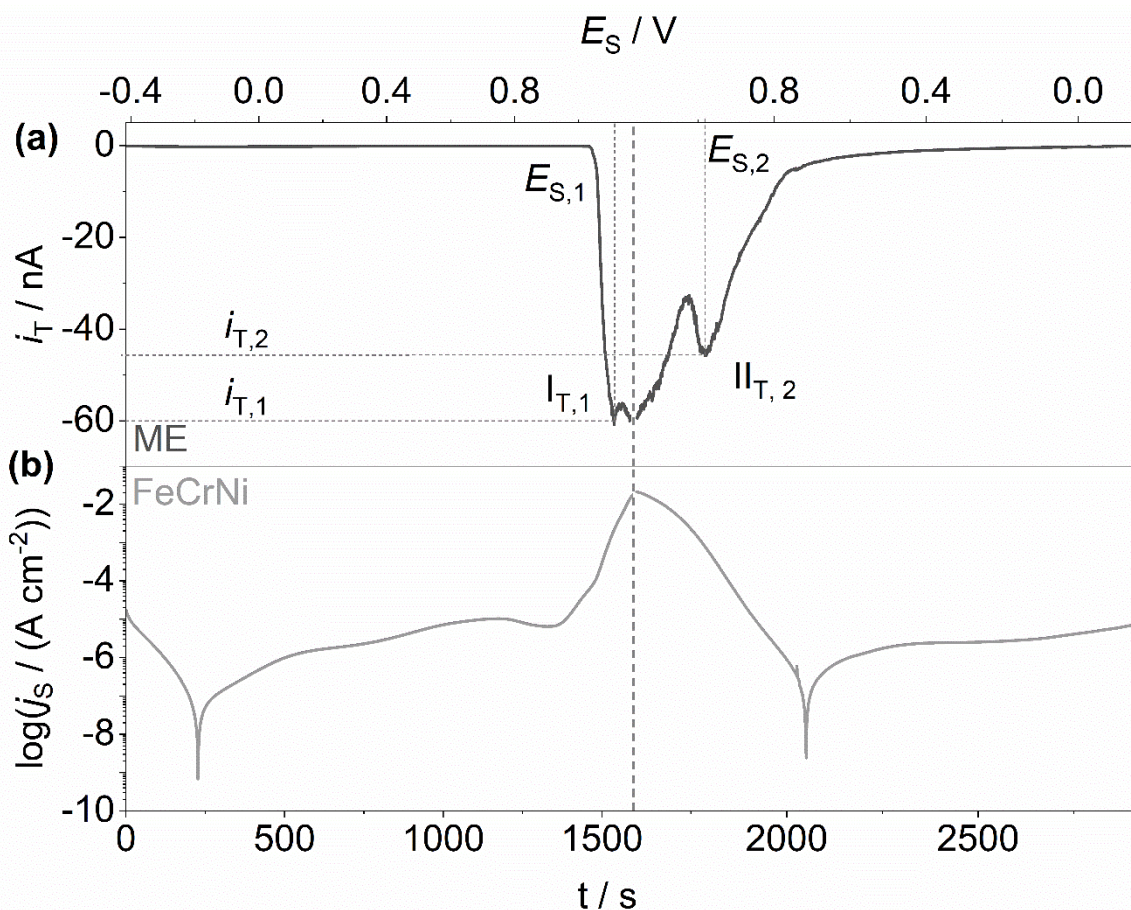


Figure 8.25. TSV-SECM of CrCoNi in artificial seawater with (a) the ME (Pt disc electrode $r = 5 \mu\text{m}$, $E_T = -0.65 \text{ V}$) current response toward the OER at the sample and (b) the CPP of the CrCoNi sample at 1 mV s^{-1} . Potentials are reported vs. Ag/AgCl/3M NaCl.

Based on the transpassive behavior described in the previous chapters, the electrolytes were also quantified through ICP-MS after the TSV-SECM scan. In reference to the UV-Vis results of the dissolution of Cr from CrCoNi in 0.1 M NaCl at pH 6.25 and 12 in Appendix 6, it has been assumed that Cr dissolves as Cr(VI) from CrCoNi and CrFeNi in artificial seawater. Furthermore, Fe from CrFeNi is assumed to dissolve as Fe(III), based on the Pourbaix diagram of pure Fe. The respective charges $Q_{\text{e-chem}}$ and Q_{ICP} are listed in Table 8.7. While the difference yields Q_{O_2} expended for OER, the results indicate that CrFeNi exhibits a higher Faradaic efficiency for the OER in artificial seawater. Compared to the Faradaic efficiencies exhibited by CrCoNi in different 0.1 M NaCl media, the Faradaic efficiencies of the two MPEAs in artificial seawater are significantly lower. To fully evaluate the viability of these two MPEAs in such a corrosive medium, further analyses are necessary, including surface morphology studies such as EC-AFM. While the oxidation state of dissolving metal may be assumed by employing the data compiled in Pourbaix diagrams, such thermodynamic equilibria may change with the alloying and electrolyte composition. Nevertheless, the CrFeNi MPEA seems to possess comparable electrochemical properties to CrCoNi and may be a viable option to replace the CrCoNi MPEA when Co should be excluded from the alloy.

Table 8.7. Derived total charges from the electrochemical measurements ($Q_{e\text{-chem}}$) and ICP-MS (Q_{ICP}) measurements for the CrCoNi and CrFeNi MPEAs in artificial seawater with respective Faradaic efficiency ($\alpha(\text{O}_2)$) for the OER.

alloy	$Q_{e\text{-chem}}$ [As cm^{-2}]	Q_{ICP} [As cm^{-2}]	Q_{O_2} [As cm^{-2}]	$\alpha(\text{O}_2) =$ $Q_{\text{O}_2}/Q_{e\text{-chem}}$ [%]
CrCoNi	2.96 ± 0.02	2.55 ± 0.01	0.41 ± 0.01	13.89 ± 0.32
FeCrNi	2.39 ± 0.23	1.74 ± 0.13	0.66 ± 0.10	27.30 ± 1.45

8.5 Conclusion

In this chapter the electrochemical behavior of the MPEAs CrMnFeCoNi, CrCoNi and CrFeNi have been examined within the transpassive region, i.e., at high anodic potentials. For the CrMnFeCoNi alloy, the application of potentials above E_{corr} leads to material degradation through pitting corrosion in 0.1 M NaCl at different pH levels. While the corrosion literature suggests that water splitting may also occur within the transpassive region, this is not observed for CrMnFeCoNi. Furthermore, EC-AFM imaging during polarization scans confirms the rapid deterioration of the material. This leads to the conclusion that CrMnFeCoNi exhibits no corrosion resistance in NaCl electrolytes and should not be used for applications in chloride-containing media.

On the contrary, the results for the CrCoNi MPEA in 0.1 M NaCl electrolytes at varying pH levels indicate that the OER and metal dissolution are concomitant processes at high anodic potentials within the transpassive region. These results are in agreement with emerging research on noble OER catalysts for which metal dissolution is also observed when applying the respective OER potentials. The increase in pH seems to result in a change in the OER mechanisms. While data retrieved for the OER in 0.1 M NaCl at pH 2 suggests the participation of the passive layer oxides in the OER mechanism, the OER appears to proceed through the oxidation of adsorbed OH^- at pH 12. Studies in Chapter 7 revealed that CrCoNi succumbs to intergranular corrosion. This was confirmed for all three pH levels of 0.1 M NaCl through EC-AFM. The EC-AFM topographies further support the simultaneous occurrence of metal dissolution with the OER. Recording impedance spectra at different polarizations confirmed the increased activity of the CrCoNi surface at high anodic potentials. At pH 2 the differentiation and quantification of dissolved Cr species, revealed that Cr(VI) contents increase with the application of higher anodic potentials, while the analysis of the electrolyte after the CPP scan of CrCoNi disclose that any dissolved Cr(VI) must have been reduced during the reverse scan. The results for the transpassive behavior of CrCoNi in 0.1 M NaCl imply a stable electrode capable of the OER under corrosive conditions.

To circumvent the negative aspects of Co sourcing, the tranpassive behavior of CrFeNi was compared to CrCoNi in artificial seawater. While both alloys exhibit OER activity in this electrolyte, CrFeNi seems to provide a higher Faradaic efficiency for the OER. Despite this result, the CPP scans suggest that CrCoNi is the more corrosion-resistant MPEA in artificial seawater. This comparison highlights the versatility of MPEAs and ease of swapping one element for another due to facile alloy production through arc melting.

9 Summary and Outlook

The degradation of metal and alloys through corrosion can be detrimental and may cause high safety risks and economical costs. While alloying elements such as Cr to stainless steel to render them corrosion resistant is common practice, the freedom of design for MPEAs offers the opportunity to tune alloy compositions deliberately to manufacture alloys with desired properties. Furthermore, the vast unexplored compositional space that this class of alloys offers, opens the possibility of rendering MPEAs with unexpected properties. To deem this relatively novel class of alloys appropriate for application in different aqueous media, it is essential to determine their corrosion properties.

In this work the general corrosion behavior of two MPEAs, CrMnFeCoNi and CrCoNi has been investigated in NaCl and H₂SO₄, which are typically studied due to their aggressiveness with respect to corrosion and omnipresence in our environment. The corrosion behavior of these two MPEAs was compared to a standard stainless steel AISI 304. While the CrMnFeCoNi MPEA exhibits corrosion characteristics comparable to AISI 304, CrCoNi exceeds these alloys with an outstanding corrosion resistance in NaCl and H₂SO₄. The CrCoNi MPEA does deteriorate minimally through intragranular corrosion in both electrolytes at high anodic potentials. CrMnFeCoNi, on the other hand, displayed different corrosion mechanisms in the electrolytes. In NaCl, it succumbs severely to pitting corrosion and in H₂SO₄, it exhibits a form of localized corrosion at, of and around inclusions. The stability of CrCoNi in highly corrosive environments has been demonstrated through the long-term exposure in 1 M H₂SO₄. After 4 weeks of immersion, CrCoNi seemed unchanged, while its EIS data showed that the passive film properties enhanced with the duration of exposure to 1 M H₂SO₄. CrMnFeCoNi, on the other hand, corroded severely during the long-term exposure in 1 M H₂SO₄.

While the rise in current density with increasing potential in the transpassive region of the CPP scan may indicate metal or passive film dissolution, it may also be the result of the OER. The investigation of the electrochemical behavior of the two MPEAs within the transpassive region showed that the CrMnFeCoNi alloy dissolves at such high anodic potentials. On the contrary, CrCoNi exhibited OER activity within the transpassive region as was determined by TSV-SECM. The results in the acidic NaCl electrolyte revealed the highest Faradaic efficiencies after the TSV-SECM scan, suggesting that the anodic passivation of CrCoNi through the CPP scan may enhance its OER activity. In NaCl electrolytes at pH 6.25 and 12, the anodic Tafel slopes suggest a change in the OER reaction mechanism at the CrCoNi surface from oxide oxidation at pH 2 to adsorbed water/OH⁻ oxidation at pH 12. This potential electrocatalytic activity in a chloride-containing electrolyte for water splitting was further investigated by examining the OER activity of CrCoNi in artificial seawater. The increased demand in Co, especially in the battery sector, deems this metal relatively expensive

and also questionable in its ethical sourcing. Hence, the MPEA CrFeNi was also investigated in artificial seawater as an alternative to CrCoNi. While both MPEAs exhibited corrosion-resistant behavior in artificial seawater, CrCoNi demonstrated superior corrosion resistance when analyzing the CPP data alone. Furthermore, TSV-SECM of CrCoNi revealed an onset of the OER at lower potentials than found for CrFeNi. However, the latter exhibited a higher Faradaic efficiency. The results of the investigations in artificial seawater showed that the exchange of Co in CrCoNi for Fe could lead to higher Faradaic efficiencies but the respective overpotentials for the OER increased.

For future research, approaches such as diffusion couples for the fast screening of phase formation and composition of the formed alloyed diffusion zone seem highly promising. This should be complemented by simulation approaches such as CALPHAD and machine learning to predict and model desired microstructures and mechanical properties.^[343] Furthermore, the automation of the manufacturing process, post manufacturing treatment and property investigation (mechanical and electrochemical) pose a viable route to obtain a vast collection of data from which future composition and respective properties can be deduced. More specifically, bearing in mind the excellent corrosion resistance of CrCoNi, respective coatings of the MPEA could be investigated for their protectiveness. With the potential of CrCoNi catalyzing reactions such as the OER, different surface preparations should be investigated. The partaking of the passive layer in the OER requires more investigations. For this different electrolytes and anodic surface passivation protocols could be used. The analysis of the passive layer thickness and composition could be performed with a glow discharge optical emission spectrometer. It allows for the quick analysis of the oxide layer composition and structure. Isotope labelling could pose another approach to track the origin of active sites partaking in the OER.^[344]

In the young history of MPEAs, CrMnFeCoNi constitutes the initial MPEA that has been investigated. While the use of Mn is important for mechanical properties, other strategies in the MPEA development need to be considered. These could include the alloying of additional elements to counteract the high dissolution rate of Mn or the usage of lower Mn concentrations within the bulk alloy to maintain the desired mechanical properties while not decreasing the corrosion resistance of the alloy.

10 Appendix

Appendix 1. Example calculations for ΔS_{conf} different MPEA compositions.

$$\Delta S_{\text{conf}} = -R \sum_n x_i \ln(x_i)$$

- equiatomic 3 elements: $x = 1/3$; $\Delta S_{\text{conf}} = 1.10R$
- 3 elements, different concentrations: $x_1 = 0.5$, $x_2 = 0.4$ and $x_3 = 0.1$; $\Delta S_{\text{conf}} = 0.94R$
- equiatomic 4 elements: $x = 0.25$; $\Delta S_{\text{conf}} = 1.28R$
- 4 elements, different concentrations: $x_1 = 0.6$, $x_2 = 0.3$, $x_3 = 0.05$ and $x_4 = 0.05$; $\Delta S_{\text{conf}} = 0.97R$
- equiatomic 5 elements: $x = 0.2$; $\Delta S_{\text{conf}} = 1.61R$
- 5 elements, different concentrations: $x_1 = 0.45$, $x_2 = 0.2$, $x_3 = 0.2$, $x_4 = 0.1$ and $x_5 = 0.05$; $\Delta S_{\text{conf}} = 1.38 R$

Appendix 2. XPS parameters of the 3p core level spectra.

Table 10.1. XPS parameters for CrMnFeCoNi.

	Cr		Mn		Fe			Co		Ni	
	3p _{met}	3p _{ox}	3p _{met}	3p _{ox}	3p _{met}	3p ²⁺	3p ³⁺	3p _{met}	3p _{ox}	3p _{3/2}	3p _{1/2}
Native											
Position	41.2	42.9	46.4	47.5	52.1	53.0	54.9	58.5	59.7	65.8	67.7
FWHM	1.0	3.0	1.1	2.3	0.7	1.8	1.9	1.1	2.6	2.1	1.9
Area	110.5	484.5	184.2	280.3	119.0	259.9	130.1	176.1	446.6	971.9	486.4
NaCl											
Position	41.2	43.4	46.3	47.4	52.1	52.8	-	58.4	59.6	65.8	67.8
FWHM	1.4	2.3	1.1	2.4	0.7	1.7	-	0.9	2.4	2.1	1.8
Area	207.4	625.8	157.2	303.9	85.2	130.0	-	103.8	307.0	635.0	317.8
H₂SO₄											
Position	41.5	43.7	46.6	48.4	52.3	53.7	54.8	58.7	59.9	66.0	68.0
FWHM	1.3	2.3	1.3	1.9	0.8	2.1	1.7	1.1	2.8	1.9	1.8
Area	226.3	762.7	299.9	253.0	112.2	529.4	264.8	181.1	384.3	704.1	352.4

Appendix

Table 10.2. XPS parameters for CrCoNi.

	Cr 3p _{met}	Cr 3p _{ox}	Co 3p _{met}	Co 3p _{ox}	Ni 3p _{3/2}	Ni 3p _{1/2}
Native						
Position	41.1	43.0	58.2	59.4	65.6	67.6
FWHM	1.2	2.8	1.1	2.1	2.2	2.0
Area	273.2	906.7	432.6	616.3	1584.5	793.1
NaCl						
Position	41.2	43.4	58.4	59.7	65.8	67.8
FWHM	1.2	2.7	1.2	1.6	2.0	1.8
Area	299.1	1223.1	460.4	295.4	1121.1	561.2
H₂SO₄						
Position	41.4	43.4	58.5	59.4	65.9	67.8
FWHM	1.3	3.0	1.0	2.1	1.9	1.9
Area	475.0	1258.1	372.8	756.0	1315.3	658.3

Appendix 3. IMFP data required for the oxide layer thickness calculation.

Table 10.3. Inelastic mean free path values obtained through the TTP-2 formula and from the NIST database for Cr, Mn, Fe, Co and Ni used for XPS quantification.

	Cr	Mn	Fe	Co	Ni
ρ [g cm ⁻³]	7.14	7.44	7.87	8.89	8.91
λ_{TTP-2} [nm]	2.38	2.34	2.30	2.23	2.25
λ_{NIST} [nm]	2.26	2.30	2.20	2.09	2.00

Table 10.4. Inelastic mean free path values obtained through the TTP-2 formula and from the NIST database for Cr₂O₃, MnO, Fe₂O₃ and CoO used for XPS quantification.

	Cr ₂ O ₃	MnO	Fe ₂ O ₃	CoO
ρ [g cm ⁻³]	5.22	5.37	5.24	6.44
E_g [eV]	3.2 ^[345]	3.6 ^[346]	2.2 ^[347]	2.5 ^[348]
λ_{TTP-2} [nm]	4.60	3.95	4.52	3.67
λ_{NIST} [nm]	4.65	4.00	4.57	3.67

Appendix 4. Light Microscope images during EC-AFM of CrMnFeCoNi.

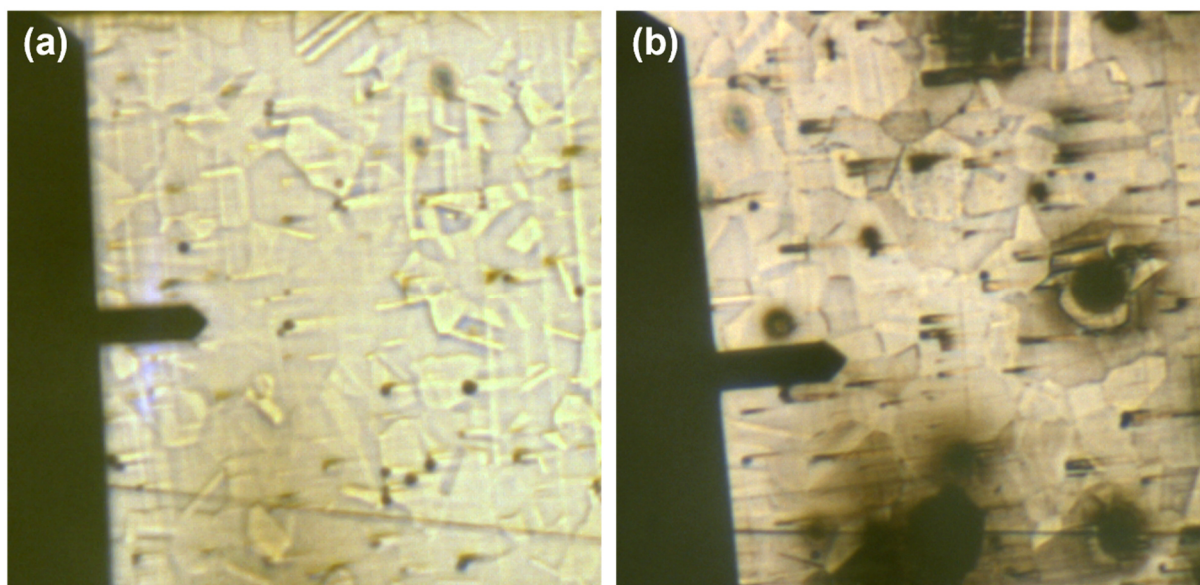


Figure 10.1. Light microscope images of (a) freshly immersed CrMnFeCoNi and (b) during the CPP scan of CrMnFeCoNi in 0.1 M NaCl at pH 2.

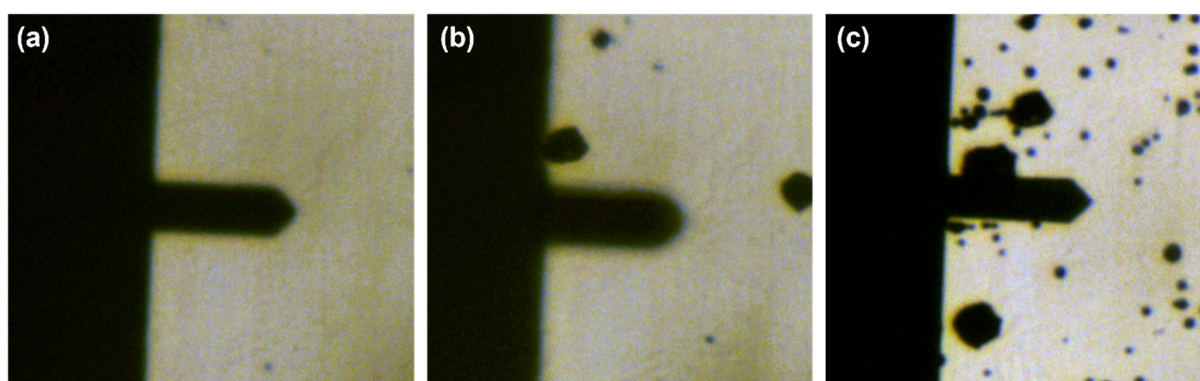


Figure 10.2. Light microscope images of (a) freshly immersed CrMnFeCoNi, (b) during the CPP scan of CrMnFeCoNi and (c) at high transpassive potentials in 0.1 M NaCl at pH 6.25.

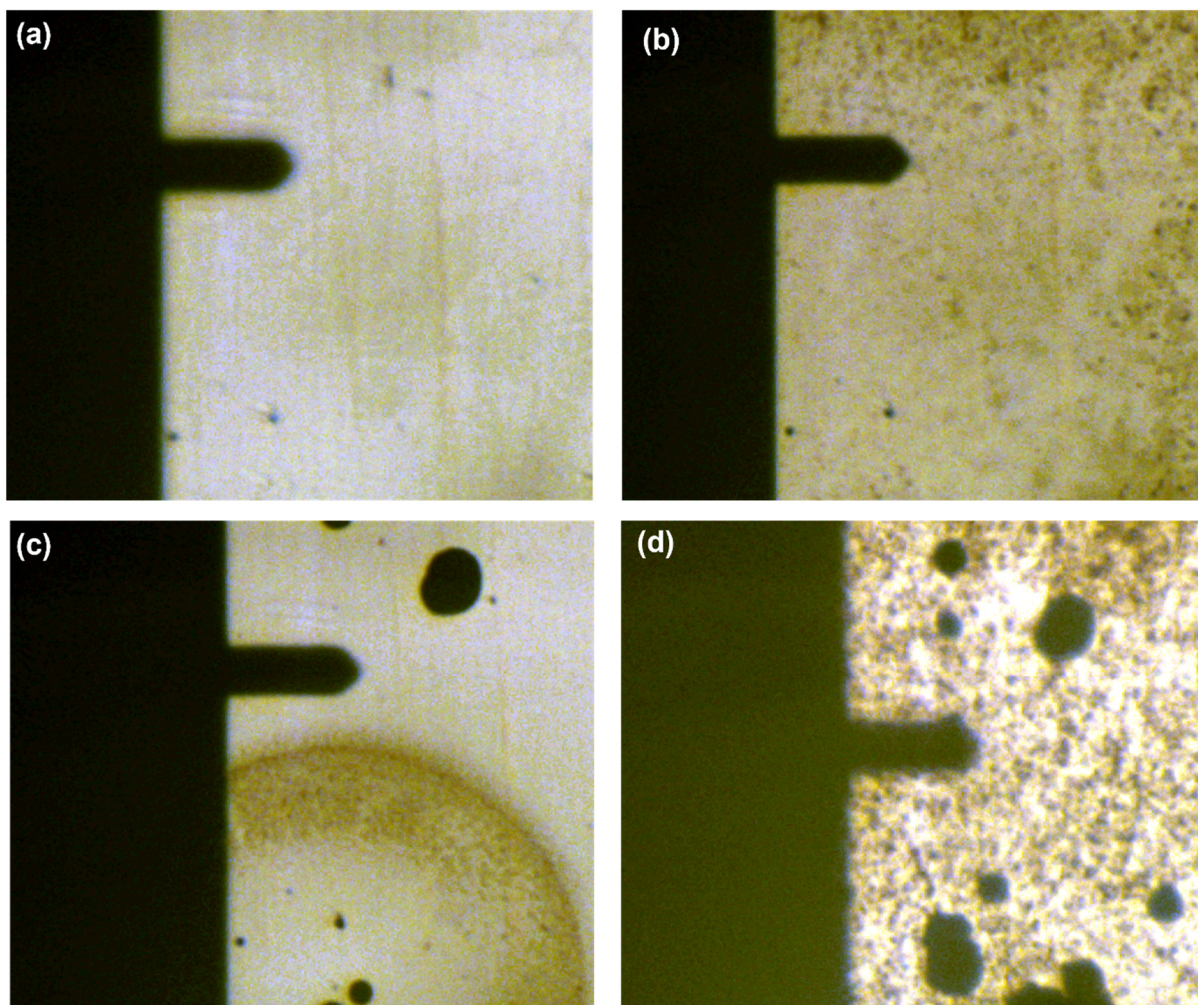


Figure 10.3. Light microscope images of (a) freshly immersed CrMnFeCoNi, (b) during the CPP scan of CrMnFeCoNi, (c) diffusion of corrosion product from pits and (d) accumulation of corrosion products high transpassive potentials in 0.1 M NaCl at pH 12. The diagram is adapted with permission from own publication^[327] published by Wiley-VCH under the terms of the CC BY 4.0 license. Copyright 2024, The Authors.

Appendix

Appendix 5. UV-Vis data for Cr and CrCoNi electrolytes after the TSV-SECM and amperometric measurements in 0.1 M NaCl at pH 2.

Table 10.5. UV-Vis data for the quantification of Cr(III) in Cr(VI) in the 0.1 M NaCl electrolyte at pH 2.

replicate	absorbance Cr _(VI)	absorbance Cr _(VI) +Cr _(III)	dilution	c(Cr _(VI)) [mmol L ⁻¹]	c(Cr _(VI) +Cr _(III)) [mmol L ⁻¹]	c(Cr _(III)) [mmol L ⁻¹]
Cr I_{T,1}						
1	0.61	0.64	10.00	1.44	1.51	0.07
2	0.60	0.64	10.00	1.43	1.51	0.08
Cr II_{T,2}						
1	0.58	0.62	25.00	3.47	3.67	0.21
2	0.61	0.62	25.00	3.60	3.70	0.10
CrCoNi I_{T,1}						
1	0.27	0.15	1.50	0.11	0.24	0.13
2	0.21	0.13	1.50	0.09	0.21	0.12
3	0.20	0.10	1.50	0.09	0.18	0.09
CrCoNi II_{T,2}						
1	0.60	0.82	5.00	0.72	0.95	0.23
2	0.53	0.74	5.00	0.64	0.87	0.23
3	0.47	0.74	5.00	0.58	0.87	0.29
Cr TSV						
1	0.66	0.69	3.00	0.47	0.54	0.07
2	0.55	0.64	3.33	0.44	0.50	0.06
CrCoNi TSV						
1	-	0.35	1.50	0.00	0.09	0.09
2	-	0.19	1.50	0.00	0.07	0.07

Appendix 6. Cr(VI) concentrations in electrolytes after TSV-SECM of CrCoNi in pH 6.25 and pH 12.

Table 10.6. Cr(VI) and Cr(III) concentrations after TSV-SECM of CrCoNi in 0.1 M NaCl at pH 6.25 and pH 12.

replicate	c(Cr _(VI)) [mmol L ⁻¹]	c(Cr _(VI) +Cr _(III)) [mmol L ⁻¹]
CrCoNi pH 6.25		
1	0.43	0.43
2	0.04	0.04
3	0.03	0.03
CrCoNi pH 12		
1	0.03	0.03
2	0.03	0.03
3	0.03	0.03

Appendix 7. EIS Spectra of CrCoNi in 0.1 M NaCl (pH2) at different DC polarizations

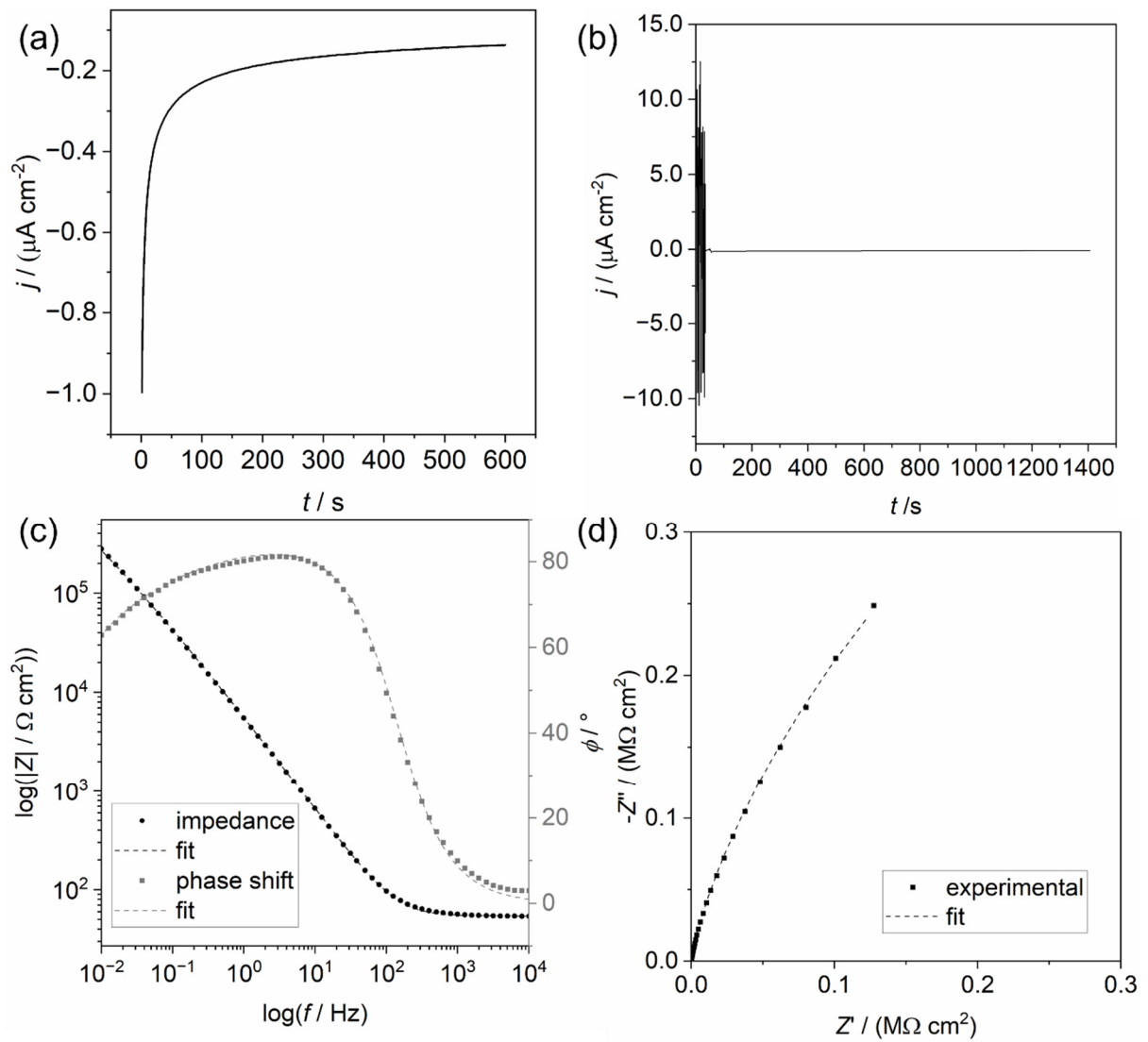


Figure 10.4. EIS data of CrCoNi in 0.1 M NaCl pH 2. (a) DC current transient at -0.25 V vs. OCP to stabilize the metal surface prior to the EIS measurement; (b) shows the DC current recorded during the EIS scan, (c) Bode plot recorded at -0.25 V vs. OCP revealing capacitor-like behavior and high polarization resistance; and (d) Nyquist plot.

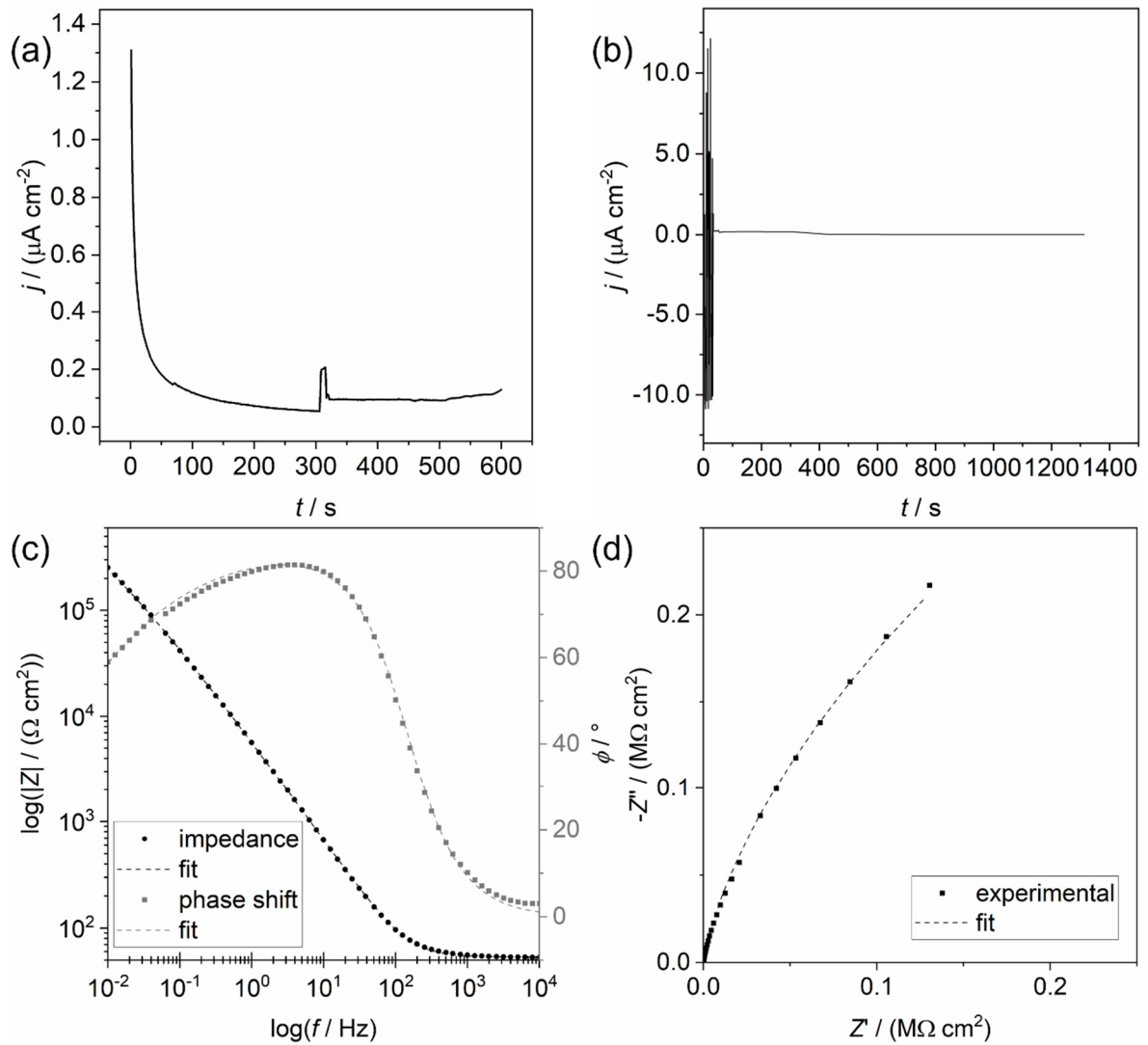


Figure 10.5. EIS data of CrCoNi in 0.1 M NaCl pH 2. (a) DC current transient at OCP to stabilize the metal surface prior to the EIS measurement; (b) shows the DC current recorded during the EIS scan, (c) Bode plot recorded at OCP revealing capacitor-like behavior and high polarization resistance; and (d) Nyquist plot.

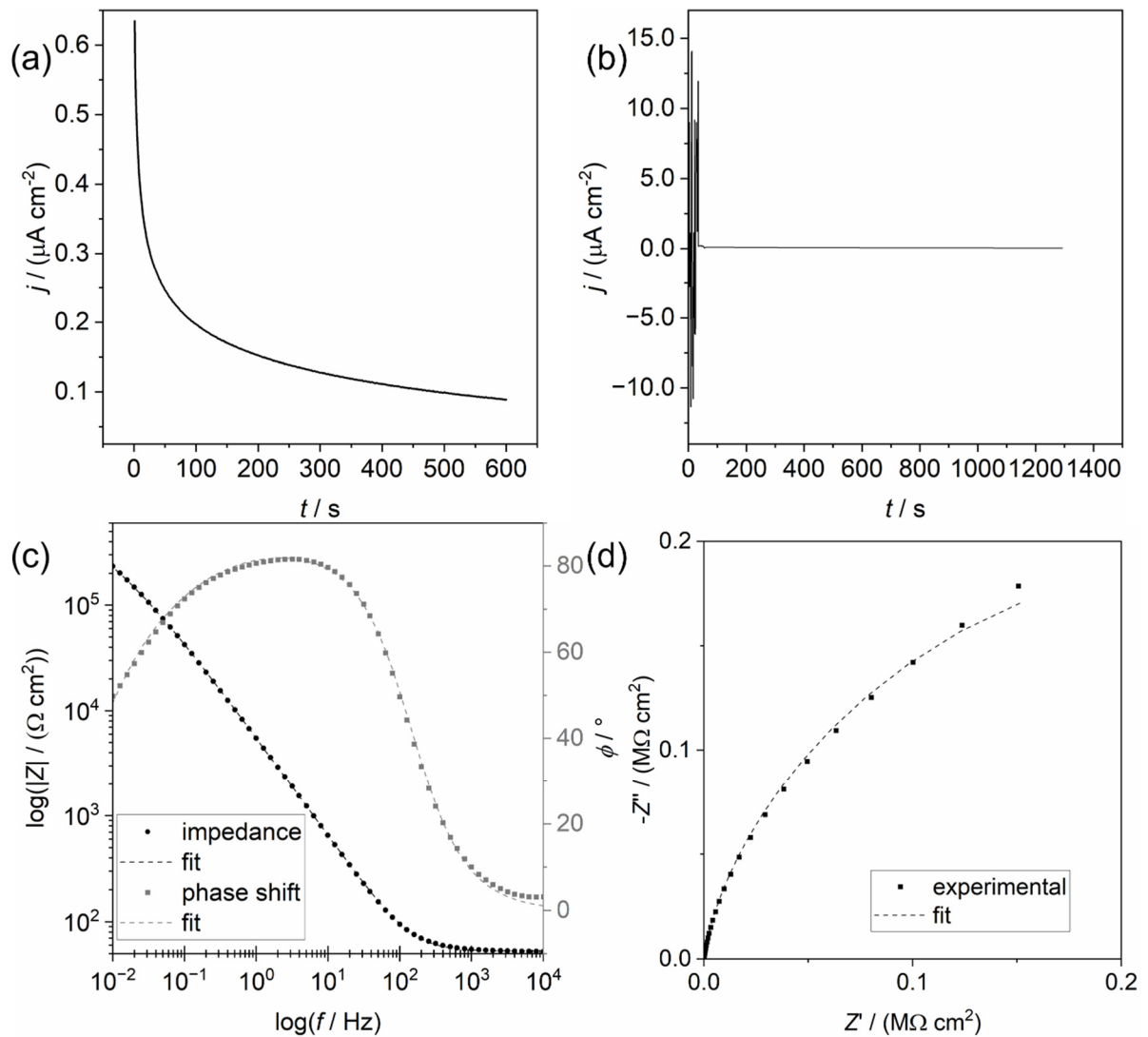


Figure 10.6. EIS data of CrCoNi in 0.1 M NaCl pH 2. (a) DC current transient at 0.4 V vs. OCP to stabilize the metal surface prior to the EIS measurement; (b) shows the DC current recorded during the EIS scan, (c) Bode plot recorded at 0.4 V vs. OCP revealing capacitor-like behavior and high polarization resistance; and (d) Nyquist plot.

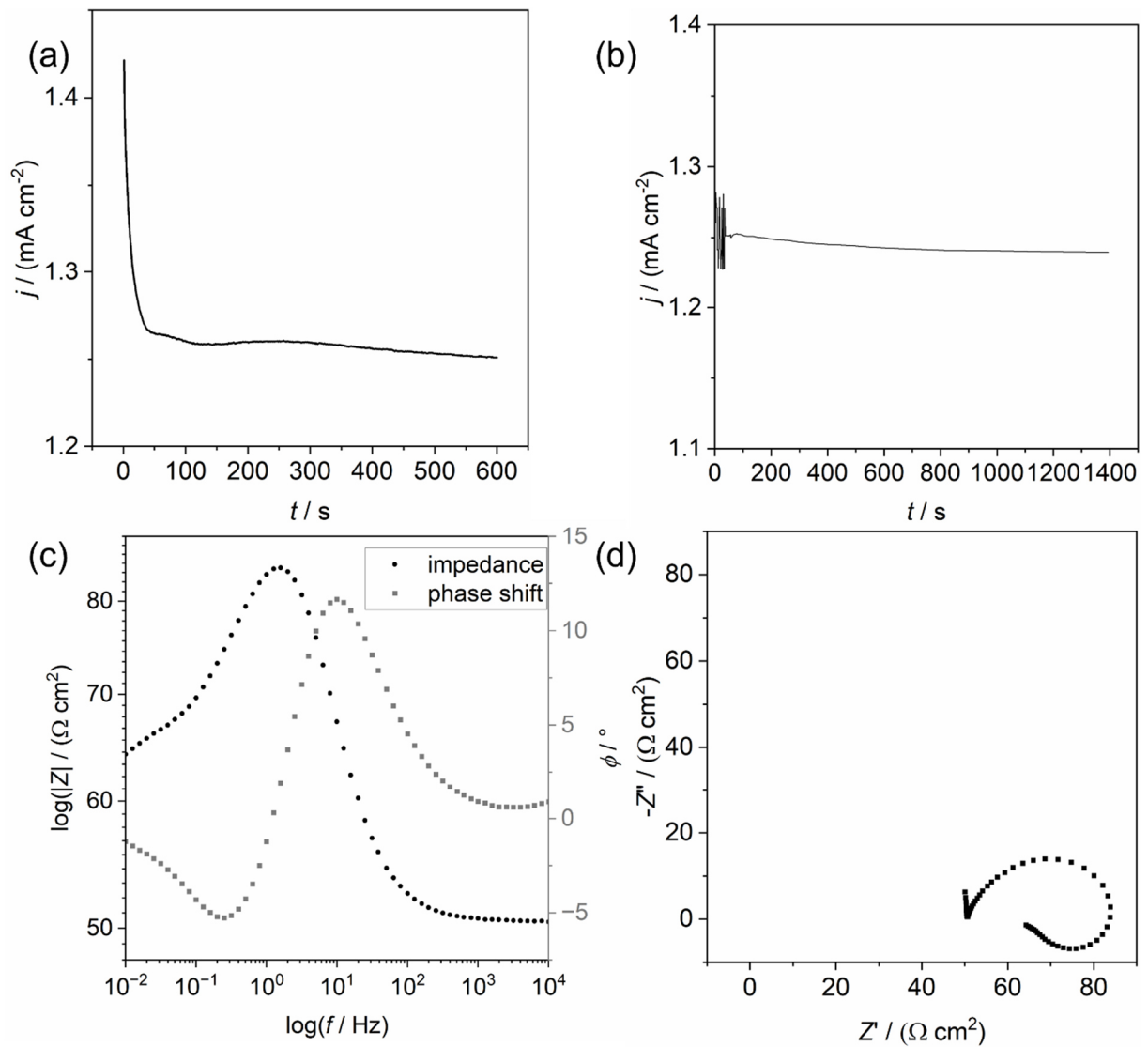


Figure 10.7. EIS data of CrCoNi in 0.1 M NaCl pH 2. (a) DC current transient at 1.0 V vs. Ag/AgCl/3M NaCl to stabilize the metal surface prior to the EIS measurement; (b) shows the DC current recorded during the EIS scan, (c) Bode plot recorded at 1.0V vs. Ag/AgCl/3M NaCl revealing inductor behavior and low polarization and charge transfer resistance and (d) Nyquist plot.

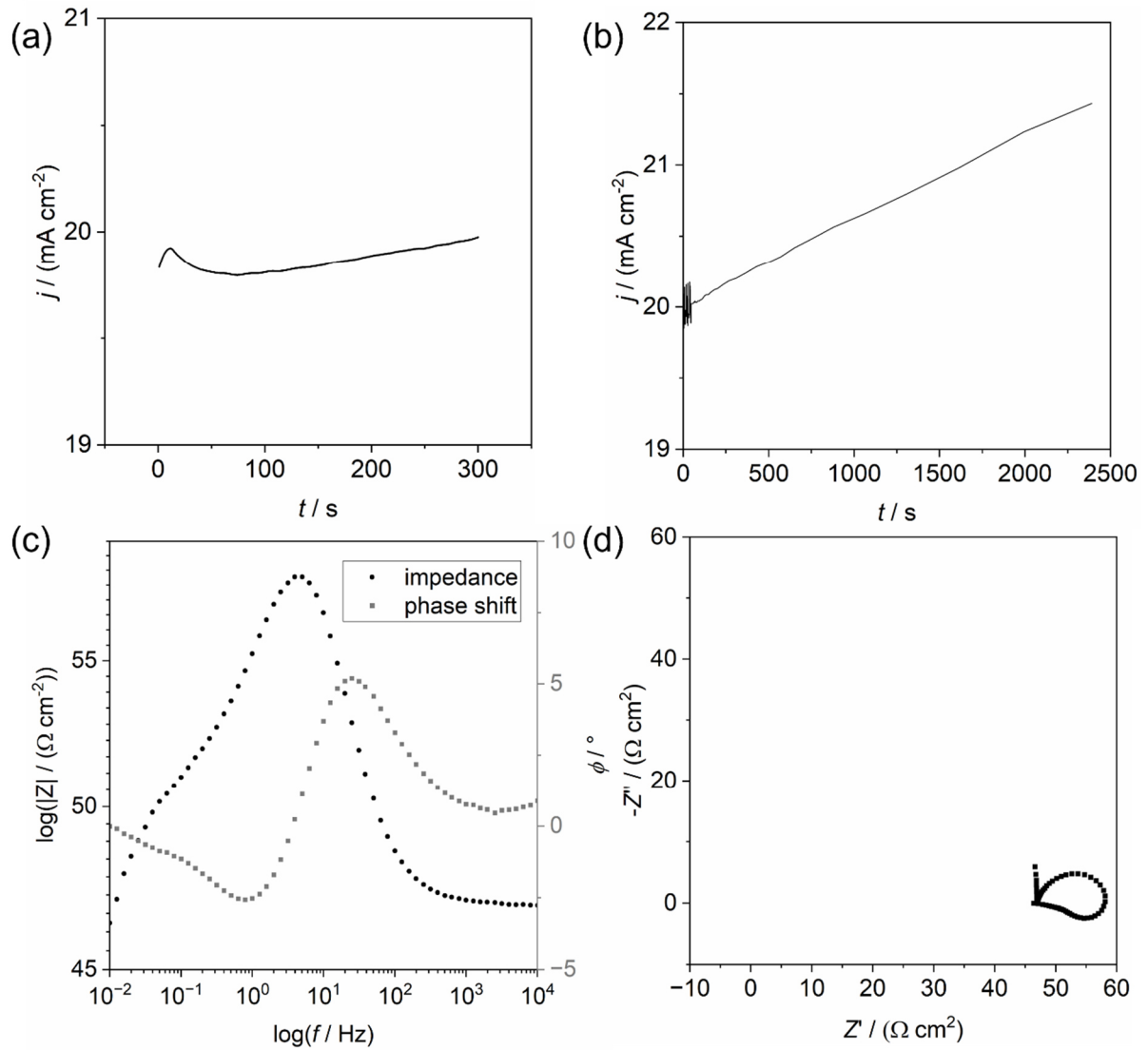


Figure 10.8. EIS data of CrCoNi in 0.1 M NaCl pH 2. (a) DC current transient at 1.15 V vs. Ag/AgCl/3M NaCl to stabilize the metal surface prior to the EIS measurement; (b) shows the DC current recorded during the EIS scan, (c) Bode plot recorded at 1.15 V vs. Ag/AgCl/3M NaCl revealing inductor behavior and low polarization and charge transfer resistance and (d) Nyquist plot.

11 List of Abbreviations

11.1 Physical Quantities

α	symmetry factor
β	Tafel slope
ΔE	passive potential region
ε	engineering strain or relative permittivity constant
η	chemical potential
θ	deviation of CPE exponent m from 1
λ	wavelength
μ_i	chemical potential
$\tilde{\mu}_i^\alpha$	electrochemical potential of species i in phase α
ν	frequency of photon
σ	engineering strain
τ	overpotential
φ	electrostatic potential
ϕ	phase angle
Φ	surface potential
ω	angular frequency
A	area
A_{tip}	amplitude of tip oscillation
c	concentration
C	capacitance
D	diffusion coefficient
d	diameter
d_{oxide}	oxide layer thickness
e	elementary charge
E	electrode potential
E°	standard electrode potential
E_{B}	binding energy

List of Abbreviations

E_b	breakdown potential
E_{corr}	corrosion potential
E_{cr}	cross-over potential
E_K	kinetic energy
E_{pit}	pitting potential
E_{pp}	primary passivation potential
E_{rp}	repassivation potential
E_S	substrate potential
F	Faraday constant or force
f	frequency
G	Gibbs free energy
H	enthalpy
I	current
i_T	tip current (for SECM)
j	current density
j_{an}	anodic current density
j_{cat}	cathodic current density
j_{corr}	corrosion current density
j_o	exchange current density
j_s	substrate current density
K	equilibrium constant
k	reaction rate constant or force constant
m	<i>CPE</i> exponent
n_e	number of exchange electron
N_i	amount of substance i
p	pressure
Q	charge
R	gas constant or resistance
r	radius
r_{corr}	corrosion rate
S	entropy
T	temperature
U	cell potential
V	volume

v_i	stoichiometric number
x, z	distance in either the x- or z-direction
Z	impedance
z_i	ionic charge

11.2 General Abbreviation

a.u.	arbitrary units
ac	alternating current
AE	auxiliary electrode
AES	Auger electron spectroscopy
AFM	atomic force microscopy
ASEC	atomic spectroelectrochemistry
bcc	body centered cubic
BSE	back scattered electrons
CPE	constant phase element
CPP	cyclic potentiodynamic polarization
CPS	counts per second
CV	cyclic voltammetry
dc	direct current
DL	diffuse layer
EC-AFM	electrochemical atomic force microscopy
EDL	electrical double layer
EDX	energy dispersive X-ray spectroscopy
EEC	electrical equivalent circuit
EIS	electrochemical impedance spectroscopy
fcc	face centered cubic
GB	grain boundary
hcp	hexagonal close packed
HER	hydrogen evolution reaction
IC mode	intermittent contact mode
ICP-MS	inductively coupled mass spectrometry
IHL	inner Helmholtz layer
IUPAC	international union of pure and applied chemistry
LOD	limit of detection

List of Abbreviations

LPP	linear potentiodynamic polarization
LPR	linear polarization resistance
LSV	linear sweep voltammetry
ME	microelectrode
MIC	microbial corrosion
MPEA	multi principal element alloy
OCP	open circuit potential
OER	oxygen evolution reaction
OHL	outer Helmholtz layer
ORR	oxygen reduction reaction
QMF	quadrupole mass filter
RDS	rate determining step
RE	reference electrode
RHE	reversible hydrogen electrode
RSF	relative sensitivity factor
SCE	saturated calomel electrode
SE	secondary electrons
SECM	scanning electrochemical microscopy
SEM	scanning electron microscopy
SG/TC	substrate generation/tip collection
SHE	standard hydrogen electrode
SKPFM	scanning Kelvin probe force microscopy
SPS	spark plasma sintering
TG/SC	tip generation/substrate collection
TLC	thin layer cell
ToF-SIMS	time of flight secondary ion mass spectrometry
TS	tensile strength
TSV	tip substrate voltammetry
WE	working electrode
XPS	X-ray photoelectron spectroscopy
YS	yield strength

12 References

- [1] R. W. Cahn, *Sādhanā* **1980**, *3*, 255-260.
- [2] B. Cantor, *Prog. Mater. Sci.* **2021**, *120*, 100754.
- [3] W. D. Callister, D. G. Rethwisch, in *Materials Science and Engineering: An Introduction*, 10 ed., Wiley, Hoboken, NJ, **2018**, pp. 347-404.
- [4] A. P. Mouritz, in *Introduction to Aerospace Materials*, Woodhead Publishing, **2012**, pp. 1-14.
- [5] M. R. da Silva, A. H. Plaine, V. E. Pinotti, E. M. Mazzer, C. Bolfarini, *J. Mater. Res.* **2023**, *38*, 96-111.
- [6] C. C. F. Xavier, J. O. Braga, M. O. Pessoa, T. Matencio, V. F. C. Lins, *Mater. Today Commun.* **2022**, *33*, 104453.
- [7] N. R. Baddoo, *J. Constr. Steel Res.* **2008**, *64*, 1199-1206.
- [8] W. D. Callister, D. G. Rethwisch, in *Materials Science and Engineering: An Introduction*, 10 ed., Wiley, Hoboken, NJ, **2018**, pp. 251-302.
- [9] B. Cantor, in *Entropy, Vol. 16*, **2014**, pp. 4749-4768.
- [10] S. Ranganathan, *Curr. Sci.* **2003**, *85*, 1404-1406.
- [11] B. Cantor, I. T. H. Chang, P. Knight, A. J. B. Vincent, *Mater. Sci. Eng. A* **2004**, *375*, 213-218.
- [12] J. W. Yeh, S. K. Chen, S. J. Lin, J. Y. Gan, T. S. Chin, T. T. Shun, C. H. Tsau, S. Y. Chang, *Adv. Eng. Mater.* **2004**, *6*, 299-303.
- [13] E. P. George, D. Raabe, R. O. Ritchie, *Nat. Rev. Mater.* **2019**, *4*, 515-534.
- [14] F. Otto, A. Dlouhý, C. Somsen, H. Bei, G. Eggeler, E. P. George, *Acta Mater.* **2013**, *61*, 5743-5755.
- [15] Z. Wu, H. Bei, G. M. Pharr, E. P. George, *Acta Mater.* **2014**, *81*, 428-441.
- [16] B. Gludovatz, A. Hohenwarter, K. V. S. Thurston, H. Bei, Z. Wu, E. P. George, R. O. Ritchie, *Nat. Commun.* **2016**, *7*, 10602.
- [17] G. Laplanche, A. Kostka, O. M. Horst, G. Eggeler, E. P. George, *Acta Mater.* **2016**, *118*, 152-163.
- [18] G. Laplanche, A. Kostka, C. Reinhart, J. Hunfeld, G. Eggeler, E. P. George, *Acta Mater.* **2017**, *128*, 292-303.
- [19] W. D. Callister, D. G. Rethwisch, in *Materials Science and Engineering: An Introduction*, 10 ed., Wiley, Hoboken, NJ, **2018**, pp. 142-179.
- [20] B. Gludovatz, A. Hohenwarter, K. V. S. Thurston, H. B. Bei, Z. G. Wu, E. P. George, R. O. Ritchie, *Nat. Commun.* **2016**, *7*.
- [21] W. J. Fu, W. Zheng, Y. J. Huang, F. M. Guo, S. S. Jiang, P. Xue, Y. Ren, H. B. Fan, Z. L. Ning, J. F. Sun, *Mater. Sci. Eng. A* **2020**, *789*.
- [22] W. D. Callister, D. G. Rethwisch, in *Materials Science and Engineering: An Introduction*, 10 ed., Wiley, Hoboken, NJ, **2018**, pp. 142-179.
- [23] J. Yang, J. Wu, C. Y. Zhang, S. D. Zhang, B. J. Yang, W. Emori, J. Q. Wang, *J. Alloys Compd.* **2020**, *819*.
- [24] H. Torbati-Sarraf, M. Shabani, P. D. Jablonski, G. J. Pataky, A. Poursaee, *Mater. Des.* **2019**, *184*.
- [25] J. Y. Wang, W. H. Li, H. L. Yang, H. Huang, S. X. Ji, J. M. Ruan, Z. L. Liu, *Corros. Sci.* **2020**, *177*.
- [26] W. D. Callister, D. G. Rethwisch, in *Materials Science and Engineering: An Introduction*, 10 ed., Wiley, Hoboken, NJ, **2018**, pp. 48-91.
- [27] G. Faraji, H. S. Kim, H. T. Kashi, in *Severe Plastic Deformation*, Elsevier, **2018**, pp. 187-222.
- [28] W. D. Callister, D. G. Rethwisch, in *Materials Science and Engineering: An Introduction*, 10 ed., Wiley, Hoboken, NJ, **2018**, pp. 92-120.
- [29] S. Guo, C. T. Liu, *Prog. Nat. Sci.: Mater. Int.* **2011**, *21*, 433-446.
- [30] A. Martin, M. Thuo, *Acc. Mater. Res.* **2023**.

- [31] J. W. Yeh, *Ann. Chim.-Sci. Mat.* **2006**, *31*, 633-648.
- [32] W. D. Callister, D. G. Rethwisch, *Materials Science and Engineering: An Introduction*, 10 ed., Wiley, Hoboken, NJ, **2018**.
- [33] W. D. Callister, D. G. Rethwisch, in *Materials Science and Engineering: An Introduction*, 10 ed., Wiley, Hoboken, NJ, **2018**, pp. 180-208.
- [34] D. B. Miracle, O. N. Senkov, *Acta Mater.* **2017**, *122*, 448-511.
- [35] F. C. Achard, *Recherches Sur Les Propriétés Des Alliages Métalliques*, Decker, **1788**.
- [36] C. S. Smith, *Four Outstanding Researches in Metallurgical History*, American Society for Testing and Materials, **1963**.
- [37] J.-W. Yeh, S.-J. Lin, T.-S. Chin, J.-Y. Gan, S.-K. Chen, T.-T. Shun, C.-H. Tsau, S.-Y. Chou, *Metallurgical and Materials Transactions A* **2004**, *35*, 2533-2536.
- [38] D. R. Gaskell, D. E. Laughlin, *Introduction to the thermodynamics of materials*, 6 ed., CRC Press, Taylor & Francis, Boca Raton, FL, **2017**.
- [39] I. A. Tomilin, S. D. Kaloshkin, *Mater. Sci. Technol.* **2015**, *31*, 1231-1234.
- [40] J.-W. Yeh, *JOM* **2013**, *65*, 1759-1771.
- [41] B. S. Murty, J. W. Yeh, S. Ranganathan, in *High Entropy Alloys*, Butterworth-Heinemann, Boston, **2014**, pp. 77-89.
- [42] Y. Zhang, T. T. Zuo, Z. Tang, M. C. Gao, K. A. Dahmen, P. K. Liaw, Z. P. Lu, *Prog. Mater. Sci.* **2014**, *61*, 1-93.
- [43] Y. Zhang, C. C. Koch, S. G. Ma, H. Zhang, Y. Pan, in *High-Entropy Alloys: Fundamentals and Applications*, Springer International Publishing, Cham, **2016**, pp. 151-179.
- [44] V. E. Gromov, S. V. Konovalov, Y. F. Ivanov, K. A. Osintsev, in *Structure and Properties of High-Entropy Alloys*, Springer International Publishing, Cham, Switzerland, **2021**, pp. 1-31.
- [45] J. Walker, D. Halliday, R. Resnick, in *Fundamentals of Physics*, 10 ed., John Wiley & Sons, Inc., **2014**, pp. 864-902.
- [46] H. Zhang, Y. Pan, Y. He, *J. Therm. Spray Technol.* **2011**, *20*, 1049-1055.
- [47] H. Zhang, Y. He, Y. Pan, *Scr. Mater.* **2013**, *69*, 342-345.
- [48] P. D. Niu, R. D. Li, T. C. Yuan, S. Y. Zhu, C. Chen, M. B. Wang, L. Huang, *Intermetallics* **2019**, *104*, 24-32.
- [49] Y. Zhang, Q. Xing, in *Encyclopedia of Materials: Metals and Alloys*, Elsevier, Oxford, **2022**, pp. 327-338.
- [50] C. J. Tong, Y. L. Chen, S. K. Chen, J. W. Yeh, T. T. Shun, C. H. Tsau, S. J. Lin, S. Y. Chang, *Metall Mater Trans A* **2005**, *36a*, 881-893.
- [51] O. N. Senkov, J. M. Scott, S. V. Senkova, D. B. Miracle, C. F. Woodward, *J. Alloys Compd.* **2011**, *509*, 6043-6048.
- [52] X. Yang, Y. Zhang, *Mater. Chem. Phys.* **2012**, *132*, 233-238.
- [53] K. Y. Tsai, M. H. Tsai, J. W. Yeh, *Acta Mater.* **2013**, *61*, 4887-4897.
- [54] Y. Xin, S. H. Li, Y. Y. Qian, W. K. Zhu, H. B. Yuan, P. Y. Jiang, R. H. Guo, L. B. Wang, *ACS Catal.* **2020**, *10*, 11280-11306.
- [55] Y. J. Zhou, Y. Zhang, Y. L. Wang, G. L. Chen, *Appl. Phys. Lett.* **2007**, *90*.
- [56] X. F. Wang, Y. Zhang, Y. Qiao, G. L. Chen, *Intermetallics* **2007**, *15*, 357-362.
- [57] O. N. Senkov, G. B. Wilks, J. M. Scott, D. B. Miracle, *Intermetallics* **2011**, *19*, 698-706.
- [58] J.-W. Yeh, in *High-Entropy Alloys: Fundamentals and Applications*, Springer International Publishing, Cham, **2016**, pp. 51-113.
- [59] B. S. Murty, J. W. Yeh, S. Ranganathan, in *High Entropy Alloys*, Butterworth-Heinemann, Boston, **2014**, pp. 13-35.
- [60] T. T. Shun, C. H. Hung, C. F. Lee, *J. Alloys Compd.* **2010**, *493*, 105-109.
- [61] S. Singh, N. Wanderka, B. S. Murty, U. Glatzel, J. Banhart, *Acta Mater.* **2011**, *59*, 182-190.
- [62] J. Kumar, N. Kumar, S. Das, N. P. Gurao, K. Biswas, *Trans. Indian Inst. Met.* **2018**, *71*, 2749-2758.
- [63] L. G. Cao, X. H. Wang, Y. M. Wang, L. L. Zhang, Y. Yang, F. B. Liu, Y. Cui, *Appl. Phys. A* **2019**, *125*.
- [64] J. J. Yi, L. Wang, M. Q. Xu, L. Yang, *Phys. Met. Metallogr.* **2021**, *122*, 1376-1381.

- [65] J. S. Langer, in *Fluctuations, Instabilities, and Phase Transitions*, Springer US, Boston, MA, **1975**, pp. 19-42.
- [66] A. Mehta, Y. Sohn, *ACS Comb. Sci.* **2020**, *22*, 757-767.
- [67] T. R. Paul, I. V. Belova, G. E. Murch, *Mater. Chem. Phys.* **2018**, *210*, 301-308.
- [68] R. Pillai, A. Chyrkin, W. J. Quadackers, *Oxid. Met.* **2021**, *96*, 385-436.
- [69] L. T. Wang, D. Mercier, S. Zanna, A. Seyeux, M. Laurent-Brocq, L. Perrière, I. Guillot, P. Marcus, *Corros. Sci.* **2020**, *167*.
- [70] K. Y. Tsai, M. H. Tsai, J. W. Yeh, *Acta Mater.* **2013**, *61*, 4887-4897.
- [71] D. Gaertner, J. Kottke, G. Wilde, S. V. Divinski, Y. Chumlyakov, *J. Mater. Res.* **2018**, *33*, 3184-3191.
- [72] J. Kottke, M. Laurent-Brocq, A. Fareed, D. Gaertner, L. Perriere, L. Rogal, S. V. Divinski, G. Wilde, *Scr. Mater.* **2019**, *159*, 94-98.
- [73] M. Vaidya, K. G. Pradeep, B. S. Murty, G. Wilde, S. V. Divinski, *Sci. Rep.* **2017**, *7*.
- [74] J. Dabrowa, M. Zajusz, W. Kuczka, G. Cieslak, K. Berent, T. Czeppe, T. Kulik, M. Danielewski, *J. Alloys Compd.* **2019**, *783*, 193-207.
- [75] W. D. Callister, D. G. Rethwisch, in *Materials Science and Engineering: An Introduction*, 10 ed., Wiley, Hoboken, NJ, **2018**, pp. 303-346.
- [76] Q. He, Y. Yang, *Front. Mater.* **2018**, *5*.
- [77] L. R. Owen, N. G. Jones, *J. Mater. Res.* **2018**, *33*, 2954-2969.
- [78] B. X. Cao, C. Wang, T. Yang, C. T. Liu, *Scr. Mater.* **2020**, *187*, 250-255.
- [79] Z. M. Li, K. G. Pradeep, Y. Deng, D. Raabe, C. C. Tasan, *Nature* **2016**, *534*, 227-+.
- [80] J. W. Bae, J. B. Seol, J. Moon, S. S. Sohn, M. J. Jang, H. Y. Um, B. J. Lee, H. S. Kim, *Acta Mater.* **2018**, *161*, 388-399.
- [81] J. Y. He, W. H. Liu, H. Wang, Y. Wu, X. J. Liu, T. G. Nieh, Z. P. Lu, *Acta Mater.* **2014**, *62*, 105-113.
- [82] W. H. Liu, Z. P. Lu, J. Y. He, J. H. Luan, Z. J. Wang, B. Liu, Y. Liu, M. W. Chen, C. T. Liu, *Acta Mater.* **2016**, *116*, 332-342.
- [83] E. J. Pickering, R. Munoz-Moreno, H. J. Stone, N. G. Jones, *Scr. Mater.* **2016**, *113*, 106-109.
- [84] Z. F. Lei, X. J. Liu, Y. Wu, H. Wang, S. H. Jiang, S. D. Wang, X. D. Hui, Y. D. Wu, B. Gault, P. Kontis, D. Raabe, L. Gu, Q. H. Zhang, H. W. Chen, H. T. Wang, J. B. Liu, K. An, Q. S. Zeng, T. G. Nieh, Z. P. Lu, *Nature* **2018**, *563*, 546-+.
- [85] Z. M. Li, *Acta Mater.* **2019**, *164*, 400-412.
- [86] K. E. Heusler, D. Landolt, S. Trasatti, **1989**, *61*, 19-22.
- [87] G. S. Frankel, in *Active Protective Coatings: New-Generation Coatings for Metals*, Springer Netherlands, Dordrecht, Netherlands, **2016**, pp. 17-32.
- [88] E. McCafferty, in *Introduction to Corrosion Science*, Springer New York, New York, NY, **2010**, pp. 13-31.
- [89] W. D. Callister, D. G. Rethwisch, in *Materials science and engineering : an introduction*, 10th edition ed., Wiley, Hoboken, NJ, **2018**, pp. 92-120.
- [90] M. J. Mehl, *J. Phys. Conf. Ser.* **2019**, *1290*.
- [91] V. Hasannaemi, S. Mukherjee, *J. Electroanal. Chem.* **2019**, *848*.
- [92] E. McCafferty, in *Introduction to Corrosion Science*, Springer New York, New York, NY, **2010**, pp. 33-56.
- [93] J. O. m. Bockris, M. A. V. Devanathan, K. Müller, J. A. V. Butler, *Proc. R. Soc. Lond.* **1963**, *274*, 55-79.
- [94] J. O. M. Bockris, A. K. N. Reddy, M. Gamboa-Aldeco, in *Modern Electrochemistry 2A: Fundamentals of Electrodeics*, Springer US, Boston, MA, **2000**, pp. 771-1033.
- [95] W. M. Haynes, 95th ed., CRC Press, Hoboken, **2014**.
- [96] E. McCafferty, in *Introduction to Corrosion Science*, Springer New York, New York, NY, **2010**, pp. 57-72.
- [97] G. Wittstock, in *Lehrbuch der Elektrochemie: Grundlagen, Methoden, Materialien, Anwendungen*, WILEY-VCH GmbH, Weinheim, Germany, **2023**, pp. 25-84.
- [98] E. McCafferty, in *Introduction to Corrosion Science*, Springer New York, New York, NY, **2010**, pp. 73-93.

- [99] M. Asadikiya, S. G. Yang, Y. F. Zhang, C. Lemay, D. Apelian, Y. Zhongt, *J. Mater. Sci.* **2021**, *56*, 12093-12110.
- [100] H. Zhao, Y. Yin, Y. X. Wu, S. Y. Zhang, A. M. Mingers, D. Ponge, B. Gault, M. Rohwerder, D. Raabe, *Nat. Commun.* **2024**, *15*.
- [101] H. Luo, Z. M. Li, A. M. Mingers, D. Raabe, *Corros. Sci.* **2018**, *134*, 131-139.
- [102] X. J. Li, P. Zhou, H. Feng, Z. H. Jiang, H. B. Li, K. Ogle, *Corros. Sci.* **2022**, *196*.
- [103] U. R. Evans, C. V. King, *J. Electrochem. Soc.* **1961**, *108*, 94C.
- [104] E. McCafferty, in *Introduction to Corrosion Science*, Springer New York, New York, NY, **2010**, pp. 95-117.
- [105] B. Beverskog, I. Puigdomenech, *Corros. Sci.* **1997**, *39*, 43-57.
- [106] A. J. Bard, L. R. Faulkner, in *Electrochemical Methods: Fundamentals and Applications*, 2 ed., John Wiley & Sons, Inc., USA, **2001**, pp. 1-43.
- [107] E. McCafferty, in *Introduction to Corrosion Science*, Springer New York, New York, NY, **2010**, pp. 119-175.
- [108] G. Wittstock, in *Lehrbuch der Elektrochemie: Grundlagen, Methoden, Materialien, Anwendungen*, WILEY-VCH GmbH, Weinheim, Germany, **2023**, pp. 85-114.
- [109] G. S. Frankel, M. Rohwerder, in *Encyclopedia of Electrochemistry*, **2007**.
- [110] Z. Ahmad, in *Principles of Corrosion Engineering and Corrosion Control*, Butterworth-Heinemann, Oxford, United Kingdom, **2006**, pp. 57-119.
- [111] P. Pedferri, in *Corrosion Science and Engineering*, Springer International Publishing, Cham, Switzerland, **2018**, pp. 1-16.
- [112] H. Parangusan, J. Bhadra, N. Al-Thani, *Emerg. Mater.* **2021**, *4*, 1187-1203.
- [113] D. D. Macdonald, *Pure Appl. Chem.* **1999**, *71*, 951-978.
- [114] U. R. Evans, *J. Chem. Soc.* **1927**, 1020-1040.
- [115] B. Kabanov, R. Burstein, A. Frumkin, *Discuss. Faraday Soc.* **1947**, *1*, 259-269.
- [116] E. S. Snavely Jr, N. Hackerman, *Can. J. Chem.* **1959**, *37*, 268-275.
- [117] R. P. Frankenthal, *Electrochim. Acta* **1971**, *16*, 1845-1857.
- [118] P. F. King, H. H. Uhlig, *J. Phys. Chem.* **1959**, *63*, 2026-2032.
- [119] N. Hackerman, *Z. Elektrochem. angew. physik. Chem.* **1958**, *62*, 632-637.
- [120] K. Lutton, J. R. Scully, in *Encyclopedia of Interfacial Chemistry*, Elsevier, Oxford, United Kingdom, **2018**, pp. 284-290.
- [121] A. Larsson, G. D'Acunto, M. Vorobyova, G. Abbondanza, U. Lienert, Z. Hegedüs, A. Preobrajenski, L. R. Merte, J. Eidhagen, A. Delblanc, J. S. Pan, E. Lundgren, *J. Alloys Compd.* **2022**, *895*.
- [122] F. Di Franco, A. Zaffora, M. Santamaria, F. Di Quarto, in *Encyclopedia of Interfacial Chemistry*, Elsevier, Oxford, **2018**, pp. 26-40.
- [123] E. McCafferty, in *Introduction to Corrosion Science*, Springer New York, New York, NY, **2010**, pp. 209-262.
- [124] H.-J. Freund, M. Heyde, H. Kühlenbeck, N. Nilius, T. Risse, S. Schaueremann, T. Schmidt, S. Shaikhutdinov, M. Sterrer, in *Springer Handbook of Surface Science* (Eds.: M. Rocca, T. S. Rahman, L. Vattuone), Springer International Publishing, Cham, **2020**, pp. 267-328.
- [125] A. G. K. J. Revesz, in *Passivity of Metals*, The Electrochemical Society, Princeton, NJ, **1978**, pp. 137-155.
- [126] F. P. Fehlner, in *Passivity of Metals*, The Electrochemical Society, Princeton, NJ, **1978**, pp. 181-183.
- [127] C. L. Mcbee, J. Kruger, *Electrochim. Acta* **1972**, *17*, 1337-&.
- [128] P. B. Sewell, C. D. Stockbridge, M. Cohen, *J. Electrochem. Soc.* **1961**, *108*, 933-941.
- [129] M. Nagayama, M. Cohen, *J. Electrochem. Soc.* **1962**, *109*, 781-790.
- [130] M. Sakashita, N. Sato, *Denki Kagaku* **1977**, *45*, 744-745.
- [131] L. T. Wang, D. Mercier, S. Zanna, A. Seyeux, M. Laurent-Brocq, L. Perriere, I. Guillot, P. Marcus, *Corros. Sci.* **2020**, *167*.
- [132] P. R. Roberge, in *Corrosion Engineering*, 1st Edition ed., McGraw-Hill Education, New York, **2008**, pp. 147-206.
- [133] E. McCafferty, in *Introduction to Corrosion Science*, Springer New York, New York, NY, **2010**, pp. 263-313.

- [134] J. R. Gavele, in *Passivity of Metals* (Ed.: J. K. R. P. Frankenthal), The Electrochemical Society, Princeton, NJ, **1978**, pp. 285-327.
- [135] S. Cao, K. Yuan, L. Sun, in *Advances in Mechanical and Electronic Engineering* (Eds.: D. Jin, S. Lin), Springer Berlin Heidelberg, Berlin, Heidelberg, **2012**, pp. 517-522.
- [136] D. Starosvetsky, R. Armon, J. Yahalom, J. Starosvetsky, *Int. Biodeterior. Biodegrad.* **2001**, *47*, 79-87.
- [137] K. V. Akpanyung, R. T. Loto, *J. Phys. Conf. Ser.* **2019**, *1378*, 022088.
- [138] V. Nguyen, R. C. Newman, N. J. Laycock, *J. Electrochem. Soc.* **2022**, *169*.
- [139] H. H. Strehblow, *Mater. Corros.* **1976**, *27*, 792-799.
- [140] G. S. Frankel, *J. Electrochem. Soc.* **1998**, *145*, 2186.
- [141] D. D. Macdonald, *Electrochim. Acta* **2011**, *56*, 1761-1772.
- [142] D. D. Macdonald, *J. Electrochem. Soc.* **1992**, *139*, 3434.
- [143] W. Khalil, S. Haupt, H. H. Strehblow, *Werkst. Korros.* **1985**, *36*, 16-21.
- [144] S. Y. Yu, W. E. O'Grady, D. E. Ramaker, P. M. Natishan, *J. Electrochem. Soc.* **2000**, *147*, 2952-2958.
- [145] M. Bettayeb, V. Maurice, L. H. Klein, L. Lapeire, K. Verbeken, P. Marcus, *J. Electrochem. Soc.* **2018**, *165*, C835-C841.
- [146] E. McCafferty, in *Introduction to Corrosion Science*, Springer New York, New York, NY, **2010**, pp. 315-356.
- [147] D. Landolt, S. Mischler, M. Stemp, *Electrochim. Acta* **2001**, *46*, 3913-3929.
- [148] S. Huang, H. Huang, W. Li, D. Kim, S. Lu, X. Q. Li, E. Holmstrom, S. K. Kwon, L. Vitos, *Nat. Commun.* **2018**, *9*.
- [149] T. Yang, Y. L. Zhao, Y. Tong, Z. B. Jiao, J. Wei, J. X. Cai, X. D. Han, D. Chen, A. Hu, J. J. Kai, K. Lu, Y. Liu, C. T. Liu, *Science* **2018**, *362*, 933-+.
- [150] Z. J. Zhang, M. M. Mao, J. W. Wang, B. Gludovatz, Z. Zhang, S. X. Mao, E. P. George, Q. Yu, R. O. Ritchie, *Nat. Commun.* **2015**, *6*.
- [151] N. A. P. K. Kumar, C. Li, K. J. Leonard, H. Bei, S. J. Zinkle, *Acta Mater.* **2016**, *113*, 230-244.
- [152] Y. Z. Shi, B. Yang, X. Xie, J. Brechtel, K. A. Dahmen, P. K. Liaw, *Corros. Sci.* **2017**, *119*, 33-45.
- [153] R.-F. Zhao, B. Ren, B. Cai, Z.-X. Liu, G.-P. Zhang, J.-j. Zhang, *Results Phys.* **2019**, *15*, 102667.
- [154] Y. Y. Chen, T. Duval, U. D. Hung, J. W. Yeh, H. C. Shih, *Corros. Sci.* **2005**, *47*, 2257-2279.
- [155] W. D. Callister, D. G. Rethwisch, in *Materials science and engineering : an introduction*, 10th edition ed., Wiley, Hoboken, NJ, **2018**, pp. 347-404.
- [156] N. Birbilis, S. Choudhary, J. R. Scully, M. L. Taheri, *npj mater. degrad.* **2021**, *5*.
- [157] J. Qi, A. M. Cheung, S. J. Poon, *Sci. Rep.* **2019**, *9*.
- [158] W. H. Guo, J. Y. Li, M. F. Qi, Y. Z. Xu, H. R. Ezatpour, *J. Alloys Compd.* **2021**, *884*.
- [159] S. Shuang, Q. Yu, X. Gao, Q. F. He, J. Y. Zhang, S. Q. Shi, Y. Yang, *J. Mater. Sci. Technol.* **2022**, *109*, 197-208.
- [160] Y. Qiu, M. A. Gibson, H. L. Fraser, N. Birbilis, *Mater. Sci. Technol.* **2015**, *31*, 1235-1243.
- [161] N. Kumar, M. Fusco, M. Komarasamy, R. S. Mishra, M. Bourham, K. L. Murty, *J. Nucl. Mater.* **2017**, *495*, 154-163.
- [162] X. L. Shang, Z. J. Wang, F. He, J. C. Wang, J. J. Li, J. K. Yu, *Sci. China Technol. Sci.* **2018**, *61*, 189-196.
- [163] S. Sahu, O. J. Swanson, T. S. Li, A. Y. Gerard, J. R. Scully, G. S. Frankel, *Electrochim. Acta* **2020**, *354*.
- [164] J. Han, A. Y. Gerard, P. Lu, J. E. Saal, K. Ogle, J. R. Scully, *J. Electrochem. Soc.* **2022**, *169*.
- [165] Y. P. Sun, A. D. Lan, Z. Wang, M. Zhang, J. W. Qiao, *J. Phys. Chem. Solids* **2022**, *161*.
- [166] G. Y. Koga, N. Birbilis, G. Zepon, C. S. Kiminami, W. J. Botta, M. Kaufman, A. Clarke, F. G. Coury, *J. Alloys Compd.* **2021**, *884*.
- [167] J. W. Wang, W. H. Wen, J. Cheng, L. Y. Dai, S. Y. Li, X. H. Zhang, Y. Yang, H. X. Li, X. B. Hou, B. Wu, J. H. Wu, *Corros. Sci.* **2023**, *218*.

- [168] X. Z. Wang, Y. F. Wang, Z. B. Huang, Q. Zhou, H. F. Wang, *Metals* **2022**, *12*.
- [169] S. Gurel, M. B. Yagci, B. Bal, D. Canadinc, *Mater. Chem. Phys.* **2020**, *254*.
- [170] A. S. Navi, S. E. Haghighi, M. Haghpanahi, A. Momeni, *J. Bionic Eng.* **2021**, *18*, 118-127.
- [171] A. F. Murray, D. Bryan, D. A. Garfinkel, C. S. Jorgensen, N. Tang, W. L. N. C. Liyanage, E. A. Lass, Y. Yang, P. D. Rack, T. G. Denes, D. A. Gilbert, *Sci. Rep.* **2022**, *12*.
- [172] B. X. Wei, J. Y. Pang, J. Xu, C. Sun, H. W. Zhang, Z. Y. Wang, C. K. Yu, W. Ke, *J. Alloys Compd.* **2021**, *875*.
- [173] T. Hanawa, *Sci. Technol. Adv. Mater.* **2022**, *23*, 457-472.
- [174] R. P. Verma, *Mater. Today Proc.* **2020**, *26*, 3148-3151.
- [175] H. Matsuno, A. Yokoyama, F. Watari, M. Uo, T. Kawasaki, *Biomater.* **2001**, *22*, 1253-1262.
- [176] Y. T. Lou, C. D. Dai, W. W. Chang, H. C. Qian, L. Y. Huang, C. W. Du, D. W. Zhang, *Corros. Sci.* **2020**, *165*.
- [177] A. M. J. Popescu, F. Branzoi, M. Burada, I. Atkinson, I. Constantin, J. C. Moreno, F. Miculescu, D. Mitrica, I. C. Badea, M. T. Olaru, V. Constantin, *Coatings* **2022**, *12*.
- [178] Y. Wang, J. S. Jin, M. Zhang, X. Y. Wang, P. Gong, J. C. Zhang, J. C. Liu, *J. Alloys Compd.* **2021**, *858*.
- [179] D. C. Kong, L. Wang, G. L. Zhu, Y. Q. Zhou, X. Q. Ni, J. Song, L. Zhang, W. H. Wu, W. Wu, C. Man, D. Shu, B. D. Sun, C. F. Dong, *J. Mater. Sci. Technol.* **2023**, *138*, 171-182.
- [180] W. R. Wang, J. Q. Wang, H. G. Yi, W. Qi, Q. Peng, *Entropy* **2018**, *20*.
- [181] R. F. Zhao, B. Ren, B. Cai, Z. X. Liu, G. P. Zhang, J. J. Zhang, *Results Phys.* **2019**, *15*.
- [182] P. Muangtong, A. Rodchanarowan, D. Chaysuwan, N. Chanlek, R. Goodall, *Corros. Sci.* **2020**, *172*.
- [183] M. Izadi, M. Soltanieh, S. Alamolhoda, S. M. S. Aghamiri, M. Mehdizade, *Mater. Chem. Phys.* **2021**, *273*.
- [184] G. A. Gaber, S. A. Abolkassem, O. A. Elkady, M. Tash, L. Z. Mohamed, *Chem. Pap.* **2022**, *76*, 1675-1690.
- [185] A. Wetzel, M. von der Au, P. M. Dietrich, J. Radnik, O. Ozcan, J. Witt, *Appl. Surf. Sci.* **2022**, *601*, 154171.
- [186] C. N. Niu, C. R. LaRosa, J. S. Miao, M. J. Mills, M. Ghazisaeidi, *Nat. Commun.* **2018**, *9*.
- [187] A. Fu, B. Liu, W. J. Lu, B. Liu, J. Li, Q. H. Fang, Z. M. Li, Y. Liu, *Scr. Mater.* **2020**, *186*, 381-386.
- [188] F. Calvao, C. E. A. Mcdonald, M. Bolay, *Extr. Ind. Soc.* **2021**, *8*.
- [189] B. M. Intelligence, Cobalt Institute, **2023**.
- [190] L. Mancini, N. A. Eslava, M. Traverso, F. Mathieux, *Resour. Policy* **2021**, *71*.
- [191] S. Choudhary, S. Zhang, S. Thomas, N. Birbilis, *ECS Adv.* **2022**, *1*, 011501.
- [192] A. Wetzel, M. von der Au, P. M. Dietrich, J. Radnik, O. Ozcan, J. Witt, *Appl. Surf. Sci.* **2022**, *601*.
- [193] Y. Shi, B. Yang, X. Xie, J. Brechtel, K. A. Dahmen, P. K. Liaw, *Corros. Sci.* **2017**, *119*, 33-45.
- [194] Y. Qiu, S. Thomas, M. A. Gibson, H. L. Fraser, K. Pohl, N. Birbilis, *Corros. Sci.* **2018**, *133*, 386-396.
- [195] Y. Z. Shi, L. Collins, R. Feng, C. Zhang, N. Balke, P. K. Liaw, B. Yang, *Corros. Sci.* **2018**, *133*, 120-131.
- [196] K. C. Leonard, T. Seufferling, in *Encyclopedia of Electrochemistry*, **2021**, pp. 1-33.
- [197] P. R. Unwin, in *Encyclopedia of Electrochemistry*, **2007**.
- [198] E. J. Calvo, in *Encyclopedia of Electrochemistry*, **2007**.
- [199] E. McCafferty, *Corros. Sci.* **2005**, *47*, 3202-3215.
- [200] C. Wagner, W. Traud, *Z. Elektrochem. Angew. Phys. Chem.* **1938**, *44*, 391-402.
- [201] F. Mansfeld, *J. Electrochem. Soc.* **1973**, *120*, 515.
- [202] C. Toparli, A. Sarfraz, A. D. Wieck, M. Rohwerder, A. Erbe, *Electrochim. Acta* **2017**, *236*, 104-115.
- [203] I. Bösing, *npj mater. degrad.* **2023**, *7*, 53.

- [204] A. Larsson, A. Grespi, G. Abbondanza, J. Eidhagen, D. Gajdek, K. Simonov, X. Yue, U. Lienert, Z. Hegedüs, A. Jeromin, T. F. Keller, M. Scardamaglia, A. Shavorskiy, L. R. Merte, J. Pan, E. Lundgren, *Adv. Mater.* **2023**, *n/a*, 2304621.
- [205] B. Speiser, in *Encyclopedia of Electrochemistry*, **2007**.
- [206] V. S. Raja, in *Non-Destructive Evaluation of Corrosion and Corrosion-assisted Cracking*, **2019**, pp. 160-197.
- [207] S. Wang, J. Zhang, O. Gharbi, V. Vivier, M. Gao, M. E. Orazem, *Nat. Rev. Methods Primers* **2021**, *1*, 41.
- [208] A. C. Lazanas, M. I. Prodromidis, *ACS Meas. Sci. Au* **2023**, *3*, 162-193.
- [209] M. R. S. Abouzari, F. Berkemeier, G. Schmitz, D. Wilmer, *Solid State Ion.* **2009**, *180*, 922-927.
- [210] J. B. Jorcin, M. E. Orazem, N. Pébère, B. Tribollet, *Electrochim. Acta* **2006**, *51*, 1473-1479.
- [211] A. Lasia, in *Electrochemical Impedance Spectroscopy and its Applications* (Ed.: A. Lasia), Springer New York, New York, NY, **2014**, pp. 271-300.
- [212] JPK Instruments AG, Germany, **2017**.
- [213] B. Voigtländer, in *Atomic Force Microscopy*, Springer International Publishing, Cham, Switzerland, **2019**, pp. 1-13.
- [214] B. Voigtländer, in *Atomic Force Microscopy*, Springer International Publishing, Cham, Switzerland, **2019**, pp. 15-33.
- [215] B. Voigtländer, in *Atomic Force Microscopy*, Springer International Publishing, Cham, Switzerland, **2019**, pp. 35-67.
- [216] B. Voigtländer, in *Atomic Force Microscopy*, Springer International Publishing, Cham, Switzerland, **2019**, pp. 231-253.
- [217] T. Glatzel, U. Gysin, E. Meyer, *Microscopy* **2022**, *71*, i165-i173.
- [218] B. Voigtländer, in *Atomic Force Microscopy*, Springer International Publishing, Cham, Switzerland, **2019**, pp. 149-159.
- [219] JPK Instruments AG, Germany, **2016**.
- [220] D. Polcari, P. Dauphin-Ducharme, J. Mauzeroll, *Chem. Rev.* **2016**, *116*, 13234-13278.
- [221] R. J. Forster, in *Encyclopedia of Electrochemistry*, **2007**.
- [222] A. J. Bard, in *Scanning Electrochemical Microscopy*, 2 ed., CRC Press, Taylor and Francis Group, Boca Raton, FL, **2012**, pp. 1-14.
- [223] V. Radtke, C. Hess, R. M. Souto, J. Heinze, *Z Phys Chem* **2006**, *220*, 393-406.
- [224] R. Cornut, S. Nunige, C. Lefrou, F. Kanoufi, *Electrochim. Acta* **2011**, *56*, 10701-10707.
- [225] K. Eckhard, X. Chen, F. Turcu, W. Schuhmann, *Phys. Chem. Chem. Phys.* **2006**, *8*, 5359-5365.
- [226] J. J. Santana, J. González-Guzmán, L. Fernández-Mérida, S. González, R. M. Souto, *Electrochim. Acta* **2010**, *55*, 4488-4494.
- [227] E. E.-D. M. El-Giar, D. O. Wipf, *J. Electroanal. Chem.* **2007**, *609*, 147-154.
- [228] A. Ul-Hamid, in *A Beginners' Guide to Scanning Electron Microscopy*, Springer International Publishing, Cham, Switzerland, **2018**, pp. 1-14.
- [229] A. Ul-Hamid, in *A Beginners' Guide to Scanning Electron Microscopy*, Springer International Publishing, Cham, Switzerland, **2018**, pp. 15-76.
- [230] A. Ul-Hamid, in *A Beginners' Guide to Scanning Electron Microscopy*, Springer International Publishing, Cham, Switzerland, **2018**, pp. 77-128.
- [231] A. Ul-Hamid, in *A Beginners' Guide to Scanning Electron Microscopy*, Springer International Publishing, Cham, Switzerland, **2018**, pp. 233-264.
- [232] A. Ul-Hamid, in *A Beginners' Guide to Scanning Electron Microscopy*, Springer International Publishing, Cham, Switzerland, **2018**, pp. 265-307.
- [233] J. F. W. Watts, J., in *An Introduction to Surface Analysis by XPS and AES*, 2nd ed., John Wiley & Sons Ltd, **2020**, pp. 1-18.
- [234] L. Zhong, D. Chen, S. Zafeiratos, *Cat. Sci. Technol.* **2019**, *9*, 3851-3867.
- [235] Z. Liu, O. Höfft, A. S. Gödde, F. Endres, *J. Phys. Chem. C* **2021**, *125*, 26793-26800.
- [236] J. F. W. Watts, J., in *An Introduction to Surface Analysis by XPS and AES*, 2nd ed., John Wiley & Sons Ltd, **2020**, pp. 19-67.

- [237] P. van der Heide, in *X-Ray Photoelectron Spectroscopy*, John Wiley & Sons, Inc., **2011**, pp. 27-60.
- [238] M. C. Biesinger, B. P. Payne, A. P. Grosvenor, L. W. M. Lau, A. R. Gerson, R. S. Smart, *Appl. Surf. Sci.* **2011**, *257*, 2717-2730.
- [239] P. van der Heide, in *X-Ray Photoelectron Spectroscopy*, John Wiley & Sons, Inc., **2011**, pp. 61-99.
- [240] T. Van Acker, S. Theiner, E. Bolea-Fernandez, F. Vanhaecke, G. Koellensperger, *Nat. Rev. Methods Primers* **2023**, *3*.
- [241] S. J. Hill, A. Fisher, M. Liezers, in *Inductively Coupled Plasma Mass Spectrometry Handbook*, **2005**, pp. 1-25.
- [242] J. H. Batey, T. Prohaska, M. S. A. Horstwood, G. M. Nowell, H. Goenaga-Infante, G. C. Eiden, in *Inductively Coupled Plasma Mass Spectrometry Handbook*, **2005**, pp. 26-116.
- [243] F. D. Speck, A. Zagalskaya, V. Alexandrov, S. Cherevko, *Angew. Chem., Int. Ed.* **2021**, *60*, 13343-13349.
- [244] K. Huang, J. Xia, Y. Lu, B. Zhang, W. Shi, X. Cao, X. Zhang, L. M. Woods, C. Han, C. Chen, T. Wang, J. Wu, Y. Huang, *Adv. Sci.* **2023**, *10*, 2300094.
- [245] G. Laplanche, U. F. Volkert, G. Eggeler, E. P. George, *Oxid. Met.* **2016**, *85*, 629-645.
- [246] G. Laplanche, P. Gadaud, O. Horst, F. Otto, G. Eggeler, E. P. George, *J. Alloys Compd.* **2015**, *623*, 348-353.
- [247] N. Wurzler, O. Sobol, K. Altmann, J. Radnik, O. Ozcan, *Mater. Corros.* **2021**, *72*, 974-982.
- [248] L. ALS Co., web.
- [249] A. D. Bokare, W. Choi, *Environ. Sci. Technol.* **2011**, *45*, 9332-9338.
- [250] H. Peng, J. Guo, G. Li, Q. Z. Cheng, Y. J. Zhou, Z. H. Liu, C. Y. Tao, *Water Sci. Technol.* **2019**, *79*, 366-374.
- [251] S. B. Basame, H. S. White, *Langmuir* **1999**, *15*, 819-825.
- [252] K. H. Büchel, H. H. Moretto, P. Woditsch, in *Industrial Inorganic Chemistry*, **2000**, pp. 1-185.
- [253] Y. Qiu, S. Thomas, M. A. Gibson, H. L. Fraser, N. Birbilis, *npj mater. degrad.* **2017**, *1*.
- [254] W. T. Wei, J. Q. Xu, W. H. Chen, L. W. Mi, J. J. Zhang, *J. Mater. Chem. A* **2022**, *10*, 2637-2671.
- [255] N. C. f. B. Information, PubChem, **2023**.
- [256] F. Brownlie, T. Hodgkiess, A. Pearson, A. Galloway, in *Corros. Mater. Degrad., Vol. 3*, **2022**, pp. 101-126.
- [257] P. Li, M. Du, *Corros. Commun.* **2022**, *7*, 23-34.
- [258] K. Matsumura, M. Nishimoto, I. Muto, Y. Sugawara, *J. Electrochem. Soc.* **2022**, *169*.
- [259] S. Esmailzadeh, M. Aliofkhazraei, H. Sarlak, *Prot. Met. Phys. Chem. Surf.* **2018**, *54*, 976-989.
- [260] G. Sander, V. Cruz, N. Bhat, N. Birbilis, *Corros. Sci.* **2020**, *177*.
- [261] L. L. Shreir, in *Corrosion, Vol. 1*, 3 ed., Butterworth-Heinemann, Oxford, **1994**, pp. 55-117.
- [262] L. Ma, E. M. Pascalidou, F. Wiame, S. Zanna, V. Maurice, P. Marcus, *Corros. Sci.* **2020**, *167*.
- [263] J. Yang, J. Wu, C. Y. Zhang, S. D. Zhang, B. J. Yang, W. Emori, J. Q. Wang, *J. Alloys Compd.* **2020**, *819*.
- [264] E. McCafferty, in *Introduction to Corrosion Science*, Springer New York, New York, NY, **2010**, pp. 177-208.
- [265] J. Y. Wang, W. H. Li, H. L. Yang, H. Huang, S. X. Ji, J. M. Ruan, Z. L. Liu, *Corros. Sci.* **2020**, *177*.
- [266] Y. Fu, C. D. Dai, H. Luo, D. Y. Li, C. W. Du, X. G. Li, *Appl. Surf. Sci.* **2021**, *560*.
- [267] Y. Z. Shi, B. Yang, X. Xie, J. Brechtel, K. A. Dahmen, P. K. Liaw, *Corros. Sci.* **2017**, *119*, 33-45.
- [268] T. Yamashita, P. Hayes, *J. Electron Spectrosc. Relat. Phenom.* **2006**, *152*, 6-11.
- [269] P. S. Bagus, C. J. Nelin, C. R. Brundle, B. V. Crist, N. Lahiri, K. M. Rosso, *J. Chem. Phys.* **2021**, *154*.

- [270] C. O. A. Olsson, D. Landolt, *Electrochim. Acta* **2003**, *48*, 1093-1104.
- [271] A. Kocijan, C. Donik, M. Jenko, *Corros. Sci.* **2007**, *49*, 2083-2098.
- [272] S. Tanuma, C. J. Powell, D. R. Penn, *Surf. Interface Anal.* **1991**, *17*, 911-926.
- [273] C. J. Powell, A. Jablonski, Version 1.2, SRD 71 ed. (Ed.: N. A. o. S. a. Technology), Gaithersburg, MD, **2010**.
- [274] S. Joiret, M. Keddou, X. R. Nóvoa, M. C. Pérez, C. Rangel, H. Takenouti, *Cem. Concr. Compos.* **2002**, *24*, 7-15.
- [275] Y. M. Chen, N. G. Rudawski, E. Lambers, M. E. Orazem, *J. Electrochem. Soc.* **2017**, *164*, C563-C573.
- [276] W. R. Wang, J. Q. Wang, Z. H. Sun, J. T. Li, L. F. Li, X. Song, X. D. Wen, L. Xie, X. Yang, *J. Alloys Compd.* **2020**, *812*.
- [277] M. Ray, V. B. Singh, *J. Electrochem. Soc.* **2011**, *158*, C359-C368.
- [278] Z. H. Han, W. N. Ren, J. Yang, A. Tian, Y. Z. Du, G. Liu, R. Wei, G. J. Zhang, Y. Q. Chen, *J. Alloys Compd.* **2020**, *816*.
- [279] C. A. Della Rovere, J. H. Alano, R. Silva, P. A. P. Nascente, J. Otubo, S. E. Kuri, *Corros. Sci.* **2012**, *57*, 154-161.
- [280] S. A. Makhlof, Z. H. Bakr, H. Al-Attar, M. S. Moustafa, *Mater. Sci. Eng. B* **2013**, *178*, 337-343.
- [281] M. M. Abdullah, F. M. Rajab, S. M. Al-Abbas, *AIP Adv.* **2014**, *4*.
- [282] B. Hirschorn, M. E. Orazem, B. Tribollet, V. Vivier, I. Frateur, M. Musiani, *J. Electrochem. Soc.* **2010**, *157*, C458-C463.
- [283] N. E. Hakiki, M. D. Belo, A. M. P. Simoes, M. G. S. Ferreira, *J. Electrochem. Soc.* **1998**, *145*, 3821-3829.
- [284] X. X. Yu, A. Gulec, K. L. Cwalina, J. R. Scully, L. D. Marks, *Corrosion* **2019**, *75*, 616-627.
- [285] M. M. Alsalem, S. Camilla, M. P. Ryan, K. S. Campbell, *Ind. Eng. Chem. Res.* **2021**, *60*, 12032-12048.
- [286] M. Bojinov, G. Fabricius, P. Kinnunen, T. Laitinen, K. Makela, T. Saario, G. Sundholm, K. Yliniemi, *Electrochim. Acta* **2002**, *47*, 1697-1712.
- [287] S. Choudhary, K. Ogle, O. Gharbi, S. Thomas, N. Birbilis, *Electrochem, Sci. Adv.* **2021**, *n/a*, e2100196.
- [288] L. Yao, X. L. Fan, C. Yan, T. Kurtén, K. R. Daellenbach, C. Li, Y. H. Wang, Y. S. Guo, L. Dada, M. P. Rissanen, J. Cai, Y. J. Tham, Q. Z. Zha, S. J. Zhang, W. Du, M. Yu, F. X. Zheng, Y. Zhou, J. Kontkanen, T. Chan, J. L. Shen, J. T. Kujansuu, J. Kangasluoma, J. K. Jiang, L. Wang, D. R. Worsnop, T. Petäjä, V. M. Kerminen, Y. C. Liu, B. W. Chu, H. He, M. Kulmala, F. Bianchi, *Environ. Sci. Tech. Lett.* **2020**, *7*, 809-818.
- [289] D. Knotkova, K. Barton, *Atmos. Environ.* **1992**, *26*, 3169-3177.
- [290] N. Ismail, F. J. Qin, C. H. Fang, D. Liu, B. H. Liu, X. Y. Liu, Z. L. Wu, Z. Chen, W. X. Chen, *Aggregate* **2021**, *2*.
- [291] S. Feliu, M. J. Bartolomé, J. A. González, S. Feliu, *J. Electrochem. Soc.* **2007**, *154*, C241-C248.
- [292] T. A. Hemkemeier, F. C. R. Almeida, A. Sales, A. J. Klemm, *Case Stud. Constr. Mater.* **2022**, *16*.
- [293] D. N. G. Krishna, J. Philip, *Appl. Surf. Sci. Adv.* **2022**, *12*.
- [294] J. I. Goldstein, D. E. Newbury, J. R. Michael, N. W. M. Ritchie, J. H. J. Scott, D. C. Joy, in *Scanning Electron Microscopy and X-Ray Microanalysis*, Springer New York, New York, NY, **2018**, pp. 1-14.
- [295] S. Choudhary, K. Ogle, O. Gharbi, S. Thomas, N. Birbilis, *Electrochem, Sci. Adv.* **2022**, *2*, e2100196.
- [296] S. Choudhary, S. Thomas, D. D. Macdonald, N. Birbilis, *J. Electrochem. Soc.* **2021**, *168*.
- [297] S. Cherevko, A. R. Zeradjanin, A. A. Topalov, N. Kulyk, I. Katsounaros, K. J. J. Mayrhofer, *ChemCatChem* **2014**, *6*, 2219-2223.
- [298] T. Binninger, R. Mohamed, K. Waltar, E. Fabbri, P. Levecque, R. Kotz, T. J. Schmidt, *Sci. Rep.* **2015**, *5*.

- [299] F. M. Li, L. Huang, S. Zaman, W. Guo, H. F. Liu, X. P. Guo, B. Y. Xia, *Adv. Mater.* **2022**, *34*.
- [300] A. Larsson, A. Grespi, G. Abbondanza, J. Eidhagen, D. Gajdek, K. Simonov, X. Q. Yue, U. Lienert, Z. Hegedus, A. Jeromin, T. F. Keller, M. Scardamaglia, A. Shavorskiy, L. R. Merte, J. S. Pan, E. Lundgren, *Adv. Mater.* **2023**.
- [301] G. L. Song, *Corros. Sci.* **2005**, *47*, 1953-1987.
- [302] A. Fattah-Alhosseini, A. Saatchi, M. A. Golozar, K. Raeissi, *Electrochim. Acta* **2009**, *54*, 3645-3650.
- [303] J. Zhang, T. Quast, W. H. He, S. Dieckhofer, J. R. C. Junqueira, D. Ohi, P. Wilde, D. Jambrec, Y. T. Chen, W. Schuhmann, *Adv. Mater.* **2022**, *34*.
- [304] I. A. Cechanaviciute, R. P. Antony, O. A. Krysiak, T. Quast, S. Dieckhofer, S. Saddeler, P. Telaar, Y. T. Chen, M. Muhler, W. Schuhmann, *Angew. Chem., Int. Ed.* **2023**.
- [305] J. P. Kollender, M. Voith, S. Schneiderbauer, A. I. Mardare, A. W. Hassel, *J. Electroanal. Chem.* **2015**, *740*, 53-60.
- [306] A. I. Mardare, J. P. Kollender, M. Hafner, A. W. Hassel, *Electrochem. Commun.* **2015**, *59*, 5-8.
- [307] K. Ogle, S. Weber, *J. Electrochem. Soc.* **2000**, *147*, 1770-1780.
- [308] M. M. Lohrengel, C. Rosenkranz, I. Kluppel, A. Moehring, H. Bettermann, B. Van den Bossche, J. Deconinck, *Electrochim. Acta* **2004**, *49*, 2863-2870.
- [309] N. Ott, P. Schmutz, C. Ludwig, A. Ulrich, *Corros. Sci.* **2013**, *75*, 201-211.
- [310] N. Ott, A. Beni, A. Ulrich, C. Ludwig, P. Schmutz, *Talanta* **2014**, *120*, 230-238.
- [311] J. H. Huang, S. B. Scott, I. Chorkendorff, Z. H. Wen, *ACS Catal.* **2021**, *11*, 12745-12753.
- [312] J. Deng, M. R. Nellist, M. B. Stevens, C. Dette, Y. Wang, S. W. Boettcher, *Nano Lett.* **2017**, *17*, 6922-6926.
- [313] J. T. Mefford, A. R. Akbashev, M. K. Kang, C. L. Bentley, W. E. Gent, H. T. D. Deng, D. H. Alsem, Y. S. Yu, N. J. Salmon, D. A. Shapiro, P. R. Unwin, W. C. Chueh, *Nature* **2021**, *593*, 67-+.
- [314] S. H. Wang, Q. Jiang, S. H. Ju, C. S. Hsu, H. M. Chen, D. Zhang, F. Song, *Nat. Commun.* **2022**, *13*.
- [315] T. K. Liu, C. H. Li, M. Olszta, J. H. Tao, A. Devaraj, *npj mater. degrad.* **2023**, *7*.
- [316] K. A. Lill, K. Fushimi, M. Seo, A. W. Hassel, *J. Appl. Electrochem.* **2008**, *38*, 1339-1345.
- [317] M. Hampel, M. Schenderlein, C. Schary, M. Dimper, O. Ozcan, *Electrochem. Commun.* **2019**, *101*, 52-55.
- [318] H. Bulter, G. Denuault, S. Matefi-Tempfli, M. Matefi-Tempfli, C. Dosche, G. Wittstock, *Electrochim. Acta* **2016**, *222*, 1326-1334.
- [319] R. M. Souto, Y. Gonzalez-Garcia, S. Gonzalez, *Corros. Sci.* **2005**, *47*, 3312-3323.
- [320] X. X. Chen, A. J. R. Botz, J. Masa, W. Schuhmann, *J. Solid State Electrochem.* **2016**, *20*, 1019-1027.
- [321] B. N. Khirak, M. Mojaddami, Z. Z. Faradonbeh, A. O. Zekiy, A. Simchi, *Energy Fuels* **2022**, *36*, 4502-4509.
- [322] W. W. Cao, X. Y. Yang, W. J. Dai, B. Wu, Y. D. Zhang, C. J. Zhao, Y. W. Sui, S. F. Huang, *New J. Chem.* **2023**, *47*, 12670-12677.
- [323] A. Kumar, M. Mucalo, L. Bolzoni, Y. M. Li, Y. D. Qu, F. Yang, *Int. J. Hydrog. Energy* **2023**, *48*, 25755-25769.
- [324] M. Mucalo, L. Bolzoni, Y. Qu, A. Kumar, Y. Li, F. Yang, *Mater. Today Sustain.* **2023**, *22*.
- [325] J. Kwon, S. Sun, S. Choi, K. Lee, S. Jo, K. Park, Y. K. Kim, H. B. Park, H. Y. Park, J. H. Jang, H. Han, U. Paik, T. S. Song, *Adv. Mater.* **2023**, *35*.
- [326] A. Wetzal, D. Morell, M. von der Au, G. Wittstock, O. Ozcan, J. Witt, *Angewandte Chemie International Edition* **2024**, e202317058.
- [327] A. Wetzal, D. Morell, M. von der Au, J. Witt, O. Ozcan, *Chemelectrochem* **2024**, *n/a*, e202400346.
- [328] Y. Shen, M. Trauble, G. Wittstock, *Anal. Chem.* **2008**, *80*, 750-759.
- [329] B. Beverskog, I. Puigdomenech, *Corros. Sci.* **1997**, *39*, 969-980.

- [330] E. M. Garcia, J. S. Santos, E. C. Pereira, M. B. J. G. Freitas, *J. Power Sources* **2008**, *185*, 549-553.
- [331] G. Inzelt, in *Encyclopedia of Applied Electrochemistry*, Springer New York, New York, NY, **2014**, pp. 207-214.
- [332] F. Y. Chen, Z. Y. Wu, Z. Adler, H. T. Wang, *Joule* **2021**, *5*, 1704-1731.
- [333] A. Kapalka, G. Fóti, C. Comninellis, *Electrochem. Commun.* **2008**, *10*, 607-610.
- [334] L. H. Zhang, Q. Fan, K. Li, S. Zhang, X. B. Ma, *Sustain. Energy Fuels* **2020**, *4*, 5417-5432.
- [335] K. X. Zhang, R. Q. Zou, *Small* **2021**, *17*.
- [336] L. G. Li, P. T. Wang, Q. Shao, X. Q. Huang, *Adv. Mater.* **2021**, *33*.
- [337] I. Betova, M. Bojinov, T. Laitinen, K. Makela, P. Pohjanne, T. Saario, *Corros. Sci.* **2002**, *44*, 2675-2697.
- [338] A. I. Karayan, E. Maya-Visuet, H. Castaneda, *J. Solid State Electrochem.* **2014**, *18*, 3191-3202.
- [339] S. Anantharaj, S. Noda, *Chemelectrochem* **2020**, *7*, 2297-2308.
- [340] X. Y. Hou, L. L. Gao, Z. D. Cui, J. H. Yin, *Iop C Ser Earth Env* **2018**, *108*.
- [341] W. S. Alloys.
- [342] Metalcor.
- [343] D. Y. Jiang, L. C. Xie, L. Q. Wang, *J. Mater. Res. Technol.* **2023**, *26*, 1341-1374.
- [344] S. Lee, K. Banjac, M. Lingenfelder, X. L. Hu, *Angew. Chem., Int. Ed.* **2019**, *58*, 10295-10299.
- [345] M. M. Abdullah, F. M. Rajab, S. M. Al-Abbas, *AIP Adv.* **2014**, *4*.
- [346] E. Kareem Jassem, A. Mustafa Abdul Majeed, N. Mossa Umran, *J. Phys. Conf. Ser.* **2019**, *1279*, 012004.
- [347] I. Sulania, J. Kaswan, V. Attatappa, R. K. Karn, D. C. Agarwal, D. Kanjilal, *AIP Conf.* **2016**, *1731*, 120021.
- [348] J. van Elp, J. L. Wieland, H. Eskes, P. Kuiper, G. A. Sawatzky, F. M. F. de Groot, T. S. Turner, *Phys. Rev. B* **1991**, *44*, 6090-6103.

13 Own Publications and Conference Contributions

13.1 Publications

- [X1] A. Wetzel, A.M. Jones. Electrically Driven N(sp²)-C(sp^{2/3}) Bond Cleavages of Sulfonamides. ACS Sustainable Chem. Eng., **2020**, 8, 8, 3487-3493.
- [X2] Wetzel A, Ozcan O, Witt J, von der Au M., Dietrich P. M., Radnik J., The comparison of the corrosion behavior of the CrCoNi medium entropy alloy and CrMnFeCoNi high entropy alloy. Journal article; Appl. Surf. Sci., **2022**, 601, 154171.
- [X3] J. Czerski, M. Mitoraj-Królkowska, E. Godlewska, A. Wetzel, J. Witt, O. Ozcan, M. Marzec, M. Goly, Corrosion and passivation of AlCrFe₂Ni₂Mo_x high-entropy alloys in sulphuric acid; Corr. Sci., **2024**, 229, 111855.
- [X4] A. Wetzel, M. von der Au, G. Wittstock, O. Ozcan, J. Witt. Transpassive Metal Dissolution vs. Oxygen Evolution Reaction: Implication for Alloy Stability and Electrocatalysis. Angew. Chem., Int. Ed., **2024**, e202317058.
- [X5] A. Wetzel, D. Morell, M. von der Au, O. Ozcan, J. Witt. Transpassive Behavior of Equimolar CrMnFeCoNi and CrCoNi Multi-Principal Element Alloys in an Alkaline NaCl Electrolyte. ChemElectroChem, **2024**, e202400346. (published after acceptance of dissertation)
- [X6] A. Wetzel, A. Hans, G. Wittstock, I. Brand, O. Ozcan, J. Witt. Long term corrosion studies of CrCoNi and CrMnFeCoNi in sulfuric acid. (In Progress).

13.2 Conference Contributions

- [Y1] A. Wetzel, O. Ozcan, J. Witt, M. Rhode. Local corrosion properties of high/medium entropy alloys in aqueous environments. Eurocorr 2020; 7-11 September 2020; Online Conference – Oral Presentation
- [Y2] M. Rhode, A. Wetzel, O. Ozcan, J. Nietzke, T. Richter, D. Schröpfer D. Hydrogen diffusion and local Volta potential in high- and medium-entropy alloys. Symposium on Materials and Joining Technology; 7-8 September 2020; Online Conference – Editor contribution
- [Y3] A. Wetzel, O. Ozcan, J. Witt, M. Rhode. Corrosion Properties and Protective Oxide Film Characteristics of CrMnFeCoNi High Entropy Alloy and CrCoNi Medium Entropy Alloy. ISE Annual 72nd meeting; 29 August – 3 September 2021; Online Conference – Oral Presentation
- [Y4] A. Wetzel, O. Ozcan, J. Witt, M. Rhode M. Corrosion Properties and Protective Oxide Film Characteristics of CrMnFeCoNi High Entropy Alloy and CrCoNi Medium Entropy Alloy. EuroMat 2021; 12-16 September 2021; Online Conference – Oral Presentation
- [Y5] A. Wetzel, O. Ozcan, J. Witt, M. Rhode. Corrosion Properties and Protective Oxide Film Characteristics of CrMnFeCoNi High Entropy Alloy and CrCoNi Medium Entropy Alloy. Eurocorr 2021; 20-24 September 2021; Online Conference – Oral Presentation
- [Y6] A. Wetzel, O. Ozcan, J. Witt, M. Rhode. Corrosion Properties and Protective Oxide Film Characteristics of CrMnFeCoNi High Entropy Alloy and CrCoNi Medium Entropy Alloy. MRS Spring Meeting 2022, Honolulu, Hawaii; 8-13 May 2022; Conference – Oral Presentation
- [Y7] A. Wetzel, O. Ozcan, J. Witt, M. Rhode. Local corrosion characteristics of CrMnFeCoNi High Entropy Alloy and CrCoNi Medium Entropy Alloy and their respective welded joints. Eurocorr 2022; Berlin, Germany; 28 August – 1 September 2022; Conference – Oral Presentation
- [Y8] A. Wetzel, O. Ozcan, J. Witt, D. Morell. The Mechanism of Passivation Breakdown of High and Medium Entropy Alloys in Aqueous NaCl Electrolytes at Different pH. GDCh Electrochemistry 2022; Berlin, Germany; 27-30 September 2022; Conference – Oral Presentation

- [Y9] A. Wetzel, O. Ozcan, J. Witt, D. Morell. Corrosion Properties of Medium Entropy Alloys under Oxygen Evolution Reaction Conditions in Aqueous Electrolytes. MRS Spring Meeting 2023; San Francisco, California, USA; 10-14 April 2023; Conference – Oral Presentation
- [Y10] A. Wetzel, O. Ozcan, Y. Yesilcicek. Old materials, New Life - Using Diffusion-Controlled Synthesis for Discovery of Novel Alloy Systems. MRS Spring Meeting 2023; San Francisco, California, USA; 10-14 April 2023; Conference – Oral Presentation
- [Y11] A. Wetzel, O. Ozcan, J. Witt, D. Morell. Passivation Breakdown of Multi Principal Element Alloys in Aqueous NaCl Electrolytes at Different pH. Eurocorr 2023; Brussels; 27-31 August 2023; Conference – Poster Contribution
- [Y12] A. Wetzel, O. Ozcan, J. Witt, D. Morell. The Interplay of Anodic Dissolution and Oxygen Evolution of Medium Entropy Alloys in Artificial Seawater. ECS Meeting 2023; Gothenburg; 8-10 October 2023; Conference – Oral Presentation and Young Researcher's Pitch

14 Curriculum Vitae

Personal Data

Name	Annica Wetzel
Date of Birth	04.08.1993
Place of Birth	Berlin
Nationality	German

Education

2020 - 2024 *PhD Project, Bundesanstalt für Materialforschung und -prüfung, Berlin*
Topic: "Corrosion Susceptibility of Multi Principal Element Alloys and their Weld Joints in Aqueous Environments"

2015 – 2019: Integrated Master Course, *Chemistry with Business Management*, University of Birmingham, Master in Science (Honours, Class II (Division I); GPA: 3.25)
Topic Bachelor Thesis: "DNA-Sequencing through Nanopore-Based Technology"
Topic Master Thesis: "Dealkylation and α -Carbon Functionalisation of Sulfonamides through Organic Electrochemistry"

2012 – 2015: Accredited Chemical Lab Assistant (Final Score: 93 Points), *Vocational Training*, (Institutes: OSZ Lise Meitner in Berlin, BBZ Chemie Berlin; Firma: Atotech Deutschland GmbH in Neuruppin and Berlin)

2006 – 2012: *Allgemeine Hochschulreife/Abitur*, Friedlieb Ferdinand Runge Gymnasium in Oranienburg (Final Grade: 1,3)

Ich versichere hiermit, dass ich diese Arbeit selbständig verfasst habe und nur die angegebene Quellen benutzt wurden. Während des Arbeitens an der Dissertation sind die unter „13.1 Publications“ aufgelisteten Veröffentlichungen entstanden. Veröffentlichte Ergebnisse aus dieser Arbeit wurden an den gegebenen Stellen dementsprechend deklariert. Die Leitlinien der guten wissenschaftlichen Praxis der Carl von Ossietzky Universität Oldenburg sind mir bekannt und wurden zur Fertigung dieser Arbeit befolgt. Des Weiteren bestätige ich, dass ich im Zusammenhang mit dem Promotionsvorhaben keine kommerziellen Vermittlungs- oder Beratungsdienste (Promotionsberatung) in Anspruch genommen habe. Die Dissertation hat weder zu Teilen noch in Gänze einer anderen wissenschaftlichen Hochschule zur Begutachtung in einem Promotionsverfahren vorgelegen.

Annica Wetzel

Berlin, 08.04.2024